HEPATIC PHOSPHOLIPID REMODELING IN METABOLIC DISORDERS

BY

YE TIAN

DISSERTATION

Submitted in partial fulfillment of the requirements
for the degree of Doctor of Philosophy in VMS - Comparative Biosciences
in the Graduate College of the
University of Illinois Urbana-Champaign, 2023

Urbana, Illinois

Doctoral Committee:

Assistant Professor Bo Wang, Chair
Associate Professor Sayeepriyadarshini Anakk
Associate Professor Erik R. Nelson
Professor Michael J. Spinella

ABSTRACT

Biological membrane is critical to various cellular functions and metabolic processes. Since the fluid-mosaic model of the lipid bilayer was proposed, myriad research investigated the interaction between membrane and proteins. However, the roles of phospholipid (PL), the main fabric of membrane, on pathophysiology have until recently remained unclear. Non-alcoholic fatty liver disease (NAFLD) is a metabolic syndrome with growing impact on global health. Recent studies have reported that hepatic PL composition in human NAFLD patients was significantly altered, suggesting potential pathological role of membrane PL composition[2,3]. Fatty acyl composition of PLs in the liver is controlled by the Lands' cycle where the fatty acyl chain in *sn-2* site will be substituted preferentially with polyunsaturated fatty acids (PUFA) by lysophosphatidylcholine acyltransferases 3 (LPCAT3)[4]. Here, we show that the expression of *LPCAT3* is dramatically suppressed in human NASH livers compared to controls. *LPCAT3* expression is inversely correlated with NAFLD activity score and fibrosis stage. Loss of *Lpcat3* in mouse liver promotes the development of both spontaneous and diet-induced NASH/HCC. Mechanistically, *Lpcat3* deficiency increases reactive oxygen species production, likely due to impaired mitochondrial homeostasis as demonstrated by reduced mitochondrial DNA content and fragmented mitochondrial morphology. Moreover, overexpressing *Lpcat3* in the liver ameliorates inflammation and fibrosis of NASH, suggesting that manipulating *LPCAT3* expression may be an effective therapeutic strategy for NASH. Interestingly, despite the promotion of NASH, mice with hepatic *Lpcat3* depletion exhibited significantly reduced blood glucose level with improved systemic metabolism. We demonstrated that hyperinsulinemia induced by high-fat diet (HFD) feeding augments hepatic Lpcat3 expression and membrane unsaturation. Loss of *Lpcat3* in the liver improves insulin resistance and blunts lipogenesis in both HFD-fed and genetic *ob/ob* mouse models. Mechanistically, *Lpcat3* deficiency directly facilitates insulin receptor endocytosis, signal transduction and hepatic glucose production suppression, and indirectly enhances fibroblast growth factor 21 (FGF21) secretion, energy expenditure, and glucose uptake in adipose tissue. These findings identify hepatic LPCAT3 and membrane phospholipid composition as a novel regulator of insulin sensitivity and energy metabolism. The dissociation between NASH and insulin resistance in Lpcat3 liver knockout mice recapitulated the phenotype of a subpopulation of NASH patients and shed light on the pathogenesis of metabolic disorders.

Key Words: Phospholipid; Insulin resistance; Non-alcoholic steatohepatitis (NASH); Mitochondria; Lipid metabolism

ACKNOWLEDGEMENT

First, I would like to thank the patient and dedicated mentorship from my advisor Dr. Bo Wang, without whose help this work would never become possible. He helped me with every detailed experiment when I first came into this lab five years ago as a total amateur in this field. He tolerates mistakes, encourages exploration, and is always there to help. I deeply appreciate his support and suggestions on my naïve ideas and career choices. He is no doubt the best mentor I have ever met and makes my journey here valuable and fruitful. I would also like to thank my committee members Dr. Sayee Anakk, Dr. Erik Nelson and Dr. Michael Spinella, who helped me a lot in my research and career development and always be nice to me at every meeting. Thank Dr. Jing Yang for his help and suggestions along the years. They are all great mentors who guided me through this journey of exploration, where I learned so much that makes me a different person than five years ago. I acknowledge the funding resources from NIH, Pfizer, UIUC cancer center and the department of comparative biosciences, without which this research could not be realized. I thank Karen Doty for her generous help on any questions I have regarding histology. I would like to thank other persons who also helped with experiments in this research, Hui Xu from Cancer Center who helped the Seahorse assay and Figen Seiler from UIC who helped with electron microscopy,

I would like to thank all my lab mates (and lunch mates), Wei, Ray, Kevin, Zhiming and Kaylie, and collaborators. They helped me a lot in my research every day and became the first one I talked to when there was a problem. There are also many names from neighboring labs that I don't have space here to recognize everyone, but I will remember all their helps these years. They are always generous and kind to help and we become friends outside of labs.

My families are the most solid support all the time even though were separated by the pandemic for four and a half years. During those years, I missed the funeral of my grandpa, who I grew up

with and was the one in my family that would listen carefully to my research. He had the most expectations of my career and was always waiting for my progressions. Missing him is the deepest scar in my heart that I will never forget. I hope this thesis can console him and make him proud.

I would also like to thank the group of friends I made here. The basketball game every week with them is critical to keeping me physically healthy. The small parties every week with them, on the other hand, keep me mentally healthy in this small town. There is an old Chinese saying, “rely on parents at home, rely on friends when out.” They helped me in my life, and I wish they all have a bright future.

Last but not least, I would like to thank my girlfriend, and sooner my wife, Jingyu, for her support, companion and lover for six years. All these years she was in China, and I am here. We overcame distance and time with devotion and understanding. She is also my best friend that I talk to every day about everything that happens in our lives. We commute thoughts about research, life, and the future, making her one of the most important parts of my life. There are tons of sparkling moments that fly before my eyes, and I shall use the rest of my life to answer.

I wish humans could solve the secret of life. I wish this planet could be free of wars. I wish every endeavor could pay off. I wish everyone is loved.

TABLE OF CONTENTS

CHAPTER 1: BACKGROUND AND SIGNIFICANCE

1.1 MEMBRANE SYSTEM IN THE CELL

Every biological system has boundaries, which in most cases are cell membranes. The understanding of membranes deepens along with the advancement of technologies since 1950s, when the nature of cell membranes as lipid bilayers was confirmed. The modern framework of cell membranes stems from the fluid mosaic model, proposed by S.J. Singer and G.L. Nicolson in 1972[6]. In this model, the cell membranes are "two-dimensional solutions of oriented globular proteins and lipids" with heterogeneity and interactions between components. The fifty years since then have seen the vigorous development and success of this model in the pathophysiological context and become the basis of our research.

1.1.1 Composition and Structure of Biological Membranes

Diverse membrane composition has been observed in different cell types, implying its importance in conveying different biological functions. Within a cell, the membranes of different organelles are continuous yet diverse in composition, which is maintained by various machineries against diffusion. The composition of different membrane systems is shown in Table 1. Phospholipids (PLs) are the major component forming the matrix of biological membranes. Most PL species contain a hydrophilic head group and two hydrophobic fatty acyl tails, except for cardiolipins, which contains four fatty acyl chains and mainly exists in mitochondria (Figure 1.1A). PLs differ in the length and saturation (number of double bonds) of fatty acyl chains and in their head groups, classifying PLs into phosphatidylcholine (PC), phosphatidylethanolamine (PE), phosphatidylserine (PS) and phosphatidylinositol (PI). Sphingolipids are also critical membrane components which have similar structure to PLs with two fatty acyl chains and a hydrophilic head.

Cholesterol presents between membrane leaflets due to its hydrophobic property and it regulates the membrane fluidity by interaction with other lipids of the membrane (Figure 1.1B).

Biological membranes systems set the boundary of a cell and compartmentalize functionally distinct cellular spaces. The structural basis of cellular membrane is lipid bilayer, with exceptions such as lipid droplets. The membranes are not homogeneous. Lipids in the membrane interact with proteins and other lipid molecules to form membrane subdomains where saturated phospholipids, sphingolipids and cholesterol are enriched (Figure 1.1C). The observation of this lateral heterogeneity of biological membranes dates back to the proposal of fluid mosaic model[6,7]. These microdomains, also known as lipid rafts, are thicker and varies in size of 10-200 nm with packed membrane structure and reduced fluidity[8,9]. About 35% of membrane proteins are associated with lipid rafts[10], including GPI-anchored proteins and palmitoylated proteins. The biological function of this segregation includes increasing the concentration of signaling receptors and inducing conformational change[9]. However, due to the difficulties in defining lipid raft, it is still mysterious how membrane microdomains participate in various cellular processes and disease pathogenesis.

The membranes are not flat either. The curvature of the membrane is required for membrane contact, fusion and budding, which are required for vesicle transportation and endocytosis. The membrane curvature forms through different mechanisms. Caveolae are small pits in the inner side of the plasma membrane formed by oligomerized caveolins, which are fatty-acylated proteins that are anchored to the cholesterol-rich membrane domains[11]. Unlike transient lipid rafts, caveolae are maintained for long periods and can be internalized with the participation of dynamin, Src kinases, protein kinase C (PKC) and actin recruitment[12]. As a consequence of this endocytosis, caveolin can also be found in the ER and Golgi, and it can be recycled back to plasma membrane. However, the regulation of this process remains obscure. Caveolae has been shown to participate in the regulation of cellular lipids. It relocates to lipid droplets in response to cholesterol treatment[13]. One evidence is the abundancy of caveolae in adipocytes. Previous studies shown that *Cav1*, gene that encodes caveolin1, are associated with fatty acid uptake and storage[12]. Recent data also implies that caveolin-associated membrane microdomain modulates insulin signaling and insulin receptor trafficing[14,15]. However, the detailed mechanism of how caveolae participates in lipid metabolism still requires further investigation.

The curvature of membrane can also be determined by other proteins and PL composition. The relative size of the head group and hydrophobic tails of lipids affects the shape of the lipid and the spontaneous curvature of the membrane. For example, conical PL such as PE, whose head is smaller than the tails, tends to form negative curvature, whereas inverted-conical lipids such as lysoPLs tends to form positive curvatures[5]. PUFAs in the PLs can reduce membrane bending rigidity, facilitating cellular processes that requires membrane deformation, including endocytosis and lipoprotein assembly[16,17]. Proteins associated with membrane curvature include BAR domain containing proteins and septins. BAR domain proteins can assemble into a crescent-shaped scaffold that binds to the membrane surface, forcing the membrane to bend[18]. Septins are a family of GTP-binding proteins that can form hetero-oligomeric complexes at curved regions of the plasma membrane and participate in cell division, exocytosis and phagocytosis[19].

1.1.2 Dynamics and Regulation of Membrane Composition

The composition of cell membrane system is tightly regulated due to its close association with the biophysical properties of membrane and its subsequent effect on cellular processes including signal transduction, energy metabolism and protein synthesis. This regulation is mainly realized through the control of the synthesis, remodeling and transportation of PL and cholesterol.

1.1.2.1 Phospholipid synthesis and remodeling

The synthesis of PLs begins with the generation of phosphatidic acid from esterification of glycerol-3-phosphate with two fatty acyl chains. Then, the phosphate group is removed by phosphatidic acid phosphatase to generate diacylglycerol. A polar head group is then attached to the phosphatidic acid through the phosphodiester bond with two strategies, where nucleotide cytidine diphosphate (CDP) plays central role. In the first strategy, the CDP activates diacylglycerol forming CDP-diacylglycerol and react with the hydroxy group of the head group, releasing a CMP and producing PL. In the second strategy, the CDP-conjugated head group is attacked by the hydroxy group of the diacylglycerol, forming a PL with release of CMP. These two strategies, named Kennedy pathway (Figure 1.2), were discovered in the 1950s by Eugene Kennedy[20]. Phosphatidylcholine (PC) is the major component of membrane PL. Except for production using the second strategy of the Kennedy pathway, the PC can also be produced by methylation of phosphatidylethanolamine (PE).

In the mammalian cells, the PLs usually contain saturated fatty acyl chain on the *sn-1* site and unsaturated fatty acyl chain on the *sn-2* site. This PL composition is mainly maintained through the Lands' cycle, where the fatty acyl chain on the *sn-2* site is hydrolyzed and substituted with another acyl-CoA by lysophospholipid acyltransferase (LPLAT). The remodeling of PCs, due to their large proportion as membrane components, is critical to cellular functions. Lysophosphatidylcholine acyltransferases (LPCATs), the enzymes that remodel PCs, include four members. LPCAT1 is mainly expressed in the lung, preferentially taking saturated fatty acids as substrate to generate components for pulmonary surfactant[21,22]. LPCAT2 is expressed in the macrophages and recent studies showed its association with the immune response[23]. LPCAT1 and LPCAT2 belong to the acylglycerolphosphate acyltransferase (AGPAT) family, which is different from LPCAT3 and LPCAT4, which belong to membrane-bound O-acyltransferase (MBOAT) family. In metabolic tissue such as liver, adipose tissue and intestine, LPCAT3 is the major enzyme that controls PC composition. It preferentially uses PUFA (arachidonic acid (20:4) and linolic acid (18:2)) as substrate and exhibits reactivity toward lysoPE and lysophosphatidylserine (lysoPS), in addition to lysoPC. Studies have shown critical roles of LPCAT3 in lipid metabolism and homeostasis[1], making it the protagonist of my work. LPCAT4 is selectively expressed in epididymis, brain, testis, and ovary, using oleic acid (18:1) as substrate.

Increasing studies recently recognized MBOAT7, another PL remodeling enzyme also known as lysophosphatidylinositol acyltransferase (LPIAT), playing important roles in liver diseases[24,25], which we will discuss in detail in late sections. Functions of other LPLATs in mammals remain mostly uncharacterized.

1.1.2.2 Phospholipid transportation

1.1.2.2.1 Intermembrane transportation and membrane contact sites

While membrane lipids are mostly synthesized in the endoplasmic reticulum (ER), they are actively transported to maintain distinct lipid components in different membranes. This transportation of lipids and proteins requires vesicle budded from ER targeting to other organelles or the plasma membrane. Vesicle trafficking is carried out in several steps: sorting and vesicle budding, motor-protein dependent transportation and recognition and tethering, docking and fusion of the vesicle to the destination membrane. Owing to the vast number of vesicles in the cell communicating various cellular compartments, the “zip code” is critical for vesicle trafficking to maintain content specificity and proper functionality of different organelles. Previous studies has established that the RAB GTPases and phosphorylated PI (PIP_x) are the tags that confer vesicle identity and serve as the “zip code”[26]. Specific Rab GTPase together with PIP_x in the membrane forms the code and recruit effector proteins that execute the following trafficking steps[27]. SNARE (soluble N-ethylmaleimide-sensitive factor attachment protein receptor) proteins are responsible for catalyzing membrane fusion in the secretory pathway. Recent data indicate that the specific pairing of SNARE and tethering proteins might also determine the destination specificity[28]. In summary, this vesicle trafficking not only transports proteins and macromolecular contents, but also mediates the lipid translocation that contributes to the membrane diversity.

A faster and more important inter-membrane lipid transportation is through lipid transfer proteins (LTP). Lipid desorption, the release of a lipid molecule from bilayer to the aqueous phase, is an entropy unfavorable process that requires high activation energy. Therefore, hundreds of LTPs have been identified from bacteria to mammalian cells, providing a hydrophobic cavity, or assembling into a channel or an open bridge at membrane contact sites (MCS) that facilitates specified lipid movement[29,30]. Opposed to vesicular transportation, LTPs usually transfer one molecule at a time with one-on-one specificity, restricting both head groups and fatty acyl components. There are various mechanisms for LTPs to transfer lipids[30]. For example, a bispecific PI transfer protein (PITP), transporting PI and PC, is a box-like LTP, that extracts a PI molecule from donor PI-enriched membrane, carries it in its cavity when it moves, and releases it to the PI-poor acceptor membrane. The PITP then travels back to the donor membrane carrying a PC molecule, redistributing PI in membranes[31]. Other LTPs containing the synaptotagmin-like mitochondrial-lipid-binding protein (SMP) domain can oligomerize and form channels or bridges connecting two membranes. For example, TMEM24, a SMP-domain containing protein, was found to mediate PI transportation between ER and plasma membrane thereby regulate insulin secretion[32]. However, some of these tubular LTPs may also transfer lipids in a shuttle mechanism. For example, cholesteryl-ester transfer protein (CETP) is a secreted tubular lipid binding protein that can transfer cholesterol-esters from high-density lipoprotein (HDL) to (very) low-density lipoprotein ((V)LDL)[33]. Although CETPs dimerize and form bridges between lipoproteins, it was shown that the CETP transfer lipids as shuttles instead of channels[30]. Recently, another family of LTPs that bulk transfer lipids were discovered. These proteins contain a repeating β-groove (RBG) element with various lengths and are found on different MCSs, mediating functions including organelle biogenesis and lipid rearrangement[34]. But their function in metabolic disorders is still mysterious.

MCSs are the primary location of LTPs. Yet, MCSs participate in various cellular processes including mitochondria dynamics (fusion/fission), autophagy, ROS and calcium signaling[35]. More interestingly, recent studies emphasized the pathogenic roles of defective MCSs in metabolic diseases. For example, mitofusin 2 (Mfn2) has been shown to transport PS from ER to mitochondria with counter-transportation of PE, and its depletion leads to severe non-alcoholic steatohepatitis (NASH) and hepatocellular carcinoma (HCC)[36]. Cholesterol is also actively transported between ER and plasma membrane, which contains about 90% of cellular cholesterol[37]. This transportation occurs in the ER-plasma membrane contact site and is mediated by oxysterol-binding protein and Aster[38,39]. Recent study showed that Aster-mediated sterol transfer affected VLDL secretion during fasting and disrupted systemic cholesterol homeostasis[40]. In the development of metabolic disorders, the contact between mitochondria and lipid droplets are critical to fatty acid metabolism[41]. It has been shown that the lipid droplet-associated mitochondria exhibited different properties including reduced β-oxidation capacity and increased pyruvate oxidation, electron transport, and ATP synthesis capacities[42]. With the advancement of imaging and structural biology, more novel pathological roles of MCSs in metabolic diseases can be expected.

1.1.2.2.2 Interleaflet translocation of lipids

PL movement between leaflets contributes to the asymmetrical distribution of PL in a bilayer, where PC and sphingomyelin are mainly present in the outer leaflet whereas PS and PE are in the cytoplasmic leaflet. Despite the rapid lateral diffusion of membrane lipids, trans-bilayer movement of phospholipids requires enzymes. There are three kinds of enzymes on the plasma membrane catalyzing PL trans-bilayer movement: flippase, which moves PL from outer leaflet to cytoplasmic leaflet, floppase, which reverses function of flippase, and scramblase, which counter-transport PLs across leaflets in both directions. The flippase and floppase move PLs against concentration gradient to create asymmetrical distribution with expense of ATP, whereas scramblase non-specifically and bidirectionally translocate PLs between the lipid bilayer and collapse the membrane asymmetry[43]. Flippase belongs to P4-ATPase family and two different families (TMEM16 and XKR) work as Ca^{2+}-dependent or caspase-dependent scramblase, respectively. It has been shown that floppases are ABC transporters, but their functions are not characterized due to lack of model systems.

One of the physiological roles of the asymmetrical PL distribution stems from the signaling functions of PS in the outer leaflet of plasma membrane. For example, when caspase is activated in response to apoptotic signals, flippases are destroyed and scramblases are activated by caspase thereby expose PS to macrophages, which possess PS receptors[43]. Recently, the roles of scramblases in the ER have drawn much attention. ER membrane scramblases TMEM41B and vacuole membrane protein 1 (VMP1) were shown to be critical to hepatic VLDL secretion and their deficiency leads to severe steatosis[44,45]. These results indicated that PL distribution and availability is tightly regulated and is critical to various cellular processes that require PL supply.

Identification and characterization of more flippases and scramblases may produce novel aspects for metabolism and pathology.

1.2 ENERGY METABOLISM AND HOMEOSTASIS

Organisms of Animalia require biomass as energy input, due to the lack of photosynthesis machinery that converts the energy from light into the form of carbohydrate. The major energy sources of mammals are carbohydrates and fatty acids. Cells catabolize these molecules to release the energy into the form of ATP, driving the lives of cells.

1.2.1 Glucose Homeostasis

Glucose is the major energy source in mammalian cells. Therefore, hypoglycemia can be vital because cells such as neurons even solely use glucose as their energy source. However, chronic hyperglycemia is also deleterious leading to kidney failure and various comorbidities.

1.2.1.1 Glucose uptake

Carbohydrates include monosaccharides such as glucose and fructose, disaccharides such as sucrose and lactose, and polysaccharides such as glycogen or starch. The dietary carbohydrates are digested and absorbed in the form of monosaccharides by glucose transporters on the enterocytes[46].

Glucose transporters includes two families of membrane proteins, one conveying the passive transportation of monosaccharides, named GLUT, and one for active transportation named Na^+/glucose cotransporters (SGTL). There are 12 members of Glut family identified but four of them (GLUT 1-4) are most characterized. GLUT1 is a ubiquitously expressed glucose transporter for basal glucose uptake. GLUT2 is highly expressed in liver, pancreatic islets, kidney and small intestine, with very low glucose affinity but high capacity to carry on extensive glucose uptake. GLUT3 is the glucose transporter of neurons with the highest glucose affinity. And GLUT4 is expressed in muscle and fat for insulin-regulated glucose uptake[47]. Transportation of fructose requires GLUT5 and GLUT7 expressed in the intestine.

The glucose uptake is mainly regulated by insulin in the muscle and adipose tissue. When blood glucose rises from food intake, insulin is secreted and increases glucose uptake by muscle and adipose tissue through GLUT4. Under unstimulated states, GLUT4 is stored in intracellular vesicles different from endosomes, named Glut4 storage vesicles (GSVs), which limits glucose uptakes. Upon insulin stimulation, AKT substrate of 160 kDa (AS160), a GSV protein containing a Rab GTPase-activating protein (GAP) domain, is phosphorylated by AKT and inactivated. The GAP facilitates the hydrolyzation of GTP, turning off the RAB GTPase and hindering vesicle translocations. Therefore, insulin signaling drives the translocation of GSVs to the plasma membrane and promotes glucose uptake through AS160[48]. Muscle harbors another mechanism that regulates this translocation. Muscle contraction increases intracellular AMP/ATP and ADP/ATP ratios, thereby activates AMP kinase (AMPK). Another GAP, Tbc1D1, can then be phosphorylated by AMPK and facilitates Glut4 translocation to increase glucose supply for energy consumption in the muscle[49]. Failure to transport Glut4 efficiently to the plasma membrane contributes to pathogenesis of insulin resistance, which we will discuss in detail in later sections.

1.2.1.2 Glucose metabolism

Glucose is highly reduced and its oxidation releases energy that drives cellular processes. After feeding when the glucose is affluent, liver and muscle synthesizes glycogen as energy storage. And when glycogen is used up under prolonged fasting, liver can synthesize glucose from pyruvate, namely gluconeogenesis, providing energy supply to other organs, especially the brain. All these processes fuel cell functions and maintain the blood glucose level within a small range.

The first step to release energy from glucose is glycolysis, which occurs in the cytosol. The glycolysis converts a glucose molecule into two pyruvates with the production of two ATP molecules and two NADH[50]. The priming of glycolysis involves two irreversible reactions that require hexokinase (HK) and phosphofructokinase 1 (PFK1) and investment of two ATPs. The product fructose 1,6-bisphosphate is then dedicated to glycolysis. The later steps of glycolysis are all reversible until the production of pyruvate by the pyruvate kinase. The irreversible reactions, requiring HK, PFK1 and pyruvate kinase, are therefore critical for the regulation of glycolysis. The metabolism of fructose joins the glycolysis pathway through the production of fructose 6-phosphate with catalyzation of hexokinase.

The gluconeogenesis is mainly carried out by the liver, which converts pyruvate to glucose, with consumption of four ATPs and 2 GTPs. Gluconeogenesis shares the reversible reactions with glycolysis. But these two opposite processes are reciprocally regulated to avoid futile cycles. The three irreversible reactions in glycolysis are bypassed in gluconeogenesis by a separate set of enzymes, and they become the regulation points. ATP or acetyl-CoA and citrate, whose concentration increases indicating sufficient energy supply, bind to and allosterically inhibit the activity of PFK-1, thereby shifting the cells to gluconeogenesis. On the contrary, binding of ADP and AMP to PFK1 activates its activity and promotes glycolysis. In the liver, glucokinase regulatory protein (GKRP) regulates glucokinase (GK, the isozyme of HK in the liver) by binding and holding it in the nucleus[51]. The increased cellular glucose competes with this interaction and release GK for glycolysis. Mutations of *GCKR*, the gene that encodes GKRP, have been identified to be associated with NAFLD by genome-wide association study (GWAS), which we will discuss in detail later.

Glycogen synthesis is a fast and efficient way to store glucose intracellularly. Glycogen is polymer of glucose with a dimer of the protein glycogenin at the core. The α-granules of glycogen in the liver can be as large as 300nm in diameter and molecular weight greater than 10^8 [50]. The synthesis of glycogen requires glycogen synthase (GS) and UDP-glucose as building blocks, which come from glucose 6-phosphate, the product of the first reaction of glycolysis. The breakdown of glycogen is carried out by glycogen phosphorylase to produce glucose 1-phosphate, which then is converted to glucose 6-phosphate by phosphoglucomutase to merge into glycolysis pathway. The regulation of glycogenolysis is regulated by the allosteric and phosphorylation of glycogen phosphorylase, in response to energy needs and glucagon signals. When glucose is low, glucagon upregulates cAMP and initiates an enzyme cascade which eventually phosphorylates and activates glycogen phosphorylase to release glucose. When glucose is sufficient, binding of glucose into glycogen phosphorylase allosterically exposes the phosphor group. Phosphoprotein phosphate 1 (PP1), activated by insulin signaling, then dephosphorylates and inactivates glycogen phosphorylase, inhibiting glycogenolysis. The glycogen synthesis is regulated by phosphorylation and dephosphorylation of GS. Glycogen synthase kinase 3 (GSK3) and AMP-activated protein kinase (AMPK) phosphorylate and inactivate GS in response to energy needs. Under high glucose supply, AKT phosphorylates and inactivates GSK3 while activates PP1 that dephosphorylates GS, thereby activating glycogenesis.

Insulin and glucagon are two major hormones that regulate blood glucose levels by coordinately regulating glycogenesis, glycolysis ang gluconeogenesis. Kinases such as PKA, in response to glucagon, and AKT (PKB), in response to insulin play central roles in this regulation by switching on and off enzymes through serial phosphorylation (Figure 3). Their regulation of glycolysis versus gluconeogenesis is mediated by fructose 2,6-bisphosphate (F26BP), which is regulated by a bifunctional protein phosphofructokinase-2/fructose 2,6-bisphosphatase (PFK-2/FBPase-2). Glucagon is secreted when blood glucose drops. It signals through cAMP mediated protein kinase A (PKA), which phosphorylates PFK-2/FBPase-2 and activates its FBPase-2 domain to convert F26BP to fructose 6-phosphate. This reduction of F26BP and its binding to PFK-1 and FBPase-1 inhibits glycolysis and promotes gluconeogenesis. On the contrary, insulin signaling activates PP1 dephosphorylates PFK-2/FBPase-2 to active PFK-2 to produce F26BP, favoring glycolysis and inhibiting gluconeogenesis[52,53]. This special regulation of glucose metabolism reveals an interesting mechanism paradigm by which glucose homeostasis is regulated. These non-transcriptional regulations of metabolism are more difficult to investigate but fascinating and should be revisited in today's research.

1.2.1.3 Insulin signaling pathway

Insulin, secreted by pancreatic β cells upon stimulation, functions primarily in liver, adipose tissue and muscle to keep the homeostasis of blood glucose level. Briefly, insulin regulates glucose homeostasis by 1) promoting glycogenesis and lipogenesis in the liver, while suppressing gluconeogenesis; 2) promoting glucose uptake and lipogenesis in the adipose tissue and 3) driving glucose uptake and glycogen synthesis in the muscle[54]. Recently, emerging studies also focus on the insulin signaling in the brain and uncover some systemic functions of insulin on glucose homeostasis control[55]. We have discussed several responses of insulin signaling including the regulation of Glut4 translocation, gluconeogenesis and glycogen metabolism. Here, we discuss in detail how the insulin signaling is transduced in the cell.

The initiation of insulin signaling is the binding of insulins to insulin receptors (InsR), a receptor tyrosine kinase, expressed on the cell membrane. InsR phosphorylates itself in response to insulin, to activate its kinase function, a process named autophosphorylation. Then, InsR phosphorylates insulin receptor substrates (IRS) in a time scale of seconds and followed by a series of phosphorylation. Phosphorylated IRS then activates PI3K which converts PIP_2 to PIP_3, a second messenger on the membrane. The central node of insulin signaling is the phosphorylation of AKT, which is activated by phosphoinositide-dependent kinase (PDK) after the conversion of PIP_2 to PIP_3. AKT is a serine/threonine protein kinase that is upstream of various metabolic pathways. The Forkhead family box O1 (FOXO1) is a transcription factor controlling gluconeogenesis. It is inactivated by phosphorylation of AKT, limiting the transcription of genes involved in gluconeogenesis, which is activated in fasted state. AKT can also activate mTORC1 by phosphorylation of TSC2, thereby activates S6 kinase (S6K) for protein synthesis and sterol regulatory element binding protein 1c (SREBP1-c) for *de novo* lipogenesis. AKT can also phosphorylate GSK3 and promotes glycogen synthesis[56]. Phosphorylase PP1 is also directly regulated by AKT through phosphorylation of a PP1 regulatory subunit PPP1R3G, participating in the regulation of glycogen synthesis and phosphorolysis[57]. Different tissues may emphasize different functions of insulin. For example, in the adipose tissue, the main function of insulin is inhibition of lipolysis and synthesis of triglyceride, while it promotes glycogen synthesis and inhibits gluconeogenesis in the liver (Figure 1.3).

Another branch of insulin signaling relies on other substrates of InsR. A docking protein Src homology and Collagen (SHC) can bind to InsR through its phosphotyrosine-binding (PTB) domain and be phosphorylated by InsR thereby interacting with adaptor protein Grb2 which contains SH2/SH3 protein binding domain. The GRB2 connects the signaling complex with son of sevenless (SOS), a guanosine nucleotide-exchange factor, which replaces GDP with GTP on the small G protein Ras. This activation of Ras then activates the phosphorylation cascade of ERK, a member of the MAPK family. Raf-1 (as MAPKKK) is recruited to Ras and activated to phosphorylate MEK (as MAPKK), which then phosphorylates ERK (MAPK) and promotes its translocation to the nucleus[58]. This signaling branch mediates a separated effect of insulin by ERK-activated transcription of genes involved in cell proliferation and differentiation, which is relatively insulated from the other metabolic effects of insulin.

1.2.1.4 Insulin resistance and type II diabetes (T2D)

The earliest clinical record of diabetic symptoms dates back to *ca* 1550 B.C. in Egypt, but not until the 2nd century was the term “diabetes” used to describe the polyuric symptom[59]. The pathogenesis of diabetes is only better understood since the discovery and isolation of insulin in the early 20th century. In recent decades, diabetes has drawn more and more attention due to its increased impact on public health. In 2021, it is estimated that approximately 537 million adults worldwide live with diabetes and about 90% of them have type 2 diabetes mellitus (T2D). The fast-growing diabetic population also costs more than 400 million USD in North America as estimated in 2021[60]. Insulin resistance is one of the major risk factors of T2D, characterized by hyperinsulinemia and hyperglycemia. It is also closely associated with other metabolic disorders including obesity and non-alcoholic fatty liver diseases (NAFLD), implying the critical roles of lipid metabolism in its development. We will discuss the current understanding of insulin resistance in different organs but with a focus on the liver.

Liver insulin resistance in T2D patients is characterized by failure to suppress gluconeogenesis but still promoting *de novo* lipogenesis, resulting in a deleterious triad of hyperglycemia, hyperinsulinemia and hypertriglyceridemia, named selective insulin resistance (SIR)[61]. It is still not clear that the mechanism of this pathway selectivity despite several proposed models, where lipids such as DAG and ceramides play critical roles[62,63]. Diacylglycerol (DAG) is an intermediate product in lipogenesis. Increased lipid production and fatty acid uptake raises hepatocellular DAG levels and activates protein kinase Cε (PKCε), an isoform of PKC in the liver. The activated PKCε translocates to the membrane and phosphorylates InsR on Thr[1160] thereby inhibiting its autophosphorylation and downstream activation of IRS and AKT[64]. Ceramides have also been found to be related to hepatic insulin resistance in human patients. Ceramides are sphingolipids that share similar structure with other PLs with two fatty acyl chains. It has been found that ceramide induces SIR by inhibiting AKT phosphorylation and hormone sensitive lipase (HSL) activity whereas promoting CD36-mediated fatty acid uptake and SREBP 1-c pathway through ceramide effector protein PKCξ or PP2A[65]. Moreover, it has been shown that a species of ceramide on mitochondria mediates fat-induced InsR by interacting with mitochondrial fission factor (Mff) and affecting mitochondrial dynamics[66]. Therefore, the location and composition of ceramides generates substantial complexities in their pathophysiological functions, which may also contribute to the controversies observed in human patients in terms of the correlation between ceramide and InsR[64,66-68].

Inflammation is another factor that contributes to insulin resistance. The excessive energy supply is stored in the adipose tissue as neutralized lipids, leading to hyperplasia (proliferation) and hypertrophy of adipose tissue. Maladaptation to this energy imbalance leads to the release of free fatty acid, adipocyte apoptosis and mechanical stress in adipose tissue, which causes inflammation[69]. In detail, free fatty acids bind to T cell receptor 4 (TLR4) on macrophages, triggering the secretion of cytokines such as tumor necropsy factor α (TNF-α). The TNF-α activates intracellular IκB kinase (IKK) and c-Jun N-terminal kinase (JNK), which in turn phosphorylates IRS-1 on serine sites, inhibiting insulin signaling[70]. Peroxisome proliferator-activated receptor γ (PPARγ), the lipid sensor of cells, is also required for macrophage activation. It has been shown that disturbing PPARγ phosphorylation can rescue adipose tissue inflammation and ameliorate systemic insulin sensitivity[71,72]. These findings emphasize the roles of lipid-induced inflammation in adipose tissue InsR, in addition to the DAG-PKCε pathway similar to that in liver.

Given that insulin receptor localized on the membrane, the membrane composition and dynamics have also been shown to modulate the insulin signaling. After stimulation by insulin, insulin receptors are internalized and translocated into the nucleus to promote the transcription of its downstream genes[73]. The endocytosis of insulin receptor is feedback regulated by extracellular signal-regulated kinase (ERK) mediated inhibitory phosphorylation of the IRS and interrupting this regulation retains insulin receptor on the membrane thus prolongs insulin signaling[74]. Alteration of membrane composition and its biophysical properties were also found to impact insulin signaling in the muscle[15]. Moreover, membrane composition changes in the macrophage mediated fat-induced inflammatory signaling, thereby leading to insulin resistance[75]. Therefore, these data imply a direct effect of cell membrane on insulin receptor signaling which requires further investigation.

1.2.1.5 Current therapeutics for T2D

The most prevalent therapeutic strategy for T2D is insulin supplement with various dosages. However, here, we will focus mainly on the oral agents that lower blood glucose levels and discuss their therapeutic targets and mechanisms for T2D treatment.

Metformin is the first-line antidiabetic drug introduced since the late 1950s. It is a Biguanide derivative originated from an ancient Europe herb, with good safety record and low cost. Although it is still not clear the exact mechanism of the glucose-lowering effect of metformin, there are several targets proposed. It has been shown that metformin inhibits the activity of complex I in the respiratory chain for oxidative phosphorylation, lowering ATP production and increasing cellular

NADH level. The increased [AMP]/[ATP] ratio and NADH/NAD+ratio shifts the cellular metabolism to energy consumption, thereby directly inhibiting gluconeogenesis and activating AMPK, which sensitizes insulin signaling[76,77]. Recent study showed that metformin binds and inhibits lysosomal proton pump v-ATPasse through a protein complex thereby activates AMPK[78]. Metformin also inhibits hepatic glucose production through lowering glycerol 3-phosphate, which signals as energy deprived state and inhibits gluconeogenesis. In addition to the energy state transition, metformin was shown to ameliorate obesity-associated meta-inflammation, which sensitizes insulin signaling. Moreover, metformin functions in the intestine to promote the secretion of incretins such as glucagon-like peptide 1 (GLP1) and modulates gut microbiota that contributes to its beneficial effects[76]. The detailed functions of metformin are still under intensive investigation, which also shed light on our understanding of systemic glucose metabolism.

Sulfonylureas are a group of insulin secretagogues for the treatment of T2DM. Currently, this family of drugs include glibenclamide gliclazide, glipizide, and glimepiride. Sulfonylureas act directly on the pancreatic β cells to stimulate insulin secretion through a membrane receptor sulfonylurea receptor 1 (SUR1). When increased blood glucose level raises intracellular ATP due to glycolysis after glucose influx, ATP-sensitive K^+ channel on the β cell membrane closes, leading to depolarization which opens Ca^{2+} channel and activates the secretion of insulin. Sulfonylureas bind to the cytosolic side of SUR1, which forms a transmembrane complex with the K^+ channel, resulting in closed K^+ channel, depolarization, and insulin secretion. Therefore, sulfonylureas can cause hypoglycemia, whereas metformin would not. Meglinides, another type of insulin secretagogues, act similarly to sulfonylureas, but with a faster effect and shorter duration[79].

Thiazolidinediones (TZDs) are PPARγ agonists that improve whole-body insulin sensitivity. This type of drug includes rosiglitazone and pioglitazone. The PPARγ is mainly expressed in the adipose tissue, where it activates genes involved in glucose uptake and lipogenesis, and represses genes involved in inflammation when activated by TZDs[80]. TZDs also function through preventing PPARγ S273 phosphorylation, which is induced in obesity and causes insulin resistance by increasing the expression of growth differentiation factor 3 (GDF3)[72,81]. TZDs produce a slowly generated anti-hyperglycemic effect, which usually requires 2–3 months to reach maximum effect. They exhibit a more durable glucose-lowering effect compared to metformin and sulfonylurea, which can be used in combination with TZDs for better outcomes.

Dipeptidyl peptidase 4 (DPP4) inhibitors, also known as gliptins, are rationally designed to inhibit DPP4, which catalyzes the cleavage of two incretins: GLP-1 and glucose-dependent insulinotropic polypeptide (GIP). It has also been shown that hepatic DPP4 mediates obesity-associated adipose tissue inflammation[82]. The therapeutic mechanisms of DPP4 inhibitors are still not clear. Increased GLP-1 and GIP promotes insulin secretion and suppresses glucagon, lowering fasting and postprandial glucose levels[83]. Although treatment of DPP4 inhibitors increases plasma GLP-1 and GIP levels, it does not block other known functions of DPP4 and increases soluble DPP4 in the blood, generating controversial results in terms of glucose sensitivity and inflammation in mouse models[82,84]. Moreover, genetic deletion of DPP4 in the liver and adipose tissue did not recapitulate the insulin sensitizing effects of DPP4 inhibitor treatment despite lower plasma DPP4 activity[84]. These results revealed a complex nature of the function of DPP4 and its inhibitors, which requires further investigation.

GLP-1 is a gut-derived peptide secreted from the intestine in response to nutrients, particularly glucose and fat. It acts on the pancreas to improve β cell neogenesis and stimulate insulin secretion, while on the hypothalamus to promote satiety and reduces food intake. Therefore, GLP-1 receptor agonists were developed to treat T2D and obesity. Currently approved T2D drugs within this category include exenatide, liraglutide, lixisenatide, dulaglutide, and semaglutide, among which only semaglutide can be taken orally. Treatment of these drugs consistently reduces HbA_{1c}, a marker for hyperglycemia, body weight and blood presser, in company with common side effects including nausea and vomiting[85]. Because of their efficacy on weight loss and reduce blood glucose, GLP-1 receptor agonists also exhibit concurrent improvement on steatosis and hepatic insulin resistance, potentiating these drugs against a broad spectrum of metabolic diseases[86].

There are several other types of antidiabetic drugs. Sodium-dependent glucose transporter 2 (SGLT-2) is a glucose transporter that reabsorbs glucose in the kidney. SGLT-2 inhibitors, such as dapagliflozin and empagliflozin, were developed to inhibit renal glucose reabsorption, leading to substantial glycosuria and lowering glucose levels[86]. α-Glucosidase inhibitors, such as acarbose and miglitol, competitively bind to and inhibit intestinal α-Glucosidase to hinder carbohydrate absorption, lowering postprandial glucose levels[79].

1.2.2 Lipid Homeostasis

1.2.2.1 Fatty acid homeostasis

Fatty acids are hydrocarbon derivatives containing a carboxyl group. According to the number of double bonds, the fatty acids can be classified into saturated fatty acids (SFA), monounsaturated fatty acids (MUFA) and polyunsaturated fatty acids (PUFA). The naming of fatty acids, such as 20:4, contains two numbers indicating the carbon number (20) and the number of double bonds (4) separated by a colon. An alternative nomenclature is generated by the position of the first double bond from the methyl end of the chain called ω-n because of its physiological associations. For example, if the first double bond from the methyl end of a PUFA is between the third and fourth carbon from methyl end, it will be named ω-3 fatty acid. Their impact on health will be discussed later.

1.2.2.1.1 Fatty acid synthesis

Fatty acid synthesis in mammalian cells mainly relies on fatty acid synthase (FAS), where the fatty acyl chain extends by two-carbons in each round of a repeating reaction sequence. Mammalian FAS1 is a homodimer of two huge polypeptides of about 240 kDa in molecular weight, containing multiple subunits to carry on the four-step reaction for chain extension. Acetyl-CoA is the starting point for fatty acid synthesis and malonyl-CoA are the building blocks. With the catalyzation of FAS1, a malonyl-CoA is added to the end of the fatty acyl chain, releasing one molecule of CO_2 in each round[50]. This reaction happens in the cytoplasm. The energy input in this process is the reducing power from NADPH and the ATP used in the generation of malonyl-CoA from acetyl-CoA by acetyl-CoA carboxylase (ACC) and in the transportation of acetyl-CoA out of mitochondria. The elongation of fatty acyl chain by Fas1 stops when it reaches 16 carbons after seven cycles, with yet unknown reason, to produce a palmitate (16:0). Therefore, with excessive energy in the form of acetyl-CoA as a product of glycolysis, cells can store them in the form of fatty acids and packed into triglycerides.

The long-chain fatty acids can further be synthesized from palmityl-CoA by elongases, encoded by *ELOVL* (elongation-of-very-long-chain-fatty acids) gene family. ELOVLs condensate malonyl-CoA to acyl-CoA, adding two carbons each time to the acyl chain, similar to FAS[87]. However, this elongation process only synthesizes SFA. The desaturation of stearate (18:0) requires stearoyl-CoA desaturase (SCD), which produces oleate ($18{:}1^{\Delta 9}$). Mammals are not able to further desaturate oleate to produce linoleate (18:2), which is required by the synthesis of other PUFAs, thereby becoming essential fatty acid that must be obtained from diet.

1.2.2.1.2 The regulation of fatty acid synthesis

The synthesis of fatty acids is tightly regulated by multiple pathways (Figure 1.4). On the post translational level, similar to the regulation of glucose metabolism, the rate-limiting enzyme ACC is feedback inhibited by palmitoyl-CoA, the product of fatty acid synthesis, whereas allosterically activated by citrate, which indicates excessive energy. When energy deprivation leads to increased [AMP], ACC will be phosphorylated and inactivated by AMPK to reduce fatty acid synthesis. On the transcription level, several pathways participate in the regulation of genes involved in fatty acid synthesis, including PPAR, SREBP-1c, carbohydrate response element binding protein (ChREBP) and liver X receptor (LXR).

PPAR, FXR and LXR are nuclear receptors. Nuclear receptors are expressed intracellularly and their signaling is transduced when binding to their substrates and translocate to the nucleus as transcription factors with the help of a coregulator. For example, retinoid X receptor (RXR) is a coregulator for PPARs, LXR and FXR, which senses fatty acids, cholesterol and bile acids, respectively[88]. There are three isoforms of PPARs: PPARα, PPARγ and PPARδ, with different expression patterns and complex functions. PPARα is activated during prolonged fasting by AMPK and glucagon induced PKA, thereby promoting fatty acid oxidation and ketogenesis in the liver. However, the roles of PPARα on *de novo* lipogenic gene expression is still controversial[89,90]. PPARγ mainly expressed in adipose tissue where it induces adipogenesis, fatty acid uptake and synthesis, and improves insulin sensitivity when activated[71,89]. PPARδ is expressed in the adipose tissue promoting thermogenesis and β-oxidation, thereby suppressing *de novo* lipogenesis[91]. Therefore, it is still not fully clear how each PPAR member affects fatty acid synthesis.

SREBP-1c is a master regulator of fatty acid synthesis. It was well established that the regulation of SREBP-2 relies on a sterol-sensing ER-to-Golgi transport mechanism, whereas the activation of SREBP-1c is in response to the energy state. After this transportation, SREBPs are cleaved by two proteolyzes to release the DNA binding domain to translocate into nucleus and activates expression of lipogenic genes by binding to the sterol regulatory element (SRE). Upon insulin stimulation, AKT phosphorylates TSC2 and activates mTOC1, which activates SREBP-1c with multiple possible mechanisms. For example, S6K downstream of mTORC1 is required for SREBP-1c processing but not its transcription[92]. The nuclear phosphatidic acid phosphatase lipin-1 and CREB-regulated transcription coactivator 2 (CRTC2) were also shown to be phosphorylated by mTORC1 thereby facilitates activation of nucleus SREBP-1c or the ER-to-Golgi translocation[93]. Insulin signaling can also activate SREBP-1c through inhibitory phosphorylation of INSIG by AKT[94]. However, it is still not clear which mechanism has the major function under different energy states. Targets of SREBP-1c includes *FASN*, *ACC, SCD1* and ELOVL6, which controls every step of fatty acid synthesis. We will discuss more details about SREBP-2 pathway later.

ChREBP exerts transcriptional control over *de novo* lipogenesis (DNL) in response to metabolites of carbohydrates, including glucose 6-phosphate and F26BP. Activated ChREBP is then translocated into the nucleus to initiate the transcription of DNL genes, including *Fasn* and *Acc*, by binding on the carbohydrate response element in the promoter[95]. This regulation by ChREBP facilitates the energy storage under fed state. LXR is a nucleus receptor that responds to cellular cholesterol levels. It regulates DNL, together with cholesterol and PL metabolism, by binding to LXR response element (LXRE) and controlling gene transcriptions. LXR forms complex with RXR, promotes DNL directly by activating the transcription of genes such as *FASN* and *SCD1*, and indirectly by promoting the transcription and processing of SREBP-1c[96]. This regulation of DNL through LXR supplies fatty acyls for esterification of cholesterol and facilitates actions of insulin to promote energy storage.

1.2.2.1.3 Fatty acid absorption and storage

Dietary fat has to be hydrolyzed by lipases before absorbed by enterocytes. The free fatty acids released from dietary TG will then be uptake by enterocytes either through passive diffusion through membrane or receptor mediated transportation. CD36, a membrane receptor for fatty acids is critical to intestinal fatty acid uptake, with unclarified detailed mechanisms. The intracellular fatty acids then bind with fatty acid-binding proteins (FABPs) for lower toxicity and transportation. To supply the absorbed fatty acids to the circulation, enterocytes esterified fatty acids to synthesize TG and load it into chylomicron, a lipoprotein that is then secreted from the basolateral side of the cell into the lymphatic system[97]. In the blood, the chylomicron can capture apolipoprotein C-II (APOC-II) and be transported to adipose tissue and muscle, where the extracellular lipoprotein lipase (LPL) helps the tissue uptake fatty acids for storage and energy supply. The remnant of chylomicron is then captured by the hepatocytes through endocytosis.

The free fatty acids in the blood are carried by albumin, the most abundant protein in the serum. Liver uptakes fatty acids through passive diffusion or protein-facilitated transportation, similar to enterocytes. CD36 and fatty acid transport proteins (FATPs) participate in the fatty acid uptake in liver adipose tissue and muscle. It was shown that CD36 acts as a fatty acid sensor and translocase that facilitates their diffusion across membrane bilaye[98]r. Recent data revealed that fatty acid binding to CD36 activates the endocytosis pathway for fatty acid uptake in adipose tissue[99]. These results indicated that CD36 could be a multifunctional fatty acid receptor adaptive to the circumstances.

Intracellular free fatty acids exhibit lipotoxicity. Therefore, fatty acids from DNL or uptake from blood must be activated by long-chain acyl-CoA synthetases (ACSL) into acyl-CoA and be stored as neutralized lipid (TG) in the lipid droplets or undergo β-oxidation. The synthesis of TG is in the mitochondria and ER membrane. The first step of TG synthesis is the esterification of acyl-CoA to glycerol 3-phosphate (G3P) by G3P acyltransferase (GPAT) which is located on the outer mitochondrial membrane (OMM). Then, the lysophosphatidic acid (LPA) molecules produced in this reaction are acylated to form phosphatidic acid by the acylglycerol-3-phosphate acyltransferases (AGPAT) located in the ER membrane. The product phosphatidic acid is available for both PL synthesis and TG synthesis. Dephosphorylation of phosphatidic acid produces DAG, which can be further acylated by DAG acyltransferase (DGAT) to form TG molecules[100]. There are two types of DGAT that are distinct in their sequences and structures: DGAT1 and DGAT2. DGAT1 is localized to the ER whereas DGAT2 is also embedded in lipid droplets. DGAT2 is a major contributor to TG synthesis and lipid droplet expansion[101]. Recently, an alternative pathway for TG synthesis has been identified. A previously uncharacterized acyltransferase DIESL (or TMEM68) synthesize TG with its regulator TMX1 with the expense of membrane PLs when deprived with lipids to support mitochondrial function[102]. However, the regulation and significance of this pathway still requires investigation.

The TG is stored in lipid droplets (LDs) of a cell. TG synthesized in the ER forms a lens of neutral lipids within the ER bilayer. When sufficient TG is accumulated, it buds out of the ER and form initial LDs by the machinery of seipin, an ER protein located on the LD budding site. A subset of the initial LDs can then recruit proteins including GPAT4 and DGAT2 for TG synthesis and perilipin for lipase-mediated lipolysis[100,101]. Hepatocytes tend to have multiple LDs whereas adipocytes have a single large LD. The size of LDs is regulated by CIDE family proteins which control LD fusion and lipid transfer, which is important to lipid utilization[103]. Moreover, LDs participate in cellular processes by forming contact sites with various organelles including ER and mitochondria. Therefore, LD is dynamically regulated as a reservoir of energy and is critical to cellular lipid metabolism and pathogenesis of metabolic disorders.

1.2.2.1.4 Lipoproteins and triglyceride (TG) transportation

The interorgan transportation of neutral fat requires lipoproteins, macromolecular complexes of apolipoproteins and lipids. There are four major types of lipoproteins that differ in size and density due to their different lipid and protein content: chylomicron, very low density lipoprotein (VLDL), low density lipoprotein (LDL) and high density lipoprotein (HDL). Apolipoproteins are lipid-binding proteins that are embedded in the lipoproteins regulating their formation and the interactions with other cells and lipoproteins. Lipoproteins can recruit or exchange some of their apolipoproteins during transportation. The unexchangeable apolipoprotein thus renders lipoprotein an identity in addition to the density.

Chylomicrons, featured with APOB-48, are large, TG-rich lipoproteins produced in the enterocytes mainly for the transportation of dietary fat. They are synthesized in the inner leaflet of the ER through the lipidation of APOB-48 by microsomal triglyceride transfer protein (MTP). After the maturation of chylomicrons in the Golgi, other exchangeable apolipoproteins such as APOA-IV are also incorporated into the chylomicrons to regulate its lipidation. And during circulation, APOC can be recruited to regulate LPL activity and the release of TG content of chylomicrons[104].

VLDL is synthesized and secreted by the liver (and partially from intestine), where the full length of APOB, APOB-100, is lipidated by MTP in the ER, similar to chylomicron synthesis in the enterocytes. VLDL secretion is critical to hepatic lipid homeostasis, and its dysregulation leads to fatty liver diseases or hyperlipidemia. For example, decreased MTP significantly reduced lipidation of APOB, thereby reduced fasting serum TG without changes in APOB levels, resulting in enhanced steatosis[105]. Conversely, overexpression of MTP dramatically increased serum TG and serum APOB levels[106]. During the ER-to-Golgi transportation, factors such as membrane composition extensively regulates VLDL maturation and secretion, as we discussed some of examples in Section 1.2.2. The deletion of a pair of VLDL cargo receptors almost fully blocked hepatic VLDL secretion and promoted hepatic lipid accumulation[107]. Mutations on genes such as *APOB* and *MTTP* are also closely associated with NAFLD and serum lipid levels. However, the detailed mechanism of hepatic VLDL secretion is still not clear. Questions are still open including how lipids are selected between storge and secretion, and how the cargo receptors regulate VLDL secretion in response to the energy state.

During the circulation, peripheral tissues uptake TG from VLDL, generating the cholesterol-rich lipoprotein LDL marked with APOB-100. LDLs are uptake by muscle and adipose tissue by LDL receptor (LDLR)-mediated endocytosis, provides esterified cholesterol cellular utilization. The remaining plasma LDLs are then recycled back to the liver, where the cholesterol is stored or converted to bile acids. LDL cholesterol can also be uptake by circulating macrophages generating foam cells that promote plaque formation in atherosclerosis. HDLs are protein-rich lipoprotein originated from liver and intestine that transport cholesterol back to the liver from foam cells and other cholesterol-rich extrahepatic cells. The interaction between HDL and LDL are important to the pathogenesis of atherosclerosis and will be discussed more in detail below.

1.2.2.2 Cholesterol Homeostasis

Cholesterol is well known for its deleterious association with cardiovascular diseases. However, it is also an indispensable component of cell membranes and precursor to steroid hormones and bile acids. In this section, we will discuss the regulation of cholesterol homeostasis, with a focus on the liver.

1.2.2.2.1 Cholesterol absorption and biosynthesis

Dietary cholesterol is uptake mainly by Niemann-Pick C1-like 1 (NPC1L1) in the brush-border enterocyte membrane. After binding to cholesterol, the NPC1L1 releases endocytic signals to internalize cholesterol, forming cholesteryl ester (CE) by acyl-CoA: cholesterol acyltransferase 2, and packing into chylomicron for secretion. Scavenger receptor class B type I (SR-BI) is a cholesterol sensor and HDL receptor in the liver and intestine. Although it is still controversial whether it mediates intestinal cholesterol uptake, the activation of SR-BI promotes the trafficking of ApoB and lipoprotein secretion[97]. Enterocytes also excrete some dietary sterols into intestinal lumen through ATP-binding cassette subfamily G member 5 (ABCG5) and ABCG8 heterodimer in the apical side for detoxification and sterol removal. This cholesterol excretion is a critical cholesterol removal pathway in mice and human, named transintestinal cholesterol excretion (TICE)[108]. The absorbed cholesterol is then secreted into the circulation in the form of chylomicrons.

All cells can synthesize cholesterol from its precursor acetate. All the 27 carbons of cholesterol originated from acetate. The first step of cholesterol synthesis is forming β-hydroxy-β-methylglutaryl-CoA (HMG-CoA) from three acetyl-CoA by acetyl-CoA acetyl transferase (ACAT) and HMG-CoA synthase (HMGCS). Note here that although HMG-CoA is also an intermediate of mitochondrial ketone body synthesis, the cytosolic HMGCS in cholesterol synthesis is distinct from its mitochondrial isozyme[50]. Next, HMG-CoA is reduced consuming two NADPH to produce mevalonate by the action of HMG-CoA reductase (HMGCR). The reaction catalyzed by HMGCR is the committed and the rate-limiting step of cholesterol biosynthesis, thereby becoming an important regulatory point of this pathway.

Mevalonate is a six-carbon intermediate which in the next step generates two activated isoprene isomers by a series of reactions. The intermediates isoprene synthesized from three acetate molecules are also essential precursors to isoprenoid products, including ubiquinone. Genes encoding the enzymes involved in these reactions are also regulation targets of cholesterol biosynthesis, including phosphomevalonate kinase (*PMVK*) and mevalonate diphosphate decarboxylase (*MVD*). Six activated isoprene forms squalene which generates the four-ring core of sterols by the action of cyclase. This step is catalyzed by farnesyl diphosphate synthase (FDPS) which elongates the chain to fifteen carbons and then squalene synthase (FDFT) that synthesizes squalene. The 3-hydroxy group is added by the action of squalene epoxidase (SQLE), which is the second committed and potentially rate-limiting step in cholesterol biosynthesis[109]. The enzymes mentioned above are all targets that regulate cholesterol biosynthesis. Some of them have already become promising therapeutic targets against familial hypercholesterolemia.

1.2.2.2.2 Regulation of cellular and serum cholesterol

Peripheral tissues, including liver, uptake LDL via LDLR-mediated endocytosis. The endosome containing LDL then fuses with lysosome where lytic enzymes degrade ApoB-100 and cholesteryl esters, releasing amino acids, TG and cholesterol. The LDL-cholesterol is mostly transported to the plasma membrane through a lysosomal protein NPC1, but its detailed mechanism is still not clear[110]. Cholesterol in the plasma membrane is intensively transported to the ER through Aster, a sterol-binding ER protein recruited to the ER-Plasma membrane contact site[39]. Cellular cholesterol homeostasis is mainly controlled by SREBP-2 in the ER in complex with SREBP cleavage-activating protein (SCAP). SCAP is a transmembrane protein in the ER where it senses the cholesterol level. When cholesterol level is low, SCAP binds to SEC23 and SEC24 of the COP-II machinery, transporting SREBP-2 from ER to the Golgi. On the Golgi, two proteases S1P and S2P sequentially cleave the SREBP-2 to release its transcription factor domain into the nucleus, where the nucleic SREBP-2 (nSREBP-2) initiates the transcription of its target genes by binding to the SRE in their promoters[93]. The target of SREBP-2 includes the whole set of enzymes required for cholesterol biosynthesis and the LDLR. When binding with cholesterol, SCAP detaches from COP-II machinery and binds to a ER-retention membrane protein, insulin-induced gene proteins (INSIGs), which retains SREBP-2 on the ER and inhibits cholesterol biosynthesis and reduces LDL uptake[111].

LXR, the sterol sensing nuclear receptor, can also regulate cellular cholesterol level. When activated by oxysterols, LXR translocated into the nucleus with RXR and activates genes involved in cholesterol efflux (*ABCG5*, *ABCG8)*, bile acid synthesis (cytochrome P450 7A1, *CYP7A1*), and reduces cholesterol uptake. Inducible degrader of the LDLR (IDOL) is a target of LXR which ubiquitylates and degrades LDLR to facilitate cholesterol removal[96]. Therefore, LXR and SREBP2 regulate cellular cholesterol level coordinately by cholesterol clearance and biosynthesis, respectively.

Serum cholesterol is mainly in its esterified form carried in the LDL and HDL. As discussed in the previous section, the peripheral tissue uptake LDL through LDLR-mediated endocytosis to gain cholesterol from the serum. HDL originates from liver and intestine as a protein-rich particle containing primarily apoA-1 and an enzyme lecithin-cholesterol acyltransferase (LCAT). The LCAT converts cholesterol and PC into cholesteryl ester when HDL encounters VLDL and chylomicrons in the circulation. HDL can also uptake cholesterol from cholesterol-rich cells such as macrophage. This process renders HDL the fame of cholesterol scavenger and in fact, its level does reversely correlate with the risk of cardiovascular disease in human cohorts[108]. Since LDL can be uptake by macrophages to promote atherosclerosis, LDL has been thought to be the "bad cholesterol" as opposed to the "good cholesterol" HDL. However, this was challenged by a study showing that increased plasma HDL due to a SR-BI mutation significantly increased the risk of cardiovascular diseases[112]. The scavenger process transforms the nascent HDL into mature spherical particles that return to liver and intestine eventually through the receptor SR-BI. The HDL is not uptake via endocytosis, instead, binding to SR-BI selectively relieves the lipids into the cell and dissociates the depleted HDL back into circulation. In the intestine, the cholesterol can be excreted into intestinal lumen, forming the TICE we mentioned before. In the liver, the cholesterol can be converted into bile and secreted into the gallbladder. Therefore, the plasma cholesterol level requires a dynamical balance, and it is cholesterol flux, rather than HDL level, that is critical to cardiovascular health.

1.2.2.2.3 Bile acid synthesis and signaling

Bile acids (BAs) are cholesterol derivatives synthesized by hepatocytes. Bile contains BAs, cholesterol, phospholipids, conjugated bilirubin dissolved in water. The major function of bile is to emulsify dietary fat to facilitate intestinal lipid absorption. Therefore, BAs exhibits relatively amphipathic structure compared to cholesterol. The primary BAs are synthesized by two pathways in the hepatocytes: the classic pathway (neutral) and the alternative (acidic) pathway. In the intestine, the primary BAs are further metabolized by gut microbiota generating dozens of secondary BAs, complexifies the BA pool. There are four general steps of primary BA synthesis: a) the initiation of BA synthesis by 7α-hydroxylation of sterol precursors, (b) further modifications to the ring structures, (c) oxidation and shortening of the side chain, and (d) conjugation of the bile acid with an amino acid, usually glycine or taurine[113]. During these steps, there are several rate-limiting enzymes that are critical to the synthesis of at least some BA species. For example, cholesterol 7α-hydroxylase (CYP7A1) catalyzes the first and rate-limiting step of BA synthesis.

Thus, this enzyme becomes an important regulatory target of BA synthesis. The major primary BA species synthesized in humans are cholic acid (CA) and chenodeoxycholic acid (CDCA), whereas in mice, CA and α- plus β-MCAs are the majority[114].

BAs can be recycled in the ileum and transferred back to liver through enterohepatic cycle. BAs function as signaling molecules by interacting with farnesoid X receptor (FXR), a nuclear receptor and a master regulator of host metabolism. FXR is highly expressed in liver and ileum, maintaining BA homeostasis by feedback control of its synthesis and enterohepatic circulation[114]. As a nuclear receptor, ligand activated FXR and RXR heterodimers translocate into nucleus and bind to the target gene promoters. In the intestine, FXR activates the expression of FGF15/19, a hormone that binds to FGFR4 receptor on the hepatocytes and inhibits the expression of BA synthesis genes. BAs can also activate Takeda G protein–coupled receptor 5 (TGR5), a $G_{\alpha s}$ protein–coupled receptor, in the intestine. TGR5 then stimulates GLP-1 secretion potentially through ATP-induced membrane depolarization, exhibiting beneficial effects on glucose homeostasis[115]. However, there is still discrepancies in the outcomes targeting TGR5 in human compared to rodents[116]. In the liver, the recycled BAs are imported by SLC10A1 (NTCP) and SLCO1A2 (OATP) and activates FXR, which then induces nuclear receptor small heterodimer partner (SHP) to inhibit BA synthesis[117]. Moreover, activation of FXR in the liver and intestine were shown to reduce DNL and lipid absorption, respectively, potentiating FXR as a therapeutic target against NAFLD[118].

1.3 MITOCHONDRIAL FUNCTIONS AND DYNAMICS

Mitochondria are well known as the powerhouse of cells since they are the location for oxidative phosphorylation (OxPhos) and fatty acid oxidation (FAO). They are thought to be originated from endosymbiotic bacteria, with their own circular genome encoding genes that are critical to energy production. They are double membrane organelles with relative permeable outer membranes and inner membranes with plentiful invaginating cristae. Mitochondria sense and signal the energy state of the cell, governs myriad cellular processes from ATP production to apoptosis. In this section, we will introduce the function and dynamics of mitochondria in mammalian cells.

1.3.1 Citric Acid cycle

The product of glycolysis, pyruvate, still contains a large portion of energy to be released. Pyruvate is transported into mitochondria via mitochondrial pyruvate carriers (MPCs) on the inner mitochondrial membrane (IMM) and participates in the citric acid cycle (TCA cycle) in the matrix. The initiation step for TCA cycle is converting pyruvate into acetyl-CoA by pyruvate dehydrogenase complex (PDH) with production of a molecule of NADH and CO_2. The acetyl-CoA is then ready to enter the TCA cycle. Firstly, the acetyl-CoA reacts with oxaloacetate to form a citrate by the catalyzation of citrate synthase, incorporating the methyl group of acetyl-CoA into citrate. Then, the citrate is converted into isocitrate through a dehydration and rehydration reaction. Next, two steps of NADH-producing oxidative decarboxylation coverts isocitrate into succinyl-CoA, producing two molecules of CO_2. Succinate is then converted from succinyl-CoA, producing either a GTP or ATP. Next, the succinate is oxidized to fumarate by succinate dehydrogenase, with production of one FADH2 from FAD. The succinate dehydrogenase is the only membrane-embedded enzyme in the TCA cycle because it also acts as Complex II in the respiratory chain, which we will discuss below. The double bond of fumarate initiates the methylene oxidation sequence, where it undergoes hydration and dehydrogenation to produce oxaloacetate, producing the third NADH molecule and ready for the aldol condensation to start the cycle again.

The TCA cycle releases and stores the redox energy from oxidating pyruvate in the form electron carriers NADH and $FADH_2$, with an efficiency of about 65%, which is much higher than the modern engines. The series of biochemical reactions elegantly collect and transform the redox energy from glucose, exhibiting fascinating nature of biology.

1.3.2 Oxidative Phosphorylation (OxPhos)

The redox energy temporarily stored in NADH and $FADH_2$ are further released through OxPhos in the IMM, where the electrons are transduced through the respiratory chain drives ATP synthesis. The respiratory chain contains a series of sequentially acting electron carriers, including ubiquinone (coenzyme Q, CoQ) and cytochromes. The electron carriers are organized in four IMM-embedded supramolecular complexes. In Complex I, an 850 kDa protein complex containing 45 different polypeptides, two electrons carried by NADH are transferred to CoQ, and four protons are pumped out to the intermembrane space against the transmembrane proton gradient. Complex II, or succinate dehydrogenase, couples the oxidation of succinate with the reduction of CoQ, passing two electrons to CoQ through FAD. The oxidation of succinate in Complex II is not coupled with proton pumping. But in Complex III, the reduced CoQ from Complex I and II passes the electrons to cytochrome c (Cyt c), pumping 2 net protons across IMM. Cyt c is a soluble protein of the intermembrane space, enabling the diffusion of Cyt c to Complex IV. Complex IV of the respiratory chain is also known as cytochrome oxidase, where electrons carried by Cyt c are delivered to O_2, producing H_2O. With every four reduced Cyt c donating four electrons, one molecule of O_2 is reduced to two H_2O with four protons from the matrix, coupled with four protons pumped into the intermembrane space (Figure 1.5). Under normal physiological conditions, Complex I, III, and IV are associated with each other, forming a super complex called respirasome, possibly for a better electron transfer, whereas Complex II is floating around.

The net effect of the electron transportation through the respiratory chain is pumping 10 protons for each oxygen consumed, thereby generating a proton gradient across the IMM, termed the proton-motive force (PMF). In actively respiring mitochondria, the electrical potential across IMM is 0.15 to 0.2 V. This PMF resulted from electron transport will then drive the ATP synthesis catalyzed by an elegant molecular machine ATP synthase to collect the energy. ATP synthase (Figure 1.5) contains two functional domains F_o and F_1, where protons bind to and drive the rotation of F_o with PMF, and this rotation leads to ATP synthesis in F_1 domain. This mechanism couples the electron flow with APT synthesis through PMF, efficiently transforming the energy in the substrates into ATP product.

During the electron transfer on the IMM, it is possible that the electron carriers, such as partially reduced CoQ, react directly with free oxygen to form the superoxide radical thereby producing reactive oxygen species (ROS) including $^{\bullet}OH$ and H_2O_2. These ROS are highly reactive and attack proteins, lipids and nucleic acids, resulting in oxidative stress. The formation of ROS is favored when the mitochondria is not producing ATP due to hypoxia with an increased QH_2/Q ratio (more reduced CoQ) and increased $NADH/NAD^+$. Therefore, modest ROS produced during respiration act as signaling molecules facilitating cellular hypoxia response and even regulating feeding behavior, energy expenditure and glucose metabolism in the central nervous system[119]. However, the quantity of ROS produced by highly activated mitochondria requires detoxification by a mechanism involving glutathione (GSH). GSH is a small peptide with three amino acids. It is produced in the cytosol and transported into mitochondria via a transporter SLC25A39[120]. Mitochondrial GSH neutralizes H_2O_2 to H_2O, meanwhile oxidizing the thiol group of cysteine from two GSH molecules forming GSSG. This GSH-GSSG cycle scavenges the excessive ROS produced by mitochondria, protecting cells from oxidative stress.

1.3.3 Fatty Acids Oxidation

Free fatty acids from lipolysis or uptake blood can be oxidized as an energy source when glucose is scarce. The activation of fatty acid occurs on the OMM where fatty acyl-CoA synthetase converts fatty acid into fatty acyl-CoA. Then, it is attached to carnitine by carnitine palmitoyl transferase 1 (CPT1) before shuttled across IMM through acyl-carnitine/carnitine cotransporter. In the matrix, the fatty acyl group reattached to CoA by CPT2. The carnitine shuttle commits fatty acid to oxidation, and the reaction by CPT1 becomes a rate-limiting step of fatty acid oxidation (FAO) that is subject to regulation.

The first stage of FAO is a series of repetitive reactions that remove a two-carbon moiety each time to convert the fatty acyl-CoA into acetyl-CoA molecules, called β oxidation. For example, the β oxidation of palmitate (16:0) will undergo seven rounds of oxidation, producing eight acetyl-CoA to the TCA cycle. The reaction unit of β oxidation requires four steps analogous to the reactions in the TCA cycle where succinate is converted to oxaloacetate. The first step is catalyzed by isozymes of acyl-CoA dehydrogenase, each specific for a range of fatty acyl chain lengths: very-long-chain acyl-CoA dehydrogenase (for chain length of 14-20 carbons, encoded by gene *ACADVL*); long-chain acyl-CoA dehydrogenase (for chain length of 12-16 carbons, encoded by gene *ACADL*); medium-chain acyl-CoA dehydrogenase (for chain length of 6-12 carbons, encoded by gene *ACADM*) and short-chain acyl-CoA dehydrogenase (for chain length of 4-8 carbons, encoded by gene *ACADS*). Two electrons released from this step are carried by FAD, then directly transferred to the ubiquinone of the electron transport chain (ETC) through the electron transfer flavoprotein (ETF). In the next three steps, the stable single bond between α and β carbon becomes a vulnerable bond due to the formation of a ketone group on the β carbon, which can then be attacked by the thiol group of CoA to release an acetyl-CoA. Each round of this 4-step oxidation reaction produces reduces two carbons from the acyl chain, producing four electrons carried by $FADH_2$ and NADH and directly sent to the ETC. The acetyl-CoA released from β oxidation next joins the TCA cycle and OxPhos, finishing the utilization of energy stored in the fatty acids.

The regulation of FAO is regulated by both substrate-level feedback controls and transcriptional and post-translational controls in response to hormones. For example, the first product of DNL malonyl-CoA inhibits CPT1 to avoid the futile cycle of DNL and FAO. High mitochondrial $NADH/NAD^+$ ratio inhibits β-hydroxyacyl-CoA dehydrogenase, the third step of β-oxidation, to block FAO. On the transcription level, PPARα, as we mentioned before, is the master regulator of FAO, controlling the expression of genes for fatty acid import (*CPT1* and *CPT2*), and acyl-CoA dehydrogenases (*ACADVL*, *ACADL*, *ACADM* and *ACADS*). Glucagon can also activate FAO through cAMP and cAMP response element binding protein (CREB) which acts as a transcription factor to activate the expression of these genes[121,122].

1.3.4 Mitochondrial Dynamics

Mitochondria are not individual compartments floating in the cell. They undergo frequent fusion and fission and move about the cell to meet regional energy requirements. The dynamics of mitochondria regulate the function and quality control of mitochondria, participating in the pathogenesis of various diseases.

Generally, mitochondria fusion occurs to increase ATP production and exchange matrix content, indicating less stress and healthier mitochondrial function. The fusion process is mediated by two mitofusins MFN1 and MFN2 on the OMM and OPA1 on the IMM. MFN1 contains a GTPase domain as a tether between fusing mitochondria, mediating the fusion of OMMs. However, how OPA1 mediates the fusion of IMMs is still not clear, mainly owing to the lack of structure analysis. The mitochondrial fusion is regulated through modulation of these protein machineries[123]. For example, ubiquitin-mediated degradation of MFN1 by PINK1 promotes fission and mitophagy in Parkinson's disease. MFN1 phosphorylation by ERK favors mitochondrial fission, contributing to the Warberg effect in cancer cells[124].

Mitochondrial fission is an important quality control process to remove the damaged mitochondria for mitophagy. This process leads to fragmentation of mitochondria, leading to less ATP production and more ROS. Yet in specialized cells such as neurons, fission is required to facilitate the redistribution of mitochondria to the distal synapse area. The fission process is primarily carried out by dynamin-related protein 1 (DRP1), a member of the dynamin superfamily of GTPase which translocates from the cytosol to mitochondria, binding to its OMM partners mitochondrial fission factor (MFF), mitochondrial dynamics protein of 49 kDa (MID49), MID51 and mitochondrial fission 1 protein (FIS1)[123]. Then, DRP1 forms a complex with its partners, forming a ring that squeezes and separates two mitochondrion fragments with the hydrolyses of GTP. The site of fission is determined by mitochondrial-ER contact sites, where the ER wraps around mitochondria, recruit DRP1 and facilitates the mitochondrial constriction[125].

DRP1 is critical to the regulation of mitochondrial fission and mitophagy. For example, mitophagy could be prevented with a dominant-negative mutant of Drp1[126]. During starvation, PKA mediated phosphorylation of DRP1 on S637 site inhibits fission and promotes fusion and ATP synthesis[127]. However, there is still controversies regarding this control[128]. Under stress, activated kinases including RAS-MAPK, PKA and ERK can phosphorylate DRP1 at S616 site, which promotes its recruitment and mitochondrial fission[129]. Overall, the dynamics of mitochondria is in response to cellular stress and energy availability, and in turn orchestrates cellular processes such as oxidation, mitophagy and apoptosis.

1.4 PATHOGENESIS AND THERAPEUTICS OF NON-ALCOHOLIC FATTY LIVER DISEASE (NAFLD)

Non-alcoholic fatty liver disease (NAFLD) is an umbrella term that encompasses a series of chronic liver conditions, including steatosis or non-alcoholic fatty liver (NAFL) and non-alcoholic steatohepatitis (NASH), which can progress to fibrosis, cirrhosis, and hepatocellular carcinoma (HCC). The global prevalence of NAFLD is increasing at a rate of approximately 1% every year, affecting 30% of the population. However, there are currently no FDA approved drugs for its treatment[130,131]. More importantly, NAFLD has become the fastest growing cause of HCC in the US, and it is estimated that the incidence rate of NAFLD-related HCC will increase by 122% in by 2030[132]. As a result, the annual medical cost associated with NAFLD has exceeded $100 billion in the US[133]. Therefore, extensive research into the pathogenesis and progression of NAFLD is urgently needed to address its global health burden.

1.4.1 Genetic Factors Involved in NAFLD Pathogenesis[1]

NAFLD patients exhibit significant variations in phenotypes, which are determined by a combination of genetic and environmental factors, as is the case with other complex traits. Previous research has revealed the important roles of genetic factors in the susceptibility and progression of NAFLD, showing the heritability of NAFLD between 22%-50%[24,134]. In recent years, an explosion of genome-wide association studies (GWAS) has identified single nucleotide polymorphisms (SNPs) that are closely correlated with NAFLD or its progression based on data from hundreds of thousands of human patients. These SNPs have been mapped to genes that are summarized in Table 1.2. Although the genes identified from GWAS shed lights on the genetics

---

[1] This section is published in its entirety in the Journal of Gastroenterology and Hepatology. This article is reprinted with the permission of the publisher and is available from https://onlinelibrary.wiley.com/doi/full/10.1111/jgh.16330 and using DOI: https://doi.org/10.1111/jgh.16330

of NAFLD, understanding the pathogenesis of NAFLD requires investigating the function of these genes and the mechanisms that connect them to NAFLD progression. In this Review, we summarize the physiological and pathological functions of genes identified from GWAS that are associated with NAFLD or its severity, focusing on recent advances in novel SNPs and proposing potential implication on understanding of NAFLD development.

1.4.1.1 *PNPLA3*

Mutations in patatin-like phospholipase domain containing 3 (*PNPLA3*) have been associated with NAFLD and its severity by multiple GWAS since 2008[135,136]. PNPLA3 is highly expressed in the liver, with higher expression in hepatic stellate cells (HSCs) than in hepatocytes[137]. PNPLA3 functions as a triglyceride (TG) remodeler[138,139] and a retinyl ester hydrolase. The rs738409[G] variant, which encodes an I148M nonsynonymous mutation in the patatin-like domain of PNPLA3, has been shown to correlate with liver fat content and fibrosis[140], cirrhosis[141], type II diabetes[142], serum liver enzyme levels[143] and alcohol-related fibrosis[144] and HCC[145]. Such significant correlation with the spectrum of liver diseases urges thorough understanding of the pathophysiological function of PNPLA3.

In hepatocytes, PNPLA3 exhibits hydrolase and acyltransferase activity towards TG[146], with preferential substrates of TG containing monounsaturated (MUFA) and polyunsaturated fatty acids (PUFA)[147,148]. Interestingly, knockout of *Pnpla3* in hepatocytes did not lead to steatosis or dysregulation of lipid homeostasis[149,150]. In contrast, overexpression of I148M mutant induced lipid accumulation due to reduced VLDL secretion[151], suggesting that mutant PNPLA3 likely gains functions other than TG hydrolase that cause steatosis. *In vitro* study from Kumari et al.[146] showed that the TG hydrolase activity of PNPLA3 is low compared to its lysophosphatidic acid acyltransferase (LPAAT) activity with a preference of PUFA as substrates. They further showed that I148M mutation promotes its LPAAT activity and lipid synthesis leading to increased cellular lipid accumulation. A recent lipidomic analysis in human livers revealed similar result showing retention of PUFA in TG in I148M carriers[152]. These results indicate that augmented enzymatic activity towards lipid synthesis likely contributes to increased susceptibility of NAFLD in I148M carriers. Another study demonstrated that PNPLA3 with I148M mutation was resistant to ubiquitin-mediated degradation, which resulted in the accumulation of PNPLA3 on hepatic lipid droplets and impaired the utilization of TG stored in lipid droplets[153].

Given the gain-of-function nature of I148M mutation, strategies targeting PNPLA3 have been tested to treat NAFLD in mouse models. Inhibition of PNPLA3 by shRNA or proteolysis-targeting chimera-mediated degradation dramatically decreased liver TG content in I148M knock-in mice[154]. Knockdown of *Pnpla3* in high-fat diet (HFD) fed rats using antisense oligo (ASO) also significantly reduced hepatic lipid content and improved insulin signaling[155]. These studies demonstrate that PNPLA3 could be a potential therapeutic target for NAFLD in human patients.

Although the roles of PNPLA3 in hepatocytes have been extensively investigated, its functions in HSCs and its correlation with fibrosis remain poorly understood. PNPLA3 has been shown to regulate retinol pool in HSCs and I148M mutation of this enzyme leads to reduced release of retinol from HSCs[137]. Although retinol metabolism in HSC lipid droplets is known to be involved in HSC activation, there is no enough evidence to link PNPLA3-related fibrosis with retinol deficiency[156]. Previous studies have shown that the expression of *PNPLA3* in HSCs is regulated by retinol availability and TGF-β signaling in response to liver damage[157,158]. Further study showed that upon HSC activation, I148M mutation resulted in lipid accumulation and fatty acid imbalance in HSCs, thereby inducing cytokine release and promoting inflammation[157]. Thus, PNPLA3 likely mediates fibrogenic and proinflammatory responses upon liver damage and HSC activation. A recent *in vitro* study using human HSCs showed that I148M variant impaired liver X receptor (LXR) signaling and cholesterol homeostasis in HSCs, leading to HSC activation and collagen synthesis[159], which contradicts previous notion that PNPLA3 mutation may be downstream of HSC activation. Given that PNPLA3 is expressed in both HSCs and hepatocytes, it is important to explore the interactions between mutant PNPLA3 in different cells to fully understand its pathologic function. Park et al. utilized human pluripotent stem cell-derived multicellular liver culture revealed a critical role of activated NF-κB-IL-6/STAT3 axis in I148M-induced NAFLD progression[160]. This model provides a profound system to investigate the roles PNPLA3 in the pathogenesis of NAFLD.

1.4.1.2 *TM6SF2*

In 2014, three studies independently found that SNPs mapped to transmembrane 6 superfamily member 2 (*TM6SF2*) gene are associated with NAFLD[161-163]. These early findings demonstrated that TM6SF2 is localized in the ER and ER-Golgi intermediate compartment of human liver cells[161], and that downregulation of *Tm6sf2* resulted in less VLDL secretion and lipid accumulation in the liver[162]. Following research confirmed the adverse effects of *TM6SF2* mutation E167K on liver TG content and fibrosis[164]. Surprisingly, E167K carriers in humans showed improved insulin sensitivity in terms of glucose production and lipolysis, despite increased lipid accumulation in the liver[165,166]. Furthermore, serum triglyceride levels were also reduced in these patients. Gene expression analysis showed that E167K mutation results in loss of function of TM6SF2. However, overexpression of *Tm6sf2* in mice exhibited similar phenotypes as mutants, with lower circulating lipids and steatosis and liver damages[167,168]. Despite the conflicting results, these studies indicate a potential deficiency in VLDL secretion in mutants and a subtype of NAFLD characterized by dissociation between hepatic lipid accumulation and insulin responses.

Subsequent mechanistic studies have aimed to uncover the mechanisms underlying this paradoxical role of *TM6SF2* deficiency in NAFLD pathogenesis. TM6SF2 is predominantly expressed in the liver and intestine, with ~10 fold higher in small intestine compared to liver in mice[169]. Depletion of *Tm6sf2* in the intestine has been shown to impair lipid absorption and cause lipid accumulation in the enterocytes. However, the contribution of its intestinal function to liver and circulation phenotype can be limited and requires further investigation[169,170]. In the liver, *Tm6sf2* deficiency induced hepatic steatosis, hypocholesterolemia, and transaminitis without dietary challenge. This phenotype was attributed to dramatic decrease in the lipidation of APOB without any effect on APOB secretion[169]. Further studies revealed deficient triglyceride-rich lipoprotein (TRL) production and subsequent hepatic lipid accumulation in E167K mutant carriers or *Tm6sf2* null mice and rats, with slight downregulation of *de novo* lipogenesis likely due to compensation[171,172]. Furthermore, hepatic depletion of *Tm6sf2* promoted diet and chemical-induced fibrosis and HCC[173], indicating its broad pathological effect in different stages of NAFLD.

In human patients carrying E167K mutation and mice lacking *Tm6sf2*, PUFA were found to be depleted from TG and phosphatidylcholine (PC) in the liver and TG in the serum, which was further confirmed by in vitro study showing that the incorporation of PUFA is deficient in E167K carriers[2,169,174]. It has been shown that increasing phospholipid saturation blocks VLDL secretion in the liver[17,175], lipid absorption in the intestine[176] and improves insulin signaling in skeletal muscles[15]. Therefore, the shift of lipid composition in the absence of TM6SF2 may contribute to the impaired VLDL secretion and lipid absorption in the liver and intestine, respectively. Interestingly, another study demonstrated that TM6SF2 forms a complex with APOB and ER lipid raft protein (ERLIN), thereby stabilizes APOB[177], implying a potential link between TM6SF2 function and membrane subdomains. Therefore, it is possible that the pathological consequence of

TM6SF2 deficiency may be attributed to imbalanced phospholipid composition. Further studies are needed to test this hypothesis.

1.4.1.3 *SUGP1*

SURP and G-patch domain containing 1 (*SUGP1*) is ubiquitously expressed in a wide range of tissues and located closely to *TM6SF2* on human chromosome 19[178]. It was first described in 2003 as a pre-mRNA splicing factor containing SURP motif and G-patch domain at C-termini, indicating a potential RNA binding function[179]. *SUGP1* and *TM6SF2* are located both in *NCAN* locus, where many SNPs have been found to be significantly associated with plasma lipid concentrations[180], hepatic steatosis, lobular inflammation and fibrosis[181]. Specifically, rs10401969, a SNP in the intron 8 of *SUGP1*, was strongly associated with liver lipid content in obese and NAFLD patients[180,182]. How this intronic SNP may contribute to hepatic lipid accumulation remains elusive.

SUGP1 depletion has been shown to involve in splicing defects caused by a cancer-related mutation of the spliceosomal gene *SF3B1*[183,184], indicating that the pathological roles of SUGP1 are likely related to dysregulation of alternative splicing. Kim et al. found that rs10401969 led to non-sense mediated *SUGP1* mRNA decay and overexpression of *Sugp1* in mouse liver increased plasma cholesterol levels[185]. On the contrary, knockdown of *SUGP1* promoted alternative splicing of 3-hydroxy-3-methylglutaryl-CoA reductase (HMGCR), a rate-limiting enzyme of cholesterol synthesis, and reduced cholesterol synthesis and increased LDL uptake[185]. While these results are in line with alternative splicing function of SUGP1 and its roles in lipid metabolism, it cannot explain how rs10401969 leads to liver lipid accumulation since rs10401969 decreases *SUGP1* expression, which is supposed to reduce lipid synthesis. Given that this SNP is located in an intron, efforts have been made to identify genes around this locus whose expression is indeed affected in steatotic patients. Among ~20 genes in this locus, only lysophosphatidic acid receptor 2 (*LPAR2*) was significantly upregulated in fatty livers[182]. This raises the possibility that lysophospholipids signaling in the liver could be involved in the pathological mechanisms underlying the SNPs found in *NCAN* locus. However, we cannot rule out the possibility that these mutations, especially synonymous SNPs, may affect other neighboring genes through transcriptional or splicing regulation.

1.4.1.4 *MBOAT7*

The membrane-bound O-acyltransferase 7 (MBOAT7) is an ER membrane protein that belongs to MBOAT family. MBOAT7 has been shown to have lysophospholipid acyltransferase activity with the substrate preference of PUFA such as arachidonic acid[186,187]. In 2015, GWAS identified risk loci in *MBOAT7* for alcohol-related cirrhosis, drawing attention of this enzyme to liver diseases[188]. Studies in human NAFLD cohorts showed close association between hepatic fat content and fibrosis and rs641738T in *MBOAT7*, which leads to decreased protein levels in the liver[189,190]. A meta-analysis with more than 1 million participants confirmed these correlations and revealed additional links to higher serum ALT and lower serum TG levels[191]. Given the enzymatic activity of MBOAT7, the mutation carriers showed severer fibrosis and increased hepatic phosphatidylinositol (PI) saturation[190]. These findings suggested that the pathophysiological role of MBOAT7 could be attributed to its phospholipid remodeling activity.

Consistent with human cohort studies, liver *Mboat7* expression was also significantly downregulated in genetic or diet-induced obesity murine models[192]. To investigate the mechanisms of MBOAT7 in the pathogenesis of NAFLD, several groups have generated *Mboat7* liver specific knockout mice and revealed spontaneous steatosis and exacerbated fibrosis under diet challenge in the knockout mice[193-195]. In agreement with its enzyme activity, hepatic *Mboat7* deficiency resulted in significant changes in PI composition in the liver and hepatocyte ER, with selective depletion of arachidonoyl-containing PIs and increased lysophospholipids[190]. Although PI only comprises about 5% of total cellular phospholipids, the change in hepatic membrane composition was shown to promote *de novo* lipogenesis mediated by SREBP1-c, and upregulate fibrogenic gene expression independent of hepatic inflammation[192,194]. However, there are still discrepancies with regard to insulin signaling and liver inflammation in these models, which requires further investigation[192,194-196]. Nevertheless, *Mboat7* deficiency alters the liver lipidome in all models, which likely contributes to NAFLD phenotypes. Therefore, these data further emphasize the important roles of lipid composition in NAFLD development.

1.4.1.5 *HSD17B13*

17β-hydroxysteroid dehydrogenase 13 (HSD17B13) is a member of hydroxysteroid dehydrogenase family with catabolism activities for estrogens and androgens. Human *HSD17B13* gene was first cloned in 2007 and has been shown to be exclusively expressed in the liver[197]. In 2018, it was first reported that a loss-of function splice variant rs72613567:TA in *HSD17B13* was significantly associated with reduced risk of NASH and fibrosis, but not steatosis, in human cohorts[198]. Furthermore, the protective effect of this variant was also verified in alcoholic-related HCC and liver injuries[198-200]. rs72613567 variant is located at a splice site outside of exon 6 of *HSD17B13*, and the T>TA mutation leads to the expression of a truncated form of this enzyme, which is unstable with less enzymatic activity[198]. Further GWAS have identified other SNPs mapped to this gene that produce different loss-of-function variants, which also showed protective effects on NAFLD[201,202].

The pathological effect of HSD17B13 dissociates inflammation and fibrosis from steatosis in NASH patients. Although variants of *HSD17B13* were highly correlated with reduced fibrosis, inflammation and risk of NASH, they had no effect on steatosis[198,201]. To decipher the mechanisms underlying its protective role against fibrosis, studies have focused on examining its enzyme activity and identifying substrates. The loss-of function variants of *HSD17B13* exhibited a reduced ability to catalyze estradiol[198] and less retinol dehydrogenase activity[201,203]. As a consequence, mutation carriers were found to have increased hepatic sex steroids, including pregnenolone and androstenediol[204]. Moreover, lipidomic and metabolomic analyses revealed increased hepatic phospholipid levels[204,205], inhibited pyrimidine catabolism[204] and decreased 3-methylglutarylcarnitine levels[206]. However, how these altered metabolic pathways contribute to fibrosis remains to be determined.

It was reported that the expression of *HSD17B13* is upregulated in NASH patients through LXRα-SREBP1-c axis, resulting in steatosis[201,207]. However, this does not explain the pro-steatosis effect of HSD17B13 deficiency. Another study showed that phosphorylation of Serine 33 in HSD17B13 by PKA facilitated lipolysis by promoting its interaction with ATGL on lipid droplets[208], which sheds new light on the role of HSD17B13 in liver diseases. Interestingly, studies using mouse models have revealed discrepancies with human data. For example, loss of *Hsd17b13* in the liver has been shown to increase hepatic fatty acid synthesis and inflammation without diet challenge[209]. Mice with whole-body deletion of *Hsd17b13* gained more body weight under chow diet, and no protective effect was observed in the knockout mice under diet-induced NAFLD conditions[210]. In contrast, protection against fibrosis was observed in AAV-mediated *Hsd17b13* shRNA knockdown mouse model on choline deficient diet[204]. Therefore, extra caution is needed when transforming mechanisms established in mouse models to humans. This species variation may also draw our attention to the unique metabolic pathways that distinguish mouse and human, where HSD17B13 acts differently.

1.4.1.6 *MARC1*

Mitochondrial amidoxime-reducing component 1 (MARC1) is a mammalian molybdenum-containing enzyme located on the outer mitochondrial membrane first discovered in 2008[211]. The activity of this enzyme family (including MARC1 and MARC2 in humans) is to reduce N-hydroxylated compounds by forming a complex with cytochrome b_5 and its reductase[212]. The physiological function of this enzyme is largely unknown, except for its involvement in drug metabolism and detoxification of metabolic products such as trimethylamine N-oxide and mutagenic DNA bases[213,214]. In 2010, a meta-analysis in European population identified a SNP (rs2642442) in the intron of *MARC1* to be significantly associated with decreased plasma total cholesterol levels[215], suggesting its potential roles in lipid metabolism. More recently, two GWAS demonstrated that rs2642438, another SNP in exon 3 of *MARC1* that encodes an p.A165T variant, is associated with less severity of NAFLD, lower hepatic fat, serum AST/ALT levels and all-cause cirrhosis[3,216]. These studies suggest significant protective effects of MARC1 against NAFLD. However, the underlying mechanisms are poorly understood.

An early study identified the p.A165T mutant in human cohorts and found dramatic decrease in N-reductive activity of MARC1[217]. However, recent structural analysis suggested conflicting results regarding the impact of p.A165T mutation on the structure and enzymatic activity of MARC1[218,219]. It is possible that MARC1 has activities other than N-reductase that may be involved in the pathological process. Interestingly, lipidomic data from human p.A165T carrier have shown increased hepatic PC levels, especially polyunsaturated PC species, indicating a potential role in phospholipid remodeling. This alteration in PC composition is opposite to what was observed in patients carrying mutations in *TM6SF2*, which promote NAFLD, raising the possibility that their pathologic roles may converge in phospholipid remodeling. A recent study on primary human hepatocytes and mouse knockdown model confirmed the protection effect of Marc1 deficiency on diet-induced steatosis and fibrosis. Interestingly, this study suggested that the physiological effect of *Marc1* knockdown may act through Kennedy pathway, a PL *de novo* synthesis pathway, and fatty acid metabolism[220]. These results consistently implied the potential roles of PL in NAFLD pathogenesis and connected it to mitochondria function. Further studies on mouse models are still required to uncover the physiological role of MARC1. Moreover, the high expression of *MARC1* in both adipose tissue and liver of humans adds more complexity to deciphering the pathological function of MARC1 in NAFLD progression.

1.4.1.7 *GCKR*

Glucokinase regulator (*GCKR*), also known as glucokinase regulatory protein (GKRP), is primarily expressed in the liver and plays a crucial role in glucose metabolism. It regulates glucose metabolism by competitively binding to glucokinase (GK), which cannot be regulated by substrate saturation or product inhibition as other hexokinases[178,221]. GWAS have identified SNPs in *GCKR* that are associated with NAFLD-related traits[24,181,202]. In fact, SNPs in *GCKR* are associated with over 130 metabolic traits and diseases, making it one of the most pleiotropic GWAS loci[222]. Specifically, variants at rs1260326, resulting in a missense mutation, have been linked to increased liver fat, fibrosis and inflammation[181,202,223], but also with lower fasting glucose and lower insulin levels[224]. The dissociation between glucose homeostasis and NAFLD observed in GWAS is likely due to its glycolysis-regulation function. We note here that although the reference allele of rs1260326 in GRCh38 human genome is T, rs1260326C appears to be more frequent in various human cohorts, and rs1260326T is the minor allele associated with multiple disease traits. Therefore, the mutant variant is considered as rs1260326C>T P446L.

It has been reported that GKRP is involved in hepatic glucose sensing and uptake[225,226], thereby contributing to improved glucose handling. The P446L variant of GKRP shows deficient binding ability with GK, leading to its release from the nucleus, which increases hepatic glucose uptake and promotes glycogen synthesis and glycolysis. This, in turn, result in excessive acetyl-CoA production and fuels the SREBP1-c mediated *de novo* lipogenesis[227,228]. This is consistent with the GWAS data showing protective effect of *GCKR* mutation on insulin resistance, with lower fasting glucose and insulin levels[224,229,230]. However, studies using human liver organoids derived from iPSCs from different mutant carriers showed impaired hepatic insulin response in P446L carriers when treated with fatty acids. The conflicting results may be attributed to the elevated "reductive stress" caused by increased NADH/NAD+ ratio during glycolysis. It was proposed that although the increased glycolysis and glucose uptake lowers blood glucose levels, the increase in free cytosolic NADH leads to higher hepatic glucose production with insulin, causing hepatic glucose intolerance[222]. Overall, the "double-edged sword" effect of GKRP could limit its potential as a therapeutic target for metabolic disorders.

The effect of GKRP in the pathogenesis of NAFLD is complex. A recent cohort study found that the P446L variant had opposite effect with different diabetic status. P446L carriers with HbA1c<5.7% (non-diabetic) showed lower lobular inflammation and NAFLD activity score (NAS), whereas patients with HbA1c>6.4% showed higher inflammation and NAS[228]. In addition, diabetic patients carrying P446L were resistant to metformin treatment, while non-diabetic carriers responded to it[228]. These results suggest a complex interplay between insulin resistance and fatty liver in carriers of GCKR mutation. Nevertheless, deciphering the pathogenesis of this mutation may reveal the role of NADH/NAD+ regulation in NAFLD development, which could uncover a novel pathway involving "reductive stress" and improve our understanding of NAFLD.

1.4.1.8 Enlightenment from genetic factors in NASH pathogenesis

Since the first assembly of whole human genome sequence, our understanding of the functions of genes in health and diseases has significantly advanced, especially with a plethora of knowledge learned from GWAS, which have identified loci associated with various traits. Although GWAS have mapped more than 100 genes linked to NAFLD-related traits from multiple large human cohort studies, they do not provide mechanistic insight into the functions of these genes. In recent years, researchers have focused on investigating the pathogenesis of these identified loci. Here, we summarized the genes commonly associated with different NAFLD traits from multiple studies, with the aim to uncover underlying mechanisms which might shed light on our understanding of NAFLD pathogenesis (Figure 1.6).

The lipid composition of TG and PC has been found to be significantly altered in carriers of many NAFLD-related mutations. Lipidomic studies have shown that mutations in *TM6SF2*, *MARC1* and *HSD17B13* significantly alter the composition of liver phospholipids and/or TG in human carriers, and *PNPLA3* and *MBOAT7* themselves possess the enzymatic activity to remodel TG and PI, respectively[3,174,190,205]. One common feature of these lipid remodeling processes is that saturation tends to increase, whereas PUFA incorporation is hindered, which is associated with increased risk or severity of NAFLD. Interestingly, lipidomic analyses of NASH patients have revealed significant decrease in PUFA content in PC and TG in NAFL livers, with no further change as progression to NASH[231,232]. Furthermore, deficiency in *Lpcat3* (*Mboat5*), an enzyme involved in PC remodeling, results in decreased PUFA in PC and increased steatosis and inflammation in the liver[17,233]. Our recent studies demonstrated that increasing membrane phospholipid saturation *per se* is sufficient to drive the initiation and progression of NASH and HCC[234]. These findings suggest that lipid remodeling may play a causal role in the pathogenesis of NAFLD. Targeting lipid remodeling could be a novel and promising therapeutic approach for NAFLD treatment.

Interestingly, some NAFLD-related mutations tend to cluster around certain regions of the genome, which are sometimes considered as large loci instead of specific genes in some GWAS. For example, the *TM6SF2* and *SUGP1* are located less than 3,000 bp apart, and the region containing these two genes, together with ~20 other nearby genes, is referred to as *NCAN* locus. The clustering of SNPs linked to similar traits may suggest aberrant expression regulation in this region, rather than dysfunction of a particular gene. A large proportion of discovered SNPs are in the intron regions, most of which are still functionally unknown. Moreover, the genes that have been mapped, such as *TM6SF6* and *SUGP1*, lack mechanistic links between the function of their encoded proteins and the associated traits. Interestingly, one study found that among the 20 genes in the *NCAN* locus, only *LPAR2* was significantly upregulated in patients with steatosis, even though SNPs were mapped to *SUGP1* from the same cohort. Therefore, focusing on the mapped genes from GWAS may mislead us away from the true genetic factors underlying NAFLD.

In many mutant carriers, serum lipids, insulin resistance and NAFLD can be dissociated. Although type II diabetes and obesity are considered as significant risk factors for NAFLD, it is important to note that not all NAFLD patients have these disorders. For example, SNP in *TM6SF2* shows protection against serum lipid and insulin resistance while promoting steatosis[162,171], while GCKR mutant exhibits opposite effect on NAFLD severity depending on diabetic background[228]. This dissociation often results from deficient VLDL secretion and increased hepatic glucose uptake, which shifts the burden from serum to the liver. This mechanism may be more informative to understand the pathology of lean NAFLD. Although lean NAFLD is considered to be benign based on serum indexes, it is histologically similar to obese NAFLD in terms of steatosis and hepatocyte ballooning[235]. This knowledge may shed light on the diagnosis and prognosis of NAFLD in lean individuals.

1.4.2 Mechanisms of NASH Pathogenesis

NASH is an advanced state of steatosis accompanied by chronic inflammation and fibrosis. Although the number of cases has risen quickly in recent years, few therapeutic options are available for NASH currently, mainly due to the lack of detailed understanding of its pathogenesis. It is still debatable in terms of the pathogenesis of NASH. A widespread model was "multiple hit", which regards simple steatosis as the first hit, and inflammation, liver injury, oxidative stress or other factors as other hits that promote steatosis to NASH[236]. This model is come up partly because steatosis is the first stage in most patients and only ~25% of NAFL or steatosis patients further become NASH, making it much less prevalent than NAFLD[133]. However, various "hit" contribute to the NASH progression, leading to the heterogeneity of NASH patients. Yet the consistencies of these "hits" lies in the generation of liver injuries due to cell deaths.

ER stress is one of the "hit" that drives NASH from steatosis. ER is the major site of protein synthesis and secretion. The ER proteostasis is maintained by the unfolded protein response (UPR), where three sensors on the ER membrane, PERK (double-stranded RNA-activated protein kinase (PKR)–like ER kinase), IRE1α (inositol requiring enzyme 1α) and ATF6 (activating transcription factor 6), monitor the unfolded or misfolded protein. Accumulation of unfolded or misfolded proteins in the ER results in ER stress, activating UPR to initiate the transcription of genes involved in protein folding, degradation, ER biogenesis and apoptosis. In the pathogenesis of NASH, ER stress can exacerbate NASH pathogenesis by promoting lipogenesis, apoptosis and inflammatory response[237]. For example, ER stress promotes the activation and translocation of SREBP-1c and SREBP2 by caspase 2-dependent cleavage and activation of S1P, promoting fat and free cholesterol accumulation in hepatocytes[238]. The IRE1α and PERK arms of UPR can trigger NF-κB activation thus promotes TNFα release by macrophages. This activated TNF signals through TNFR, promoting lipogenesis, cell death, inflammation and HCC development[239]. Moreover, a recent study showed that activation of IRE1α stimulated the release of hepatocyte-derived ceramide-rich extracellular vesicles which recruit macrophage infiltration in the liver, elevating inflammation in NASH[240]. These results emphasized how ER stress contributes to the pathogenesis of NASH, but how is the ER stress initiated? It has been shown that the lipidome has significantly changed in obese context. The increased SFA and membrane PC directly alters the calcium homeostasis of ER and initiates ER stress[241]. In addition to PC quantity, the increased saturation of PC observed in obese mice and NASH patients was shown to induce ER stress and inflammation[233]. Therefore, these results illustrate the critical roles of ER stress in both steatosis and liver injury, promoting all "hits" of NASH.

Oxidative stress is another factor that is massively investigated in NASH pathogenesis. Although being critical signaling molecules at low quantity, excessive ROS generated due to mitochondrial dysfunction is detrimental and can lead to cell death. In the pathogenesis of NASH, mitochondrial dysfunction can be induced by lipotoxic lipids such as free cholesterol and ceramide. Cholesterol accumulation in mitochondria blocks mitochondrial GSH import, alters morphology and disturbs membrane potential of mitochondria, promoting oxidative stress and TNF-induced steatohepatitis[242,243]. Mitochondrial membrane ceramides, on the other hand, has been shown to interact with MFF to promote mitochondrial fragmentation, compromising mitochondrial functions and promotes insulin resistance and diet-induced NASH[66,244]. ROS generated from mitochondria promotes NASH and HCC by attacking lipids, proteins and genomes. For example, oxidized PL generated from lipid peroxidation can impact mitochondrial function, resulting in increased ROS production and enhanced liver and systemic inflammation[245]. These products of peroxidized lipids can also act as damage-associated molecular patterns (DAMP) and form oxidative stress-derived epitopes (OSE), which can be uptake by B cells and dendritic cells and present to T_H cells, activating macrophages and NKT cells and stimulating inflammatory responses in NASH[246]. Previous studies also showed that oxidative stress led to chromosomal instability in terms of increased double strand breaks and chromosomal translocations in primary mouse embryonic fibroblasts[247]. And increased ROS resulting from mitochondrial genome instability could promote intestinal tumorigenesis[248]. However, although increased oxidative stress has been shown to be a specific etiology of NASH-induced HCC, how oxidative stress leads to genome instability in NASH and HCC context is still not clear[249].

Bile acids (BA) metabolism has been shown to be dysregulated in NASH patients, whose circulating and liver BA are both significantly increased with an association to the severity of disease[250,251]. Human patients with NASH-associated HCC also showed increased bile acid synthesis compared to other HCC patients, indicating a potential inhibited FXR signaling[249]. Studies in mouse models of NASH consistently showed increased serum BA levels but varies in liver BA biosynthesis[252-254]. Increased BA was shown to promote NASH and HCC through activated inflammation and tissue stemness, yet the detailed mechanism is still lacking[253,255]. Although it is still not clear whether the increased circulating BA is the primary cause or the consequence of NASH, FXR activation and reduction of BA has become a promising therapeutic target against NASH. Inhibition of BA reabsorption by blocking its ileal transporter ASBT significantly improved steatosis, glucose metabolism and hepatic inflammation[256]. FXR activation has been shown to reduce hepatic lipogenesis and bile acid levels, leading to decreased intestinal lipid absorption and attenuated steatosis[118]. There are also several FXR agonists currently under clinical trials, which we will further discuss in the next section.

To summarize, the current understanding of NASH pathogenesis is initiated from lipotoxicity due to the accumulating lipotoxic lipids, such as free fatty acid, free cholesterol and ceramide in hepatocytes. These lipotoxic lipids disrupts organelle functions and leads to ER stress and oxidative stress, inducing inflammatory response and subsequent cell death. The tissue damage thereby activates fibrogenesis and regeneration, eventually develop NASH, cirrhosis and HCC (Figure 1.7)[257,258].

1.4.3 Current Therapeutic Targets of NAFLD

Based on the understanding of NASH pathogenesis, there are many ongoing tests for its treatment, with different targets including lipid metabolism and inflammation in the liver. In addition, many extrahepatic targets are being intensively investigated. However, currently, there is still no FDA-approved drugs targeting NASH, reemphasizing the complexity of this disease.

Reducing fatty acid and lipogenesis in the hepatocytes is an important strategy based on the concept of lipotoxicity. Antagonists targeting enzymes in lipogenesis like ACC1 and SCD1 have been shown improved steatosis and inflammation. However, the shortness of ACC inhibitor is the compensatory increase of SREBP1 activity which increases circulatory TG content generated from peripheral free fatty acids[259]. The SCD1 inhibitor Aramchol did not meet the prespecified significance level for liver fat reduction, but with promising safety and patient tolerance[260]. Agonists targeting PPARα and PPARγ are shown to improve steatosis, inflammation and hepatocellular ballooning as well as hepatic fibrosis, due to the β-oxidation-promoting effects of PPARs. Induction of PPAR in adipose tissue can redispose the lipid out from liver, improving liver lipid burden at the expense of overall weight gain[257]. However, a PPARα/δ agonist Elafibranor, despite showing improvement on insulin resistance, inflammation and fibrosis in preclinical models and early clinical studies, failed to meet the predefined objectives in a phase III trial which is now closed[261]. Another PPAR agonist Lanifibranor showed promising result in a phase II trial and is currently under a phase III trial[262].

As we discussed in the previous section, FXR is also a promising therapeutic target against NASH. FXR agonist Obeticholic acid (OCA) has been shown to significantly improve NAFLD activity score and mean fibrosis stage in both phase II and III trials in patients with NASH and significant fibrosis[261]. However, in a phase III trial, the NASH resolution endpoint was not met, with adverse events such as elevated LDL at early stage of treatment, despite significant improvement in fibrosis[263]. Therefore, combined treatment might be required for OCA and its prescribed area has to be carefully constricted. Another FXR agonist Tropifexor has recently finished a phase II trial, showing improvement in biomarkers of liver injury and indirect indicators of histologic improvement after 48 weeks of treatment, with an early increase in LDL cholesterol. However, greater histologic improvement of fibrosis or resolution of NASH relative to placebo was not observed, indicating potentially different therapeutic mechanisms compared to OCA[264].

Some hormones that improve systemic metabolism are promising targets for NASH. FGF21 has been shown with beneficial effect on insulin signaling and energy expenditure in mouse models, and short-term trial also showed improved steatosis, insulin resistance and liver stiffness[265]. Efruxifermin, a long-acting Fc-FGF21 fusion protein has shown significantly reduced hepatic fat fraction with safety. But its efficacies on other NASH parameters still requires investigation[266]. GLP-1 receptor agonists, such as Liraglutide and Semaglutide, are currently being tested and improvement has been reported for NASH, with expected significantly weight loss[261].

Several other therapeutic targets are under clinical trials. Intervention of hepatic inflammatory response has been investigated. The C–C motif chemokine receptor 2 (CCR2)–CCR5 chemokine axis amplifies the liver's innate immune response and links inflammation to activation of hepatic stellate cells and fibrogenesis. Cenicriviroc an antagonist of CCR2-CCR5, has been shown to improve fibrosis with a favorable safety and tolerability profile. But the following study was terminated due to the lack of efficacy[261]. Inhibition of SGLT1/2, the sodium-glucose cotransporter, by Licogliflozin, exhibited reduced body weight, serum AST and ALT, and liver fat[267]. Other SGLT2 inhibitors are also used in the treatment of T2D, indicating the common features and therapeutic strategies of metabolic disorders.

Currently the therapeutic targets and treatment candidates are mainly activators or repressors for a specific pathway or hormone signaling. This will undoubtedly come with many side effects given the fact that the pathogenesis and signaling network of NASH is complex and interactive. Moreover, despite plentiful targets and promising drugs discovered in preclinical models, all of them so far are failed in clinical trials. This discouraging fact emphasizes significant discrepancies between human and mouse models, which are extensively used in research. Therefore, better preclinical models are required that mimic human physiology and recapitulate human NASH pathogenesis. Nonhuman primate model might be a prominent choice in the future[268]. Furthermore, combined therapies with tissue specific delivery strategies might minimize the side effect from their diverse functions in other organs.

1.5 TABLES AND FIGURES

Table 1.1 Rat hepatic membrane lipid composition[269].

Phospholipid class (%)	Liver					
	PM	ER-S	ER-R	Mito	IMM	OMM
PC	24.5	44.8	56.5	36.8	35.8	40.5
PE	11.2	17.4	21.9	31.5	36.1	27.1
PI	3.69	5.42	8.45	6.00	1.89	7.50
Cardiolipin	NA	1.54	1.13	13.5	19.2	8.48
Sphingolipid	13.1	9.94	3.66	2.18	0.75	3.93
Cholesterol	43.2	19.2	6.10	9.09	5.66	10.7
Other lipids	4.26	1.78	2.25	0.91	0.57	1.70

ER-S: Smooth ER; ER-R: Rough ER.

Table 1.2 Genetics and Experimental Models of GWAS identified genes related to NAFLD.

Gene	SNPs	Correlation with NAFLD	Function	Mouse model	Phenotypes	Ref.
PNPLA3	rs738409 rs2896019 rs3747207	Promote	Retinyl ester hydrolase, TG acyltransferase	*Pnpla3* KO	No difference in energy, glucose and lipid homoeostasis or hepatic steatosis or injury	ref[149], ref[150]
				OE of I148M in liver	Increased formation of fatty acids and TAG, impaired hydrolysis of TAG, and relative depletion of TAG long-chain polyunsaturated fatty acids	ref[135], ref[151]
				KD of *Pnpla3* by ASO	Reduced hepatic steatosis, decreased fatty acid esterification and increased hepatic insulin sensitivity	ref[155]
				shRNA KD of *Pnpla3* in I148M OE mice	Reduced liver TG level	ref[154]
				OE of *PNPLA3* in cell lines	Increased cellular lipid synthesis	ref[146]
TM6SF2	rs58542926	Promote (with improved insulin sensitivity)	Not clear	*TM6SF2* siRNA inhibition in human cell lines	Reduced secretion of TG-rich lipoproteins (TRLs) and increased cellular TG concentration and lipid droplet content	ref[163]
				AAV-shRNA KD of *Tm6sf2* in mouse liver	Lower plasma cholesterol and TG levels and increased liver TG and cholesterol ester	ref[162]
				Liver-specific *Tm6sf2* OE and KO	OE of *Tm6sf2* increases liver TG and cholesterol on chow or HFD; No change in liver TG and cholesterol levels in *Tm6sf2* KO	ref[167]

				Tm6sf2 whole-body KO	Blocked VLDL secretion and higher liver lipids	ref[169]
				AAV-mediated OE of wild-type or E167K *TM6SF2*	Lower liver and serum lipids with reduced fibrosis	ref[173]
SUGP1	rs8107974	Promote	RNA splicing factor	Liver *Sugp1* OE	Increased plasma TG and cholesterol	ref[185]
MBOAT7	rs626283 rs641738	Promote	lysophospholipid acyltransferase	Global *Mboat7* KD by ASO	Promoted NAFLD development on HFD and impaired insulin signaling	ref[192]
				Liver-specific *Mboat7* KO	Increased liver inflammation and fibrosis on HFCDD	ref[193]
				Liver-specific *Mboat7* KO	Develop steatosis on chow diet and fibrosis on HFD	ref[194, 195]
HSD17B13	rs13118664 rs9992651	Protect	hydroxysteroid dehydrogenase for estrogens and androgens	*Hsd17b13* global KD by AAV-shRNA	Protects from CD induced fibrosis.	ref[204]
				transgenic *HSD17B13* S33A mutation (HSD17B13 33A/A) KI mouse	Develop spontaneous hepatic steatosis and increased inflammation	ref[208]
				Hsd17b13 global KO	Hepatic steatosis and increased inflammation.	ref[209]
				Hsd17b13 whole-body KO	Higher body weight on chow diet. No difference on body weight, liver TG, inflammation and fibrosis on HFD and WD.	ref[210]
MARC1	rs2642438	Protect	molybdenum-containing enzyme catabolizing N-hydroxylated compounds	Liver specific *Marc1* KD	Protects against diet induced NASH with lower liver lipids and fibrosis.	ref[220]

Table 1.2 Cont.

GCKR	rs780094 rs1260326	Promote	Competitively binding and regulating glucokinase	No mouse model specific for NASH

HFCDD = high- fat, methionine- low, choline- deficient diet; HFD = High fat diet; OE = overexpression; CD = choline deficient; KO = knockout; KD = knockdown; KI = knock-in; WD = western diet.

Table 1.2 Cont.

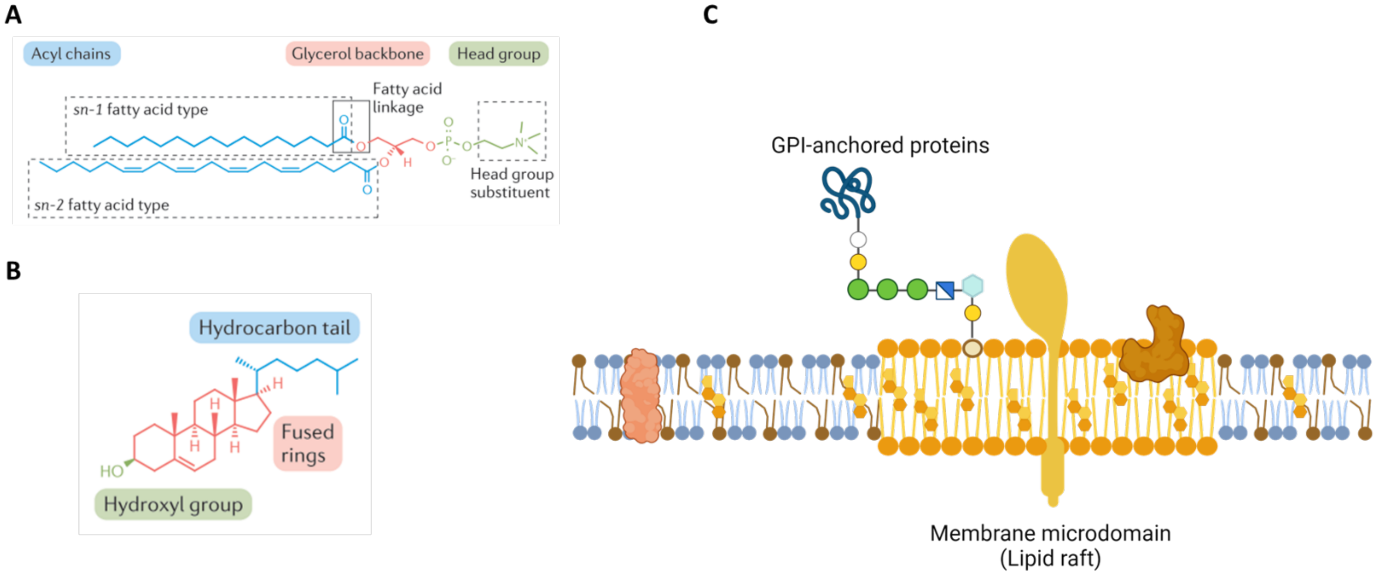

Figure 1.1 Membrane lipids and structure. (A) The structure of phospholipid. (B) The structure of cholesterol[5]. (C) Schematic picture of membrane structure, showing microdomains.

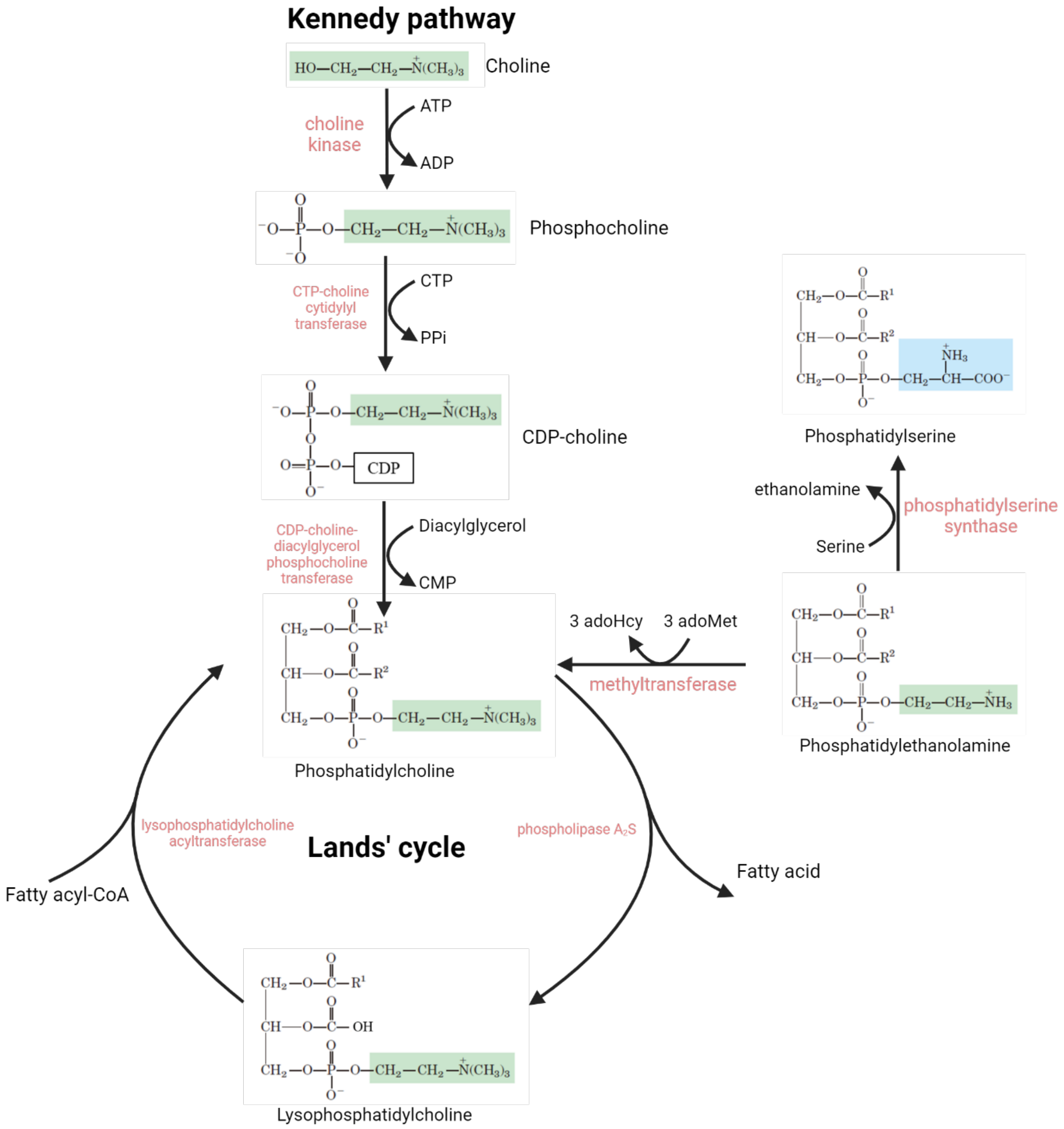

Figure 1.2 Phosphatidylcholine (PC) synthesis and remodeling. PC is synthesized through two pathways in mammalian cells. In the Kennedy pathway, choline group is activated by CDP, then added to DAG as a head group. PC can also be converted from phosphatidylethanolamine (PE), through methylation by PE methyltransferase. The fatty acyl composition is regulated by the Lands' cycle, where the fatty acyl chain on the sn-2 site is remodeled favoring polyunsaturated fatty acids[1]. CTP: cytidine triphosphate; CMP, cytidine monophosphate; adoHcy, S-adenosyl homocysteine; adoMet, S-adenosyl methionine.

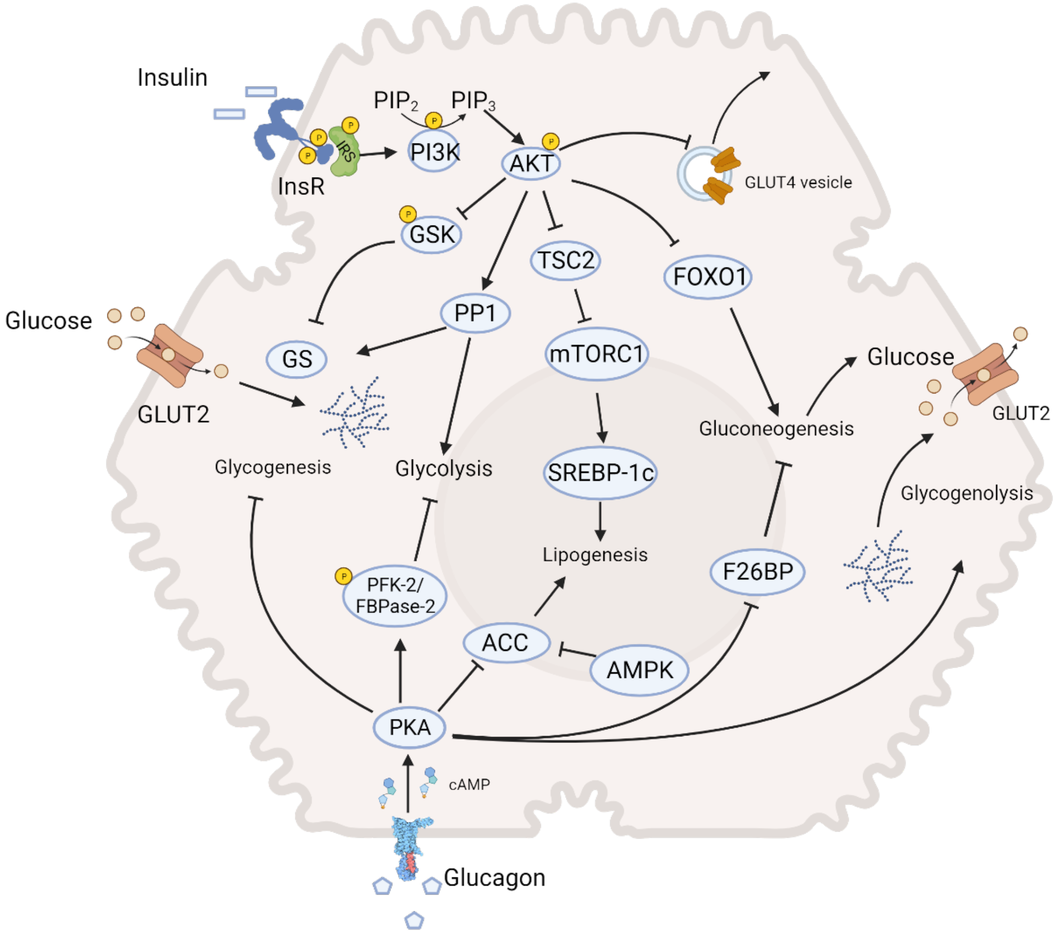

Figure 1.3 Integrative regulation of glucose metabolism. The central node of insulin signaling is AKT (PKB), which activates glycolysis, glycogenesis, lipogenesis and inhibits gluconeogenesis. On the contrary, PKA is the central regulator of glucagon signaling, which opposes the effects of insulin. Abbreviations: SREBP-1c: sterol regulatory element binding protein 1c; TSC2, tuberous sclerosis 2; PKA: protein kinase A; cAMP: cyclic adenosine monophosphate; AMPK: AMP kinase; FOXO, forkhead family box O; GSK3, glycogen synthase kinase 3; IRS, insulin receptor substrate; PP1: phosphoprotein phosphatase 1; GS: glycogen synthase; PFK-2/FBPase-2: phosphofructokinase-2/fructose 2,6-bisphosphatase.

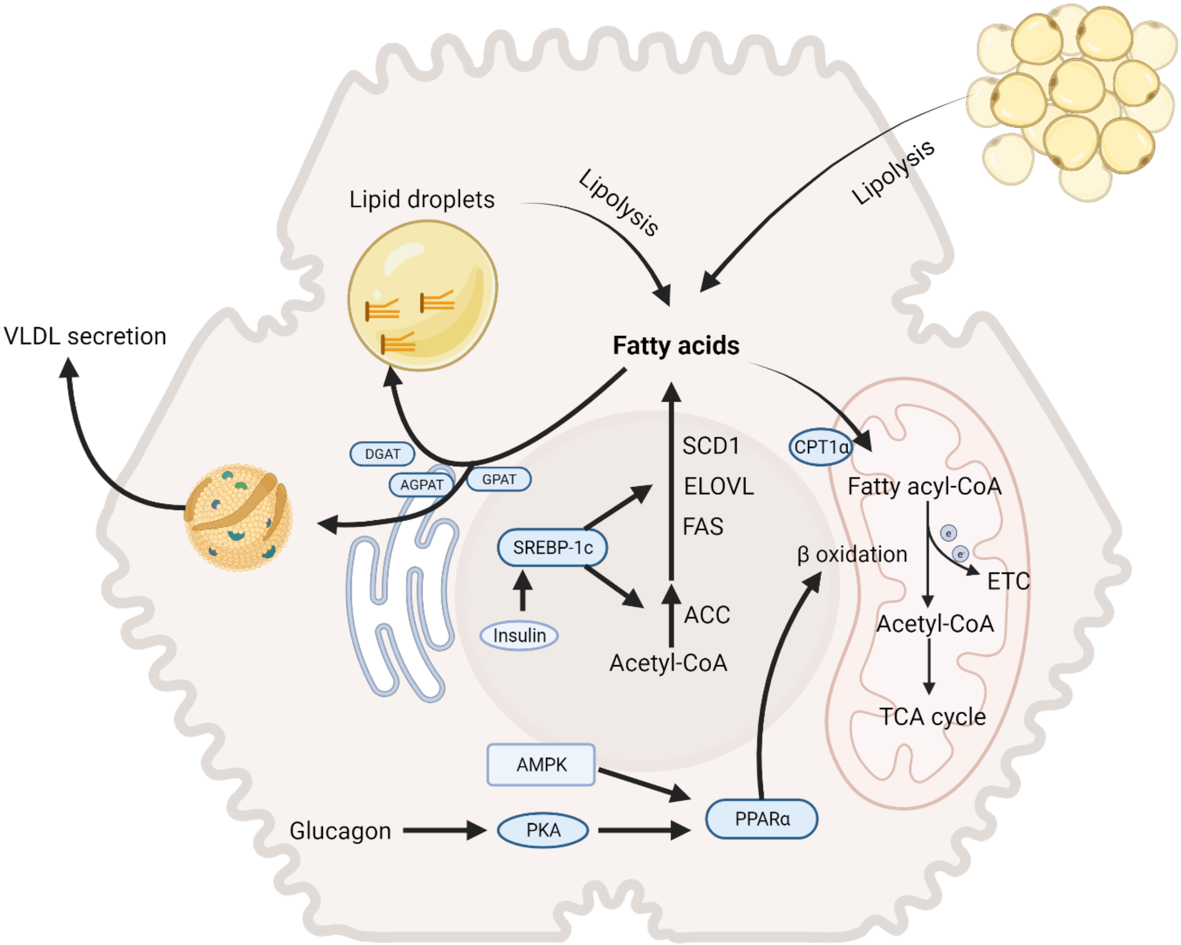

Figure 1.4 The regulation of fatty acid metabolism in hepatocytes. Fatty acid synthesis is promoted by insulin-induced activation of SREBP-1c, thereby storing excessive glucose in the form of fatty acids. PPARα is a fatty acid oxidation activator in response to energy deprivation. Abbreviations: ACC: acetyl-CoA carboxylase; FAS: fatty acid synthase; ELOVL: fatty acid elongase; SCD1: steroyl-CoA desaturase 1; CPT1α: carnitine palmitoyltransferase 1α; ETC: electron transport chain; peroxisome proliferator-activated receptor α; AMPK: AMP-activated kinase; PKA: protein kinase A; DGAT: diacylglycerol O-acyltransferase; GPAT: glycerol-3-phosphate acyltransferase; AGPAT: 1-Acylglycerol-3-phosphate O-acyltransferase; SREBP-1c: sterol regulatory element binding transcription factor 1-c.

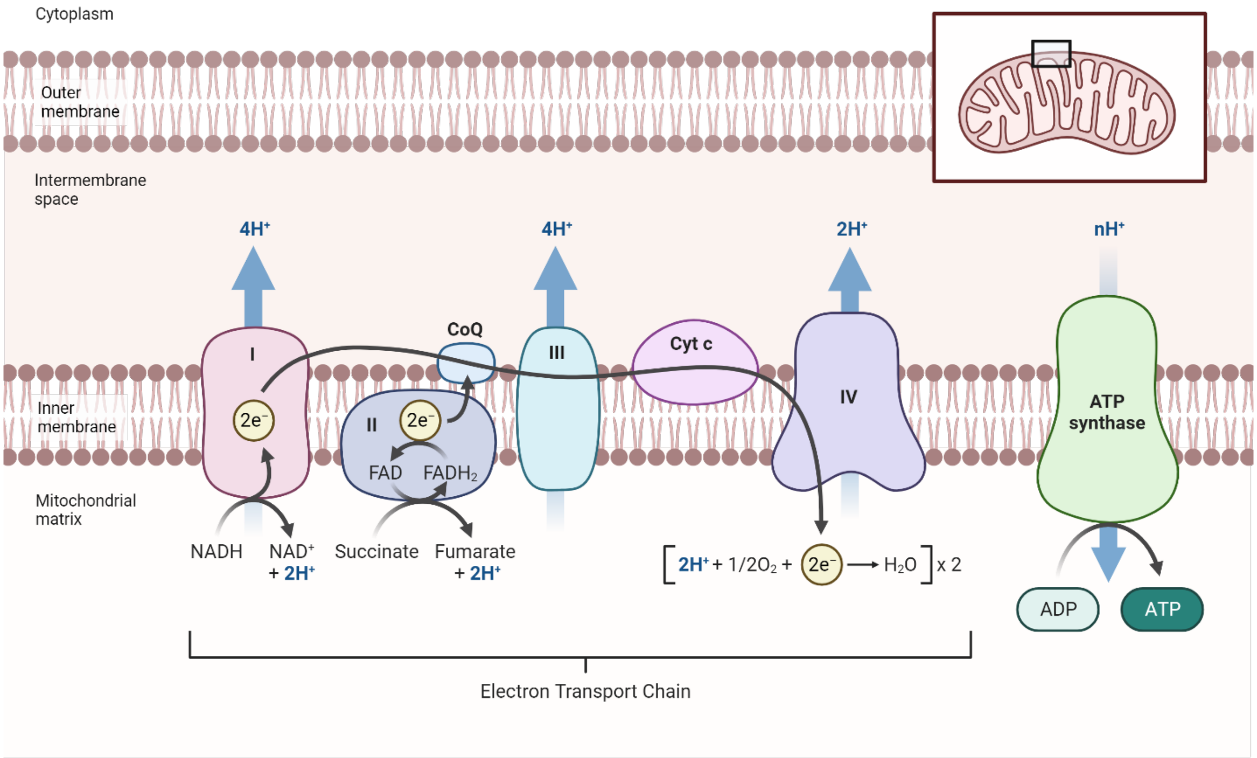

Figure 1.5 Mitochondrial electron transport chain. Electrons released from oxidation of substrates are carried by CoQ and cytochrome c to oxygen. This electron transport is coupled with proton efflux, generating proton-motive force that drives ATP synthesis by ATP synthase. This process is carried out in the inner mitochondrial membrane.

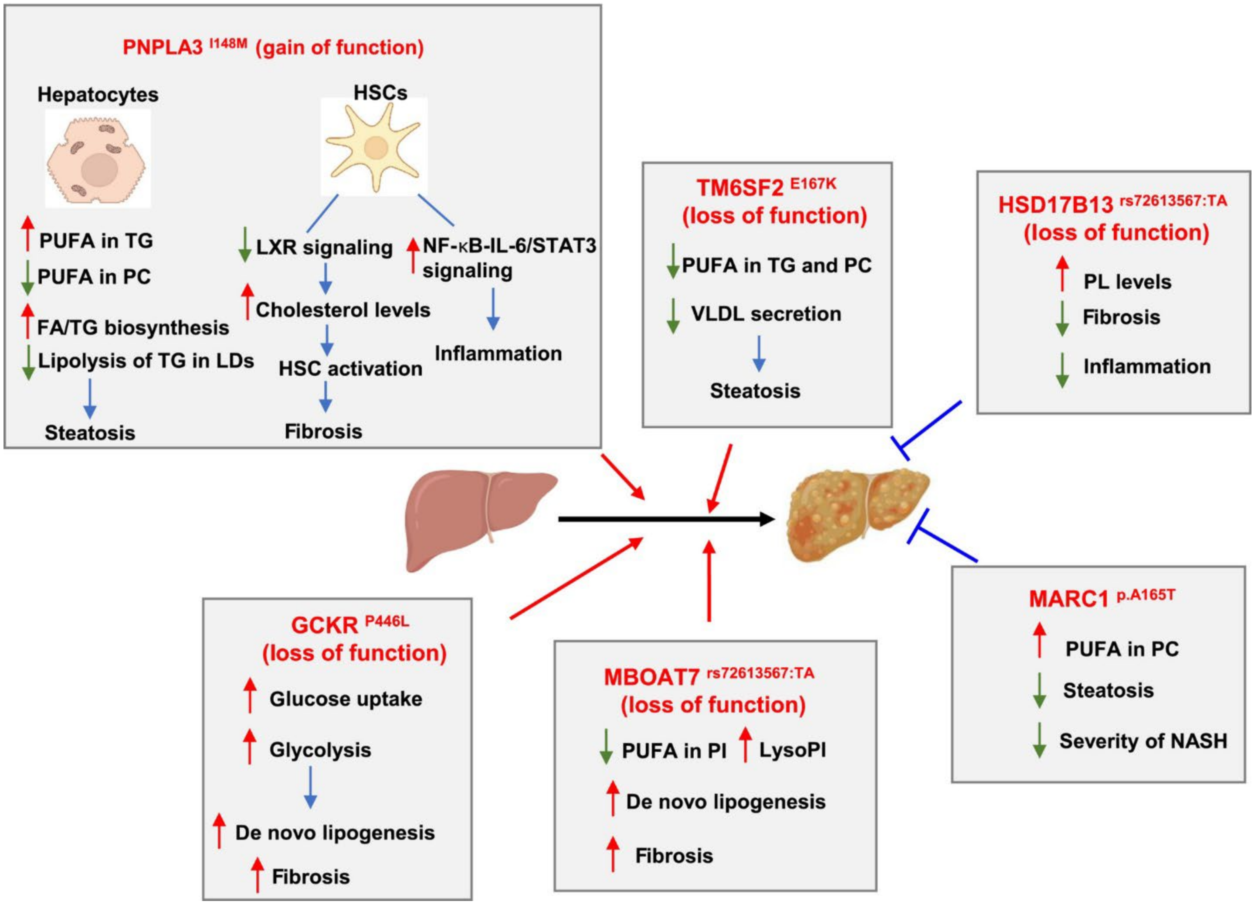

Figure 1.6 Most common genetic variants associated with non-alcoholic fatty liver disease and their roles in its progression. FA, fatty acids; GCKR, glucokinase regulator; HSCs, hepatic stellate cells; HSD17B13, 17β-hydroxysteroid dehydrogenase 13; IL-6, interleukin-6; LDs, lipid droplets; LXR, liver X receptor; MARC1, mitochondrial amidoxime-reducing component 1; MBOAT7, membrane-bound O-acyltransferase 7; NASH, non-alcoholic steatohepatitis; NF-κB, nuclear factor-κB; PC, phosphatidylcholine; PI, phosphatidylinositol; PL, phospholipids; PNPLA3, patatin-like phospholipase domain containing 3; PUFA, polyunsaturated fatty acids; STAT3, signal transducer and activator of transcription 3; TG, triglyceride; TM6SF2, transmembrane 6 superfamily member 2; VLDL, very low-density lipoprotein.

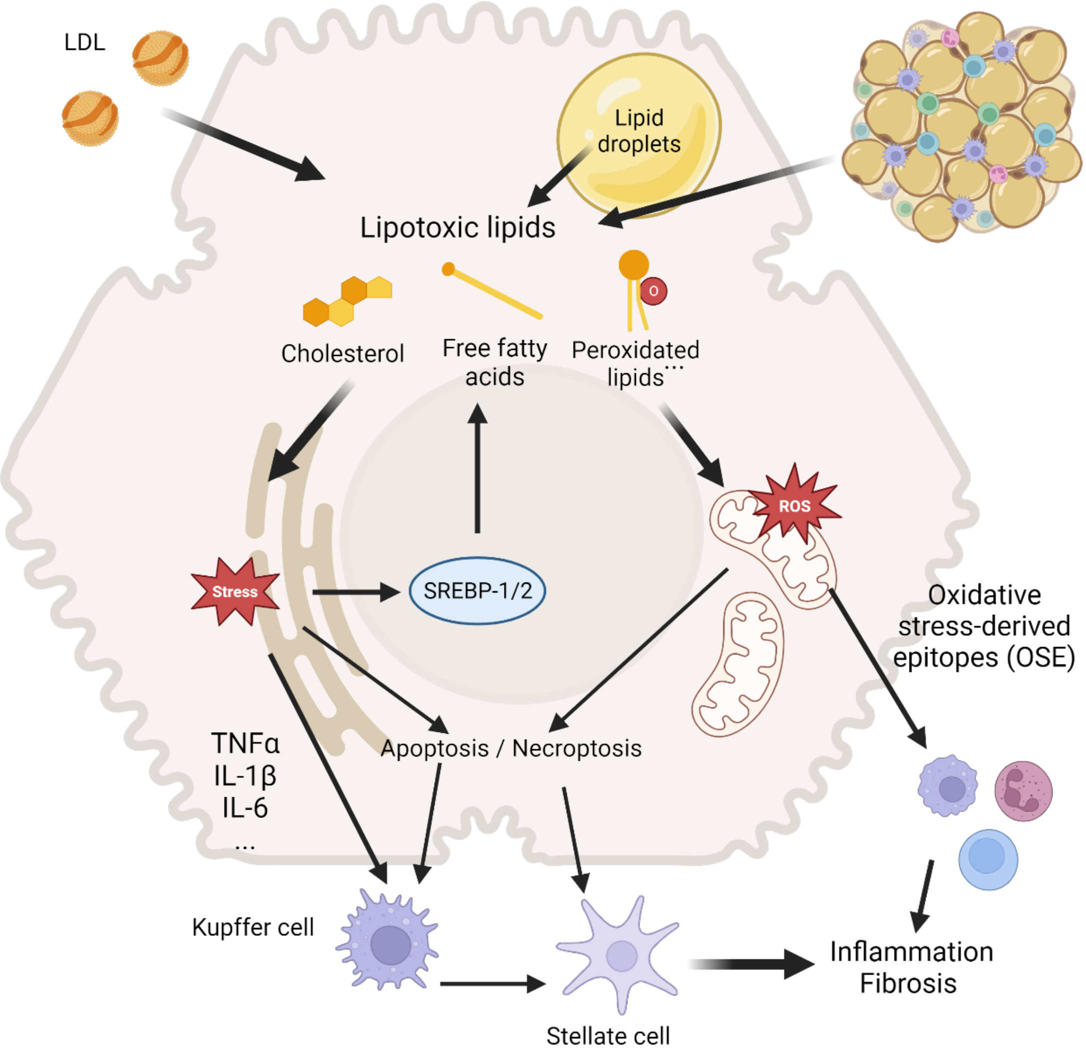

Figure 1.7 Current understanding of NASH pathogenesis. Inflammation and fibrosis caused by cell death is the direct promoter of NASH. The hepatocyte injury in NASH is mainly generated from ER stress or oxidative stress, which can be induced by lipotoxic lipids. Therefore, accumulating lipotoxicity due to metabolic dysregulation is the primary driver of NASH[257]. Abbreviations: SREBP-1/2: sterol regulatory element binding transcription factor 1/2; ROS: reactive oxygen species; LDL: low-density lipoprotein; TNFα: tumor necrosis factor α; IL: interleukin.

CHAPTER 2. HEPATIC PHOSPHOLIPID REMODELING MODULATES INSULIN SENSITIVITY AND SYSTEMIC METABOLISM[2]

ABSTRACT

The liver plays a central role in regulating glucose and lipid metabolism. Aberrant insulin action in the liver is a major driver of selective insulin resistance, in which insulin fails to suppress glucose production but continues to activate lipogenesis in the liver, resulting in hyperglycemia and hypertriglyceridemia. The underlying mechanisms of selective insulin resistance are not fully understood. Here we show that hepatic membrane phospholipid composition controlled by Lysophosphatidylcholine acyltransferase 3 (LPCAT3) regulates insulin signaling and systemic glucose and lipid metabolism. Hyperinsulinemia induced by high-fat diet (HFD) feeding augments hepatic *Lpcat3* expression and membrane unsaturation. Loss of *Lpcat3* in the liver improves insulin resistance and blunts lipogenesis in both HFD-fed and genetic *ob/ob* mouse models. Mechanistically, *Lpcat3* deficiency directly facilitates insulin receptor endocytosis, signal transduction and hepatic glucose production suppression, and indirectly enhances fibroblast growth factor 21 (**FGF21**) secretion, energy expenditure, and glucose uptake in adipose tissue. These findings identify hepatic LPCAT3 and membrane phospholipid composition as a novel regulator of insulin sensitivity and provide insights into the pathogenesis of selective insulin resistance (Figure 2.15).

---

[2] This chapter is published in its entirety in the Advanced Science. This article is reprinted with the permission of the publisher and is available from https://onlinelibrary.wiley.com/doi/full/10.1002/advs.202300416 and using DOI: https://doi.org/10.1002/advs.202300416

2.1 INTRODUCTION

The prevalence of type 2 diabetes (T2D) has increased dramatically due to the global rise in obesity, sedentary lifestyle, and energy-dense diets. T2D is characterized by relative insulin deficiency caused by pancreas β-cell dysfunction and insulin resistance in metabolic organs, including liver, muscle and adipose tissue[270,271]. The liver plays a central role in regulating glucose and lipid homeostasis. In normal liver, insulin binds to the insulin receptor (INSR), recruits insulin receptor substrates (IRS), and activates PI3K/Akt and its downstream effectors to stimulate glycogen synthesis and suppress gluconeogenesis[272]. Additionally, insulin is known to increase *de novo* lipogenesis and promote the esterification and secretion of triglyceride (TG) in the liver, thereby contributing to fatty liver and hypertriglyceridemia in T2D[273]. Aberrant insulin action in the liver is believed to be a major driver of insulin resistance, in which insulin fails to adequately suppress hepatic glucose production (HGP), but paradoxically continues to promote lipid biosynthesis, leading to hyperglycemia and hypertriglyceridemia[61]. Therefore, the lipid-promoting effect of insulin is maintained, while the control of HGP is defective during insulin resistance, a phenomenon known as selective insulin resistance. However, despite the extensive characterization of downstream signaling cascades in insulin's control of glucose and lipid metabolism, how insulin differentially regulates glucose and lipid metabolism in insulin resistant liver remains obscure.

Phospholipids (PLs) are major components of biological membranes that separate cellular contents from the surrounding environment, form organelles, and provide platforms for cellular processes, such as signal transduction, vesicle trafficking and molecular transport[274,275]. The chain length and number of double bonds in the fatty acids of PLs determine the biophysical properties of membranes, thereby affecting the function of membrane-bound proteins and processes associated with membranes[1,5]. In mammalian cells, PL composition is largely controlled by Lands' cycle, in which phospholipase A2 hydrolyzes sn-2 fatty acyl chain of PLs and lysophospholipid acyltransferase synthesizes a new PL species by incorporating another fatty acyl chain to the sn-2 site[4]. We previously identified a PL remodeling enzyme, lysophosphatidylcholine acyltransferase 3 (Lpcat3), as a major determinant of membrane PL composition in the liver[233]. Lpcat3 preferentially drives the incorporation of polyunsaturated fatty acids (PUFAs) into phosphatidylcholine (PC) to generate polyunsaturated PCs. We have shown that loss of *Lpcat3* in the liver selectively reduces polyunsaturated PCs in membrane and consequently decreases membrane fluidity, resulting in impaired SREBP-1c processing and lipogenesis, and VLDL secretion[17,96,176,276,277].

Here we show that high-fat diet (HFD) feeding augments *Lpcat3* expression and increases polyunsaturated PL composition in the liver. Knockout of *Lpcat3* in the liver (LKO) improves insulin sensitivity and glucose tolerance in both HFD-fed and *Leptin* deficient *ob/ob* mice. Furthermore, *Lpcat3* deficiency suppresses the expression of SREBP-1c and lipogenic genes in HFD-fed and *ob/ob* mouse liver. Mechanistic studies demonstrate that loss of hepatic *Lpcat3* enhances insulin sensitivity through both cell-autonomous effects by facilitating insulin signal transduction in early endosomes, and nonautonomous effects by increasing FGF21 secretion, energy expenditure, and glucose uptake in brown adipose tissue (BAT). These findings reveal an unrecognized reciprocal regulation between insulin signaling and PL remodeling, and highlight a mechanism whereby hepatic membrane PL composition mediates both pro-lipogenesis and anti-HGP effects of insulin in the liver, providing novel insight into the pathogenesis of selective insulin resistance.

2.2 MATERIALS AND METHODS

2.2.1 Mice

All animal procedures were conducted in compliance with protocols approved by the Institutional Animal Care and Use Committee (IACUC) at University of Illinois at Urbana-Champaign (Protocol #21200). *Lpcat3$^{fl/fl}$* and *Lpcat3$^{fl/fl}$*; *Albumin-Cre* mice have been described before[17]. *ob/ob* and *Fgf21-/-* mice were acquired from the Jackson Laboratory. All mice were housed under pathogen-free conditions in a temperature-controlled room with a 12 h light/dark cycle. Mice were fed chow diet (LabDiet #5001) or high-fat diet (Research Diets #D12492). All experiments were performed with male mice unless otherwise stated. For RNA and whole liver protein analysis, liver tissues were collected and snap frozen in liquid nitrogen and stored at −80°C. In the fasting and refeeding experiments, the fasting group was fasted overnight, and the refeeding group was fasted overnight and then refed with a HFD for 2 h. For food intake measurement, mice were housed individually in cages and food weight was measured daily. Mouse blood was collected by retro-orbital bleeding before sacrificing or by tail bleeding, and plasma was obtained by centrifugation. Plasma insulin and FGF21 levels were measured using Insulin ELISA kit (Crystal Chem) and Mouse/Rat FGF21 ELISA kit (BioVendor), respectively. For *in vivo* insulin signaling, insulin (Novolin N, Human) was injected to anesthetized mice retro-orbitally, and the liver was then perfused with PBS from *vena cava* and harvested at different time points.

2.2.2 Glucose and insulin tolerance test

Mice were fasted for at least 5 h in the morning and intraperitoneally (i.p.) injected with glucose or insulin (Novolin N, Human). Glucose was given at 1 g/kg body weight (BW) diluted in PBS. Insulin was given at 0.5 U/kg BW for chow diet-fed mice and 1 U/kg BW for HFD-fed and *ob/ob* mice. Blood glucose levels were measured from tail bleeding using a glucometer (OneTouch Ultra2) at designated time points.

2.2.3 Indirect Calorimetry and Body Composition Measurements

Metabolic rates were measured by indirect calorimetry in open-circuit Oxymax chambers in the Comprehensive Lab Animal Monitoring System (CLAMS) (Columbus Instruments). Mice were housed individually in the chamber, and O_2 gas was calibrated before monitoring. The chamber was maintained at 23°C with 12-hour light/12-hour dark cycles, and food and water were available ad libitum. O_2 consumption and CO_2 production were measured directly as continuously accumulated data. Energy expenditure (EE) was calculated as $(3.815+1.232*RER)*VO_2$ and linear regression analysis of covariance (ANCOVA) was used to determine mass-independent effect between F/F and LKO mice as reported before[278,279]. Estimated EE was calculated by univariate generalized linear model (GLM) with body mass set to the average of both control and LKO mice. Body composition (whole-body fat and lean mass) was determined using Echo MRI Body Composition Analyzer.

2.2.4 Phospholipid analyses

Mouse livers were snap-frozen in liquid nitrogen. Livers were homogenized on ice in phosphate buffered saline. Homogenates were subsequently subjected to a modified Bligh-Dyer lipid extraction[280] in the presence of lipid class internal standards, including 1-0-heptadecanoyl-sn-glycero-3-phosphocholine, 1,2-dieicosanoyl-sn-glycero-3-phosphocholine[281]. Lipid extracts were diluted in methanol/chloroform (4/1, vol/vol), and molecular species were quantified using electrospray ionization mass spectrometry on a triple quadrupole instrument (Themo Fisher Quantum Ultra) employing shotgun lipidomic methodologies[282]. PC molecular species were quantified as chlorinated adducts in the negative ion mode using neutral loss scanning for 50 amu (collision energy = 24 eV). Individual molecular species were quantified by comparing the ion intensities of the individual molecular species to that of the lipid class internal standard with additional corrections for type I and type II 13C isotope effects[282]. Each molecular species indicated in Figure 1C was verified by concomitant analyses of samples using product ion scanning for individual fatty acid constituents, including palmitoleic, palmitate, linoleate, oleate, stearate, arachidonate and docosohexadecanoate (product ion scans in m/z of 253.2, 255.2, 279.3, 281.3, 283.3, 303.4 and 327.4, respectively, at a collision energy + 35 eV).

2.2.5 Endosome isolation

Liver endosomes were isolated as described[283]. Briefly, liver tissues were homogenized in homogenization buffer (HB) (250 mM sucrose, 3 mM imidazole pH = 7.4, 1 mM EDTA, supplemented with protease and phosphatase inhibitors) using Dounce tissue grinder. The homogenate was centrifuged at 1600 g for 10 min at 4°C to remove cell debris. Then, the supernatant was mixed thoroughly with 62% sucrose at a ratio of 1:1.36 (Homogenate:sucrose, v/v), overlaid with 1.5 volumes of 35% sucrose, 1 volume of 25% sucrose and finally the tube was filled up with HB. The samples were then centrifuged at 21,000 g for 3 h at 4°C. Six fractions were collected from the top for western blot analysis.

2.2.6 INSR compartmentation assay

Membrane and cytosol fractionation was performed as previously described[284]. Briefly, tissue samples were homogenized in ice-cold buffer A (20 mM Tris-HCl, pH 7.4, 1 mM EDTA, 0.25 mM EGTA, 250 mM sucrose, and freshly added protease and phosphatase inhibitors, Roche Diagnostics). Debris was removed by centrifugation (5 min, 280 g, 4°C). The lysate was centrifuged (100,000 g, 60 min at 4°C), and an aliquot of the supernatant was saved as the cytosolic fraction. The pellet was washed once in ice-cold buffer B (250 mM Tris-HCl, pH 7.4, 1 mM

EDTA, 0.25 mM EGTA, 2% Triton X-100, and freshly added protease and phosphatase inhibitors). The pellet was resuspended in buffer B by sonication, incubated at 4°C for 45 minutes to solubilize membrane proteins and centrifuged at 100,000 g for 60 min at 4°C. An aliquot of the supernatant was saved as the membrane fraction.

2.2.7 Total internal reflection (TIRF) microscopy imaging

Primary hepatocytes isolated from chow diet-fed control and LKO mice were seeded on collagen coated coverslips (Neuvitro GG181.5COLLAGEN), followed by treatment with Cy3 labeled insulin (5 nM) or Alexa 568-Transferrin (10 µg/ml). Single Molecule tracking was performed immediately after treatments in a custom-built TIRF microscope (IX73, Olympus) equipped with a 100× oil immersion objective (PlanApo, 100×, N.A. 1.49). A 488 nm (for Cy3-insulin) or a 561 nm (for Alexa568-Transferrin) wavelength laser was used as the light source. Power of the laser was controlled using neutral density filters. Individual labelled molecules were seen as diffraction-limited spots on the cell surface in immediate contact with the coverslip on the glass bottom dish. The fluorescence from the single spots was collected by the same objective, passing an emitter and captured by an Electron Multiplying Charge Coupled Device (EMCCD) camera (iXon U797, Andor Technology). A total of 2000 frames/trajectory was acquired for each field of view with an integration time of 50 ms. Particles in time-stamped images were analyzed by FIJI.

2.2.8 Liposome treatment

All the phospholipids used in the study were purchased from Avanti Polar Lipids. Liposomes were generated as described[285] and were composed of DPPC(16:0/16:0)/PAPC(16:0/20:4), DSPE-PEG, and DOTAP at the molar ratio of 76.2:3.8:20. The amount of phospholipid is determined such that the final liposome concentration is 1mM in PBS whose volume is enough to treat cells. Phospholipids dissolved in chloroform were evaporated under a stream of nitrogen gas and thoroughly dried by rotary vacuum dryer. Dry phospholipids were then hydrated in PBS at a temperature above its transition temperature and vortexed vigorously. The phospholipid solution was passed through 50–80 nm PCTE membrane filters (Sterlitech) 10 times to make small unilaminar liposomes. Liposomes with different phospholipid composition were treated to primary hepatocytes at final concentration of 100 μM for 15 min before insulin treatment and TIRF imaging.

2.2.9 Hyperinsulinemic-euglycemic clamp to assess insulin sensitivity in awake mice

Hyperinsulinemic–euglycemic clamp experiments were conducted at the National MMPC at UMass Medical School as previously described[286]. In brief, survival surgery was performed 5–6 days before the clamp experiments to establish an indwelling catheter in the jugular vein. On the day of the clamp experiments, mice were fasted overnight (about 17 h), and a 2 h hyperinsulinemic–euglycemic clamp was conducted in awake mice with a primed and continuous infusion of human insulin (150 mU/kg body weight priming followed by 2.5 mU/kg/min; Humulin, Eli Lilly). To maintain euglycemia, 20% glucose was infused at variable rates during clamps. Whole-body glucose turnover and hepatic glucose production were assessed with a continuous infusion of [3-^{3}H] glucose (PerkinElmer) before and during the clamp, and 2-deoxy-D-[1-^{14}C] glucose (2-[^{14}C] DG) (PerkinElmer) was administered as a bolus (10 μCi) at 75 min after the start of clamps to measure insulin-stimulated glucose uptake in individual organs. At the end of the clamps, mice were anesthetized, and tissues were taken for biochemical analysis.

Glucose concentrations were analyzed using 5–10 μL plasma and Analox GM9 Analyzer (Analox Instruments). Plasma concentrations of [3-^{3}H] glucose, 2-[^{14}C] DG and ^3H_2O were determined following deproteinization of plasma samples as previously described[286]. For the determination of

2-[^{14}C] DG-6-phosphate content in tissues, tissue samples were homogenized, and the supernatants were subjected to an ion-exchange column to separate 2-[^{14}C] DG-6-phosphate from 2-[^{14}C] DG. Rates of HGP and whole-body glucose turnover were determined as previously described[286]. The insulin-stimulated rate of HGP was determined by subtracting the glucose infusion rate from the whole-body glucose turnover. Insulin-stimulated glucose uptake in individual tissues, skeletal muscle, WAT and BAT, was assessed by determining the content of 2-[^{14}C] DG-6-phosphate in each tissue as well as the 2-[^{14}C] DG profile in plasma.

2.2.10 Cell culture

Hepa 1-6 cell line was maintained in Dulbecco's modified Eagle's medium (DMEM) supplemented with 10% fetal bovine serum (FBS), 4.5 g/L glucose, 1 mM sodium pyruvate and 5mM L-glutamine at 37°C with 5% CO_2. Hepa 1-6 cells were treated with insulin (5 nM) for 0, 1, 4 and 12 h, and cells were harvested for gene expression analysis. Primary hepatocytes were isolated as previously described[276]. Briefly, we cannulated the inferior *vena cava* of anesthetized mice and perfused the liver with 37°C liver perfusion medium (0.5 mM EGTA and 10 mM HEPES in Hanks solution) for 5 min, then with 40 µg/mL 37°C Liberase TM in 10 mM HEPES-buffered William's medium E for another 10 min. Perfused and digested liver was removed and placed in William's medium E, and cells were dispersed. We filtered the resulting cell suspension through a 100-µm cell strainer and washed 3 times with William's medium E. Live cells were counted using trypan blue staining. Primary hepatocytes were used only when the viability was above 85%. 1×10^6 live cells were seeded per well of 6-well collagen I–coated plates in William E medium supplemented with 2 mM glutamine, 10 mM HEPES, 1% penicillin and streptomycin (P/S) and 5% FBS. After 3 to 4 hours, cells were washed twice with 2 mL PBS and cultured in maintenance medium (William E medium supplemented with 2mM glutamine, 10 mM HEPES, 1% P/S and 0.2% fatty acid-free BSA).

2.2.11 Histology

Tissues were collected, fixed in 10% buffered formalin, embedded in paraffin, sectioned at 4-10 µm and stained with hematoxylin and eosin at the University of Illinois Histology Lab.

2.2.12 Gene expression analysis

Total RNA was isolated from tissues with Trizol (Invitrogen), cDNA was synthesized, and gene expression was quantified by BioRad CFX384 Touch Real-Time PCR Detection System with SYBR Green (BioRad). For ASO injected mice, total RNA was isolated with Direct-zol RNA Kits (Zymo Research), and cDNA was synthesized using iScript™ cDNA Synthesis Kit (BioRad). The sequences of primers used in this study were listed in supplemental table.

2.2.13 Western-Blotting

Whole cell and liver tissue were homogenized and sonicated in RIPA buffer (50 mM Tris–HCl, pH 7.4, 150 mM NaCl, 0.1% Triton X-100, 0.5% sodium deoxycholate, 0.1% SDS) supplemented with protease inhibitors (Roche Molecular Biochemicals) and phosphatase inhibitors (Thermo Fisher Scientific). Adipose tissue protein extraction was conducted as described previously[287]. The homogenate was then cleared by centrifugation. After determining protein concentrations using BCA kits (Thermo Fisher Scientific), 45 µg of proteins were mixed with sample buffer (BioRad), loaded to 4-15% precast gel (BioRad) for electrophoresis and transferred to PVDF membranes (Amersham International, GE Healthcare). Membranes were then blocked with blocking buffer (5% milk or BSA in 0.1% TBST) for 1 h at room temperature and then incubated with primary antibodies (Table 2.1) diluted in blocking buffer at 4°C overnight. After washing with 0.1% TBST 4 times, membranes were incubated with secondary antibodies diluted in blocking buffer for 1 h at room temperature. Membranes were developed using ECL western blotting substrate (Thermo Scientific) and were exposed to X-ray film (FUJI) in a dark room. Antibodies used in this study were listed in the supplemental table.

2.2.14 Detergent resistant membrane (DRM) isolation

Mouse liver DRM was isolated as previously described[288], with modifications. Briefly, 50-100 mg fresh livers were collected and homogenized on ice with Dounce tissue grinder in TNE buffer (150 mM NaCl, 2 mM EDTA, 50 mM Tris–HCl, pH 7.4) supplemented with protease and phosphatase inhibitors. The homogenate was centrifuged at 380 g for 5 min at 4°C to get rid of tissue debris and intact cells. The supernatant was mixed with 2X volume of OptiPrep (60% iodixanol), overlaid with 30% iodixanol, then with TNE in a TLS55 centrifuge tube and centrifuged at 55,000 r.p.m. for 2 h. The fraction in the upper interface was collected as the DRM sample.

2.2.15 Lipid extraction and measurement

Liver tissues were snap-frozen in liquid nitrogen at the time of harvest. To extract lipids, liver tissues were cut, weighed and homogenized in water. After transferring the homogenate into glass tubes, lipids were extracted by adding 2 mL chloroform/methanol (2:1 v/v), mixed thoroughly by vortexing and centrifuged at 3,000 r.p.m. for 5 min at 4°C. Lipids in the lower layer were then carefully collected and air-dried overnight. The lipids were dissolved in ethanol and diluted in PBS for lipid measurements. Serum was directly used for lipid measurements. Serum and hepatic lipids were measured with the Wako L-Type TG M kit and the Wako HR series NEFA- HR(2) kit.

2.2.16 Liver DAG measurement

Around 10 mg liver samples were homogenized in PBS. Lipid was then extracted and DAG concentration was measured following manufacturer's instructions. The final DAG concentration was normalized to sample wet weight.

2.2.17 Hepatic glucose production

Primary hepatocytes were isolated and cultured overnight in collagen-coated 12-well plates. Then, change culture media to fasting media (DMEM without glucose, glutamine and phenol red) to fast cells for 6 hours. The glucose production was stimulated by adding 20mM lactate and 2mM pyruvate into the media with or without 10 nM insulin. The media was then collected 3 hours after treatment and the glucose concentration was measured using a highly sensitive glucose kit. The hepatic glucose production rate was normalized to protein quantity of each well.

2.2.18 Lipidomic assay

Lipidomic analyses were carried out at the University of California, Los Angeles (UCLA) lipidomics core. The UCLA lipidomics core protocol has been previously described[289]. In brief, for tissue, 50-100 mg of frozen liver were placed in a 2 mL homogenizer tube pre-loaded with 2.8 mm ceramic beads (Omni #19-628). PBS was added to the tube, and the sample was homogenized in the Omni Bead Ruptor Elite (3 cycles of 10 seconds at 5 m/s with a 10 second dwell time). For lipid extraction, 3-6 mg of tissue homogenate were transferred to a glass tube for lipid extraction using a modified Bligh and Dyer extraction[280]. Prior to biphasic extraction, a 13-lipid class Lipidyzer Internal Standard Mix was added to each sample (AB Sciex, 5040156). Following two successive extractions, pooled organic layers were dried down using a Genevac EZ-2 Elite. Lipid samples were resuspended in 1:1 methanol/dichloromethane with 10 mM Ammonium Acetate and transferred to robovials (Thermo 10800107) for analysis. Samples were analyzed on the Sciex Lipidyzer Platform for targeted quantitative measurement of 1100 lipid species across 13 classes. Differential Mobility Device on Lipidyzer was tuned with SelexION tuning kit (Sciex 5040141). Instrument settings, tuning settings and the MRM list available upon request. Data analysis was performed on the Lipidyzer software. Quantitative values were normalized to mg of liver.

2.2.19 Prostaglandin E2 (PGE2) measurement

Mouse livers were harvested and snap-frozen in liquid nitrogen. Frozen samples were homogenized in 500 µL of cold PBS containing indomethacin (10 mg/mL) using a tissue homogenizer. The suspension was sonicated, followed by centrifugation for 10 minutes at 12,000 r.p.m. PGE2 levels in the supernatant were measured using a PGE2 ELISA Kit (Thermo Fisher Scientific).

2.2.20 Statistical analysis

For all studies, results from quantitative experiments were expressed as means ± SEM. GraphPad Prism 9.0 (San Diego, CA) was used for all statistical analyses. Where appropriate, significance was calculated by Student's t test, one- or two-way ANOVA with Tukey's or Sidak's multiple comparison test.

2.3 RESULTS

2.3.1 Lpcat3 expression is induced by insulin signaling

Our previous observation that *Lpcat3* expression is increased in *ob/ob* mouse liver promoted us to hypothesize that LPCAT3 and PL remodeling may be involved in the pathogenesis of insulin resistance[276]. In support of this hypothesis, insulin treatment indeed significantly increased mRNA levels of *Lpcat3* in Hepa 1-6 cells (Figure 2.1A), which was comparable to the induction of known downstream genes of insulin, *Srebf-1c* and *Fasn*. Furthermore, *Lpcat3* expression was increased by two-fold in the livers of HFD-fed C57BL/6 mice (Figure 2.1B). Mass spectrometry analysis revealed that polyunsaturated PCs, especially arachidonoyl-containing PCs, were dramatically elevated, while saturated and monosaturated PCs were decreased in HFD-fed livers (Figure 2.1C), suggesting that hyperinsulinemia in both genetic- and diet-induced mouse models enhances *Lpcat3* expression and membrane PL unsaturation in the liver.

2.3.2 Loss of Lpcat3 in the liver enhances insulin sensitivity

To determine if PL composition modulates insulin sensitivity, we characterized glucose metabolism in *Lpcat3* liver-specific knockout (LKO) mice, which exhibit opposite PL composition compared to obese and HFD-fed livers[17]. Although the floxed control and LKO mice had similar body weight on chow diet (Figure 2.2A), intraperitoneal glucose tolerance test (IPGTT) showed that LKO mice cleared glucose load more efficiently than control mice (Figure 2.2B). Control and LKO mice had comparable serum insulin levels upon glucose injection, suggesting that enhanced glucose clearance was not caused by increased insulin secretion (Figure 2.2C). Insulin tolerance test (ITT) further corroborated that LKO mice were more insulin sensitive compared to control mice (Figure 2.2D). Insulin signaling is dynamically regulated during fasting and refeeding. To determine if LPCAT3 modulates the activity of insulin signaling during this process, we fasted LKO and control mice overnight and refed them with HFD for 2 h. Blood glucose levels were significantly lower in LKO mice, albeit much lower serum insulin levels compared to control mice (Figure 2.2E and 2.2F). These data demonstrated that LPCAT3 and membrane PL composition modulate insulin sensitivity under physiological conditions.

2.3.3 Lpcat3 deficiency protects mice from HFD-induced obesity and insulin resistance

Next, we examined if LPCAT3 and PL remodeling play any roles in HFD-induced insulin resistance. Surprisingly, LKO mice gained significantly less body weight after 12-week HFD feeding compared to controls (Figure 2.3A). Magnetic Resonance Imaging (MRI) analysis of body composition showed that the difference in body weight was primarily due to lower whole body fat mass, particularly subcutaneous white adipose tissue (sWAT) in HFD-fed LKO mice (Figure 2.4A-2.4D). Further investigation suggested that this resistance to HFD-induced weight gain was not due to reduced food consumption or lipid absorption in LKO mice (Figure 2.4E-2.4G).

Similar to chow diet-fed mice, HFD-fed LKO mice were more glucose tolerant and insulin sensitive as demonstrated by GTT and ITT analyses (Figure 2.3B and 2.3C). Reduced fasting blood glucose, serum insulin levels and homeostatic model assessment of insulin resistance (HOMA-IR) further confirmed improved insulin sensitivity in LKO mice on HFD (Figure 2.3D-2.3F). Gene expression analysis showed that glucose-6-phosphotase (*G6pc*) was downregulated, while glycogen synthase 2 (*Gys2*) was upregulated in LKO livers. The expression of lipogenic genes was significantly suppressed in the absence of *Lpcat3* (Figure 2.3G). LKO mice exhibited lower serum triglyceride and non-esterified fatty acid (NEFA) levels accompanied by hepatic accumulation of triglyceride and NEFA upon HFD feeding (Figure 2.4H-2.4K), likely due to impaired VLDL secretion[17]. Histological analysis showed much less inflammation in WAT of LKO mice compared to control mice on HFD (Figure 2.3H), which was supported by a significant decrease in the expression of cytokine *Ccl3* and macrophage markers *F4/80* and *Cd68* (Figure 2.3I). Taken together, these data indicate that *Lpcat3* deficiency improves both hyperglycemia and hypertriglyceridemia in HFD-induced insulin resistance.

2.3.4 Loss of Lpcat3 improves insulin resistance in ob/ob mice

To further assess the involvement of LPCAT3 activity in the pathogenesis of insulin resistance, we crossed LKO mice with *ob/ob* mice to generate *ob/ob*, *Lpcat3*$^{\mathrm{fl/fl}}$, *Cre-* (OB) and *ob/ob*, *Lpcat3*$^{\mathrm{fl/fl}}$, *Cre+* (OLKO) mice. Unlike HFD-fed mice in C57BL/6 background, knockout of *Lpcat3* in the liver did not affect body weight gain in *ob/ob* mice (Figure 2.6A and 2.7A). There was a slight decrease in the weight of epididymal WAT (eWAT), but not sWAT in OLKO mice (Figure 2.7B and 2.7C). OLKO and OB mice had comparable daily food consumption (Figure 2.7D).

Despite no body weight differences, OLKO mice were more glucose tolerant and insulin sensitive compared to OB mice (Figure 2.6B and 2.6C). Consistently, OLKO mice showed lower fasting blood glucose, serum insulin levels and HOMA-IR (Figure 2.6D-2.6F). The expression of *Srebp-1c* and lipogenic genes was reduced in OLKO livers compared to that in OB livers, while the expression of gluconeogenic genes was not altered (Figure 2.6G). Surprisingly, OLKO mice had increased serum triglyceride and NEFA levels, whereas hepatic triglyceride and NEFA levels were comparable (Figure 2.7E-2.7H). Similar to HFD-fed mice, the inflammatory cell infiltration as well as the expression of macrophage markers and cytokines in WAT were dampened in OLKO mice (Figure 2.6H and 2.6I). Notably, the expression of lipase genes, *Hsl* and *Atgl*, was significantly upregulated in eWAT but not in sWAT in OLKO mice (Figure 2.7I), which may be responsible for smaller eWAT but not sWAT in OLKO mice, and likely contributes to an increase in serum NEFA levels in OLKO mice.

2.3.5 Lpcat3 deficiency increases insulin sensitivity partially through facilitating insulin signal transduction in early endosomes

Several lipid classes, such as free fatty acids (FFAs), DAG, and ceramides, are known to mediate insulin resistance in the liver[290,291]. To determine if loss of *Lpcat3* affects the levels of these lipids, we performed a shotgun lipidomic analysis in both chow and HFD-fed mouse livers. In agreement with impaired VLDL secretion, a majority of lipid classes were increased in LKO livers compared to controls (Figure 2.5A and 2.5B), including ceramide, FFAs, DAG and TG (Figure 2.5C-2.5F). In agreement with the enzyme activity of LPCAT3 that prefers unsaturated FA as substrate, unsaturated FA, but not saturated FA, was increased in LKO livers (Figure 2.5G). Prostaglandin E2 (PGE2), a product of arachidonic acid metabolism, has been shown to contribute to insulin resistance[292]. The levels of PGE2 were comparable between control and LKO mice on chow or

HFD (Figure 2.5H), suggesting that PGE2 is unlikely to be involved in the regulation of insulin signaling in the absence of *Lpcat3*.

To explore the mechanisms by which PL composition modulates insulin sensitivity, we first determined if insulin signaling was altered in LKO livers. Western blot analysis showed that insulin-stimulated expression of phospho-AKT (p-AKT) levels were increased in chow diet-fed LKO mice (Figure 2.8A). Similarly, p-AKT levels were dramatically enhanced in OLKO livers (Figure 2.8B), suggesting that *Lpcat3* deficiency potentiates hepatic insulin signaling. To further test cell autonomous effects of LPCAT3 on insulin signaling and its kinetics, we treated primary hepatocytes with insulin for different time points and measured p-AKT levels. Similar to *in vivo* data, p-AKT levels were elevated in LKO hepatocytes and remained higher at 25 min post treatment, while p-AKT levels started to decrease in control hepatocytes at this time (Figure 2.8C). This indicates that *Lpcat3* deficiency not only increases the intensity but also extends the duration of insulin signaling. Consistent with enhanced insulin sensitivity, primary hepatocytes isolated from LKO mice showed dramatic reduction in glucose production compared to controls (Figure 2.8D). Thus, these data support a cell-autonomous mechanism involving alterations in PL composition.

Insulin signaling is regulated by the abundance and compartmentalization of insulin receptor (INSR) in the plasma membrane[56,293]. Western blot analysis showed no difference in INSR protein levels between control and LKO livers (Figure 2.9A). It has been shown that increasing membrane saturation facilitates the compartmentalization and activity of membrane-bound proteins by recruiting them to microdomains[294]. Our data showed that INSR was primarily localized in CD71 enriched non-raft domains (fraction #3 and #4) in plasma membrane (Figure 2.9B). Furthermore, insulin treatment did not drastically alter INSR localization. These data indicate that increased insulin sensitivity in LKO mice is unlikely caused by changes in INSR expression or its distribution/recruitment to different compartments in plasma membrane.

Upon insulin binding, INSR internalizes into early endosomes, which become signaling endosomes and comprise an important compartment in insulin signal transduction[295]. Given that membrane curvature, largely determined by membrane PL composition, regulates endocytosis[296], we first examined the insulin signal intensity in different subcellular compartments. As shown in Figure 2.8E, p-AKT levels were higher in both plasma membrane and cytosol in LKO livers, further corroborating our observations in primary hepatocytes. Next, we purified endosomes from livers of control and LKO mice retro-orbitally injected with insulin for 5 min. We found that RAB5, a marker of early endosomes, was enriched in fractions #2 and #3 in LKO livers compared to control livers (Figure 2.8F), despite comparable RAB5 levels in whole tissue lysates from control and LKO livers (Figure 2.9C). Moreover, INSR and phosphorylated INSR levels were higher in early endosomes of LKO livers. Next, we directly visualized insulin-dependent INSR internalization using total internal reflection (TIRF) microscopy. We monitored the kinetics of insulin endocytosis in control and LKO primary hepatocytes treated with Cy3-insulin. We found that Cy3-insulin signals started to decrease within 50 seconds and disappeared ~100 seconds after treatment in LKO hepatocytes (Figure 2.8G and Video S1)[3]. In contrast, most of Cy3-insulin signals remained on plasma membrane during the course of recording of ~200 seconds in control hepatocytes (Figure 2.8G and Video S2). In comparison, transferrin endocytosis was not affected by *Lpcat3* deficiency (Figure 2.9C, Video S3 and S4). To determine if altered endocytosis is caused by changes in membrane PL composition, we treated primary hepatocytes with liposomes containing 16:0/16:0 PC (DPPC) or 16:0/20:4 PC (PAPC) and monitored Cy3-insulin

---

[3] Videos in this Chapter are available online: https://onlinelibrary.wiley.com/doi/full/10.1002/advs.202300416 as supporting materials.

internalization. Indeed, DPPC treatment promoted Cy3-insulin internalization (Figure 2.8G and Video S5), whereas PAPC had little effect in control hepatocytes (Figure 2.8G and Video S6). In contrast, the impact of liposomes on LKO hepatocytes was not as pronounced as in control hepatocytes (Figure 2.8G, Video S7 and S8). Mass spectrometry analysis showed that DPPC levels were increased by more than 10-fold after liposome treatment, while PAPC levels were only slightly increased in control hepatocyte and failed to rise in LKO hepatocytes (Figure 2.9E), indicating that PLs in liposomes undergo active remodeling process and PAPC cannot be incorporated into membrane in the absence of LPCAT3. Nevertheless, these data suggest that loss of *Lpcat3* likely enhances insulin sensitivity through facilitating INSR internalization and insulin signal transduction in early endosomes.

2.3.6 Loss of Lpcat3 increases systemic insulin sensitivity by enhancing glucose uptake in brown fat

Our observations that LKO mice were less obese on HFD and were protected from adipose tissue inflammation led us to speculate that peripheral insulin sensitivity might be altered in these mice. To examine this further, we performed hyperinsulinemic-euglycemic clamp experiments in awake HFD-fed control and LKO mice. The clamp data indicate that LKO mice are more insulin sensitive than control mice, as demonstrated by a marked decrease in basal glucose levels, and more than 2-3-fold increases in glucose infusion rate (GIR) and whole-body glucose turnover (Rd) in LKO mice during the clamps (Figure 2.10A-2.10C). While basal hepatic glucose production (HGP) rates were similar, the HGP during clamps was decreased by ~20% in LKO livers compared to controls (Figure 2.10D). As a result, LKO mice exhibited a higher insulin-mediated suppression of HGP (Figure 2.10E). Insulin-stimulated glucose uptake in BAT was increased by ~30%, whereas glucose uptake was not altered in muscle but reduced in eWAT in LKO mice (Figure 2.10F-

2.10H). However, compared to BAT and muscle, the contribution of WAT in glucose disposal was negligible. Taken together, these data suggest that both suppressed glucose production in the liver and increased glucose uptake in the BAT contribute to the improved insulin sensitivity in HFD-fed LKO mice.

2.3.7 Lpcat3 deficiency induces FGF21 secretion and enhances energy expenditure

Next, we explored the mechanisms by which changes in hepatic PL composition affect body weight gain and glucose uptake in BAT. Our previous published transcriptional profiling in chow diet-fed mice showed that despite marked changes in membrane composition in LKO livers, the effect on gene expression was limited on chow diet[17]. Only 17 genes were altered by more than 2-fold in LKO livers, including one of the top upregulated genes, fibroblast growth factor 21 (*Fgf21*) (Figure 2.11A). The upregulation of *Fgf21* was further confirmed by qPCR (Figure 2.11B). *Fgf21* encodes a hormone that plays a key role in regulating energy homeostasis[265,297]. Moreover, FGF21 has been shown to enhance insulin sensitivity by increasing glucose uptake in BAT and WAT[298-300]. Therefore, loss of *Lpcat3* in the liver likely improves systemic insulin sensitivity and metabolism via the effects of circulating FGF21, namely, enhanced energy expenditure and glucose uptake in adipose tissues. Consistent with increased *Fgf21* expression in the liver, serum FGF21 levels trended towards an increase in chow diet-fed LKO mice (Figure 2.11C). Similarly, hepatic *Fgf21* mRNA and serum FGF21 levels were increased by ~3-fold and more than 6-fold in HFD-fed LKO mice compared to control mice, respectively (Figure 2.11D and 2.11E). The activation of FGF21 signaling was supported by the phosphorylation of its downstream ERK in WAT of LKO mice (Figure 2.11F). Next, we measured energy metabolism in HFD-fed mice by indirect calorimetry using the Comprehensive Lab Animal Monitoring System (CLAMS). LKO mice showed a dramatic increase in energy expenditure (Figure 2.11G and 2.11H), while physical activity and respiratory exchange ratio (RER) were not affected (Figure 2.11I and 2.11J). Taken together, these results demonstrate that loss of *Lpcat3* protects mice from diet-induced obesity likely through increased energy expenditure.

Similarly, *Fgf21* expression was upregulated in the livers of OLKO mice (Figure 2.13A). Serum FGF21 levels were increased by ~1.6-fold in OLKO mice compared to OB mice (Figure 2.13B). However, we did not observe any difference between OB and OLKO mice in energy expenditure, physical activity and RER in CLAMS analysis (Figure 2.13C-2.13F), likely because *ob/ob* mice have much higher basal FGF21 levels and are FGF21 resistant[301].

2.3.8 FGF21 mediates the effects of Lpcat3 deficiency on energy expenditure, but not insulin sensitivity

To determine if loss of *Lpcat3* increases energy expenditure and systemic insulin sensitivity through FGF21, we crossed *Fgf21*-/- mice with LKO mice to generate *Lpcat3*$^{fl/fl}$, *Cre-*, *Fgf21-/-* (F/F, *Fgf21*-/-) and *Lpcat3*$^{fl/fl}$, *Cre+*, *Fgf21-/-* (LKO, *Fgf21-/-*) mice. *Fgf21* deletion blunted the protection of LKO mice from HFD-induced obesity (Figure 2.12A). Consistently, CLAMS analysis showed that enhanced energy expenditure in HFD-fed LKO mice were abolished by *Fgf21* depletion (Figure 2.12B and 2.12C), whereas physical activity and RER remained unaltered (Figure 2.12D and 2.12E). Interestingly, GTT and ITT analyses demonstrated that loss of *Fgf21* had little impact on the improved insulin sensitivity in HFD-fed LKO mice. In fact, compared to the controls, LKO, *Fgf21-/-* mice remained insulin sensitive (Figure 2.12F and 2.12G). Western blot analysis revealed that p-AKT levels were significantly higher in the livers and WAT of LKO, *Fgf21-/-* mice compared to those in F/F, *Fgf21*-/- mice (Figure 2.14). Histology analysis revealed that LKO, *Fgf21-/-* mice had less infiltration of inflammatory cells in WAT compared to F/F, *Fgf21*-/- mice (Figure 2.12H), which may contribute to the enhanced insulin sensitivity in LKO independent of FGF21. These data indicate that FGF21 mediates the effect of *Lpcat3* deficiency on energy homeostasis, but not the enhanced insulin sensitivity in LKO mice.

2.4 DISCUSSION

A central paradox of type 2 diabetes is selective insulin resistance, in which insulin fails to suppress hepatic glucose production but continues to stimulate lipogenesis, resulting in hyperglycemia and hypertriglyceridemia[61]. However, the underlying mechanisms are unclear. Here we showed that membrane PL composition, controlled by LPCAT3, modulates insulin action on both glucose and lipid metabolism in the liver, and that upregulation of *Lpcat3* expression by hyperinsulinemia and the increase in PL unsaturation are involved in the pathogenesis of insulin resistance, especially hepatic selective insulin resistance. Deletion of *Lpcat3* ameliorates insulin resistance and blunts lipogenesis in both diet- and obesity-induced models, thus alleviating the deleterious effects of insulin resistance on both glucose and lipid metabolism. We further showed that membrane PLs regulate insulin signaling by directly affecting INSR trafficking, and indirectly modulating systemic insulin sensitivity through the action of FGF21 on peripheral tissues. These findings highlight a novel regulatory mechanism of insulin sensitivity by membrane PL composition at both cellular and systemic levels.

Obesity and nonalcoholic fatty liver disease (NAFLD) are major risk factors for insulin resistance and T2D. Hepatic lipid accumulation is crucial for the development of hepatic insulin resistance[290,291]. The levels of several lipids, including FFAs, DAG, ceramides and triglycerides, inversely correlate with insulin sensitivity. Studies have demonstrated that saturated, but not unsaturated, FAs induce insulin resistance likely through stimulating inflammation and increasing ceramide biosynthesis in muscle and adipose tissue[302]. Unlike FFAs, whose saturation impairs insulin sensitivity, our data suggest that increasing membrane PL saturation improves insulin sensitivity and protects mice from diet induced obesity, challenging the conventional notion that saturated fat is always harmful for the body. Furthermore, although LKO mice had higher ceramide, DAG and triglyceride accumulation in liver, they exhibited reduced HGP during insulin infusion and were more insulin sensitive. These data strongly suggest that loss of *Lpcat3* in the liver is sufficient to overcome the detrimental effect of lipid accumulation on insulin signaling, and that hepatic membrane PL composition could be a more prominent determinant of insulin sensitivity. It has been recognized that some patients with NAFLD do not develop obesity and insulin resistance, even though they have higher lipid content in the liver[303]. Notably, several recent studies have shown that some of these patients have reduced polyunsaturated PLs in the liver, similar to the lipid profile of LKO livers[2,152]. Thus, our study shed light on the underlying mechanisms of how these patients maintain insulin sensitivity despite massive lipid accumulation. Our observation that insulin stimulates *Lpcat3* expression and membrane PL composition modulates insulin sensitivity suggests a reciprocal regulation between insulin and membrane PL remodeling that may have physiological and pathological functions. Under physiological conditions, such as fasting/refeeding, insulin increases *Lpcat3* expression and membrane polyunsaturated PLs, which promote lipogenesis and the conversion of carbohydrates into fatty acids. Under insulin resistance, hyperinsulinemia leads to an excessive increase in *Lpcat3* expression and membrane unsaturation, which enhances lipogenesis and VLDL secretion, resulting in hypertriglyceridemia. On the other hand, increased membrane unsaturation, in turn, blunts insulin signal transduction, thus providing negative feedback to attenuate insulin signaling. The aberrant negative feedback likely leads to insufficient suppression of HGP and hyperglycemia. Signal transduction has been shown to be influenced by lipid organization of subdomains surrounding receptors[304]. There are contradictory reports regarding the localization of INSR in plasma membrane. Some studies claim that INSR is localized in more saturated, detergent resistant raft domains[305], while others show that it is primarily in more fluid, non-raft regions and will translocate to raft domains upon insulin binding[67]. Our data showed that INSR is mainly present in the non-raft fraction. We did not observe noticeable translocation of INSR after insulin stimulation. Therefore, the organization of lipid raft in plasma membrane is unlikely to be involved in the activation of INSR in LKO livers. It is well documented that early endosomes are essential sites of signal transduction for receptor kinase mediated signaling pathways, including INSR[295,306,307]. Our data support the notion that changes in biophysical properties influence the endocytosis of INSR, thereby facilitating signal transduction. However, detailing these biophysical changes and elucidating how they influence INSR movement will require further study with specialized tools and systems. Nevertheless, our data suggests that membrane dynamics may play an important role in insulin signaling *in vivo*.

Another interesting finding of this study was the profound induction of FGF21 in LKO mice, which is a critical mediator of the systemic effects of hepatic *Lpcat3* deficiency. FGF21 is a hormone with pivotal functions in the regulation of energy homeostasis and metabolism[265,297]. Chronic FGF21 treatment in diet-induced obese mice promotes thermogenesis and energy expenditure, resulting in weight loss [308-310]. Our data demonstrated that the reduced obesity in LKO mice could be attributed to increased energy expenditure. It has been demonstrated that FGF21 improves insulin sensitivity by increasing glucose uptake in BAT and WAT[298-300]. Surprisingly, LKO mice remain insulin sensitive in the absence of FGF21, indicating that *Lpcat3* deficiency enhances insulin signaling in the liver and adipose tissue independent of FGF21.

In conclusion, our study unveils LPCAT3 as a novel mediator of reciprocal regulation between phospholipid remodeling and insulin signaling that contributes to the pathogenesis of insulin resistance. These findings support an emerging view of dynamic manipulation of membrane biophysical properties as a regulatory mechanism in the control of metabolism.

2.5 TABLE AND FIGURES

Table 2.1 Resource table

REAGENT or RESOURCE	SOURCE	Catalog #
Antibodies		
Rabbit monoclonal anti-phospho-AKT	Cell Signaling	4060S
Rabbit polyclonal anti-AKT	Cell Signaling	9272S
Rabbit monoclonal anti-INSR	Cell Signaling	3025T
Rabbit monoclonal anti- phosphor-INSR	Cell Signaling	3024T
Mouse monoclonal anti-GAPDH	Millipore	MAB374
Rabbit monoclonal anti-β-actin	Cell Signaling	4970S
Rabbit monoclonal anti-RAB5	Cell Signaling	3547T
Rabbit monoclonal anti-phospho-ERK	Cell Signaling	4370S
Rabbit monoclonal anti-ERK	Cell Signaling	4695
Rabbit monoclonal anti-FLOT1	Cell Signaling	18634S
Mouse monoclonal anti-CD71	Santa Cruz Biotechnology	sc-65882
IgG (H+L) Goat anti-Rabbit, HRP	Invitrogen	656120
Goat anti-Mouse IgG(H+L) Secondary Antibody, HRP	Invitrogen	31430
Chemicals, Peptides, and Recombinant Proteins		
Insulin, human recombinant, zinc solution (for cell treatments)	Thermo Fisher	12585014
Novolin® human insulin (for mouse experiments)	Novo Nordisk	0169-1833-11
Insulin (Human) - Cy3 Labeled	Phoenix Pharmaceuticals	FC3-035-06
Transferrin From Human Serum, Alexa Fluor™ 568 Conjugate	Invitrogen	T23365
Critical Commercial Assays		
Prostaglandin E2 Parameter Assay Kit	R&D Systems	KGE004B
Ultra Sensitive Mouse Insulin ELISA Kit	Crystal Chem	MSPP-90080
Fibroblast Growth Factor 21, FGF21, Mouse/Rat ELISA	BioVendor	102552-226
DAG assay kit	Cell Biolabs, Inc	MET-5028
Deposited Data		
Microarray data	Rong et al., 2015	GSE98516
Experimental Models: Organisms/Strains		
Mouse: Lpcat3 Floxed Alb-Cre mice	Rong et al., 2015	N/A
Mouse: C57BL/6J	The Jackson Laboratory	000664
Mouse: B6.Cg-Lep^{ob}/J	The Jackson Laboratory	000632
Mouse: B6.129Sv(Cg)-Fgf21tm1.1Djm/J	The Jackson Laboratory	033846

Oligonucleotides (qPCR primers)		
m36B4-F	AGATGCAGCAGATCCGCAT	
m36B4-R	GTTCTTGCCCATCAGCACC	
mLpcat3-F	GGCCTCTCAATTGCTTATTTCA	
mLpcat3-R	AGCACGACACATAGCAAGGA	
mFasn-F	ACCACCAGAGACCGTTATGC	
mFasn-R	CAGCAGAGTCTACAGCTACCT	
mFgf21-F	CACCCAGGATTTGAATGACC	
mFgf21-R	CTGGGGGTCTACCAAGCATA	
mElovl6-F	ACAATGGACCTGTCAGCAAA	
mElovl6-R	GTACCAGTGCAGGAAGATCAGT	
mTnfα-F	TGCCTATGTCTCAGCCTCTTC	
mTnfα-R	GAGGCCATTTGGGAACTTCT	
mPepck-F	CTGCATAACGGTCTGGACTTC	
mPepck-R	CAGCAACTGCCCGTACTCC	
mG6pc-F	CGACTCGCTATCTCCAAGTGA	
mG6pc-R	GTTGAACCAGTCTCCGACCA	
mGys2-F	CCAGCTTGACAAGTTCGACA	
mGys2-R	ATCAGGCTTCCTCTTCAGCA	
mCcl3-F	CAGGCATTCAGTTCCAGGTC	
mCCl3-R	TGCCCTTGCTGTTCTTCTCT	
mCd68-F	CTTCCCACAGGCAGCACAG	
mCd68-R	AATGATGAGAGGCAGCAAGAGG	
mF4/80-F	CTTTGGCTATGGGCTTCCAGTC	
mF4/80-R	GCAAGGAGGACAGAGTTTATCGTG	
mSrebf1c-F	GGAGCCATGGATTGCACATT	
mSrebf1c-R	GGCCCGGGAAGTCACTGT	
mScd1-F	CGAAGTCCACGCTCGATCTC	
mScd1-R	TGTGGGCCGGCATGAT	
mHsl-F	CCAGCCTGAGGGCTTACTG	
mHsl-R	CTCCATTGACTGTGACATCTCG	
mAtgl-F	GGATGGCGGCATTTCAGACA	
mAtgl-R	CAAAGGGTTGGGTTGGTTCAG	
mAcaca-F	GATGAACCATCTCCGTTGGC	
mAcaca-R	GACCCAATTATGAATCGGGAGTG	
Software and Algorithms		
GraphPad Prism	GraphPad Software	https://www.graphpad.com/scientificsoftware/prism/
R	R Core Team	https://www.r-project.org/
ImageJ	NIH	https://imagej.nih.gov/ij/

Table 2.1 (Cont.)

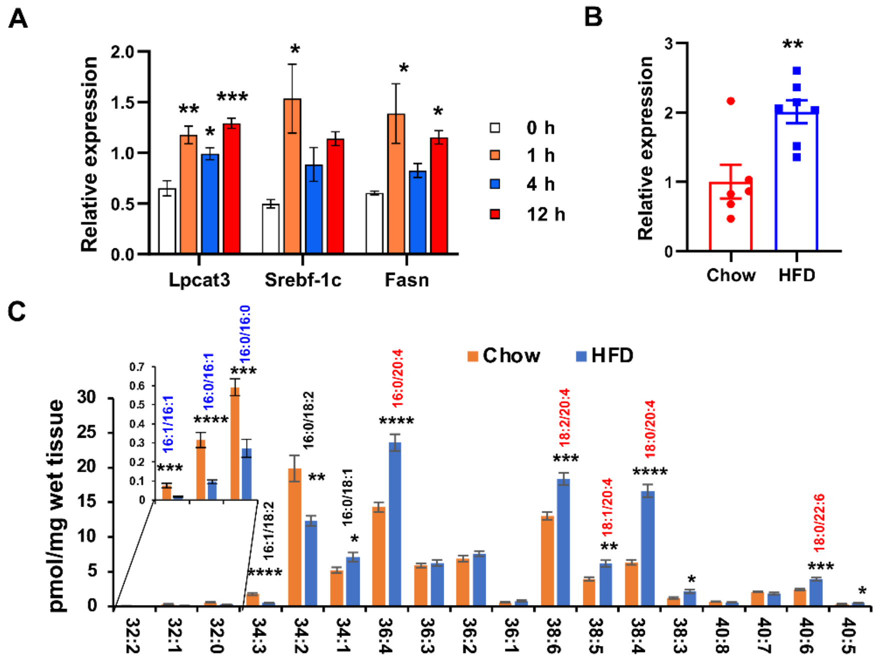

Figure 2.1 *Lpcat3* expression is regulated by insulin signaling.

(A) Expression of *Lpcat3* and insulin-responsive genes (*Srebf-1c* and *Fasn*) in Hepa 1-6 cells treated with insulin (5 nM) for different time points. (B) *Lpcat3* mRNA levels in livers of *C57BL/6* mice fed chow and HFD for 16 weeks. (C) Mass spectrometry analysis of phosphatidylcholine (PC) composition in livers of chow (n=6) and HFD-fed (n=8) *C57BL/6* mice for 16 weeks.

Data are presented as means ± SEM. Statistical analysis was performed with one-way ANOVA (A), Student's t test (B-C). *P < 0.05, **P < 0.01, ***P < 0.001, ****P < 0.0001.

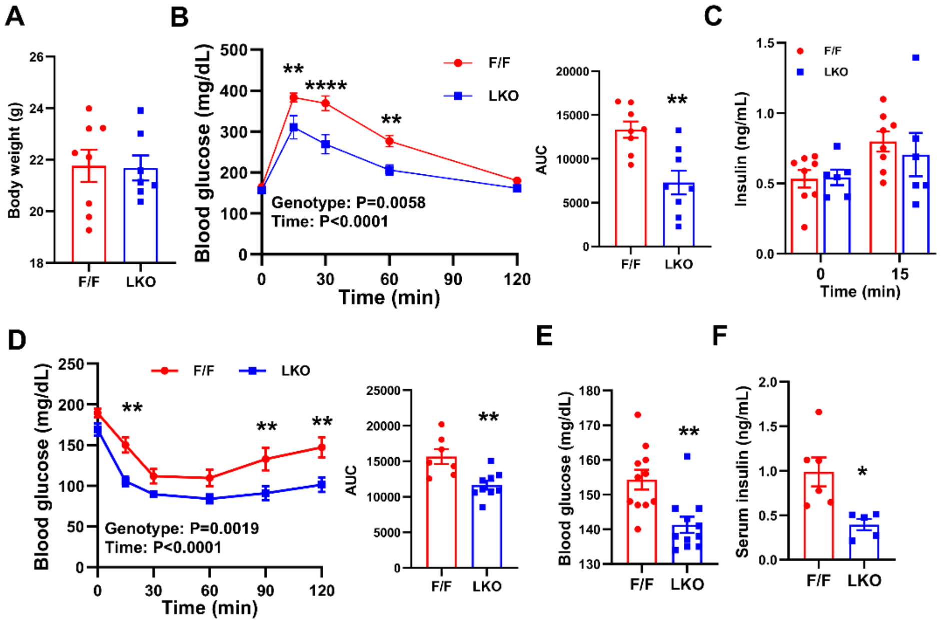

Figure 2.2 Loss of *Lpcat3* in liver enhances insulin sensitivity in chow diet-fed mice.

(A) Body weight of chow diet-fed *Lpcat3*$^{fl/fl}$ (F/F) and *Lpcat3*$^{fl/fl}$ *Albumin-Cre* (LKO) mice when Glucose tolerance test (GTT) and insulin tolerance test (ITT)were performed. (B) GTT in chow diet-fed control F/F and LKO mice. AUC: area under the curve. The P values of source of variation were provided. (C) Serum insulin levels during GTT analysis. (D) ITT in chow diet-fed control F/F and LKO mice. (E-F) Blood glucose (E) and serum insulin levels (F) in chow diet fed control F/F and LKO mice after fasting/refeeding. Mice were fasted overnight and refed with HFD for 2 h.

Data are presented as means ± SEM. Statistical analysis was performed with Student's t test (A, AUC in B and D, E-F), and two-way ANOVA (B-D). *P < 0.05, **P < 0.01, ****P < 0.0001.

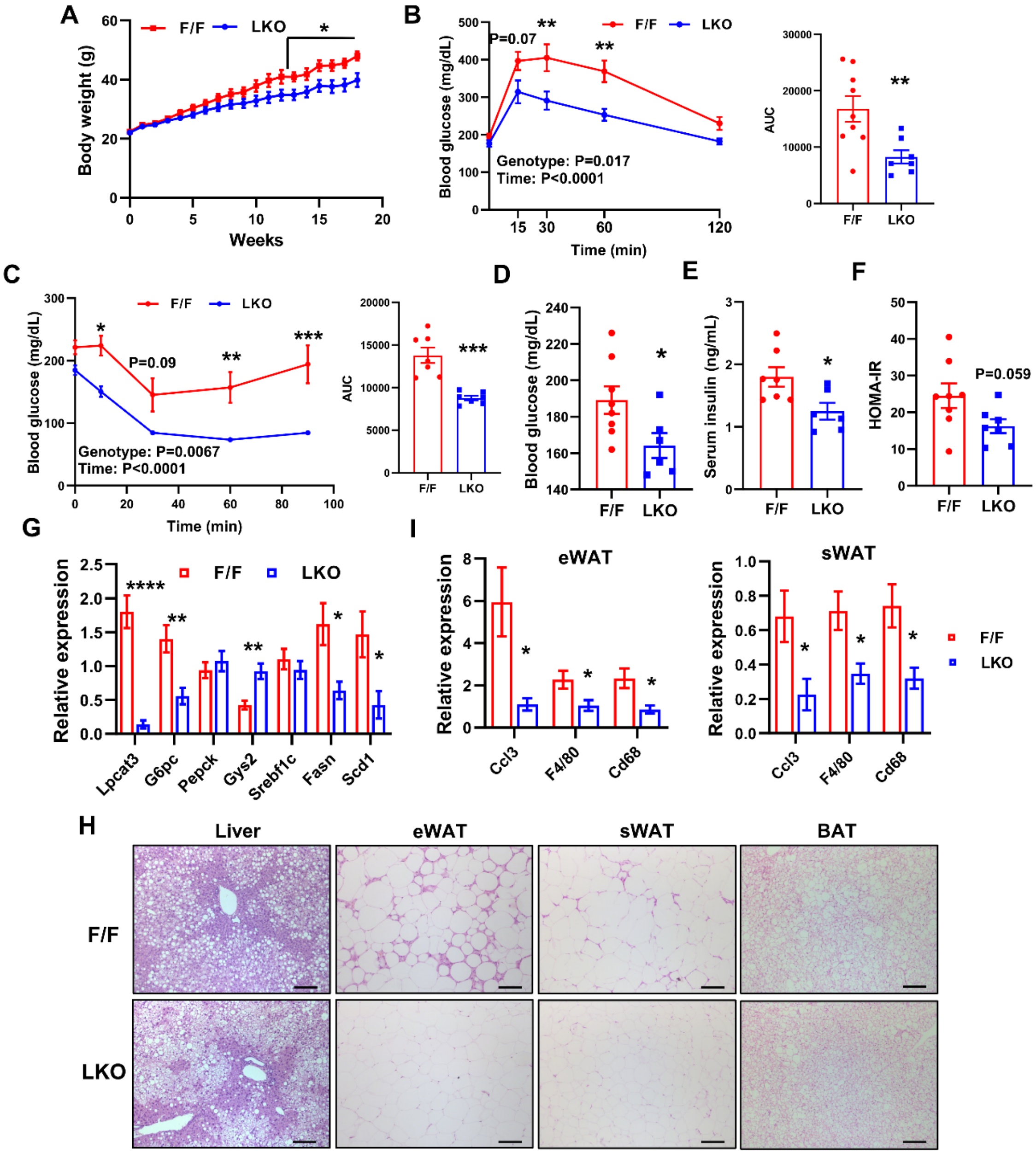

Figure 2.3. LKO mice are protected from HFD-induced obesity and insulin resistance.

(A) Growth curve of control F/F and LKO mice on HFD (n=7/group). (B-C) GTT (B) and ITT (C) in HFD-fed F/F and LKO mice. (D-F) Fasting blood glucose (D), serum insulin levels (E) and HOMA-IR (F) of HFD-fed F/F and LKO mice. (G) Expression of selected genes in livers of HFD-fed F/F and LKO mice (n=6-8/group). (H) Representative histology of liver, white adipose tissue (eWAT and sWAT), and brown adipose tissue (BAT) from HFD-fed F/F and LKO mice. Scale bar: 100 µm. (I) Expression of inflammation-related genes in eWAT and sWAT of HFD-fed F/F and LKO mice (n=7-9/group).

Data are presented as means ± SEM. Statistical analysis was performed with Student's t test (A, AUC in B-C, D-G, I), two-way ANOVA (B-C). *P < 0.05, **P < 0.01, ***P < 0.001, ****P < 0.0001.

(Figure 2.3 Cont.)

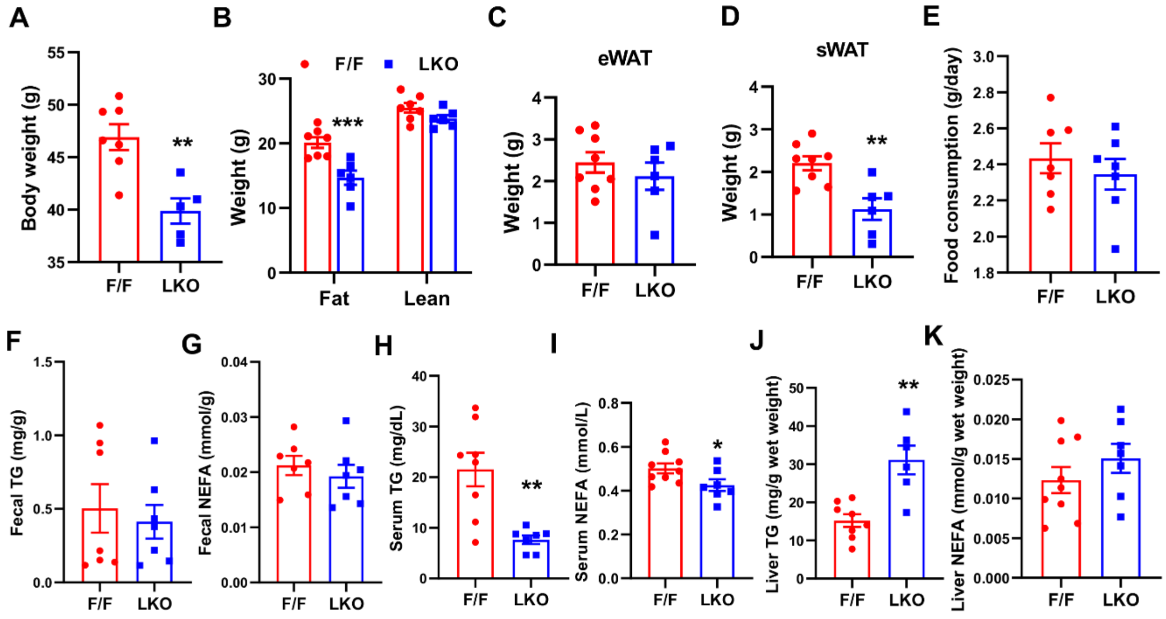

Figure 2.4. Hepatic *Lpcat3* deficiency improves HFD-induced insulin resistance.

(A) End point body weight of HFD-fed F/F and LKO mice. (B-D) Body composition analyzed by Echo-MRI (B) and tissue weight of eWAT (C) and sWAT (D) from HFD-fed F/F and LKO mice. (E) Daily food consumption of F/F and LKO mice on HFD. Data was presented as average of four days. (F-G) Fecal Triglyceride (F) and non-esterified fatty acid (G) levels of F/F and LKO mice on HFD. (H-K) Serum triglyceride (H) and non-esterified fatty acids (NEFA) (I) levels and liver triglyceride (J) and NEFA (K) levels of HFD-fed F/F and LKO mice.

Data are presented as means ± SEM. Statistical analysis was performed with Student's t test (A, C-K) and two-way ANOVA (B). $^{*}P < 0.05$, $^{**}P < 0.01$, $^{***}P < 0.001$.

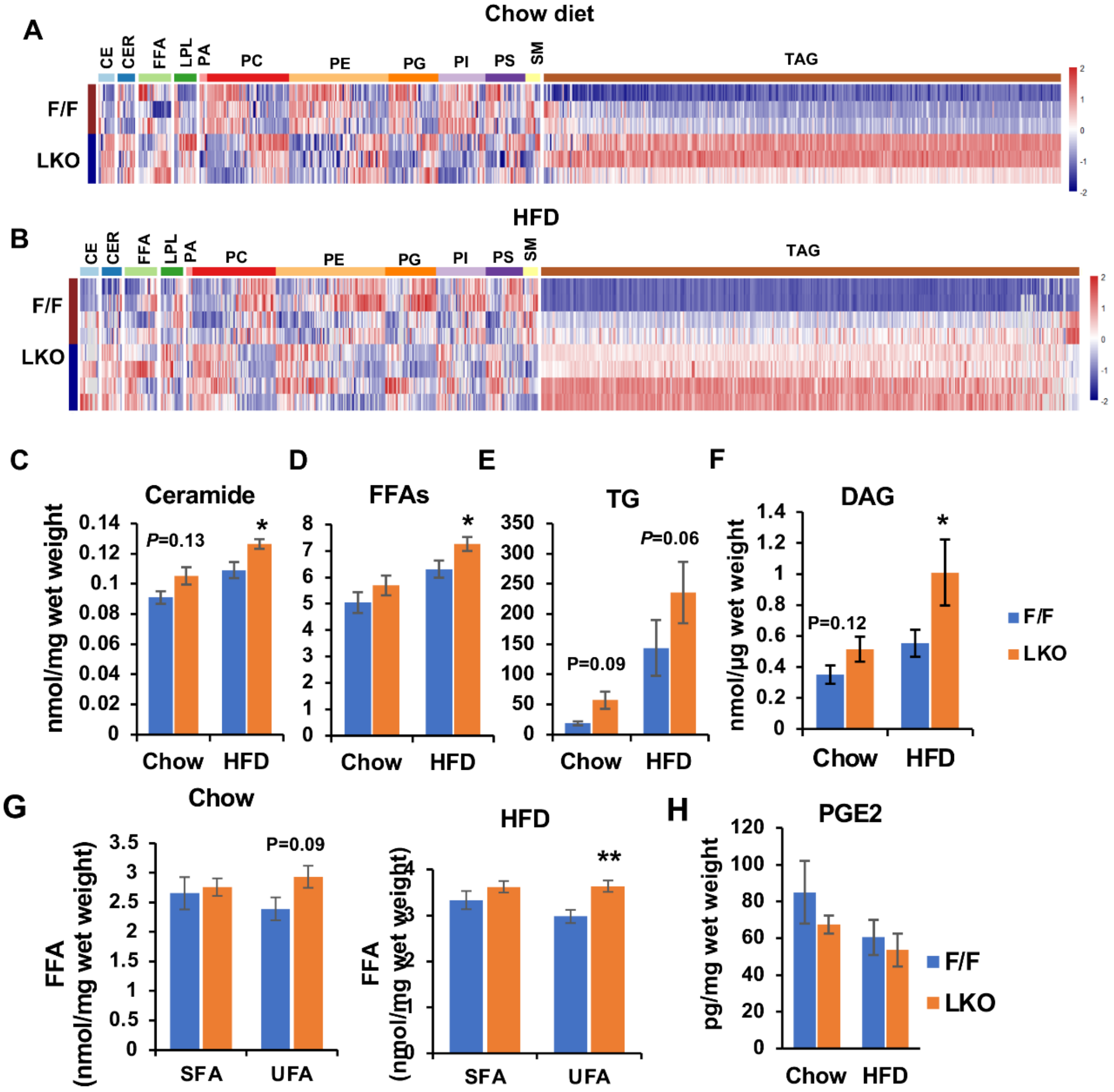

Figure 2.5. Shotgun lipidomic analysis of lipids in LKO mouse livers.

(A-B) Heatmap of lipid classes in the livers of F/F and LKO mice fed chow (A) and HFD (B) (n=3-4/group). (C-E) Lipidomic quantification of ceramides, free fatty acids (FFAs) and triacylglycerides (TAGs) in the livers of F/F and LKO mice fed chow and HFD (n=3-4/group). (F) Quantification of diacylglycerol (DAG) in the livers of F/F and LKO mice fed chow and HFD (n=5-8/group). (G) Lipidomic quantification of saturated FFA (SFA) and unsaturated FFA (UFA) in the livers of F/F and LKO mice fed chow and HFD (n=3-4/group). (H) Liver prostaglandin E2 levels of *Lpcat3*$^{fl/fl}$ (F/F) and *Lpcat3*$^{fl/fl}$ *Albumin-Cre* (LKO) mice fed on chow and HFD (n=4-6/group).

Data are presented as means ± SEM. Statistical analysis was performed with Student’s t test. *$P < 0.05$, ** $P < 0.05$.

(Figure 2.5 Cont.)

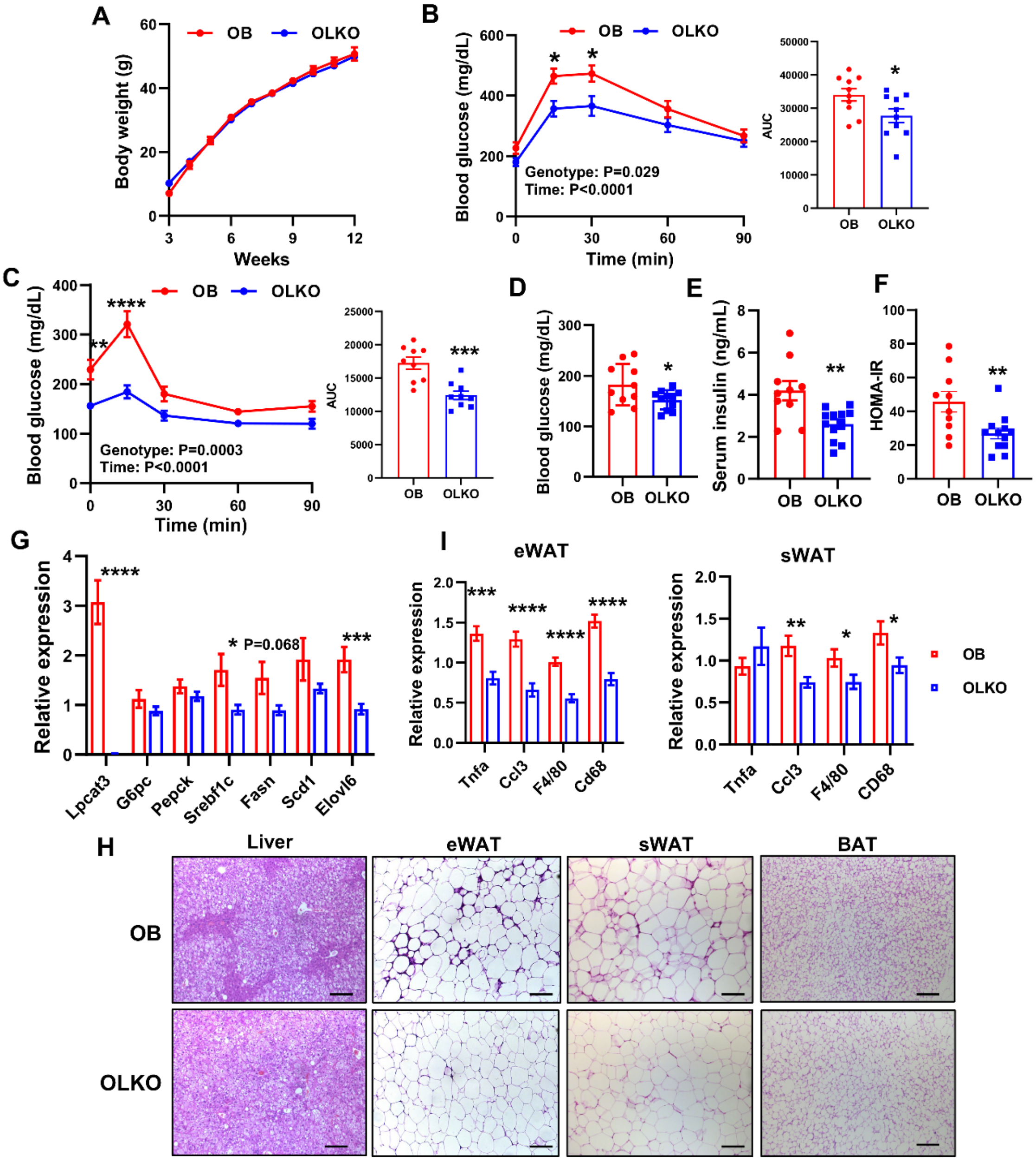

Figure 2.6. **Loss of *Lpcat3* in the liver improves insulin resistance in *ob/ob* mice.**

(A) Growth curve of *ob/ob, Lpcat3*$^{fl/fl}$ (OB) and *ob/ob, Lpcat3*$^{fl/fl}$ *Albumin-Cre* (OLKO) mice (n=10/group). (B-C) GTT and ITT in OB and OLKO mice. (D-F) Fasting blood glucose (D), serum insulin levels (E) and HOMA-IR (F) of OB and OLKO mice. (G) Expression of selected genes in the livers of OB and OLKO mice (n≥10/group). (H) Representative histology of liver, epididymal white adipose tissue (eWAT), subcutaneous white adipose tissue (sWAT) and BAT from OB and

OLKO mice. Scale bar: 100 µm. (I) Expression of inflammation-related genes in eWAT and sWAT of OB and OLKO mice ($n \geq 10$/group).

Data are presented as means ± SEM. Statistical analysis was performed with Student's t test (A, AUC in B-C, D-G, I), two-way ANOVA (B-C). *$P < 0.05$, **$P < 0.01$, ***$P < 0.001$, ****$P < 0.0001$.

(Figure 2.6 Cont.)

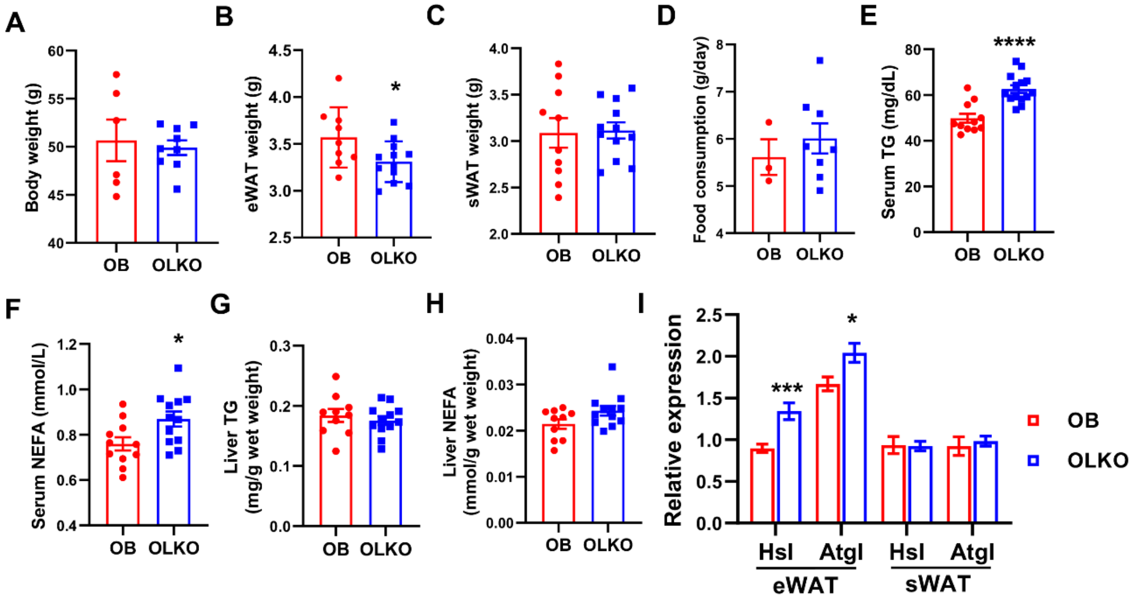

Figure 2.7. *Lpcat3* deficiency in the liver improves insulin resistance in *ob/ob* mice.

(A) End point body weight of *ob/ob Lpcat3$^{fl/fl}$* (OB) and *ob/ob Lpcat3$^{fl/fl}$ Albumin-Cre* (OLKO) mice. (B-C) Tissue weight of eWAT (B) and sWAT (C) in OB and OLKO mice. (D) Daily food consumption of OB and OLKO mice. Data was presented as an average of three days. (E-H) Serum triglyceride (E) and non-esterified fatty acids (NEFA) (F) levels and liver triglyceride (G) and NEFA (H) levels of OB and OLKO mice. (I) Expression of lipases in eWAT and sWAT of OB and OLKO mice (n≥10/group).

Data are presented as means ± SEM. Statistical analysis was performed with Student's t test. *P < 0.05, ***P < 0.001, ****P < 0.0001.

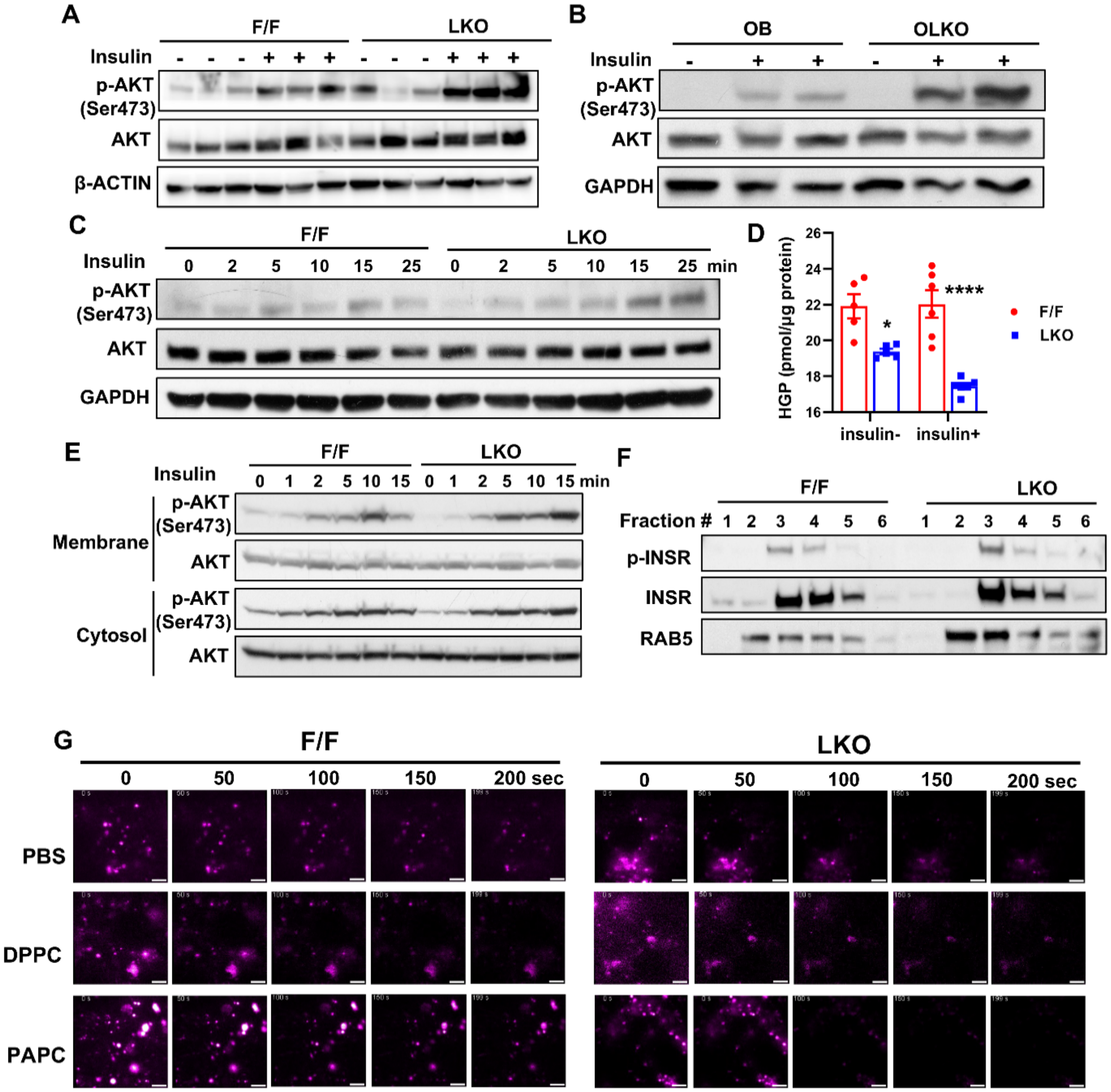

Figure 2.8. ***Lpcat3* deficiency enhances insulin signal transduction in hepatocytes through facilitating insulin receptor internalization to early endosomes.**

(A) Western blot analysis of p-AKT (Ser473) levels in livers from chow diet-fed F/F and LKO mice treated with insulin. Female mice were fasted overnight and i.p. injected with insulin (1 U/kg BW) for 15 min. (B) Western blot analysis of p-AKT levels in livers from OB and OLKO mice treated with insulin. Mice were fasted overnight and retro-orbitally injected with insulin (2 U/kg BW) for 15min. (C) Western blot analysis of p-AKT levels in primary hepatocytes treated with insulin. Primary hepatocytes were isolated from F/F and LKO mice and treated with insulin (1 nM) for different time points. (D) Hepatic glucose production (HGP) assay. Primary hepatocytes were isolated from F/F and LKO mice, cultured in glucose free medium for 6 h before treated with lactate and pyruvate with or without insulin (10 nM) for 3 h. (E) Western blot analysis of p-AKT levels in membrane and cytosol fractions purified from livers of insulin treated mice. Chow diet-fed F/F and LKO mice were fasted overnight and injected with insulin (1 U/kg BW) through vena cava for different time points. (F) Western blot analysis of p-INSR in early endosomes isolated from livers of F/F and LKO mice treated with insulin. Mice were fasted overnight and injected with insulin (1 U/kg BW) for 5 min. (G) Representative images of TIRF microscopy of primary hepatocytes isolated from F/F and LKO mice and treated with liposomes followed by Cy3-insulin.

Data are presented as means ± SEM. Statistical analysis was performed with two-way ANOVA (D). $^{*}P < 0.05$, $^{****}P < 0.0001$.

(Figure 2.8 Cont.)

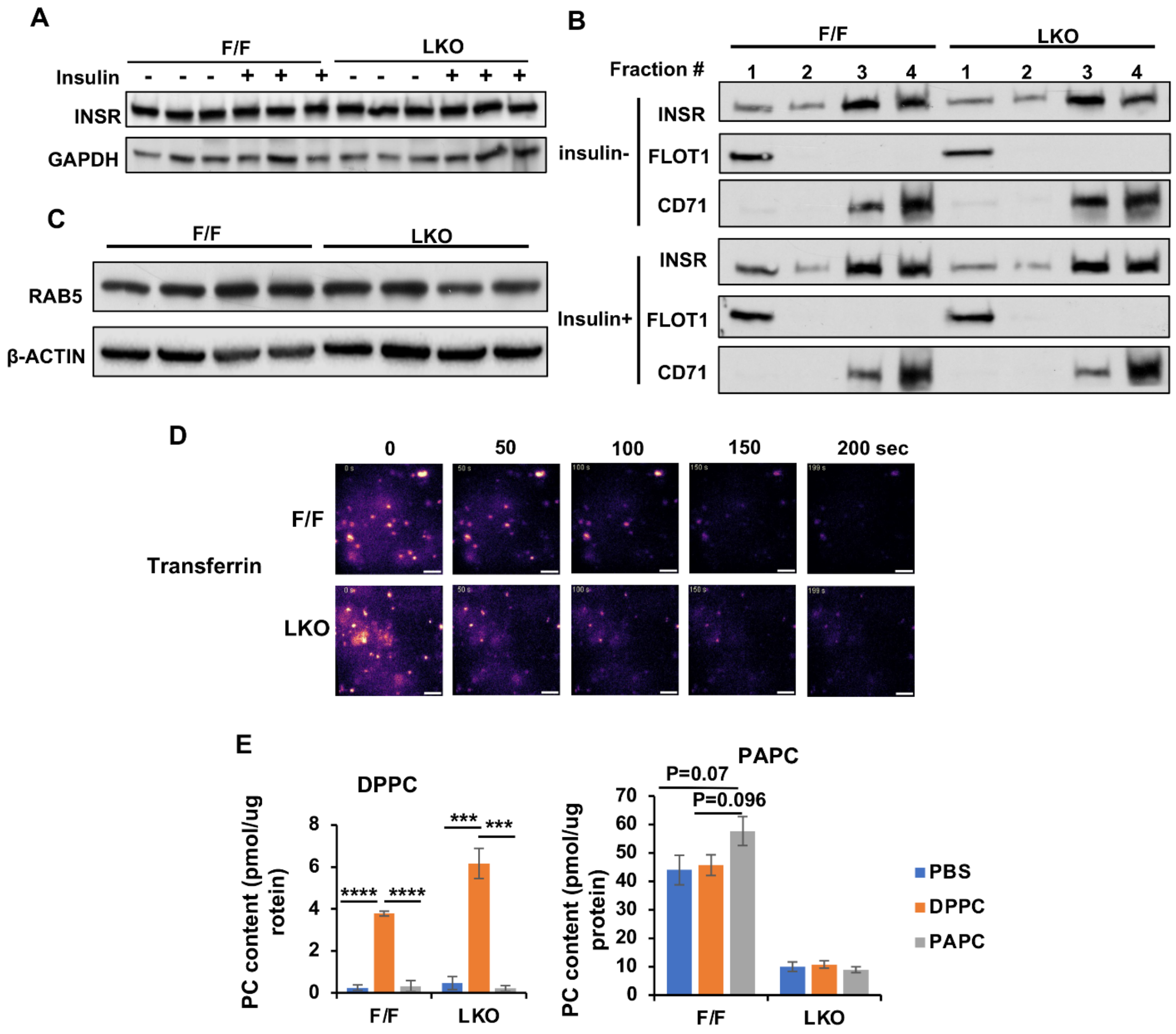

Figure 2.9. **Loss of *Lpcat3* does not affect INSR protein levels or its localization.**

(A) Western blot analysis of total insulin receptor (INSR) levels in female chow diet-fed F/F and LKO mouse livers. (B) Western blot analysis of INSR localization in different microdomains of hepatic plasma membrane before and after insulin treatment. Detergent resistant and non-resistant fractions were purified from chow diet-fed F/F and LKO mice before and after retro-orbital injection of insulin (1 U/kg BW). (C) Western blot analysis of RAB5 levels in whole tissue lysates from F/F and LKO mouse livers. (D) Representative images of TIRF microscopy of primary hepatocytes isolated from F/F and LKO mice and treated with Alexa 568-transferrin. (E) Mass spectrometry analysis of PC content in primary hepatocytes treated with liposomes containing DPPC or PAPC.

Data are presented as means ± SEM. Statistical analysis was performed with one-way ANOVA (E). ***$P < 0.001$, ****$P < 0.0001$.

(Figure 2.9 Cont.)

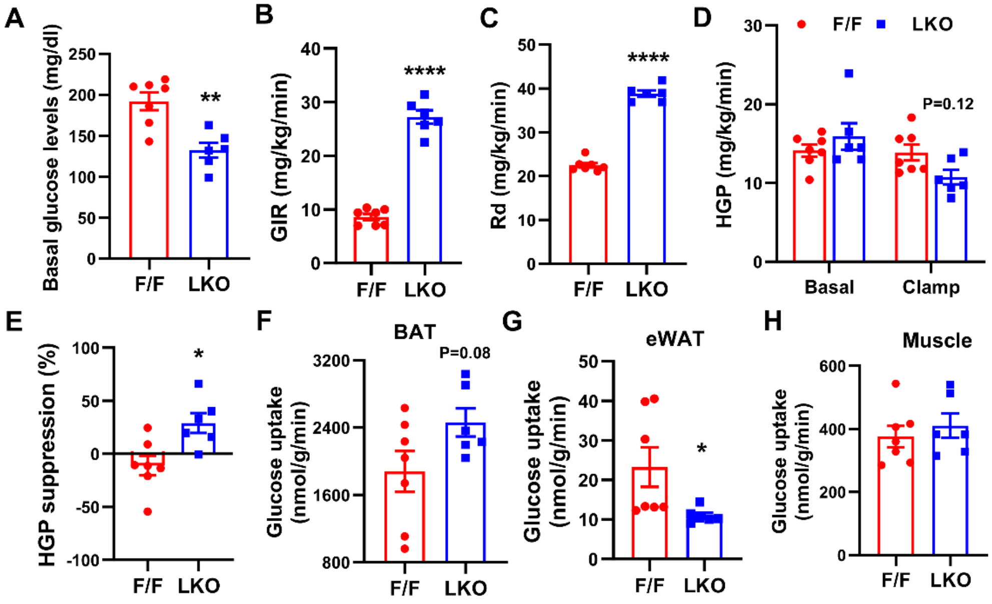

Figure 2.10. Loss of *Lpcat3* in liver suppresses HGP and increases glucose uptake in brown adipose tissue (BAT).

(A-H) Hyperinsulinemic-euglycemic clamp analysis of F/F and LKO mice fed with HFD for 12 weeks. (A) Basal glucose levels, (B) Glucose infusion rate (GIR), (C) Whole-body glucose turnover (Rd), (D) HGP at basal and during insulin clamp, (E) Insulin-mediated suppression of HGP, (F-H) Insulin-stimulated glucose uptake in intrascapular BAT, eWAT and gastrocnemius skeletal muscle (n=6-7/group).

Data are presented as means ± SEM. Statistical analysis was performed with Student's t test (A-C, E-H) and two-way ANOVA (D). $^{*}P < 0.05$, $^{**}P < 0.01$, $^{****}P < 0.0001$.

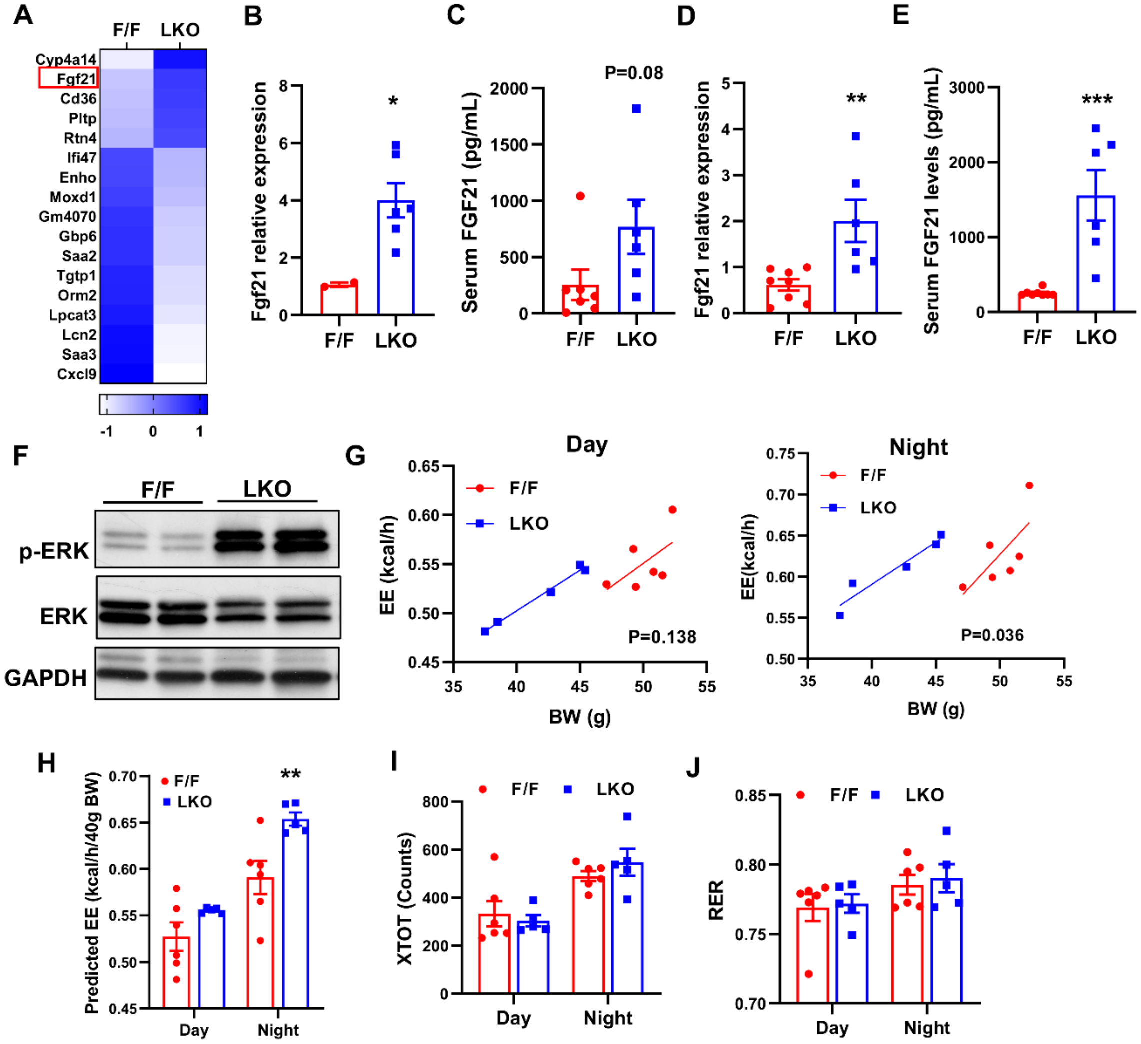

Figure 2.11 Loss of *Lpcat3* in the liver increases FGF21 secretion and energy expenditure. (A) Heatmap of dysregulated genes based on previously published microarray data in livers of chow diet-fed F/F and LKO mice (n=5/group). (B-C) *Fgf21* mRNA levels in the livers (B) and serum FGF21 levels (C) of chow diet fed F/F and LKO mice. (D-E) *Fgf21* mRNA levels in the livers (D) and serum FGF21 levels (Ea) of HFD fed F/F and LKO mice. (F) Western blot analysis of p-ERK in eWAT of HFD-fed F/F and LKO mice. (G) Energy expenditure (EE) analyzed by regression analysis of covariance (ANCOVA). (H) EE estimated by univariate generalized linear model (GLM) with body mass set to 46.3 g (average body mass of F/F and LKO mice on HFD). (I-J) Physical activity (I) and respiratory exchange ratio (RER) (J) in HFD-fed F/F and LKO mice.

Data are presented as means ± SEM. Statistical analysis was performed with Student's t test (B-E), ANCOVA (G), and two-way ANOVA (H-J). *P < 0.05, **P < 0.01, ***P < 0.001.

(Figure 2.11 Cont.)

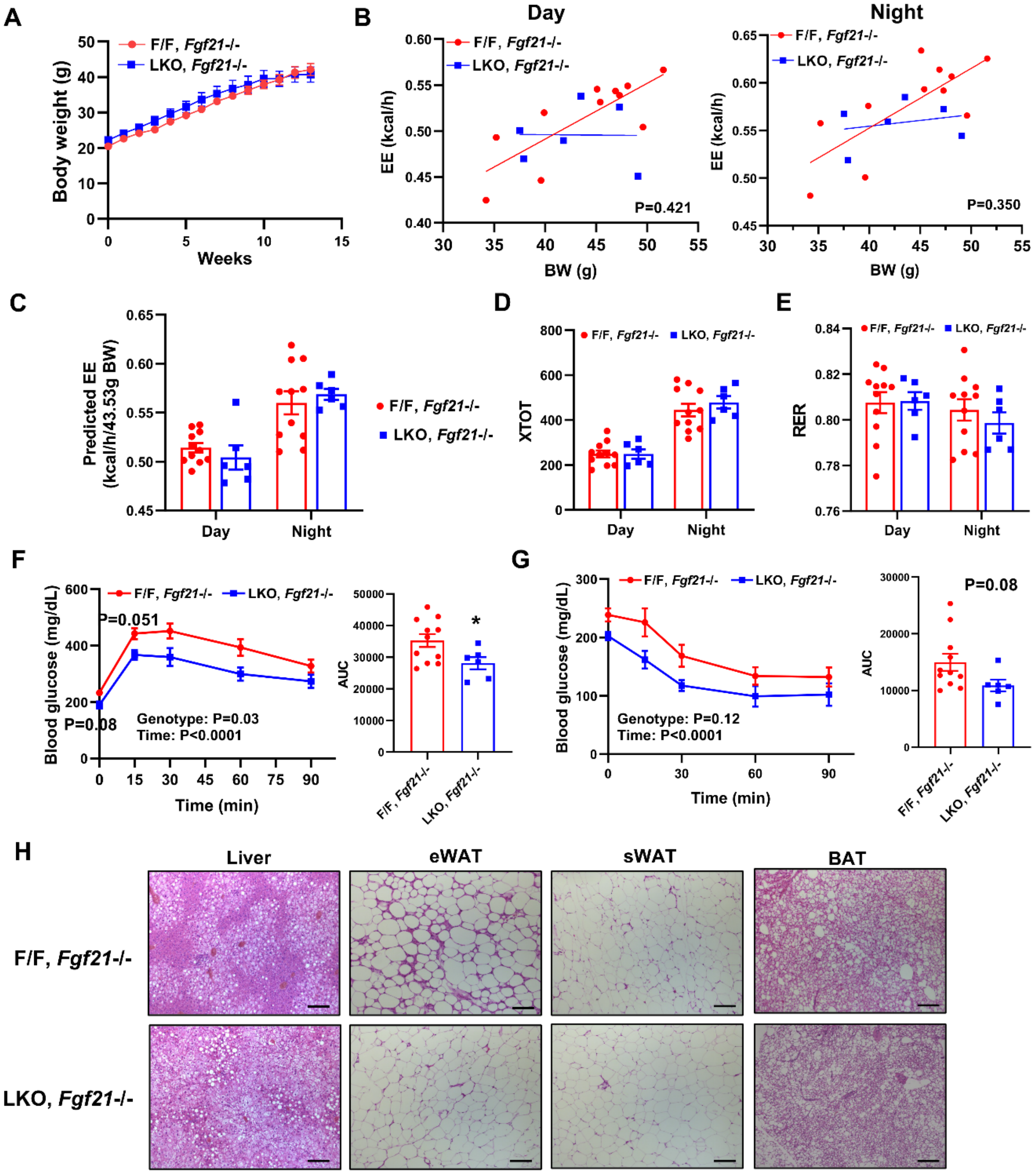

Figure 2.12 FGF21 mediates the effects of *Lpcat3* deficiency on energy expenditure, but not insulin sensitivity.

(A) Growth curve of *Lpcat3*$^{fl/fl}$,*Cre-, Fgf21-/-* (F/F, *Fgf21*-/-) and *Lpcat3*$^{fl/fl}$*, Cre+, Fgf21-/-* (LKO, *Fgf21*-/-) mice on HFD (n=6 and 11/group). (B) Energy expenditure (EE) analyzed by regression analysis of covariance (ANCOVA). (C) EE estimated by univariate generalized linear model (GLM) with body mass set to 43.53 g (average body mass of F/F, *Fgf21*-/- and LKO, *Fgf21*-/-

mice on HFD). (D-E) Physical activity (D) and respiratory exchange ratio (RER) (E) in F/F, *Fgf21*-/- and LKO, *Fgf21*-/- mice fed with HFD. (F-G) GTT and ITT analyses of HFD fed F/F, *Fgf21*-/- and LKO, *Fgf21*-/- mice. (H) Representative histology of liver, epididymal white adipose tissue (eWAT), subcutaneous white adipose tissue (sWAT) and BAT from HFD fed F/F, *Fgf21*-/- and LKO, *Fgf21*-/- mice. Scale bar: 100 µm.

Data are presented as means ± SEM. Statistical analysis was performed with Student's t test (A, AUC in G and H), ANCOVA (B) and two-way ANOVA (C-G). $^*P < 0.05$.

(Figure 2.12 Cont.)

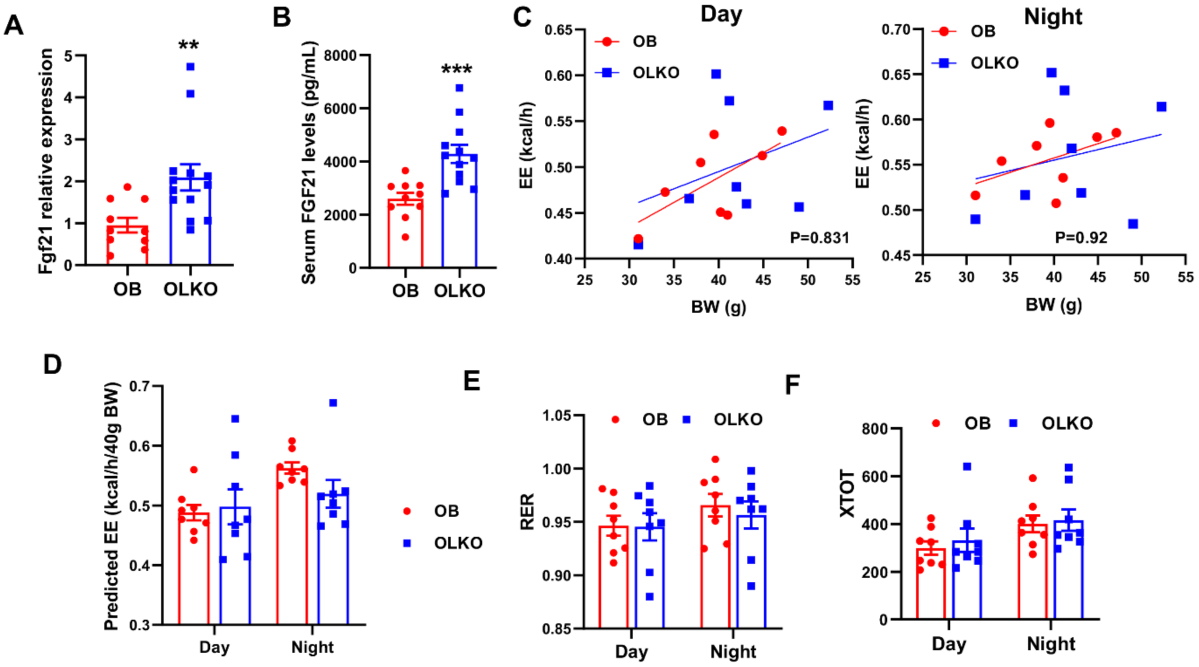

Figure 2.13 Loss of *Lpcat3* has no effect on energy expenditure in *ob/ob* mice.

(A-B) *Fgf21* mRNA levels in the livers (A) and serum FGF21 levels (B) of OB and OLKO mice. (C) Energy expenditure (EE) analyzed by regression analysis of covariance (ANCOVA). (D) EE estimated by univariate generalized linear model (GLM) with body mass set to 40.3 g (average body mass of OB and OLKO mice). (E-F) RER (E) and physical activity (F) of OB and OLKO mice.

Data are presented as means ± SEM. Statistical analysis was performed with Student's t test (A-B), ANCOVA (C) and two-way ANOVA (D-F). $^{*}P < 0.05$, $^{**}P < 0.01$, $^{***}P < 0.001$.

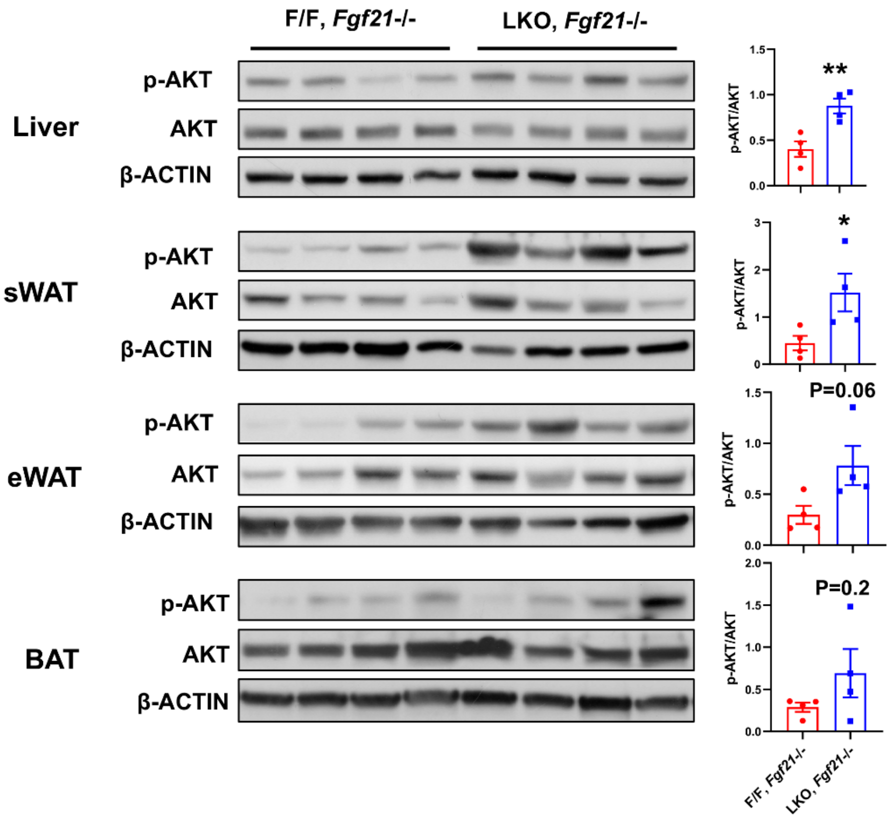

Figure 2.14 Loss of *Lpcat3* enhances insulin signaling in the liver and adipose tissue independent of FGF21.

Western blot analysis of pAKT (Ser473) levels in HFD-fed F/F, *Fgf21*-/- and LKO, *Fgf21*-/- mouse tissues. Mice were fed HFD for 12 weeks, fasted overnight and i.v. injected with insulin (1 U/kg BW) for 15 min.

Data are presented as means ± SEM. Statistical analysis was performed with Student's t test. $*P < 0.05$, $**P < 0.01$.

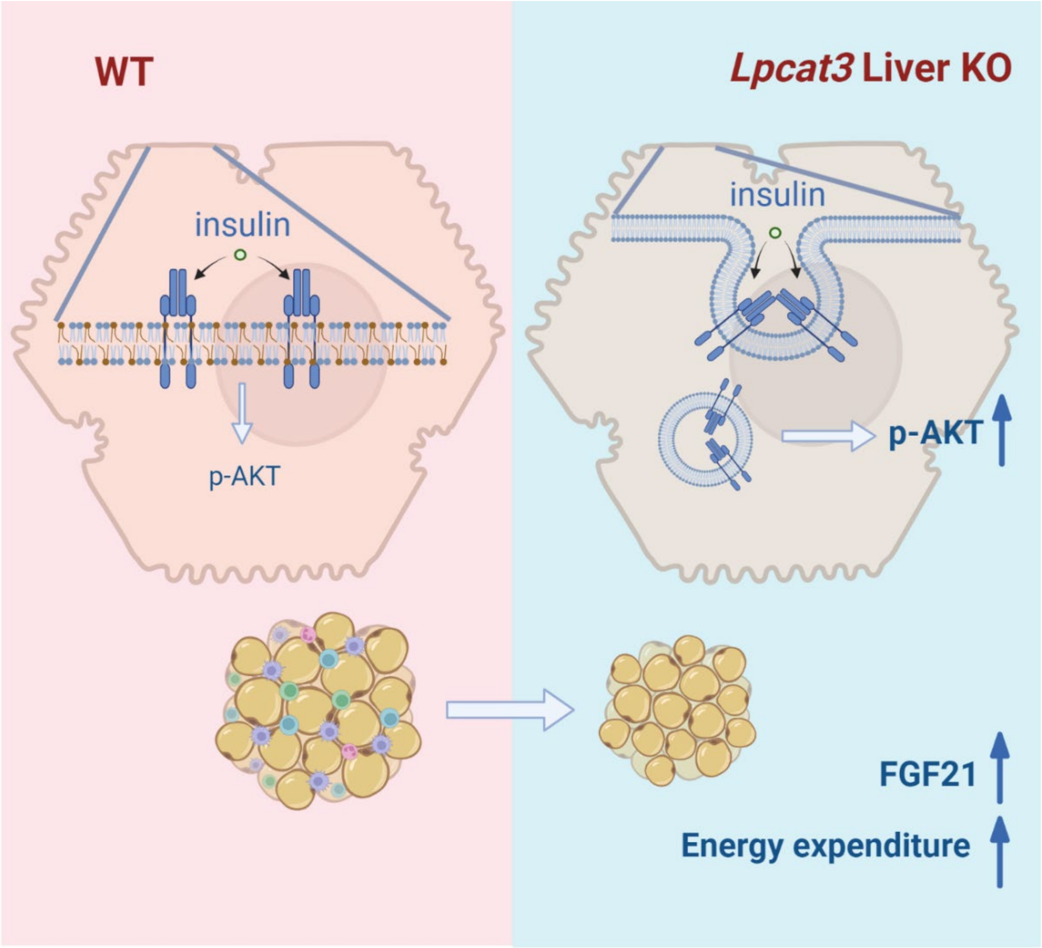

Figure 2.15 Graphical abstract showing hepatic phospholipid remodeling modulates cellular insulin receptor signaling and affects systemic metabolism by inducing circulating Fgf21.

CHAPTER 3. TARGETING PHOSPHOLIPID REMODELING PATHWAY IMPROVES INSULIN RESISTANCE IN DIABETIC MOUSE MODELS[4]

ABSTRACT

Previous studies have revealed that membrane phospholipid composition controlled by lysophosphatidylcholine acyltransferase 3 (LPCAT3) is involved in the development of insulin resistance in type 2 diabetes. In this study, we aimed to investigate the therapeutic potential of targeting *Lpcat3* in the treatment of insulin resistance in diabetic mouse models. *Lpcat3* expression was suppressed in the whole body by antisense oligonucleotides (ASO) injection or in the liver by adeno-associated virus (AAV)-encoded Cre in high-fat diet (HFD)-induced and genetic *ob/ob* type 2 diabetic mouse models. Glucose tolerance test (GTT), insulin tolerance test (ITT), fasting blood glucose and insulin levels were used to assess insulin sensitivity. Lipid levels in the liver and serum were measured. The expression of genes involved in *de novo* lipogenesis was analyzed by real-time RT-PCR. Metabolic rates were measured by indirect calorimetry using the Comprehensive Lab Animal Monitoring System (CLAMS). Our data demonstrate that acute knockout of hepatic *Lpcat3* by AAV-Cre improves both hyperglycemia and hypertriglyceridemia in HFD-fed mice. Similarly, whole body ablation of *Lpcat3* by ASO administration improves obesity and insulin resistance in both HFD-fed and *ob/ob* mice. These findings demonstrate that targeting LPCAT3 could be a novel therapy for insulin resistance (Figure 3.9).

---

[4] This chapter is published in its entirety in the FASEB J. This article is reprinted with the permission of the publisher and is available from https://faseb.onlinelibrary.wiley.com/doi/full/10.1096/fj.202301122RR and using DOI: https://doi.org/10.1096/fj.202301122RR

3.1 INTRODUCTION

In 2021, diabetes is estimated to affect approximately 500 million people worldwide, with about 90% of them having type 2 diabetes[311], which has become one of the fastest growing health concerns of the century[312,313]. Insulin resistance is a major risk factor for type 2 diabetes comorbidities, including hypertriglyceridemia. This is mainly driven by the defective glucose production suppression combined with intact promotion of lipogenesis upon insulin signaling in the liver, also known as selective insulin resistance[61,271,314]. This paradoxical effect dampens the therapeutic efficacy of insulin due to increased lipid production, necessitating further investigation into its pathology.

Phospholipids are major constituents of biological membranes, and their fatty acyl chains exhibit high levels of diversity in length and degree of saturation. These characteristics of phospholipids not only determine the biological properties of membranes, but also influence membrane-associated processes, thereby playing a crucial role in regulating pathophysiological conditions[1,275]. In mammalian cells, phospholipid composition is primarily maintained through the Lands' cycle, a remodeling process of de-acylation and re-acylation[4]. Lysophosphatidylcholine acyltransferases 3 (LPCAT3) is an enzyme highly expressed in the liver, intestine, and adipose tissues that preferentially incorporates polyunsaturated fatty acyl chain into the sn-2 site of lysophospholipids[233,315]. Recent studies have highlighted the crucial roles of membrane phospholipid composition in the regulation of metabolism. LPCAT3 has been shown to maintain lipid homeostasis by controlling the lipidation and secretion of very-low-density lipoprotein (VLDL) and chylomicron in the liver and intestine, respectively[17,176]. *Lpcat3* deficiency blunts SREBP-1c activation and lipogenic gene expression in the liver[276]. Interestingly, LPCAT3 and phospholipid remodeling also play a role in regulating glucose metabolism and contributing to the development of insulin resistance in type 2 diabetes. It has been shown that *Lpcat3* expression and the levels of polyunsaturated phospholipids are increased in the livers of high fat diet (HFD)-fed and *ob/ob* mice[276,316], two well established models of insulin resistance. Furthermore, deletion of *Lpcat3* in the liver significantly improves hepatic insulin resistance and systemic metabolism. Mechanistically, hepatic *Lpcat3* deficiency enhances insulin signal transduction by promoting insulin receptor endocytosis and increases energy expenditure by inducing FGF21 secretion[316]. In the muscle, LPCAT3 affects insulin sensitivity by modulating plasma membrane lipid organization and insulin receptor phosphorylation[15]. These findings suggest that *Lpcat3* could be a novel target to treat insulin resistance.

In this study, we tested the therapeutic potential of targeting *Lpcat3* using ASO- and adeno-associated virus (AAV)-mediated suppression of *Lpcat3* in diabetic mouse models. We showed that acute knockout of *Lpcat3* in the liver using AAV improves hyperglycemia and hypertriglyceridemia in mice fed a high-fat diet. Treatment with ASO to ablate *Lpcat3* effectively mitigates obesity and insulin resistance in both HFD-fed and *ob/ob* mice. These findings suggest that targeting *Lpcat3* and phospholipid remodeling could provide a promising therapeutic strategy for insulin resistance in type 2 diabetes.

3.2 MATERIALS AND METHODS

3.2.1 Animals

All animal procedures were conducted in compliance with protocols approved by the Institutional Animal Care and Use Committee (IACUC) at University of Illinois at Urbana-Champaign (UIUC). *Lpcat3*$^{fl/fl}$ mice have been described before[17]. *ob/ob* mice were acquired from the Jackson Laboratory. All mice were housed under pathogen-free conditions in a temperature-controlled room with a 12 h light/dark cycle. Mice were fed chow diet (LabDiet #5001) or high-fat diet

(Research Diets #D12492). All experiments were performed with male mice unless otherwise stated. For RNA analysis, liver tissues were collected and snap frozen in liquid nitrogen and stored at −80°C. For food intake measurement, mice were housed individually in cages and food weight was measured daily. Mouse blood was collected by retro-orbital bleeding under anesthesia before sacrificing or by tail bleeding, and plasma was obtained by centrifugation. Plasma insulin levels were measured using Insulin ELISA kit (Crystal Chem).

3.2.2 Glucose and insulin tolerance test

Mice were fasted for at least 5 h in the morning and intraperitoneally (i.p.) injected with glucose or insulin (Novolin N, Human). Glucose was given at 1 g/kg body weight (BW) diluted in PBS. Insulin was given at 0.5 U/kg BW for chow diet-fed mice and 1 U/kg BW for HFD-fed and *ob/ob* mice. Blood glucose levels were measured from tail bleeding using a glucometer (OneTouch Ultra2) at designated time points.

3.2.3 Indirect calorimetry and body composition measurements

Metabolic rates were measured by indirect calorimetry in open-circuit Oxymax chambers in the Comprehensive Lab Animal Monitoring System (CLAMS) (Columbus Instruments). Mice were housed individually in the chamber, and O_2 gas was calibrated before monitoring. The chamber was maintained at 23°C with 12-hour light/12-hour dark cycles, and food and water were available ad libitum. O_2 consumption and CO_2 production were measured directly as continuously accumulated data. Energy expenditure (EE) was calculated as $(3.815+1.232*RER)*VO_2$ and linear regression analysis of covariance (ANCOVA) was used to determine mass-independent effect between F/F and LKO mice as reported before [278,279]. Estimated EE was calculated by univariate generalized linear model (GLM) with body mass set to the average of both treatment groups. Body composition (whole-body fat and lean mass) was determined using Echo MRI Body Composition Analyzer.

3.2.4 Histology

Tissues were collected, fixed in 10% buffered formalin, embedded in paraffin, sectioned at 4-10 μm and stained with hematoxylin and eosin at the University of Illinois Histology Lab.

3.2.5 Gene expression analysis

Total RNA was isolated from tissues with Trizol (Invitrogen), cDNA was synthesized, and gene expression was quantified by BioRad CFX384 Touch Real-Time PCR Detection System with SYBR Green (BioRad). For ASO injected mice, total RNA was isolated with Direct-zol RNA Kits (Zymo Research), and cDNA was synthesized using iScript™ cDNA Synthesis Kit (BioRad).

3.2.6 Protein analysis

For *in vivo* insulin signaling, insulin (Novolin N, Human) was injected to overnight fasted mice retro-orbitally. Then, the liver, muscle, and adipose tissues were harvested 10 min post insulin injection. phospho-AKT levels were assessed by Western blot analysis in tissue lysates as described [234]. Briefly, tissues were homogenized and sonicated in RIPA buffer (50 mM Tris–HCl, pH 7.4, 150 mM NaCl, 0.1% Triton X-100, 0.5% sodium deoxycholate, 0.1% SDS) supplemented with protease inhibitors (Roche Molecular Biochemicals) and phosphatase inhibitors (Sigma Aldrich). The homogenate was then cleared by centrifugation. After quantifying protein concentration using BCA kits (Thermo Fisher Scientific), 25 μg of proteins were mixed with sample buffer (BioRad), loaded to 4%-15% precast gel (BioRad) for electrophoresis and transferred to PVDF membranes (Amersham International, GE Healthcare). Membranes were then blocked with blocking buffer (5% BSA in 0.1% TBST) for 1 h at room temperature and then incubated with primary antibodies at 4℃ overnight diluted in blocking buffer. After washed with

0.1% TBST for 4 times, membranes were incubated with secondary antibodies diluted in blocking buffer for 1 h at room temperature. Membranes were developed using ECL western blotting substrate (Thermo Scientific) and were exposed to X-ray film (FUJI) in dark room.

3.2.7 Postprandial lipid absorption assay

Lipid absorption assay was performed as previously described[317]. Briefly, mice were fasted for 4 h and gavaged with corn oil (10 µg/g body weight). Plasma was collected through tail vein at 0, 1, 2, 4 and 6 h and plasma lipids were measured with Wako triglyceride kit.

3.2.8 Lipid extraction and measurement

Liver tissues were snap-frozen in liquid nitrogen at the time of harvest. To extract lipids, liver tissues were cut, weighed and homogenized in water. After transferring the homogenate into glass tubes, lipids were extracted by adding 2 mL chloroform/methanol (2:1 v/v), mixed thoroughly by vortexing and centrifuged at 3,000 r.p.m. for 5 min at 4°C. Lipids in the lower layer were then carefully collected and air-dried overnight. The lipids were dissolved in ethanol and diluted in PBS for lipid measurements. Serum was directly used for lipid measurements. Serum and hepatic lipids were measured with the Wako L-Type TG M kit and the Wako HR series NEFA- HR(2) kit.

3.2.9 Phospholipid analyses

Mouse tissues were snap-frozen in liquid nitrogen. Tissues were homogenized on ice in phosphate buffered saline. Homogenates were subsequently subjected to a modified Bligh-Dyer lipid extraction [280] in the presence of lipid class internal standards, including 1-0-heptadecanoyl-sn-glycero-3-phosphocholine, 1,2-dieicosanoyl-sn-glycero-3-phosphocholine [281]. Lipid extracts were diluted in methanol/chloroform (4/1, vol/vol), and molecular species were quantified using electrospray ionization mass spectrometry on a triple quadrupole instrument (Themo Fisher Quantum Ultra) employing shotgun lipidomic methodologies[282]. Phosphatidylcholine (PC) molecular species were quantified as chlorinated adducts in the negative ion mode using neutral loss scanning for 50 amu (collision energy = 24 eV). Individual molecular species were quantified by comparing the ion intensities of the individual molecular species to that of the lipid class internal standard with additional corrections for type I and type II 13C isotope effects[282].

3.2.10 Antisense oligonucleotide (ASO) treatment

For acute ASO studies, C57BL/6 mice fed with HFD for 8 weeks or *ob/ob* mice at 6-7 weeks of age were subcutaneously injected with either control or *Lpcat3* ASO (GTACATAGTAGGCTTG) at 25 mg/kg twice per week for 4-5 weeks. Body weight was monitored weekly, and body composition was measured by Echo MRI analysis. GTT and ITT were performed on weeks 3 and 4. At the end of ASO treatment, tissues were resected and subjected to gene expression analysis.

3.2.11 Adeno-associated virus (AAV) mediated liver specific *Lpcat3* knockout

For liver-specific acute knockout of *Lpcat3*, *Lpcat3* $^{fl/fl}$ mice fed with HFD for 8 weeks were retro-orbitally injected with $1\text{x}10^{11}$ GC/mouse either AAV8-TBG-iCre (VB1724, Vector Biolabs) or control virus AAV8-TBG-GFP (VB1743, Vector Biolabs) in 100 µL saline under anesthesia. Mice were then continued to be fed with HFD for 4 weeks to characterize metabolic features.

3.2.12 Statistical analysis

For all studies, results from quantitative experiments were expressed as means ± SEM. GraphPad Prism 9.0 (San Diego, CA) was used for all statistical analyses. Where appropriate, significance was calculated by Student’s t test, one- or two-way ANOVA with Tukey’s or Sidak’s multiple comparison test.

3.3 RESULTS

3.3.1 Acute deletion of *Lpcat3* in the liver ameliorates insulin resistance in HFD-fed mice

Our previous studies have demonstrated that *Lpcat3* expression in the liver is induced by insulin and increased polyunsaturated PC levels contribute to the development of selective insulin resistance[316]. To determine if targeting *Lpcat3* expression in the liver could improve hyperglycemia and hypertriglyceridemia, we fed *Lpcat3* floxed mice with HFD for 8 weeks and retro-orbitally injected mice with either an AAV8 expressing the codon improved Cre recombinase driven by liver-specific promoter TBG (AAV8-TBG-iCre) or a control AAV encoding eGFP (AAV8-TBG-eGFP). Both groups of mice exhibited similar body weight gain and body composition 4 weeks after the viral injection (Figure 3.1A-3.1C). Realtime RT-PCR confirmed liver specific knockout of *Lpcat3* upon AAV injection (Figure 3.1D). Intraperitoneal glucose tolerance test (IPGTT) showed that Cre-injected mice cleared glucose load more efficiently than eGFP-injected control mice (Figure 3.1E-3.1F). Insulin tolerance test (ITT) demonstrated that Cre-injected mice were slightly more insulin sensitive compared to controls (Figure 3.1G-3.1H). Furthermore, acute knockout of *Lpcat3* significantly reduced fasting blood glucose levels (Figure 3.1I), while no differences in serum insulin levels and HOMA-IR were observed (Figure 3.1J-3.1K).

It has been shown that *Lpcat3* deficiency suppresses lipogenesis and VLDL secretion in the liver[17,276]. Indeed, gene expression analysis showed that acute knockout of *Lpcat3* decreased the expression of SREBP-1c and its downstream lipogenic targets (Figure 3.2A). Serum triglyceride levels were markedly reduced with a concomitant increase in hepatic lipid accumulation upon *Lpcat3* deletion (Figure 3.2B-3.2E). Histology analysis revealed less inflammation in WAT, especially in epididymal white adipose tissue (eWAT) of Cre injected mice (Figure 3.2F).

Consistent with our previous report, acute knockout of *Lpcat3* increased energy expenditure during dark cycle (Figure 3.2G-3.2I), while food consumption, physical activity and respiratory exchange ratio (RER) were not affected (Figure 3.2J-3.2L).

3.3.2 Whole-body silencing of Lpcat3 improves HFD-induced obesity and insulin resistance

Next, we investigated the effect of global suppression of *Lpcat3* on insulin sensitivity and lipid metabolism. We first subcutaneously injected chow diet-fed C57BL/6 mice with ASO targeting *Lpcat3* (*Lpcat3*-ASO) or control ASO (Con-ASO) twice per week for two weeks and measured the knockdown efficiency in different tissues. Realtime RT-PCR analysis showed marked inhibition of *Lpcat3* expression in several metabolic organs, including liver, intestine, muscle and adipose tissues (Figure 3.3A). Next, we fed C57BL/6 mice with HFD for 8 weeks and subcutaneously injected ASOs for another 5 weeks. *Lpcat3* suppression resulted in a gradual decrease in body weight (Figure 3.3B). Next, we evaluated insulin sensitivity through glucose and insulin tolerance tests before any significant differences in their body weights emerged. Similar to chronic or acute liver-specific *Lpcat3* knockout (LKO), global suppression of *Lpcat3* expression significantly improved glucose intolerance and insulin resistance (Figure 3.3C-3.3H), and dramatically lowered fasting blood glucose levels, serum insulin levels and HOMA-IR (Figure 3.3I-3.3K). The final body weight showed a ~15% decrease in mice injected with Lpcat3-ASO, primarily in adipose tissues (Figure 3.3L-3.3N). We previously have shown that *Lpcat3* deficiency in the intestine suppresses food intake on HFD[176]. However, at 5-week post ASO injection, we did not observe any significant difference in food intake between *Lpcat3*- and Con-ASO injected mice (Figure 3.3O), likely because the mice have adapted to HFD over time.

In contrast to LKO mice, which displayed reduced serum lipid levels accompanied by hepatic lipid accumulation (Figure 3.2B-3.2E), we found no differences in serum or hepatic triglyceride and NEFA levels were observed between Con-ASO and *Lpcat3*-ASO treated mice (Figure 3.4A-3.4D), despite a marked reduction in the expression of SREBP-1c and lipogenic genes (Figure 3.4E). Our previous studies have demonstrated that loss of *Lpcat3* in the intestine impairs lipid absorption[176]. Indeed, mice treated with Lpcat3-ASO showed a trend toward reduced lipid output when subjected to oil gavage (Figure 3.4F), which may explain the absence of lipid accumulation in the liver. Histological analysis showed no overt difference in the liver and adipose tissues between control and *Lpcat3* ASO injected mice (Figure 3.4G). Metabolic rate analysis did not show any difference in energy expenditure or physical activity (Figure 3.4H-3.4K). However, *Lpcat3*-ASO injected mice exhibited a decrease in RER (Figure 3.4L), suggesting a higher utilization of fat as the body's primary fuel source. This shift in fuel utilization may contribute to the reduced adipose tissue weight and the absence of overt hepatic lipid accumulation in these mice.

3.3.3 ASO-mediated knockdown of Lpcat3 increases membrane saturation and enhances insulin signaling

Our previous studies have revealed that *Lpcat3* deficiency in the liver improves insulin sensitivity through both cell-autonomous mechanisms involving increased membrane saturation and improved insulin signal transduction, and cell-nonautonomous mechanisms, driven by enhanced FGF21 secretion[316]. Gene expression analysis showed a marked reduction in *Lpcat3* expression in metabolic organs, including liver, muscle, adipose tissues, following ASO treatment in HFD fed mice (Figure 3.5A). Phospholipid analysis revealed substantial alterations in PC composition in the liver, similar to the changes observed in LKO livers. characterized by a decrease in arachidonoyl-containing PCs and an increase in saturated and monosaturated PCs (Figure 3.5B).

In contrast, the PC composition in muscle and adipose tissues was less affected (Figure 3.5C-3.5E), showing only slight increases in monosaturated PCs and modest decreases in arachidonoyl-containing PCs. In line with our findings in LKO mice, we observed a ~3-fold increase in serum FGF21 levels in mice treated with Lpcat3-ASO (Figure 3.5F). Western blot analysis showed a slight elevation in pAKT levels in the liver and BAT of mice treated with Lpcat3-ASO compared to those treated with Con-ASO (Figure 3.6A-3.6D), indicating enhanced insulin signaling.

3.3.4 Global suppression of Lpcat3 ameliorates obesity and insulin resistance in ob/ob mice

Next, we examined how global knockdown of *Lpcat3* affects metabolism in a genetically obese mouse model. Starting at 6 weeks old, *ob/ob* mice were subcutaneously injected with control or *Lpcat3* targeting ASO twice per week for 5 weeks. Similar to HFD-fed mice, *Lpcat3*-ASO treatment reduced body weight gain in *ob/ob* mice with a significant decrease in adipose tissue weight (Figure 3.7A-3.7D). Mice injected with Con- and *Lpcat3*-ASO had comparable food consumption (Figure 3.7E), indicating that the body weight difference was not caused by a difference in energy intake. GTT and ITT analysis in mice with comparable body weight showed significant improvement in glucose tolerance and insulin sensitivity in *Lpcat3*-ASO injected mice (Figure 3.7F-3.7K). Moreover, *Lpcat3*-ASO injected mice had lower fasting blood glucose, serum insulin levels and HOMA-IR than Con-ASO injected mice (Figure 3.7L-3.7N).

Whole-body suppression of *Lpcat3* expression had no effect on serum triglyceride and NEFA levels or hepatic NEFA levels, but significantly decreased hepatic triglyceride levels (Figure 3.8A-3.8D), which was likely a result of decreased expression of lipogenic genes in the liver (Figure 3.8E). Histology analysis also showed less lipid accumulation in the liver, while no difference in the histology of adipose tissues was observed (Figure 3.8F). CLAMS analysis revealed a slight increase in energy expenditure in *Lpcat3*-ASO injected *ob/ob* mice during light cycle (Figure 3.8G-3.8I), while physical activity was not different between groups (Figure 3.8J). Interestingly, there was a significant reduction in RER in *Lpcat3*-ASO injected mice (Figure 3.8K), suggesting that fat was utilized more as an energy source. Furthermore, the expression of lipases was significantly enhanced in the adipose tissues of *Lpcat3*-ASO injected mice (Figure 3.8L). Thus, reduced RER and increased lipase expression may contribute to smaller fat depots in *Lpcat3*-ASO injected mice.

3.4 DISCUSSION

Phospholipid composition in biological membranes has been increasingly recognized to have significant impact on normal physiological processes and pathological conditions. In previous studies, we have demonstrated that LPCAT3 and phospholipid remodeling are involved in the regulation of VLDL secretion[17], SREBP-1c-mediated lipogenesis in the liver[276], and chylomicron metabolism in the intestine in normal physiology[176]. Our recent investigations have further revealed the involvement of LPCAT3 in the development of disease conditions[234,316], including selective insulin resistance in type 2 diabetes. Specifically, we have found that hyperinsulinemia increases hepatic *Lpcat3* expression and polyunsaturated PC levels, and that chronic *Lpcat3* deficiency in the liver improves insulin sensitivity in both HFD-fed and genetic *ob/ob* mouse models. In this study we show that acute targeting of *Lpcat3* in the liver through AAV-Cre mediated knockout or whole body *Lpcat3* knockdown via ASO injection improves insulin resistance in both HFD-fed and *ob/ob* mice. These studies provide a proof of concept that manipulating *LPCAT3* expression and membrane phospholipid composition could be a potential therapeutic strategy for treating insulin resistance in type 2 diabetes.

The pathogenesis of insulin resistance involves multiple metabolic organs, including liver, muscle and adipose tissues[318-321]. Insulin signaling regulates glucose homeostasis by suppressing glucose production in the liver and enhancing glucose uptake in the muscle and adipose tissues. Interestingly, we and others have demonstrated that LPCAT3 and phospholipid composition modulate insulin signaling and glucose metabolism in both the liver and muscle[15,316]. Loss of *Lpcat3* in the liver improves insulin sensitivity through both cell autonomous and nonautonomous effects. Increasing membrane phospholipid saturation facilitates insulin receptor internalization and downstream signal transduction and increases FGF21 secretion and glucose uptake in brown adipose tissues[316]. Similarly, *Lpcat3* deficiency in the muscle enhances insulin sensitivity by increasing membrane lipid clustering and potentiating insulin action[15]. Although it is unclear whether phospholipid remodeling affects insulin signaling and glucose uptake in adipose tissue, we believe that the improved insulin sensitivity in ASO treated mice could be attributed, at least partially, to the effects of *Lpcat3* suppression in both the liver and muscle.

It is well established that hyperinsulinemia activates SREBP-1c, leading to enhanced lipogenesis, but fails to suppress glucose production in the livers of type 2 diabetic patients, a phenomenon referred to as selective insulin resistance[61,302]. Our studies have shown that LPCAT3 and membrane unsaturation mediate both lipid promoting and anti-glucose producing effects of insulin. Thus, we anticipate that inhibiting *Lpcat3* could improve both hyperglycemia and hypertriglyceridemia in HFD-induced or genetic ob/ob insulin resistant models. Indeed, acute knockout of *Lpcat3* by AAV-Cre injection lowered both blood glucose and triglyceride levels. Similarly, ASO treatment in HFD-fed and *ob/ob* mice also resulted in decreased blood glucose levels. We also observed a marked reduction in hepatic triglyceride levels in *ob/ob* mice. Surprisingly, serum triglyceride levels were not affected after ASO treatment, despite the significant suppression of SREBP-1c expression and its downstream targets involved in lipid *de novo* synthesis in ASO treated livers. We reason that altered lipid metabolism resulting from *Lpcat3* knockdown in other organs, such as adipose tissue and intestine, may have obscured the effect of *Lpcat3* suppression on hepatic lipid metabolism. Indeed, thanks to the reduced lipid absorption caused by the suppression of *Lpcat3* in the intestine, HFD-fed mice treated with ASO showed no discernible difference in hepatic triglyceride levels compared to controls. This observation implies that ASO-mediated whole body *Lpcat3* knockdown mitigated the development of steatosis in mice with hepatic specific *Lpcat3* knockout, enhancing the potential of ASO treatment as a therapeutic approach for diet-induced insulin resistance.

It is interesting to note that treatment with ASO significantly reduced body weight gain, particularly body fat mass, in both HFD-fed and *ob/ob* mice. Although our previous studies have shown that knockout of *Lpcat3* in the liver increases energy expenditure though FGF21 induction [316], there was no difference in energy expenditure between *Lpcat3*-ASO and control-ASO treated mice. Previous research has demonstrated that *Lpcat3* deficiency impairs lipid absorption in the intestine [176], which likely contributes to less body weight gain on HFD. In *ob/ob* mice, we found that knockdown of *Lpcat3* increased the expression of lipolytic enzymes in adipose tissues and reduced RER, suggesting that Lpcat3-ASO injected mice predominantly utilize fat as energy source. However, it remains to be determined how changes in membrane phospholipid composition affect energy, lipid and glucose metabolism in adipose tissues.

In summary, our data demonstrate that targeting *Lpcat3* expression improves obesity and insulin resistance in both HFD-fed and genetic *ob/ob* models, which could be a novel therapeutic approach to treat obesity and insulin resistance.

3.5 LIMITATION OF THE STUDY

In our study, we assessed the therapeutic potential of acute *Lpcat3* depletion against insulin resistance in several mouse models. Although both liver-specific and whole-body knockdown of *Lpcat3* improved insulin sensitivity, the transition to future clinical applications requires further investigation, given the difference between mouse models and human patients. Furthermore, the physiological function of LPCAT3 remains unclear in other organs such as brain and pancreas. Therefore, potential side effects associated with whole-body *Lpcat3* inhibition, although not evident in our study, necessitate comprehensive characterization and scrutiny.

3.6 FIGURES

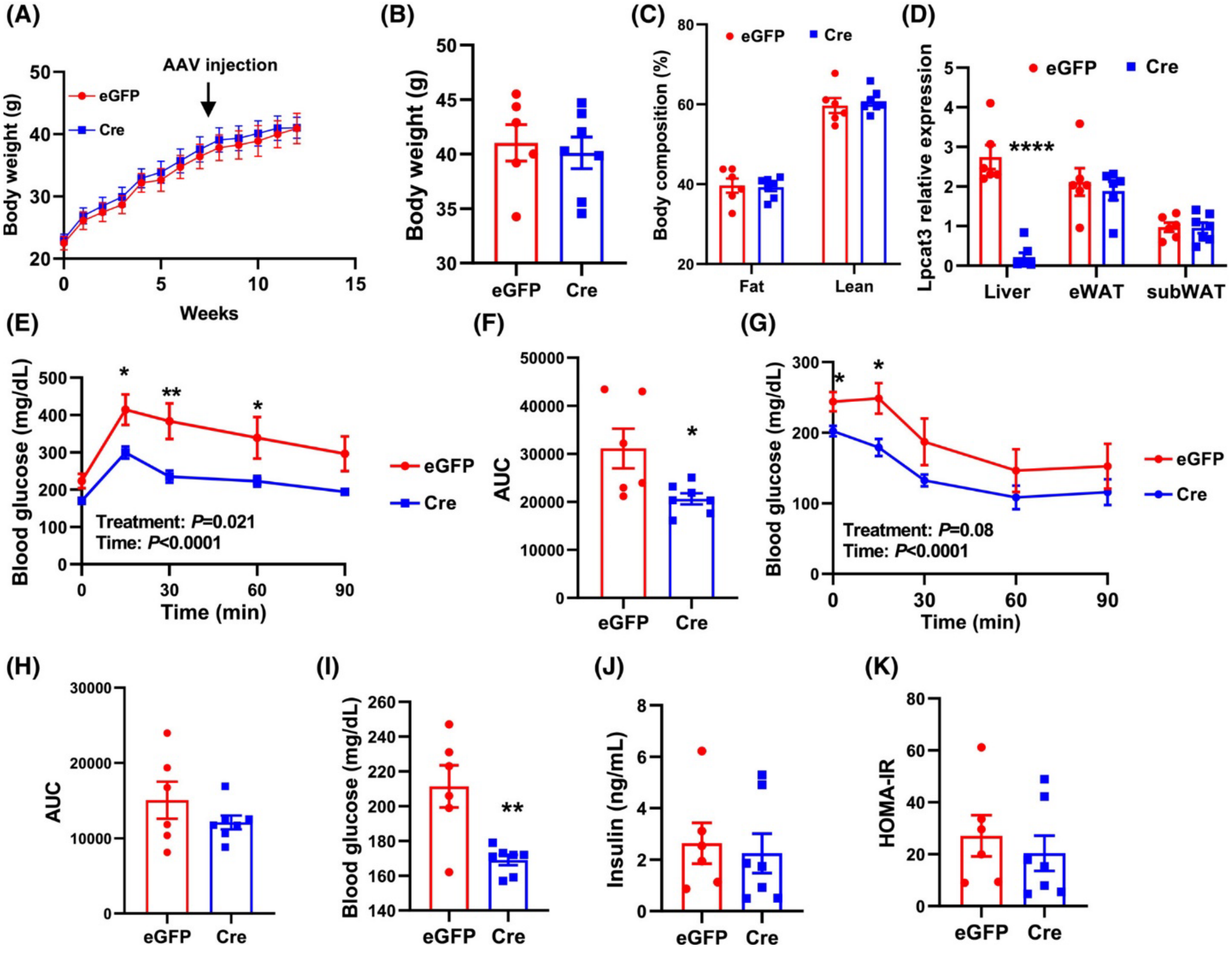

Figure 3.1. Acute deletion of *Lpcat3* in the liver improves insulin sensitivity in HFD-fed mice. (A) Growth curve of *Lpcat3*$^{fl/fl}$ mice fed HFD for 8 weeks followed by retro-orbital injection with AAV8-TBG-eGFP or AAV8-TBG-iCre (n=6-7/group). (B-C) Body weight and body composition in AAV injected HFD fed mice. (D) Lpcat3 mRNA levels in the liver and adipose tissues in AAV injected HFD fed mice. (E-H) GTT, ITT and area under the curve (AUC) analysis in HFD-fed *Lpcat3*$^{fl/fl}$ mice injected with AAV8-TBG-eGFP or AAV8-TBG-iCre (n=6-7/group). (I-K) Fasting blood glucose (I), serum insulin levels (J) and HOMA-IR (K) of HFD-fed *Lpcat3*$^{fl/fl}$ mice injected with AAV8-TBG-eGFP or AAV8-TBG-iCre (n=6-7/group).

Data are represented as means ± SEM. Statistical analysis was performed with two-way ANOVA (C, E and G) and Student's t test (B, D, F, H-K). *$P < 0.05$, **$P < 0.01$, ****$P < 0.0001$.

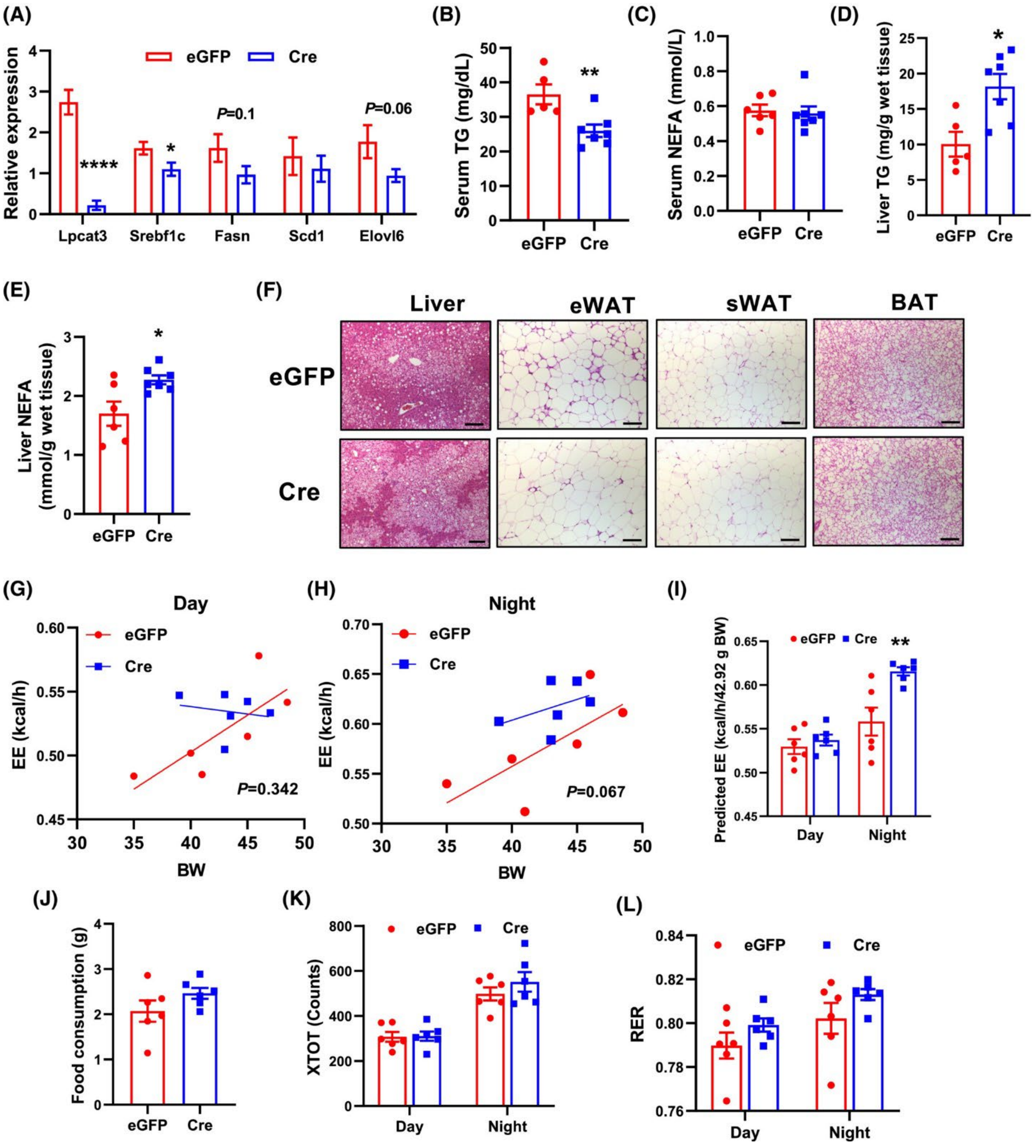

Figure 3.2. Acute deletion of *Lpcat3* in the liver improves hypertriglyceridemia in HFD-fed mice.

(A) Expression of selected genes in the livers of HFD-fed *Lpcat3*$^{fl/fl}$ mice injected with AAV8-TBG-eGFP or AAV8-TBG-iCre (n=6-7/group). (B-E) Serum triglyceride (B) and NEFA (C) levels and liver triglyceride (D) and NEFA (E) levels of HFD-fed *Lpcat3*$^{fl/fl}$ mice injected with

AAV8-TBG-eGFP or AAV8-TBG-iCre. (F) Representative histology of liver, epididymal white adipose tissue (eWAT), subcutaneous white adipose tissue (sWAT) from HFD-fed *Lpcat3*$^{fl/fl}$ mice injected with AAV8-TBG-eGFP or AAV8-TBG-iCre. Scale bar: 100 μm. (G-H) Energy expenditure (EE) analyzed by regression analysis of covariance (ANCOVA). (I) EE estimated by univariate generalized linear model (GLM) with body mass set to 42.92 g (average body mass of AAV8-TBG-eGFP or AAV8-TBG-iCre injected mice on HFD). (J-L) Food consumption (J), physical activity (K) and respiratory exchange ratio (RER) (L) in HFD-fed *Lpcat3*$^{fl/fl}$ mice injected with AAV8-TBG-eGFP or AAV8-TBG-iCre.

Data are presented as means ± SEM. Statistical analysis was performed with Student's t test (A-E, J), ANCOVA (G-H), and two-way ANOVA (I, K, L). $^{*}P < 0.05$, $^{**}P < 0.01$, $^{****}P < 0.0001$.

(Figure 3.2 Cont.)

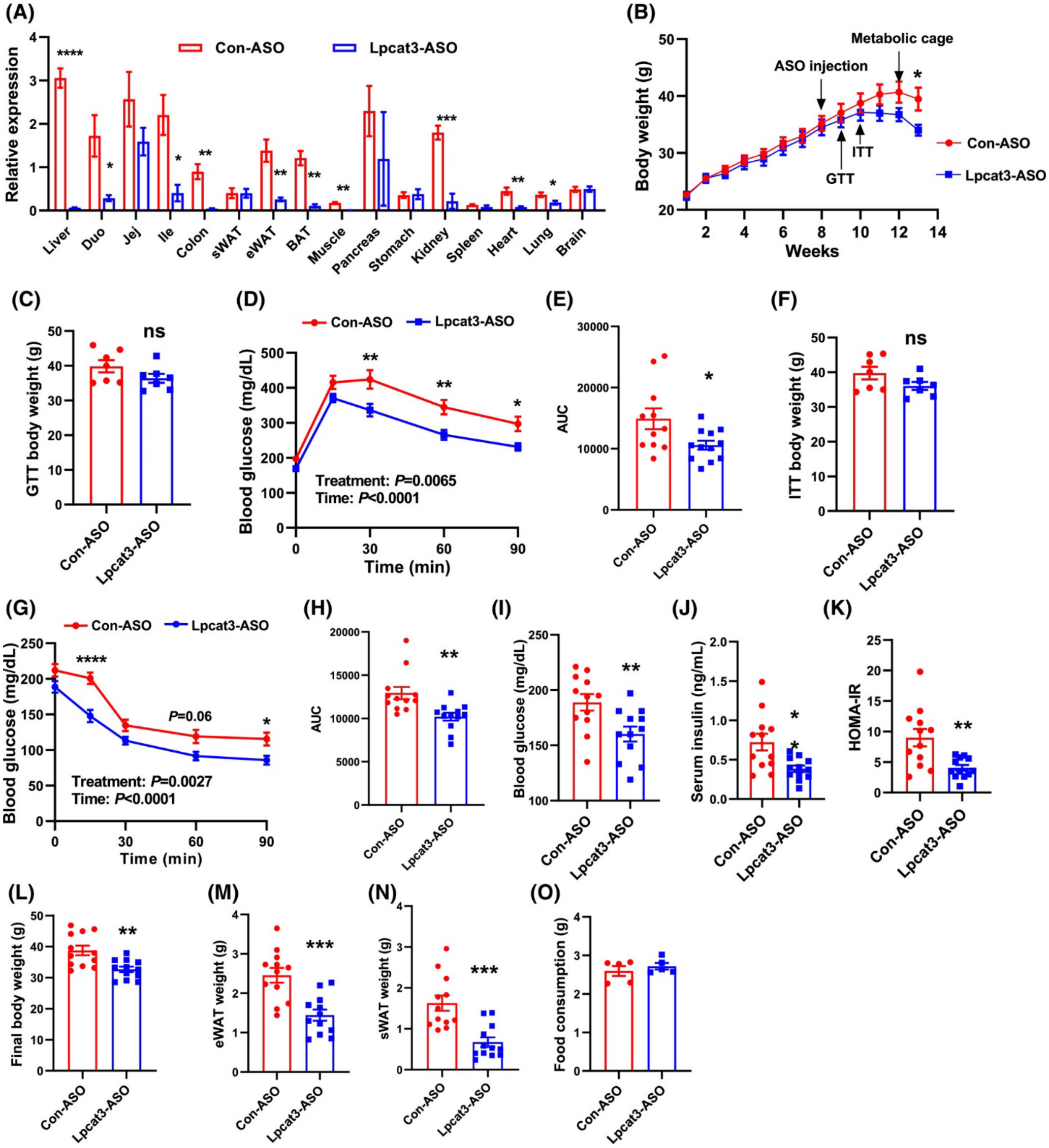

Figure 3.3 Whole-body silencing Lpcat3 expression improves HFD-induced obesity and insulin resistance.

(A) Expression of Lpcat3 in different tissues of chow diet-fed C57BL/6 mice subcutaneously injected with control and Lpcat3 targeting ASOs (n = 5–8/group). (B) Growth curve of C57BL/6 mice fed HFD for 8 weeks followed by subcutaneous injection with control (Con-ASO) or Lpcat3 targeting ASO (Lpcat3-ASO) (n = 12/group). (C and F) Mouse body weight when GTT and ITT were performed. (D–E and G-H) GTT, ITT, and area under the curve (AUC) analysis in HFD-fed C57BL/6 mice injected with Con-ASO or Lpcat3-ASO (n = 11–12/group). (I–K) Fasting blood glucose (I), serum insulin levels (J) and HOMA-IR (K) of HFD-fed C57BL/6 mice injected with Con-ASO or Lpcat3-ASO. (L–N) Final body weight (L), eWAT weight (M), and sWAT weight (N) of HFD-fed C57BL/6 mice injected with Con-ASO or Lpcat3-ASO. (O) Food consumption of HFD-fed C57BL/6 mice injected with Con-ASO or Lpcat3-ASO.

Data are presented as means ± SEM. Statistical analysis was performed with Student's t-test (A–C, E, F, H–O), and two-way ANOVA (D and G). *p < .05, **p < .01, ***p < .001, ****p < .0001.

(Figure 3.2 Cont.)

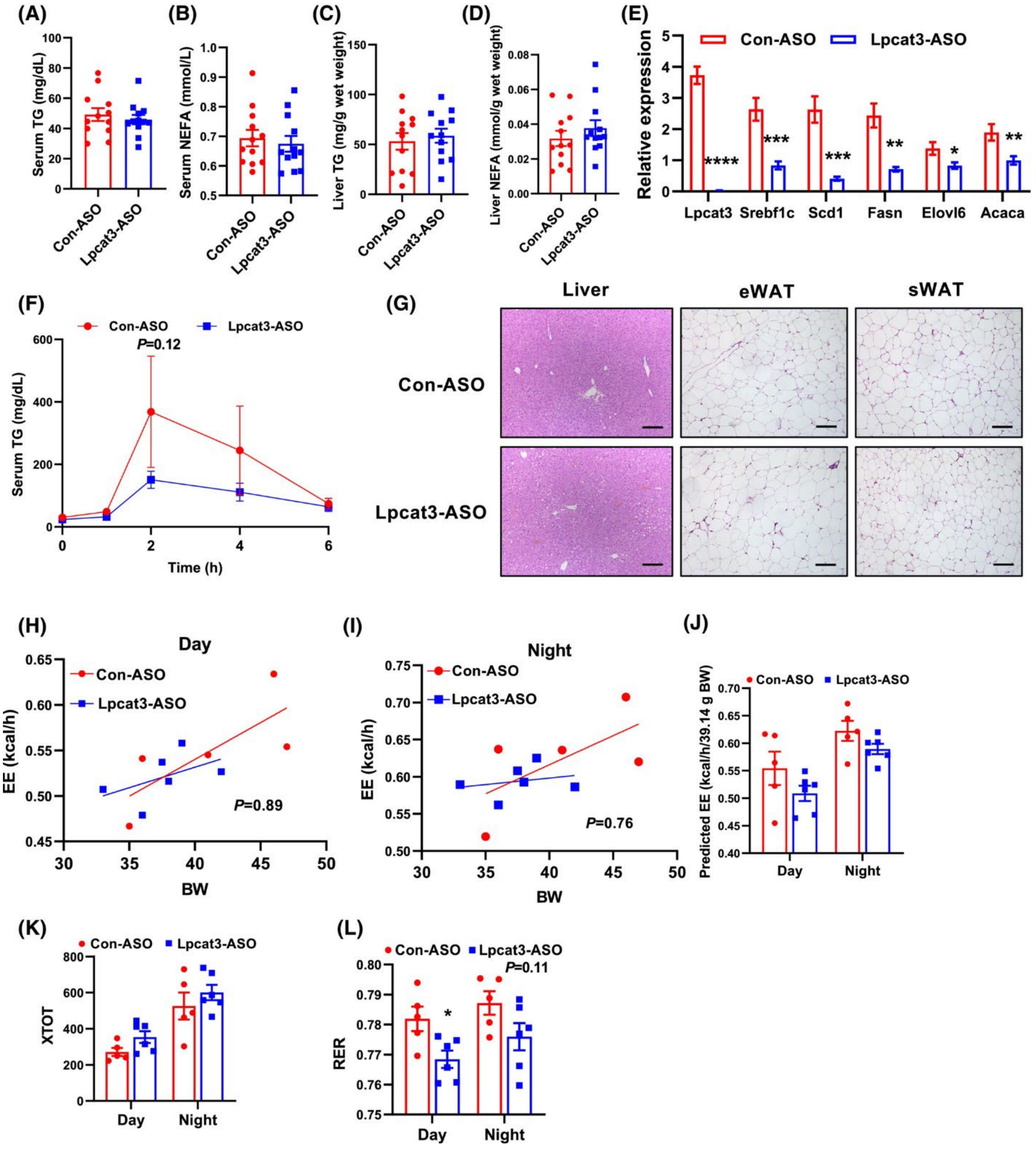

Figure 3.4 Whole-body silencing Lpcat3 expression has no effect on lipid and energy metabolism in HFD-fed mice.

(A–D) Serum triglyceride (A) and NEFA (B) levels and liver triglyceride (C) and NEFA (D) levels of HFD-fed C57BL/6 mice injected with Con-ASO or Lpcat3-ASO. (E) Expression of selected genes in the livers of HFD-fed C57BL/6 mice injected with Con-ASO or Lpcat3-ASO (n = 12/group). (F) Postprandial lipid absorption analysis in HFD-fed C57BL/6 mice injected with

Con-ASO or Lpcat3-ASO (n = 4–5/group). (G) Representative histology of liver, eWAT and sWAT from HFD-fed C57BL/6 mice injected with Con-ASO or Lpcat3-ASO. Scale bar: 100 µm. (H and I) Energy expenditure (EE) analyzed by regression analysis of covariance (ANCOVA). (J) EE estimated by univariate generalized linear model (GLM) with body mass set to 39.14 g (average body mass of Con-ASO or Lpcat3-ASO-injected mice on HFD). (K and L) Physical activity (K) and respiratory exchange ratio (RER) (L) in HFD-fed Lpcat3fl/fl mice injected with Con-ASO or Lpcat3-ASO.

Data are presented as means ± SEM. Statistical analysis was performed with Student's t-test (A–E), ANCOVA (H and I), and two-way ANOVA (F, J–L). $^*p < .05$, $^{**}p < .01$, $^{***}p < .001$, $^{****}p < .0001$.

(Figure 3.4 Cont.)

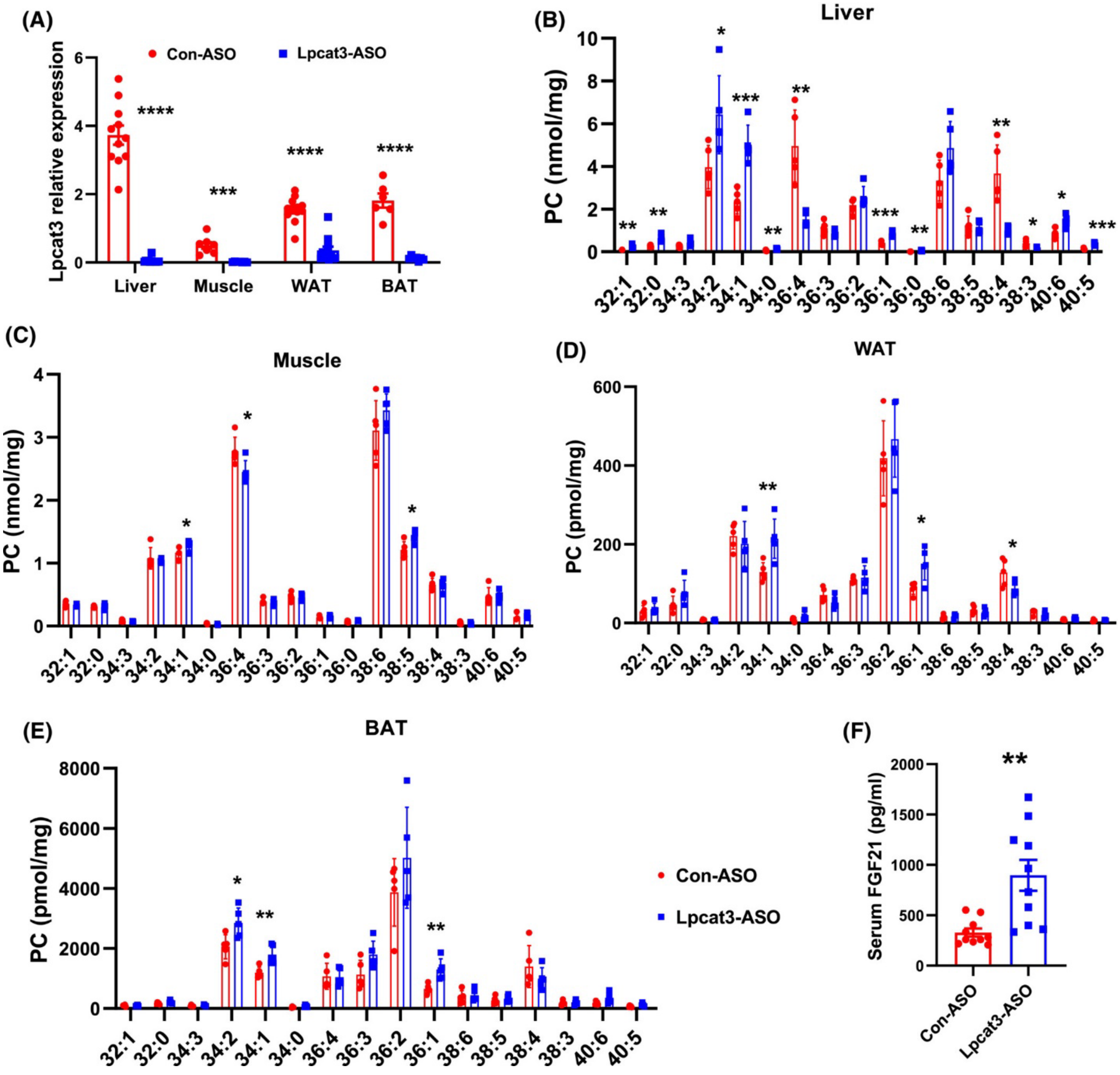

Figure 3.5 Whole-body silencing Lpcat3 expression alters phospholipid composition in metabolic organs.

(A) Expression of Lpcat3 in different tissues of HFD-fed C57BL/6 mice subcutaneously injected with control and Lpcat3 targeting ASOs (n = 6–12/group). (B–E) PC composition in the liver, muscle, WAT, and BAT of HFD-fed mice injected with ASO (n = 5/group). (F) Serum FGF21 levels in HFD-fed mice injected with ASO (n = 10/group).

Data are presented as means ± SEM. Statistical analysis was performed with Student's t-test. $^{*}p < .05$, $^{**}p < .01$, $^{***}p < .001$, $^{****}p < .0001$.

(Figure 3.5 Cont.)

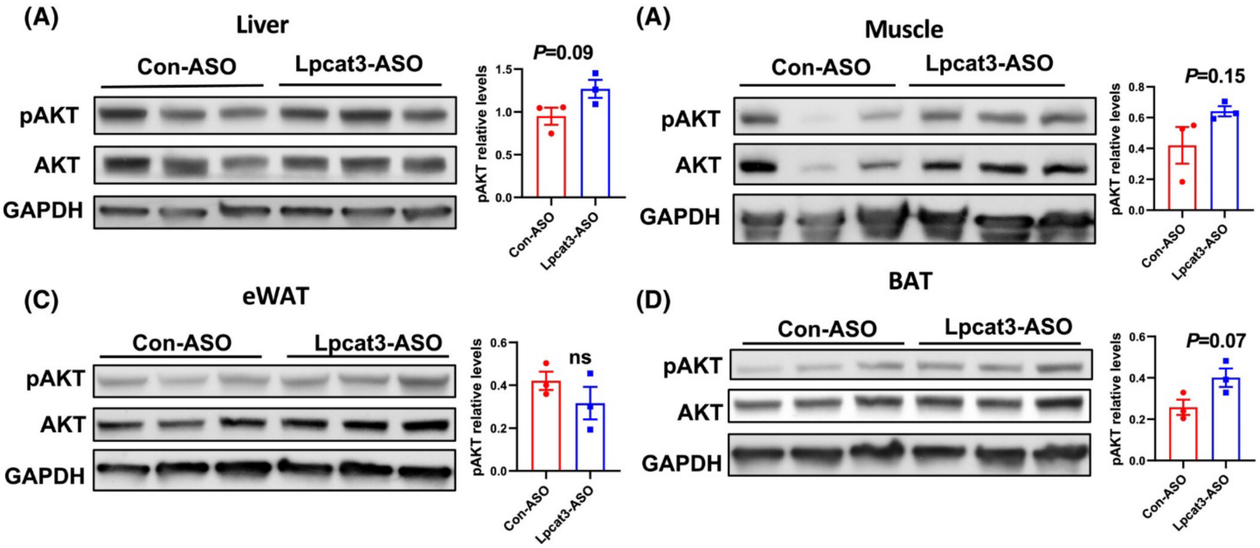

Figure 3.6 Whole-body silencing Lpcat3 expression enhances insulin signaling in the liver and BAT.

(A–D) Western blot analysis of p-AKT levels in the liver, muscle, WAT, and BAT from ASO treated HFD-fed mice. Mice were fasted overnight and retro-orbitally injected with insulin (1 U/kg BW) for 10 min.

Data are presented as means ± SEM. Statistical analysis was performed with Student's t-test.

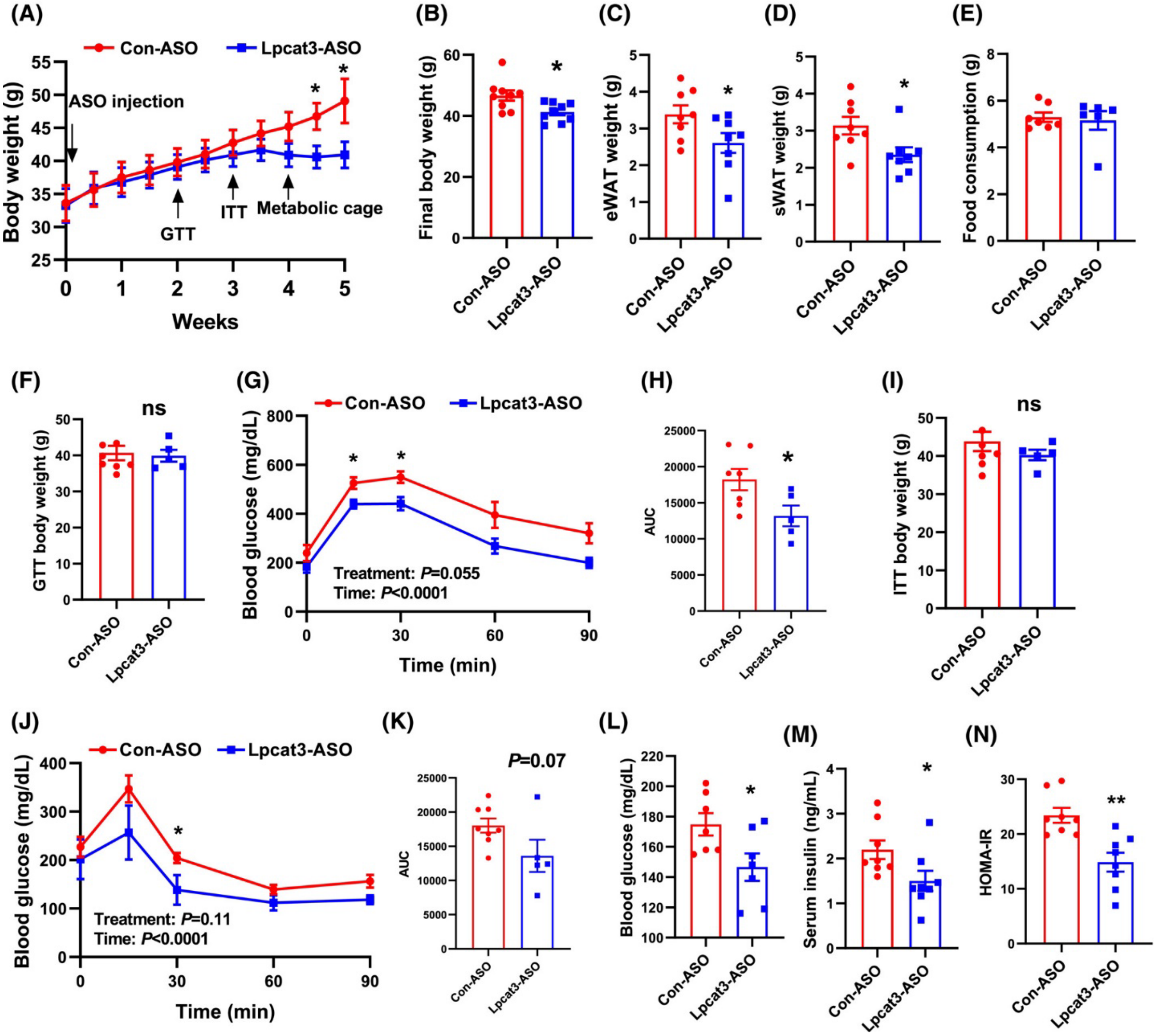

Figure 3.7 Global suppression of Lpcat3 ameliorates obesity and insulin resistance in ob/ob mice.

(A) Growth curve of ob/ob mice injected with Con-ASO or Lpcat3-ASO (n = 8/group). (B–D) Body weight (B), eWAT weight (C), and sWAT weight (D) of ob/ob mice injected with Con-ASO or Lpcat3-ASO. (E) Daily food consumption of ob/ob mice injected with Con-ASO or Lpcat3-ASO. (F–K) GTT, ITT, and area under the curve (AUC) analysis in ob/ob mice injected with Con-ASO or Lpcat3-ASO (n = 5-8/group). (L–N) Fasting blood glucose (L), serum insulin levels (M) and HOMA-IR (N) of ob/ob mice injected with Con-ASO or Lpcat3-ASO.

Data are presented as means ± SEM. Statistical analysis was performed with Student's t-test (A–F, H-I, K–N), and two-way ANOVA (G and J). $^{*}p < .05$, $^{**}p < .01$.

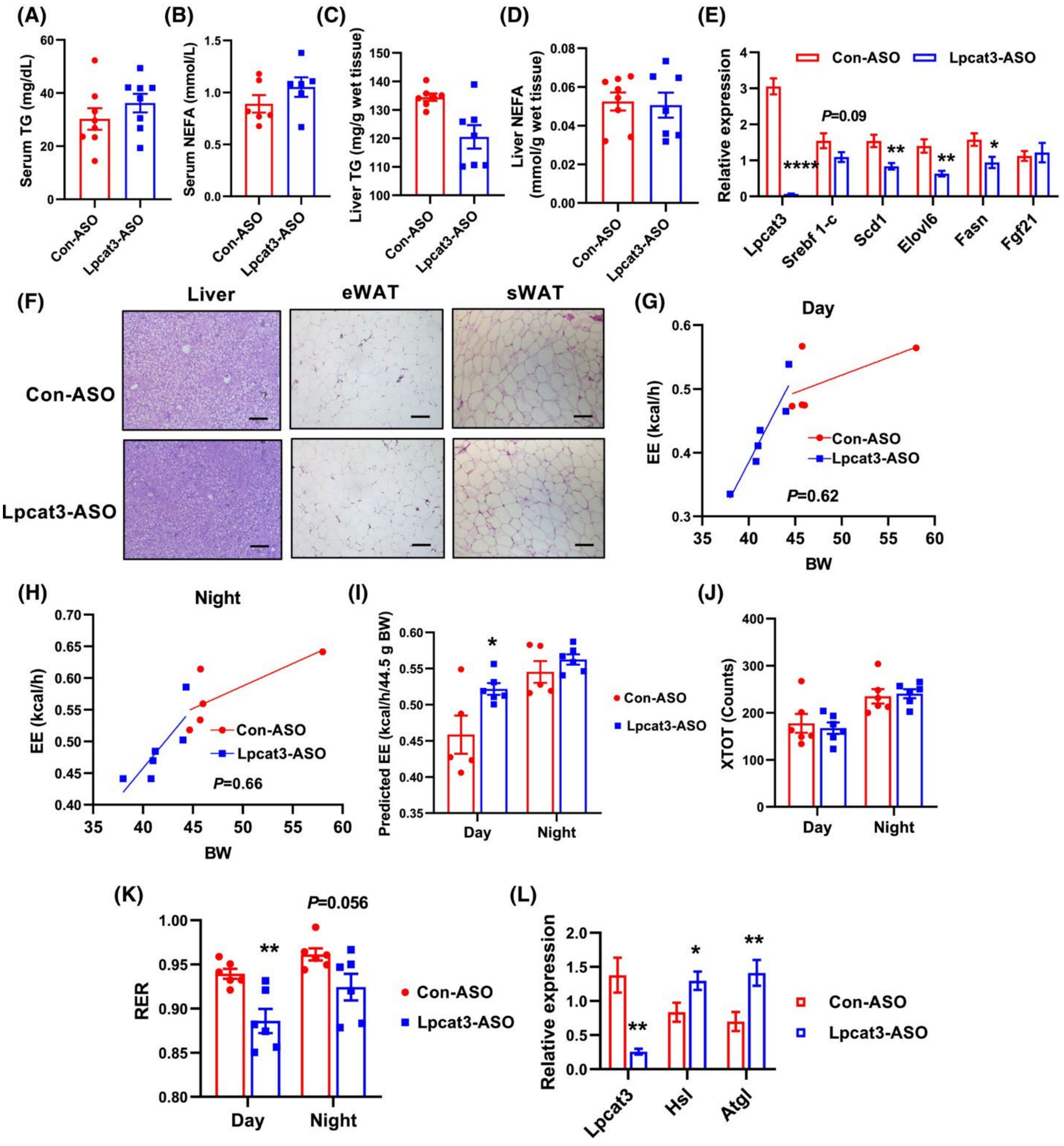

Figure 3.8 Global suppression of Lpcat3 has no effect on lipid metabolism in ob/ob mice.

(A–D) Serum triglyceride (A) and NEFA (B) levels and liver triglyceride (C) and NEFA (D) levels of ob/ob mice injected with Con-ASO or Lpcat3-ASO. (E) Expression of selected genes in the livers of ob/ob mice injected with Con-ASO or Lpcat3-ASO (n = 7–8/group). (F) Representative histology of liver, eWAT and sWAT from ob/ob mice injected with Con-ASO or Lpcat3-ASO. Scale bar: 100 µm. (G and H) Energy expenditure (EE) analyzed by regression analysis of covariance (ANCOVA). (I) EE estimated by univariate generalized linear model (GLM) with body mass set to 44.5 g (average body mass of Con-ASO or Lpcat3-ASO injected ob/ob mice). (J and K) Physical activity (J) and respiratory exchange ratio (RER) (K) in ob/ob mice injected with Con-ASO or Lpcat3-ASO. (L) Expression of Lpcat3 and lipases in eWAT of ob/ob mice injected with Con-ASO or Lpcat3-ASO (n = 7–8/group).

Data are presented as means ± SEM. Statistical analysis was performed with Student's t-test (A–E), ANCOVA (G and H), and two-way ANOVA (I–K). *$p < .05$, **$p < .01$, ****$p < .0001$.

(Figure 3.8 Cont.)

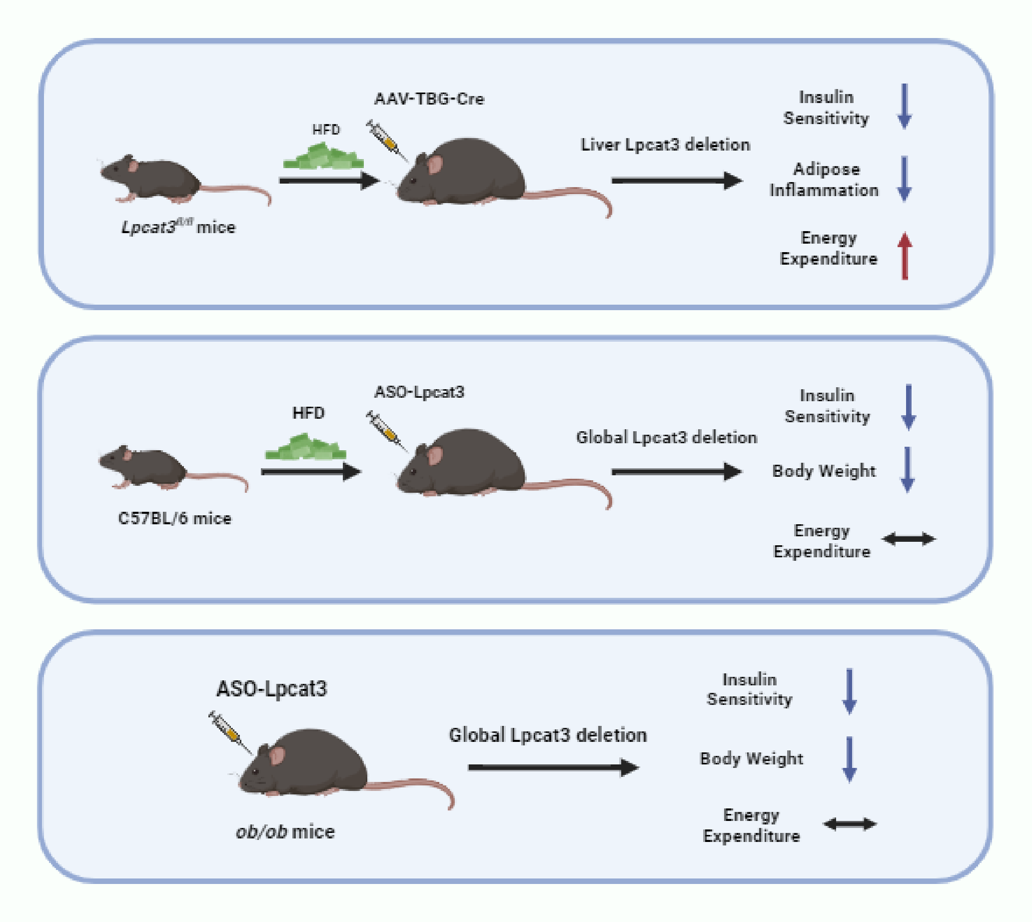

Figure 3.9 Graphical abstract showing inhibiting hepatic Lpcat3 by either AAV-induced knockdown or ASO injection ameliorates insulin resistance in different mouse models.

CHAPTER 4. MEMBRANE PHOSPHOLIPID REMODELING MODULATES NONALCOHOLIC STEATOHEPATITIS PROGRESSION BY REGULATING MITOCHONDRIAL HOMEOSTASIS[5]

ABSTRACT

Background & Aims: Nonalcoholic steatohepatitis (NASH), characterized by inflammation and fibrosis, is emerging as a leading etiology of hepatocellular carcinoma (HCC). Lipidomics analyses in the liver have shown that the levels of polyunsaturated phosphatidylcholine (PC) are decreased in NASH patients, but the roles of membrane PC composition in the pathogenesis of NASH has not been investigated. Lysophosphatidylcholine acyltransferase 3 (LPCAT3), a phospholipid (PL) remodeling enzyme that produces polyunsaturated PLs, is a major determinant of membrane PC content in the liver.

Approach & Results: The expression of *LPCAT3* and the correlation between its expression and NASH severity were analyzed in human patient samples. We examined the effect of *Lpcat3* deficiency on NASH progression using *Lpcat3* liver specific knockout mice (LKO). RNA sequencing, lipidomics, and metabolomics were performed in liver samples. Primary hepatocytes and hepatic cell lines were used for *in vitro* analyses. We show that *LPCAT3* is dramatically suppressed in human NASH livers, and its expression is inversely correlated with NAFLD activity score and fibrosis stage. Loss of *Lpcat3* in mouse liver promotes both spontaneous and diet-induced NASH/HCC. Mechanistically, *Lpcat3* deficiency enhances reactive oxygen species production due to impaired mitochondrial homeostasis. Loss of *Lpcat3* increases inner mitochondrial membrane PL saturation and elevates stress-induced autophagy, resulting in

---

[5] This chapter is published in its entirety in the Hepatology. This article is reprinted with the permission of the publisher and is available from https://journals.lww.com/hep/fulltext/9900/membrane_phospholipid_remodeling_modulates.359.aspx and using DOI: 10.1097/HEP.0000000000000375

reduced mitochondrial content and increased fragmentation. Furthermore, overexpressing *Lpcat3* in the liver ameliorates inflammation and fibrosis of NASH.

Conclusions: These results demonstrate that membrane PL composition modulates the progression of NASH and that manipulating LPCAT3 expression could be an effective therapeutic for NASH (Figure 4.17).

4.1 INTRODUCTION

Non-alcoholic fatty liver disease (NAFLD) has become the most common chronic liver disease around the world, affecting approximately 25% of the adults[322]. With complex yet poorly understood pathologies, liver can progress from simple steatosis to nonalcoholic steatohepatitis (NASH), featured with inflammation and fibrosis, and finally to cirrhosis and hepatocellular carcinoma (HCC)[323]. Genome-wide associate studies (GWAS) have identified single nucleotide polymorphism (SNP) in several genes to be closely associated with the risk or severity of NASH development, including patatin like phospholipase domain containing 3 (PNPLA3), transmembrane 6 superfamily member 2 (TMSF62) and mitochondrial amidoxime reducing component 1 (MARC1)[324,325]. However, the mechanisms underlying these genetic variants in the pathogenesis of NASH are not clear.

Lipidomics analyses in the liver have shown that the levels of polyunsaturated phosphatidylcholine (PC), especially arachidonic acid (20:4)-containing PC, are decreased in NASH, while total PC content is not altered[326,327]. Interestingly, recent studies have demonstrated that hepatic polyunsaturated PC levels are correlated with NASH-related genetic variants. For example, the levels of polyunsaturated PC species are increased in the liver of patients carrying a protective variant in MARC1 gene[3]. In contrast, patients with NASH-promoting variants in TM6SF2 and PNPLA3 genes have reduced polyunsaturated PCs and increased saturated PCs in the liver compared to non-carriers[2,152]. These studies suggest that hepatic polyunsaturated PC content is inversely correlated with the risk or severity of NASH in humans. However, the role of altered PC composition in the pathogenesis of NASH and the underlying mechanisms have not been investigated.

The composition of membrane PCs is regulated by Lands cycle, where PCs are remodeled by substitution of the fatty acyl chain on the sn-2 site through the sequential activity of phospholipase A2s (PLA2s) and lysophosphotidylcholine acyltransferases (LPCATs)[4]. LPCAT3 is the most abundant LPCAT in the livers of both human and mouse. Due to its substrate preference of polyunsaturated fatty acyl chains, LPCAT3 has been shown to be a critical determinant of membrane PC composition, especially the levels of polysaturated PCs[1]. Previous studies have shown that loss of *Lpcat3* in the liver selectively reduces membrane polyunsaturated PCs without affecting total PC levels, which results in increased membrane saturation, impaired very low-density lipoprotein (VLDL) secretion and hepatic steatosis[17]. However, whether and how LPCAT3 modulates the progression of NAFLD from steatosis to NASH remain elusive.

In this study, we demonstrate that *LPCAT3* is suppressed in human NASH livers and its expression is inversely correlated with NAFLD activity score (NAS) and fibrosis stage. We show that deletion of *Lpcat3* in mouse liver leads to the development of spontaneous NASH and HCC with age. *Lpcat3* liver knockout (LKO) mice are also prone to diet-induced NASH and HCC progression. We further show that loss of *Lpcat3* reduces PC and cardiolipin unsaturation in the inner mitochondrial membrane (IMM) and exacerbates mitochondrial oxidation, which leads to the overproduction of reactive oxygen species (ROS). Moreover, *Lpcat3* deficiency decreases mitochondrial DNA content and induces fragmented mitochondrial morphology, likely due to enhanced mitochondrial damage and autophagy. Finally, we show that overexpression of *Lpcat3* in the liver ameliorates inflammation and fibrosis in a diet-induced mouse NASH model. These data provide strong evidence that changes in membrane PC composition *per se* is sufficient to drive the initiation and progression of NASH and that manipulating PC content through *LPCAT3* activation could be a novel therapeutic approach for NASH.

4.2 METHODS

4.2.1 Animal models

All animal procedures were conducted in compliance with protocols approved by the Institutional Animal Care and Use Committee (IACUC) at University of Illinois at Urbana-Champaign (UIUC). *Lpcat3*$^{fl/fl}$ and *Lpcat3*$^{fl/fl}$; *Albumin-Cre* mice have been described [17]. Briefly, gene targeting vector was electroporated into JM8A1.N3 ES cell line from C57BL/6N mice. Targeted ES cell clones were injected into C57BL/6J blastocysts to generate chimeric mice, which was bred with C57BL/6J mice to obtain heterozygous knockout mice (*Lpcat3*$^{+/-}$). *Lpcat3*$^{+/-}$ mice were mated with mice expressing a Flpe recombinase transgene on C57BL/6J background to generate *Lpcat3*$^{Fl/+}$ mice, which were crossed with albumin-*Cre* on C57BL/6J background to generate *Lpcat3*$^{Fl/Fl}$, *Albumin-Cre+* (LKO) and *Lpcat3*$^{Fl/Fl}$*, Albumin-Cre-* (control) mice. Both LKO and control mice were on mixed 87.5% C57BL/6J and 12.5% C57BL/6N background. All mice were housed under pathogen-free conditions in a temperature-controlled room with a 12 h light/dark cycle. Mice were fed chow diet (Lab Diet #5001) or NASH diet (Envigo, TD.120528) with a high sugar solution (23.1 g/L d-fructose and 18.9 g/L d-glucose). All experiments were performed with male mice. Mice were sacrificed after 6 h fasting and liver tissues were collected and snap frozen in liquid nitrogen and stored at −80°C. Mouse blood was collected by retro-orbital bleeding before sacrificing or by tail bleeding, and serum was obtained by centrifugation.

4.2.2 NAFLD human patient study

The NAFLD human patient liver specimens were previously described[328]. Liver specimens from 15 unidentifiable normal individuals without known liver diseases, 15 individuals with steatosis, and 15 individuals with severe NASH-fibrosis were obtained from the Liver Tissue Cell Procurement and Distribution System (LTCDS) that operates under a contract from the NIH. The correlation between *LPCAT3* expression and NAS/fibrosis stage was analyzed from GSE193084[329].

4.2.3 Phospholipid analysis

Phospholipids were quantified as previously described[176,276,277]. Lipids were extracted from liver tissues and isolated IMM via modified Bligh-Dyer extraction with the addition of lipid class-specific internal standards as described previously[280]. Lipidomics were performed using a Q Exactive mass spectrometer paired with a Vanquish UHPLC System (Thermo Scientific)[330]. Chromatographic separation was achieved using a Accucore™ C30 column 2.1 mm × 150 mm (Thermo Scientific) with mobile phase A composed of 60% acetonitrile, 40% water, 10 mM ammonium formate, and 0.1% formic acid and mobile phase B composed of 90% isopropanol, 10% acetonitrile with 2 mM ammonium formate, and 0.02% formic acid. CL, PC, and PE species were analyzed via parallel reaction monitoring and quantitated with the application of isotopomer corrections and normalization to the mass of mitochondrial protein for each sample. Aliphatic constituents were confirmed via analyzing the MS/MS spectra obtained for each species for corresponding fragments (e.g., *m/z* 281.2 for C18:1).

4.2.4 Cell culture

Hepa 1-6 cell line was maintained in Dulbecco's modified Eagle's medium (DMEM) supplemented with 10% fetal bovine serum (FBS), 4.5 g/L glucose, 1 mM sodium pyruvate and 5 mM L-glutamine at 37°C with 5% CO2. For *Lpcat3* knockdown, Hepa 1-6 cells were treated with control or *Lpcat3* antisense oligo (ASO) (5'-GTACATAGTAGGCTTG-3') at 5 µM for 48 h before experiments. For MitoTracker staining, control and *Lpcat3* ASO knockdown cells were seeded on glass bottom dish and incubated with 200 nM MitoTracker Red FM for 30 min at 37°C. The cells were then washed and imaged on Nikon Eclipse Ti Confocal Microscope with 37°C chamber.

Primary hepatocytes were isolated from chow diet- or NASH diet-fed *Lpcat3*$^{fl/fl}$, *Lpcat3*$^{fl/fl}$*; albumin-Cre* mice. Briefly, we cannulated the inferior *vena cava* of anesthetized mice and perfused the liver with 37°C liver perfusion medium (0.5 mM EGTA and 10 mM HEPES in Hanks solution) for 5 min, then digested with 40 µg/ml Liberase TM in 10 mM HEPES-buffered William's medium E at 37°C for another 5 min. Digested liver was removed and placed in William's medium E, and cells were dispersed. For chow diet fed mice, we filtered the resulting cell suspension through a 70 µm cell strainer and washed 3 times with William's medium E. Live cells were counted using trypan blue staining. Primary hepatocytes were used only when the viability was above 85%. For NASH diet fed mice, we followed previously described procedure[331]. Briefly, after cells were dispersed and pelleted, 25% Percoll were used to isolate viable hepatocytes by centrifuging at 100 g for 5 min. Then, cells were washed with plating media and seeded into plates. 1 × 10^6 live cells were seeded per well of 6-well collagen I–coated Biocoat plates in William E medium supplemented with 2 mM glutamine, 10 mM HEPES, 1% penicillin and streptomycin (P/S) and 5% FBS. After 3 to 4 hours, cells were washed twice with 2 ml PBS and cultured in maintenance medium (William E medium supplemented with 2 mM glutamine, 10 mM HEPES, 1% P/S and 0.2% fatty acid-free BSA) before treated with 250 µM BSA conjugated palmitate acid and 200 µM carnitine, or 200 μM methyl-β-cyclodextrin-cholesterol. Glass bottom dish (Cellvis) were coated with collagen I at 5 ug/cm^2 for imaging of primary hepatocytes.

4.2.5 Protein analysis

Whole cell and liver tissue were homogenized and sonicated in RIPA buffer (50 mM Tris–HCl, pH 7.4, 150 mM NaCl, 0.1% Triton X-100, 0.5% sodium deoxycholate, 0.1% SDS) supplemented with protease inhibitors (Roche Molecular Biochemicals) and phosphatase inhibitors (Sigma Aldrich). The homogenate was then cleared by centrifugation. After quantifying protein concentration using BCA kits (Thermo Fisher Scientific), 25 μg of proteins were mixed with sample buffer (BioRad), loaded to 4%-15% precast gel (BioRad) for electrophoresis and transferred to PVDF membranes (Amersham International, GE Healthcare). Membranes were then blocked with blocking buffer (5% BSA in 0.1% TBST) for 1 h at room temperature and then incubated with primary antibodies at 4℃ overnight diluted in blocking buffer. After washed with 0.1% TBST for 4 times, membranes were incubated with secondary antibodies diluted in blocking buffer for 1 h at room temperature. Membranes were developed using ECL western blotting substrate (Thermo Scientific) and were exposed to X-ray film (FUJI) in dark room.

4.2.6 Immunostaining

Fixed liver tissue was processed and embedded in paraffin by the Histology laboratory at University of Illinois. Sections of livers were deparaffined and boiled for 15 min in 10 mM sodium citrate (pH = 6) and cooled to room temperature. Sections were then washed with 0.025% TBST and blocked by 10% goat serum with 1% BSA in TBS for 1 h at room temperature. Primary antibody targeting α-SMA (Cell Signaling Technology, 19245) or alpha-fetoprotein (Proteintech, 14550-1-AP) was applied to slides at 1:500 diluted in 1% BSA in TBS and incubated overnight at 4°C. After wash with 0.025% TBST, EnVision+ System- HRP Labelled Polymer Anti-Rabbit

(Dako) was applied to sections and then incubated with DAB (Vector Laboratories), counter stained with hematoxylin, and mounted for imaging. For *in situ* measurement of apoptosis in the liver, TUNEL assay was conducted using Click-iT™ Plus TUNEL Assay Kits (Thermo Fisher Scientific) following manufacturer's instructions.

4.2.7 Lipid extraction and measurement

Liver tissues were snap-frozen in liquid nitrogen at the time of harvest. To extract lipids, liver tissues were cut, weighed and homogenized in water. After transferring the homogenate into glass tubes, lipids are extracted by adding 2 mL chloroform/methanol (2:1 v/v), mixing thoroughly by vortex and centrifuging 3,000 r.p.m. for 5 min at 4°C. The lower layer containing lipids was then carefully collected and air-dried overnight. The liver lipids were dissolved in ethanol and diluted in PBS for lipid measurements. Serum and liver lipids were measured with the Triglycerides Reagent (Thermo Fisher Scientific), total cholesterol reagent (Thermo Fisher Scientific), free cholesterol E kit (Fujifilm) and the Wako HR series NEFA- HR(2) kit (Fujifilm).

4.2.8 Gene expression analysis

Total RNA was isolated from tissues or cells with Trizol (Invitrogen). cDNA was synthesized and gene expression was quantified by BioRad CFX384 Touch Real-Time PCR Detection System with SYBR Green (BioRad). Primers are listed in the supplementary table.

4.2.9 Histology

Tissues were fixed in 10% formalin overnight and kept in 70% ethanol before use. The fixed tissues were then processed in the University of Illinois Histology Lab and embedded in paraffin. For Sirius Red staining, slides were stained with 0.1% (w/v) Sirius red F3B and 0.1% fast green in saturated picric acid for 1 h at room temperature after deparaffined. Then, the slides were washed with acidified water (0.5% acetic acid, v/v) and then dehydrated for mounting. NAFLD activity score (NAS) was blindly assessed by an experienced pathologist according to Kleiner Scoring System[332].

4.2.10 Adeno-associated virus (AAV) mediated overexpression

Adeno-associated virus serotype 8 (AAV8) containing either hepatocyte-specifically expressed TBG-Lpcat3 (AAV8- TBG-Lpcat3) or the control vector (AAV8-TBG-eGFP) were purchased from the VECTOR Biolabs. C57BL/6 mice were fed with NASH diet for 7 weeks before retro-orbital injection of $2x10^{11}$ GC/mouse control or Lpcat3 expressing AAV. Mice were fed with NASH diet for another 9 weeks before sacrificing.

4.2.11 RNA sequencing analysis

Total RNAs were extracted from frozen mice livers using TRIzol reagent. Ribosomal RNA was removed with the FastSelect HMR kit (Qiagen). The RNAseq libraries were prepared with the Kapa Hyper Stranded mRNAseq Sample Prep kit (Roche). The libraries were pooled; quantitated by qPCR and sequenced on one SP lane for 101 cycles from one end of the fragments on a NovaSeq 6000. Fastq files were generated and demultiplexed with the bcl2fastq v2.20 Conversion Software (Illumina). The Fastq files were then mapped to the GRCm39 mouse genome from GENCODE using STAR[333]. The count matrix were generated using Rsubread[334] and the differentially expressed genes were analyzed using DESeq2[335]. For Gene Ontology analysis, genes with adjusted p-value less than 0.05 and fold change > 1.5 were selected for the enrichment analysis.

4.2.12 Total and mitochondrial reactive oxygen species (ROS) measurement

Total ROS in primary hepatocytes was determined with Total ROS detection Kit (ENZ-51011 Enzo Life Sciences Inc.) and mitochondrial ROS levels were quantified as MitoSOX (Invitrogen) signal following the manufacturers' instructions.

4.2.13 Hepatocytes H_2O_2 emission assay

Hydrogen peroxide released from primary hepatocytes were measured by Amplex^{TM} UltraRed Reagent following manufacturer's instructions. Briefly, reaction mixture containing 50 μM Amplex^{TM} UltraRed Reagent and 0.1 U/mL horseradish peroxidase (HRP) in William's media E with HEPES was prewarmed at 37°C. Primary hepatocytes from F/F and LKO mice on chow diet were isolated and live hepatocytes were selected using 25% Percoll®. Then, primary hepatocytes were added into prewarmed reaction mixture at density of 4? 10^4 cells/well and incubated for 1 h at 37°C in the presence of BSA or BSA conjugated palmitate (250 μM). Fluorescence was measured using SpectraMax ID5 plate reader (530/585 nm, ex/em).

4.2.14 Liver metabolomics

Hydrophilic metabolites were extracted from snap frozen livers for analysis at Metabolomics Core Facility at Northwestern University. Briefly, about 30 mg tissues were homogenized in cooled 80% methanol (v/v) at a ratio of 20 μL/mg tissue. 200 μL of the homogenate were transferred into a tube pre-added with 800 μL of pre-cooled 80% methanol (v/v) and incubated at -80°C overnight. Then, the homogenates were vortexed and centrifuged at 20,000 g for 30 min at 4°C. The supernatant was collected for analysis with LC/MS and the pellets were dissolved for protein quantification.

4.2.15 Mitochondria DNA (mtDNA) copy number

Total liver DNA from F/F and LKO mice were isolated using GeneJET Genomic DNA Purification Kit (Thermo Fisher Scientific) according to manufacturer's instruction. mtDNA was quantified as previously described[336] by qPCR using primers specific for the mitochondrial D-loop region or a specific region of mtDNA that is not inserted into nuclear DNA (non-NUMT). Nuclear DNA encoding Tert and B2m was used for normalization.

4.2.16 Mitochondria and inner mitochondrial membrane (IMM) isolation

Crude mitochondria were isolated as previously described[337]. Briefly, about 0.3 g liver was homogenized in isolation buffer (IB) containing 10 mM Tris-MOPS, 1 mM EGTA/Tris pH 7.4, and 200 mM sucrose. The homogenate was centrifuged at 700 g for 10 min at 4°C to remove tissue debris and nucleus. The supernatant was then centrifuged at 7,000 g for 10 min at 4°C to collect crude mitochondria. The pallets were washed with IB and snap frozen or used for IMM isolation. To isolate IMM, about 20 μg (protein weight) mitochondria were resuspended in 200 μL IB and incubated with equal volume 2.4 mg/mL digitonin in IB for 15 min at 4°C. The IMM was obtained by centrifugation at 9,500 g for 10 min at 4°C. The pellets were washed once and collected as IMM fraction. The supernatant was centrifuged at 144,000 g for 1 h at 4°C to collect outer mitochondrial membrane (OMM).

4.2.17 Transmission electron microscopy (TEM)

TEM analysis was performed at Electron Microscopy Core of University of Illinois at Chicago. Livers from chow diet- or NASH diet-fed mice were quickly dissected and rinsed in the fixative (2% glutaraldehyde, 2% paraformaldehyde in phosphate buffer, pH 7.4, Electron Microscopy Sciences). The samples were then rinsed in phosphate buffer, incubated in Osmium tetroxide with potassium ferrocyanide, and rinsed with water. Samples were en-bloc stained with filtered uranyl acetate overnight and dehydrated in ethanol series. Samples were then subsequently infiltrated with 1:1 and 1:4 acetonitrile: epoxy mixture and finally infiltrated with Lx112 epoxy mixture (Ladd, Inc), and hardened at 80 °C for 2 days. After embedding, samples were trimmed, and cut into 90-100 nm sections with a diamond knife. Sections were stained with Uranyl Acetate and Lead Citrate and were visualized on a Hitachi H600 Electron Microscope at 75 KV. Images were taken with plate film and scanned at 3200 dpi for digital images.

4.2.18 Seahorse assay

Oxygen consumption was assessed using the Seahorse XFe96 Flux Analyzer (Agilent), according to the mitochondria stress test protocol provided by the manufacturer. Briefly, 2 μg of isolated crude hepatic mitochondria were analyzed in mitochondrial assay solution (MAS), containing 70 mM sucrose, 220 mM mannitol, 10 mM KH2PO4, 5 mM MgCl2, 2 mM HEPES, 1 mM EGTA, 10 mM succinate, 2 μM Rotenone, 4 mM ADP, and 0.2% (w/v) fatty acid-free BSA, pH 7.2 at 37°C. After measuring baseline OCR, Oligomycin (2 μM final), FCCP (4 μM final) and Antimycin A (4 μM final) were injected serially. *Lpcat3* knockdown Hepa 1-6 cells were seeded into Seahorse XF96e cell culture microplates (Agilent) overnight before changing to Seahorse base medium with 25 mM glucose, 1 mM sodium pyruvate and 2 mM L-glutamine. The OCR was measured and analyzed following manufacturer's instruction.

4.2.19 Fatty acid oxidation rate measurement

Liver fatty acid oxidation (FAO) rate was measured using kit purchased from Biomedical Research Service, State University of New York (cat. #: E-141) following manufacturer's instruction. Briefly, liver tissues were lysed and homogenized before incubation with FAO substrate (octanoyl-CoA) in 37°C for 2 h. The FAO rate was measured by colorimetric reading at 492 nm.

4.2.20 Serum AST and ALT activity measurement

Serum AST and ALT activity were measured by assay kits purchased from Biomedical Research Service, State University of New York following manufacturer's instruction (cat #: E-115, E-116). Briefly, serum was diluted 10× and mixed with substrates of AST or ALT and incubated for 1 h at 37°C before reading at 492 nm.

4.2.21 Measurement of glutathione (GSH) and oxidized GSH (GSSG)

Liver GSH and GSSG levels were collected from metabolomics analysis. GSSG and total GSH levels were measured by GSH/GSSG-Glo Assay (Promega) following manufacturer's instruction. Briefly, isolated mitochondria were weighed and resuspend with 20 volumes of PBS (20 µL/mg) and diluted 10× with PBS. Then, 25 µL diluted mitochondria were used to measure GSG and total GSH following the procedures for suspension cells.

4.2.22 Autophagy detection staining

Primary hepatocytes from chow diet fed control and LKO mice were isolated and cultured overnight with or without 200 µM cyclodextrin-cholesterol in the maintenance media. The primary hepatocytes were seeded on both collagen-coated coverslips and 96-well plate, for imaging and plate reading, respectively. Autophagic vacuoles and autophagic flux were analyzed using autophagy assay kit (Abcam, Cat# 139484) following manufacturer's instructions. The cells on coverslips were imaged by confocal microscope and the fluorescent signal was measured by plate reader in well-scan mode.

4.2.23 Quantification and statistical analysis

All data are presented as mean ± SEM. Most of our data follow normal distribution, and comparisons were performed using the unpaired 2-tailed Student's t-test, with significance defined as a p value < 0.05. For data that do not follow normal distribution, non-parametric t-test was used to calculate the p value. GraphPad Prism 9.0 (San Diego, CA) was used for all statistical analysis. Western blot data were quantified using ImageJ.

4.2.24 Data availability

RNA sequencing data have been deposited at Gene Expression Omnibus (accession numbers GSE218075). Original data or any additional information required to reanalyze the data reported in this paper will be available from the lead contact upon request.

4.3 RESULTS

4.3.1 Hepatic *LPCAT3* expression is inversely correlated with NAFLD progression

To investigate whether *LPCAT3* is dysregulated during the progression of NAFLD, we measured its mRNA levels in liver biopsies from a cohort of normal, NAFLD with simple steatosis and NASH with fibrosis patients. Realtime RT-PCR results showed that *LPCAT3* is gradually downregulated in steatosis and NASH livers (Figure 4.1A). Next, we analyzed *LPCAT3* expression in another published transcriptome data with histological gradings of liver biopsies obtained from 213 NAFLD patients (GSE193084)[329]. Association analysis showed that *LPCAT3* expression was inversely correlated with NAS and fibrosis stage (Figure 4.1B and 4.1C). These results demonstrate that downregulation of *LPCAT3* expression likely contributes to the progression of NAFLD and NASH.

4.3.2 Mice lack of Lpcat3 in the liver develop spontaneous NASH and HCC with age

Next, we investigated if dysregulation of *LPCAT3* and PC composition are the driver or the consequence of NAFLD progression. We examined the livers of age matched 16~24 months old LKO mice on regular chow diet. The liver weight to body weight ratio was significantly increased in LKO mice (Figure 4.2A). Hepatic triglyceride (TG), non-esterified fatty acid (NEFA), total and free cholesterol were significantly higher in LKO mice (Figure 4.2B). Serum cholesterol and TG, but not NEFA, were decreased or trended towards a decrease in LKO mice (Figure 4.3A-4.3D). More strikingly, aged LKO mice exhibited histopathological manifestations of NASH in the absence of any dietary or chemical challenges. Histological analysis revealed moderate lipid accumulation in hepatocytes, and massive central and intralobular infiltration of immune cells (Figure 4.2C). Signs of hepatocellular injury were also present in LKO livers as demonstrated by the presence of ballooning hepatocytes and Mallory-Denk bodies. Sirius red staining revealed increased fibrosis in LKO livers compared to controls (Figure 4.2C and 4.2D). Accordingly, LKO livers had a much higher NAS (Figure 4.2E). Strikingly, half (6 out of 12) of LKO mice developed spontaneous HCC, which was confirmed by positive staining of AFP (Figure 4.2F). These data strongly indicate that membrane PC composition is critical for liver homeostasis and that changes in PC composition caused by *Lpcat3* deficiency *per se* are sufficient to drive the pathogenesis of NASH and HCC.

4.3.3 Loss of Lpcat3 promotes diet-induced NASH and HCC

Next, we tested if loss of *Lpcat3* promotes diet-induced NASH development. We fed control and LKO mice a NASH-inducing diet (NASH diet), which has been shown to induce NASH in mouse liver that closely recapitulates human NASH[338]. LKO mice exhibited significantly higher liver weight to body weight ratio after 12 and 30 weeks of diet feeding (Figure 4.5A). Lipid measurement showed higher hepatic TG and cholesterol levels in LKO livers (Figure 4.5B), while hepatic NEFA and serum lipids were largely unchanged after 12 weeks of diet feeding (Figure 4.5B-4.5C). Histological analysis demonstrated that LKO mice developed more pronounced steatosis, lobular inflammation, and fibrosis compared to control mice as shown by H&E and Sirius red staining as early as 12 weeks on NASH diet (Figure 4.4A-4.4B). Increased fibrosis was also confirmed by higher hydroxyproline levels in LKO livers (Figure 4.5D). Immunostaining of α-smooth muscle actin (α-SMA), a marker of activated hepatic stellate cells (HSCs) that is critical in liver fibrogenesis, manifested more activated HSCs in LKO livers (Figure 4.4A). Consequently, LKO mice showed much higher NAS after 12 weeks of diet feeding and trended towards an increase in 30-week fed livers (Figure 4.4C). In agreement with histology data, mRNA level of tumor necrosis factor-alpha (*Tnfα*) and collagen synthesis genes were significantly upregulated in the liver of LKO mice (Figure 4.4D-4.4E). Apoptotic cell death was significantly increased in LKO mice under NASH diet (Figure 4.5E). Moreover, serum aspartate transaminase (AST) and alanine transaminase (ALT) activities were also higher in LKO mice, indicating increased liver damages (Figure 4.5F). As a result of more severe NASH, all LKO mice (7 out of 7) developed AFP positive HCC after 50 weeks of diet feeding (Figure 4.4F). In contrast, only one third (2 out of 6) of control mice had tumors. Moreover, LKO mice developed more tumors compared to control mice (Figure 4.4F).

4.3.4 Lpcat3 deficiency increases reactive oxygen species (ROS) production

Next, we sought to explore the mechanisms by which loss of *Lpcat3* promotes NASH progression. Previous studies have shown that acute knockdown of *Lpcat3* in the liver induces ER stress[233], which is known to promote cell death and NASH progression[339]. Realtime RT-PCR analysis showed that most of the ER stress genes, except *Atf3*, were not altered in LKO livers after 12 weeks of diet feeding (Figure 4.7A), suggesting that ER stress is unlikely a major contributor to NASH development in LKO mice. Next, we profiled gene expression in the livers of control and LKO mice fed NASH diet for 12 weeks by RNA sequencing analysis and found ~500 upregulated genes and ~200 downregulated genes in LKO livers compared to controls (Figure 4.7B). Among the upregulated genes, Gene Ontology (GO) analysis revealed strong enrichment for genes involved in inflammatory response and proinflammatory cytokines production in LKO livers (Figure 4.6A), which is consistent with enhanced inflammation in histology. Furthermore, ROS production was one of the upregulated GO terms in LKO livers. Interestingly, electron and proton transport were among the top downregulated GO terms in LKO livers (Figure 4.6B). Mitochondrial electron transport chain is a major site of ROS production[340]. Indeed, hepatic ROS levels were ~1.5-fold higher in LKO mice compared to controls (Figure 4.6C). Consistently, the levels of dehydroascorbic acid, a marker of oxidative stress[341], was significantly increased in LKO livers (Figure 4.7C). MitoSox staining of primary hepatocytes isolated from 9-week NASH diet fed control and LKO mice further confirmed elevated ROS in the absence of *Lpcat3* (Figure 4.7D and 4.6D). Similar results were also observed in *Lpcat3* acute knockdown Hepa cells (Figure 4.7E-4.7F). ROS is known to oxidize vital cellular components such as DNA, lipids and proteins, thereby inducing cell death and liver damage[342]. The levels of 4-Hydroxynonenal (4-HNE), a product of lipid peroxidation by ROS, was dramatically increased in LKO livers (Figure 4.6E). Previous studies have shown that oxidative stress and lipid peroxidation activate c-Jun-N-terminal kinase (JNK) pathway in NASH livers[343]. Western blot analysis showed that JNK pathway was dramatically increased in LKO livers compared to controls, whereas two other MAPK pathways, ERK and p38 pathway, were not significantly altered (Figure 4.6F). Hepatocytes have developed a range of antioxidant strategies to cope with oxidative stress, including glutathione (GSH) and catalase in the peroxisome[344]. Measurement of GSH and GSH/GSSG ratio showed a trend towards an increase in LKO livers likely due to compensatory responses (Figure 4.7G-4.7H). In contrast, catalase levels were slightly reduced, albeit an increase in peroxisomal marker PMP70 (Figure 4.7I). Nevertheless, these data demonstrated that loss of *Lpcat3* enhances ROS production, which likely contributes to the pathogenesis of NASH.

4.3.5 Lpcat3 deficiency impairs mitochondrial homeostasis

Mitochondria dysfunction plays a key role in the pathogenesis of NASH[345]. Further analysis of RNA sequencing data showed that a majority of mitochondria encoded genes were significantly downregulated in LKO livers (Figure 4.9A). Strikingly, mitochondrial DNA (mtDNA) content was dramatically reduced in the livers of 3-month-old chow diet fed and NASH diet fed LKO mice (Figure 4.8A). Furthermore, mtDNA content was gradually decreased with the progression of NAFLD in both control and LKO mice, suggesting that decrease in mitochondria content may contribute to disease progression. Consistent with reduced mitochondrial content in LKO livers, western blot analysis showed less mitochondrial respiratory complexes I, II and IV in whole liver lysate (Figure 4.8B). Similarly, COX IV and TOM20, two mitochondrial proteins were also reduced in LKO livers (Figure 4.9B). In contrast, mitochondrial complexes I and V were increased in isolated mitochondria from LKO livers compared to controls (Figure 4.8C), probably as a compensation for the reduced mitochondrial content. The purity of isolated mitochondria was confirmed by immunoblotting with cellular compartment markers (Figure 4.9C). The changes in mitochondrial complexes appeared to be a secondary effect of *Lpcat3* deficiency as their levels were not altered in *Lpcat3* acute knockdown cells (Figure 4.9D). Electron microscopy (EM) analysis revealed altered mitochondrial morphology as demonstrated by more fragmented mitochondria in both chow diet and NASH diet fed LKO livers (Figure 4.8D). Quantification of mitochondrial morphology showed more circular mitochondria in LKO hepatocytes. Similar morphology change was also observed in *Lpcat3* knockdown cells stained with mitotracker (Figure 4.9E). Interestingly, we also observed some mitochondria undergoing fission and autophagosome like structures in the livers of LKO mice fed NASH diet (Figure 4.8D), suggesting that loss of *Lpcat3* may affect mitochondrial remodeling.

4.3.6 Lpcat3 deficiency alters mitochondrial dynamics and elevates stress-induced autophagy

We next investigated the mechanisms of decreased mitochondrial content and increased mitochondrial fragmentation in mice lacking *Lpcat3*. Mitochondrial homeostasis is regulated by a balance of mitochondrial biogenesis and degradation, and mitochondrial fission/fusion[346]. There was no difference in the expression of Pgc1a and Sirt1, two genes involved in mitochondrial biogenesis, in NASH diet fed mouse livers between genotypes (Figure 4.11A), suggesting that reduced mitochondrial content is unlikely caused by altered mitochondrial biogenesis. Consistent with some mitochondria undergoing fission in EM analysis, we observed increased expression of DRP1 and reduced expression of OPA1 (Figure 4.10A), two proteins that play critical roles in fission and fusion, respectively, indicating that loss of Lpcat3 likely promotes mitochondrial fission but suppresses fusion, thereby resulting in more fragmented mitochondria.

Previous studies have demonstrated that ROS-mediated damages to the organelles induce autophagy as a responsive mechanism to clear damaged organelles[347]. It has been shown that 4-HNE activated JNK pathway mediates the induction of autophagy response[348]. Considering that ROS/4-HNE production and JNK activation were enhanced in LKO livers, we hypothesized that loss of Lpcat3 augments autophagy in response to increased oxidative stress and results in reduced mitochondria content. Indeed, we observed the presence of autophagosome structures in EM analysis of LKO liver sections (Figure 4.8D). To further test our hypothesis, we examined autophagy pathways in NASH diet fed livers. Although there was no difference in early mitophagy markers, such as BNIP3, PINK1 or PARKIN levels in both isolated mitochondria and whole liver lysate between control and LKO mice (Figure 4.11B-4.11C), markers of macroautophagy required for mitochondrial turnover by the lysosome, including ATG5-ATG12 conjugates and LC3 processing, were increased in LKO livers compared to controls (Figure 4.10B). It is well documented that lipid overload in hepatocytes, especially FFA and cholesterol, leads to organelle damage, inflammation, and fibrosis[349,350]. We next tested if Lpcat3 deficiency also potentiates autophagy response in the presence of lipid accumulation in primary hepatocytes. Consistent with in vivo results, FFA treatment increased LC3 processing in LKO hepatocytes (Figure 4.11D). Interestingly, cholesterol treatment induced more pronounced autophagy response in LKO hepatocytes, including upregulation of ATG7, ATG5-ATG12 conjugate and ATG16L1 (Figure 4.11E). Furthermore, autophagy staining revealed more autophagic vacuoles in LKO hepatocytes compared to controls upon starvation or cholesterol treatment (Figure 4.10C). Thus, ROS overproduction and lipid accumulation caused by Lpcat3 deficiency likely work together to enhance autophagy in response to stress-induced damage in LKO livers.

4.3.7 Loss of Lpcat3 increases inner mitochondrial membrane (IMM) phospholipid saturation and mitochondrial oxidation

Given that LPCAT3 functions through remodeling membrane PL, we hypothesized that *Lpcat3* deficiency may affect mitochondrial PL composition, thereby altering mitochondrial homeostasis. We focused on IMM because most of mitochondrial electron transport and oxidative phosphorylation occur in IMM. IMM was purified from mitochondria by osmotic swelling and ultracentrifugation. The enrichment of IMM was confirmed by western blot analysis of COX IV, an IMM localized protein (Figure 4.13A). In agreement with LPCAT3 enzymatic activity, PL profiling showed dramatic decrease in polyunsaturated especially 18:2- and 20:4-containing PCs (Figure 4.12A, 4.13B and Table 4.3) and PEs (Figure 4.13B and 4.13C) in the IMM of both chow and NASH diet fed LKO mice without affecting total PC or PE levels. Interestingly, the FA composition of Cardiolipin (CL), another class of essential mitochondria-specific PLs, was also drastically altered in LKO livers as demonstrated by significant reduction in 18:2- and 20:4-containing CLs (Figure 4.12B, 4.13B and Table 4.4), whereas total CL levels were not changed. Mitochondrial membrane PL composition has been shown to be critical in modulating mitochondria functions, including oxidative respiration and ROS production[351]. Next, we evaluated the effect of *Lpcat3* deficiency on mitochondria function by seahorse analysis. Consistent with increased mitochondrial complexes, both basal and maximal oxygen consumption rate (OCR) were higher in mitochondria isolated from NASH diet fed LKO mice (Figure 4.12C-4.12D), which was also confirmed in *Lpcat3* acute knockdown cells (Figure 4.13D). Moreover, LKO mitochondria showed increased fatty acid oxidation compared to controls (Figure 4.12E), which is known to be a major source of ROS production[352]. Indeed, LKO hepatocytes produced ~3.5-fold and ~2.2-fold more H_2O_2 under basal and palmitate-treated conditions, respectively (Figure 4.12F). Thus, these data suggest that increasing IMM saturation by *Lpcat3* deficiency may enhance mitochondrial oxidative phosphorylation, which contributes to ROS overproduction and leads to cell damage, inflammation, and NASH progression.

4.3.8 Hepatic Lpcat3 deficiency dramatically elevates serum bile acid levels by promoting liver bile clearance.

The dysregulation of bile acid (BA) metabolism has been recognized in NASN patients and various mouse models[251,353]. Research in human patients revealed that serum BA levels are significantly increased in NAFLD patients and correlated with disease severity[251]. However, whether this BA dysregulation is the cause or the consequence of NASH is still not clear. We evaluated the gene expression profile in livers of LKO and control mice after 12-weeks NASH diet feeding. Surprisingly, key genes involved in BA synthesis are significantly suppressed, with promoted expression of BA basolateral export genes and reduced BA import genes (Figure 4.16 A), indicating potentially activated FXR signaling in LKO livers that exhibited a BA clearance trend (Figure 4.16 B). Consistent with these results, the serum BA levels are increased by around ten times in LKO mice, with dramatically elevated primary BA species especially taurine-conjugated BAs (Figure 4.16 C-4.16 D). However, we did not observe significant reduction in total hepatic BA levels between LKO and control mice (Figure 4.16 E-4.16 F), suggesting that increased BA synthesis due to excessive substrate, instead of aberrant FXR activation, might be the initiation of this BA clearance in LKO livers. Previous studies have shown similar hepatic BA clearance marks without significant changes in hepatic BA levels in methionine-choline deficient (MCD) diet-fed mice, a mouse model that induce NASH by blocking VLDL secretion[252,354]. Therefore, these data suggested a possible mechanism by which serum BA is elevated in NASH patients.

4.3.9 Overexpression of Lpcat3 in the liver ameliorates diet-induced NASH progression

Our results demonstrated that loss of *Lpcat3 per se* is sufficient to promote the initiation and progression of NASH in mice and that downregulation of *LPCAT3* is likely involved in the pathogenesis of NASH in at least some human patients. We next examined if overexpression of *Lpcat3* could attenuate steatosis to NASH progression. To test this, we fed C57BL/6 mice with NASH diet for 7 weeks to initiate steatosis, and then i.v. injected AAV encoding eGFP control or *Lpcat3* driven by a liver specific TBG promoter, followed by another 9 weeks of diet feeding (Figure 4.15A). There was no body weight difference between control and *Lpcat3* overexpression mice during the diet feeding (Figure 4.15B). Liver weight to body weight ratio was decreased by more than 20% in *Lpcat3* overexpressing mice compared to eGFP injected control mice (Figure 4.15C). Lipids quantification showed slight decrease in hepatic TG and free cholesterol levels, but not total cholesterol or NEFA levels in *Lpcat3* overexpressing mice (Figure 4.15D). Serum TG and cholesterol levels were also trended towards a decrease upon *Lpcat3* overexpression (Figure

4.15E). Histology analysis revealed less steatosis, inflammation, fibrosis and activated HSCs in *Lpcat3* overexpressing livers (Figure 4.14A-4.14B). Accordingly, *Lpcat3* overexpression lowered NAS compared to eGFP controls (Figure 4.14C). Serum ALT and AST activities were also reduced by *Lpcat3* overexpression (Figure 4.15F), suggesting less liver damage. RNA sequencing analysis revealed that metabolic processes were top GO terms among upregulated genes (Figure 4.14D), and the top processes among downregulated genes were all related to immune response or immune cell activation (Figure 4.14E), further corroborating that *Lpcat3* overexpression mitigates inflammation during NASH progression. Consistently, realtime RT-PCR analysis showed significant decrease in the expression of *Tnfα, Ccl3* and collagen synthesis genes in *Lpcat3* overexpressing livers (Figure 4.14F). Western blot analysis demonstrated reduced 4-HNE levels in *Lpcat3* overexpression livers (Figure 4.15G), indicating that *Lpcat3* overexpression attenuates inflammation and fibrosis during NASH progression at least partially through alleviating oxidative stress.

4.4 DISCUSSION

The prevalence of NASH, a progressive inflammatory form of NAFLD, is dramatically increasing and has emerged as a significant contributor to the health burden of chronic liver diseases[355]. Approximately 25% of NASH patients will progress to liver cirrhosis and in some cases to HCC[356]. Despite much effort, the molecular mechanisms that underlie the progression of NASH are not well understood. Our data demonstrated that mice lacking *Lpcat3* in the liver develop spontaneous histopathological manifestations of NASH, suggesting that changes in membrane PL composition *per se* is sufficient to drive the pathogenesis of NASH. More importantly, *LPCAT3* expression is progressively decreased in human NAFLD and NASH livers, and is inversely correlated with NAS and fibrosis stage, suggesting that suppression of *LPCAT3* likely contributes to the development of NAFLD/NASH in humans. These studies highlight a novel mechanism by which membrane PL remodeling modulates the pathogenesis of NASH.

Our studies provide insight into the potential mechanisms how genetic variants contribute to the pathogenesis of NASH. The loss-of-function variant (I148M) in *PNPLA3* gene is associated with increased risk of NASH[357]. Interestingly, the levels of polyunsaturated PCs are reduced in homozygous I148M livers[152]. Similarly, carriers of *TM6SF2* E167K variant have decreased expression of TM6SF2 and increased risk of NAFLD and NASH[358]. Further studies found that hepatic synthesis of PCs from PUFAs is impaired in E167K livers, resulting in deficiency in polyunsaturated PCs[2]. In contrast, a missense variant (A165T) in *MARC1* gene has been shown to be protective against liver cirrhosis[359], and is associated with decreased severity of NASH [3]. Lipidomics analysis revealed that carriers of A165T variant have higher hepatic polyunsaturated PCs compared to non-carriers[3]. Taken together, these studies demonstrate that hepatic polyunsaturated PC content is inversely correlated with the risk or severity of NASH in humans. Our data provide direct *in vivo* evidence to support that changes in PC composition contribute to NASH pathogenesis. It would be of interest to examine if *LPCAT3* expression is altered in the livers of patients carrying these variants.

Interestingly, metabolism of other PLs, such as phosphatidylinositol (PI), have also been associated with NASH in human and mouse models. GWAS studies have identified variants near membrane-bound O-acyltransferase domain containing 7 (*MBOAT7*) locus to be associated with fibrosis in NASH[360]. *MBOAT7* encodes a lysophosphatidylinositol (LPI) acyltransferase enzyme that preferentially catalyzes synthesis of arachidonoyl-containing PI species. Several studies have demonstrated that *Mboat7* deficiency promotes steatosis and fibrosis[361,362]. It has been shown that *Mboat7* inhibition enhances lipogenesis and promotes inflammation and fibrosis likely due to the accumulation of its substrate LPI or metabolites derived from arachidonic acid. In contrast, there was no difference in LPC or arachidonic acid metabolite prostaglandin E2 (PGE2) between LKO and control mice (data not shown). Thus, the mechanism by which *Lpcat3* deficiency promotes NASH progression is likely different from that of *Mboat7* suppression.

Accumulating evidence suggests that mitochondria play a key role in the pathophysiology of NASH[363]. Strikingly, we found that mtDNA content was significantly reduced in the livers of both chow diet and NASH diet fed LKO mice. Furthermore, mtDNA content is gradually decreased with the progression of NAFLD/NASH in both control and LKO livers, suggesting that decrease in mitochondria content likely contributes to disease progression. It has been shown that mitochondrial dysfunction induces the overproduction of ROS, which oxidizes vital cellular components such as DNA, lipids and proteins, thereby inducing cell death and liver damage, triggering inflammatory responses and fibrosis in NASH livers[364]. Indeed, we observed enhanced ROS levels and byproducts of oxidative stress in LKO livers. Interestingly, both basal and maximal OCR are increased in purified mitochondria from LKO livers. Therefore, lipid accumulation and augmented mitochondrial fatty acid β-oxidation likely lead to ROS overproduction in LKO livers, which in turn causes enhanced mitochondrial damage and autophagy, resulting in less mtDNA content. In addition, loss of *Lpcat3* also leads to mitochondrial fragmentation, likely caused by increased mitochondrial fission and decreased fusion. Mitochondrial fission and fusion are important mechanisms to maintain functional mitochondria in response to stresses[365]. Fusion helps alleviate stress by mixing the contents of partially damaged mitochondria, while fission removes damaged mitochondria and promotes apoptosis in the presence of high levels of cellular stress. Thus, altered mitochondrial dynamics in LKO livers could be a compensatory response induced by excessive stress and damage.

In agreement with LPCAT3 enzymatic activity, there is dramatic decrease in polyunsaturated PCs in the IMM, where electron transport and oxidative phosphorylation occur. CL is another class of mitochondria-specific PLs that are composed of two phosphatidic acid (PA) groups linked by a glycerol. Interestingly, the composition of PUFA in CL is also dramatically decreased in LKO livers. Changes in CL fatty acyl composition have been implicated in etiology of mitochondrial dysfunction and its associated pathophysiological conditions that are characterized by increased levels of oxidative stress, including NAFLD/NASH, diabetes, neurodegeneration, and ageing [351]. Furthermore, it has been shown that increased ROS production requires fragmentation of mitochondria [366]. We observed more fragmented mitochondria in LKO livers. The altered mitochondrial morphology in LKO livers is likely a direct consequence of decreased PL unsaturation as acute knockdown of *Lpcat3* in Hepa cells also results in less mitochondrial network, but we cannot rule out the contribution of enhanced oxidative stress in LKO livers. Nevertheless, these data indicate that LPCAT3 and PL remodeling are critical in maintaining mitochondria homeostasis. Although the mechanism of *Lpcat3* deficiency in NASH development is likely to be multifactorial, our data showed that altered mitochondrial dynamics and function play important roles in NASH progression in the absence of *Lpcat3*.

Currently, there is no FDA approved drugs or effective therapeutics for NASH other than lifestyle intervention, which is only effective at early stage of NASH. The observation that overexpression of *Lpcat3* in the liver reduces hepatic triglyceride levels and attenuates inflammation and fibrosis is inspiring. Although further studies are needed to understand how *Lpcat3* overexpression affects lipid metabolism and the progression of NASH, these studies provided a proof of concept that manipulating *LPCAT3* expression or activity could represent a novel therapeutic strategy for NASH.

4.5 TABLES AND FIGURES

Table 4.1 Antibodies used in this study

Antibody	Source	Catalog #
Rabbit monoclonal anti-α-Smooth Muscle Actin	Cell Signaling Technology	19245S
Rabbit polyclonal anti-AFP	Proteintech	14550-1-AP
Rabbit monoclonal anti-TOM20	Cell Signaling Technology	42406
Rabbit monoclonal anti-OPA1	Cell Signaling Technology	80471
Rabbit monoclonal anti-DRP1	Cell Signaling Technology	8570
Mouse monoclonal anti-GAPDH	Millipore	MAB374
Rabbit monoclonal anti-MFF	Cell Signaling Technology	84580
Rabbit monoclonal anti-Phospho-DRP1 (S637)	Cell Signaling Technology	6319
Rabbit monoclonal anti-Phospho-DRP1 (S616)	Cell Signaling Technology	4494
Rabbit monoclonal anti-phospho-ERK	Cell Signaling Technology	4370
Rabbit monoclonal anti-ERK	Cell Signaling Technology	4695
Rabbit monoclonal anti-ATG12	Cell Signaling Technology	4180
Rabbit polyclonal anti-ATG3	Cell Signaling Technology	3415
Rabbit monoclonal anti-ATG7	Cell Signaling Technology	8558
Mouse monoclonal anti-PMP70	Sigma-Aldrich	SAB4200181
Rabbit monoclonal anti-Catalase	Cell Signaling Technology	14097
Rabbit polyclonal anti-CoxIV	Cell Signaling Technology	4844
Mouse monoclonal anti-Calnexin	Santa Cruz Biotechnology	sc-23954
Mouse monoclonal anti-Pan-cadherin	Santa Cruz Biotechnology	sc-59876
Rabbit monoclonal anti-Phospho-p38 MAPK (Thr180/Tyr182)	Cell Signaling Technology	4511
Rabbit monoclonal anti-p38 MAPK	Cell Signaling Technology	8690
Rabbit monoclonal anti-Phospho-SAPK/JNK (Thr183/Tyr185)	Cell Signaling Technology	4668
Rabbit polyclonal anti-SAPK/JNK	Cell Signaling Technology	9252
Rabbit polyclonal anti-BNIP3	Cell Signaling Technology	3769
Rabbit polyclonal anti-PINK1	Novus	BC100-494
Mouse monoclonal anti-PARKIN	Santa Cruz Biotechnology	sc-32282
Total OXPHOS Rodent WB Antibody Cocktail	Abcam	ab110413
Rabbit monoclonal anti-ATG16L1	Cell Signaling Technology	8089
Rabbit monoclonal anti-LC3I/II	Cell Signaling Technology	12741
Rabbit monoclonal anti-ATG5	Cell Signaling Technology	12994
Mouse monoclonal anti-4-Hydroxynonenal (4-HNE)	R&D Systems	MAB3249
IgG (H+L) Goat anti-Rabbit, HRP	Invitrogen	656120
Normal goat serum	Jackson ImmunoResearch Inc.	005-000-121
EnVision+ System-HRP Labelled Polymer Anti-Rabbit	Agilent	K4003
Goat anti-Mouse IgG(H+L) Secondary Antibody, HRP	Invitrogen	31430

Table 4.2 Primer sequences used in this study

m36B4-F	AGATGCAGCAGATCCGCAT
m36B4-R	GTTCTTGCCCATCAGCACC
mLpcat3-F	GGCCTCTCAATTGCTTATTTCA
mLpcat3-R	AGCACGACACATAGCAAGGA
hLpcat3-F	CCACTCCCTGCTGTGTATTG
hLpcat3-R	AGAAGGTAGGCCATCTGGAA
mCol1a1-F	GTGGTGACAAGGGTGAGACA
mCol1a1-R	GAGAACCAGGAGAACCAGGA
mCol3a1-F	TACACCTGCTCCTGTGCTTC
mCol3a1-R	CATTCCTCCCACTCCAGACT
mTnfa-F	TGCCTATGTCTCAGCCTCTTC
mTnfa-R	GAGGCCATTTGGGAACTTCT
mTgfb-F	ACTGATACGCCTGAGTGGCT
mTgfb-R	CCCTGTATTCCGTCTCCTTG
mPgc1a-F	TATGGAGTGACATAGAGTGTGCT
mPgc1a-R	CCACTTCAATCCACCCAGAAAG
mSirt1-F	GCTGACGACTTCGACGACG
mSirt1-R	TCGGTCAACAGGAGGTTGTCT
mCcl3-F	TGC CCT TGC TGT TCT TC TCT
mCcl3-R	CAGGCATTCAGTTCCAGGTC
mIl1b-F	AGAAGCTGTGGCAGCTACCTG
mIl1b-R	GGAAAAGAAGGTGCTCATGTCC
mAtf3-F	GAGGATTTTGCTAACCTGACACC
mAtf3-R	TTGACGGTAACTGACTCCAGC
mAtf4-F	CCTTCGACCAGTCGGGTTTG
mAtf4-R	CTGTCCCGGAAAAGGCATCC
mBip-F	ACTTGGGGACCACCTATTCCT
mBip-R	ATCGCCAATCAGACGCTCC
mChop-F	CCACCACACCTGAAAGCAGAA
mChop-R	AGGTGAAAGGCAGGGACTCA
mXbp1s-F	GGTCTGCTGAGTCCGCAGCAGG
mXbp1s-R	AGGCTTGGTGTATACATGG
mXbp1t-F	TTGTCACCTCCCCAGAACATC
mXbp1t-R	TCCAGAATGCCCAAAAGGAT

Table 4.3 PC species identified in NASH diet fed IMM.

PC Species **Bold: significantly different**	m/z	Aliphatic Constituents **Bold = predominant**	Notes
32:2	774.5292	**Di16:1**	
32:1	776.5449	**16:0/16:1**	
32:0	778.5606	**Di16:0**	
p34:1	788.5847	**p-16:1/18:0**	
34:3	800.5448	**18:2/16:1**; 18:3/16:0	18:2/16:1 is 3 times as much as 18:2/16:1
34:2	802.5605	16:0/18:2; 16:1/18:1	16:1/18:1 is slightly more than 16:0/18:2
34:1	804.5762	**16:0/18:1**; 16:1/18:0	16:0/18:1 is 100 times more than 16:1/18:0
34:0	806.5919	**16:0/18:0**	
p36:1	816.616	p-18:1/18:0; **p-18:0/18:1**	p-18:0/18:1 is 10 times more than p-18:1/18:0
36:5	824.5447	**16:1/20:4**	
36:4	826.5604	**16:0/20:4**	
36:3	828.5761	**18:2/18:1;** 20:3/16:0; 20:2/16:1	18:2/18:1>20:3/16:1>>>20:2/16:1
36:2	830.5918	**Di18:1**; 18:0/18:2; 16:0/20:2	Di18:1>>18:0/18:2>>>16:0/20:2
36:1	832.6075	**18:1/18:0**; 16:0/20:1	18:1/18:0 is 100 times more than 16:0/20:1
36:0	834.5688	**Di18:0**	
38:6	850.5603	**16:0/22:6;** 18:2/20:4	16:0/22:6 >>> 18:2/20:4
38:5	852.576	**16:0/22:5**; 18:1/20:4	16:0/22:5 > 18:1/20:4
38:4	854.5917	**18:0/20:4**; 18:1/20:3	100x
38:3	856.6074	**18:0/20:3**; 18:2/20:1; 16:0/22:3	18:0/20:3 >> 18:2/20:1 >>> 16:0/22:3
40:8	874.5602	**18:2/22:6**	
40:7	876.5759	**18:1/22:6**	
40:6	878.5916	**18:0/22:6**	
40:5	880.6073	**18:0/22:5**; 20:1/20:4	18:0/22:5 >>> 20:1/20:4

Table 4.4 CL species identified in NASH diet fed IMM.

CL Species **Bold: significantly different**	m/z	Aliphatic Constituents **Bold = predominant**	Notes
68:6	1395.9333	14:0/tri18:2; **di16:1/di18:2**	di16:1/di18:2 is 10 times more than 14:0/tri18:2
68:5	1397.949		
68:4	1399.9647	di16:0/di18:2; **di16:1/di18:1**	
68:3	1401.9804	16:1/16:0/18:2/18:0; **di16:1/18:1/18:0;** **16:1/16:0/di18:1**	di16:1/18:1/18:0 and 16:1/16:0/di18:1 levels are similar, and much more than 16:1/16:0/18:2/18:0
68:2	1403.9961	**Di16:0/di18:1**	
70:7	1421.9489	16:1/tri18:2;	
70:6	1423.9646	16:0/tri18:2**;** **16:1/18:1/di18:2**	16:1/18:1/di18:2 is 2 times more than 16:0/tri18:2
70:5	1425.9803		
70:4	1427.996	**16:1/tri18:1;** 16:0/18:0/di18:2;	16:1/tri18:1 is 3 times more than 16:0/18:0/di18:2
70:3	1430.0117	**16:1/di18:1/18:0;** **16:0/tri18:1;** 16:0/18:0/18:1/18:2	16:1/di18:1/18:0 and 16:0/tri18:1 levels are similar
72:9	1445.9448		
72:8	1447.9645	Di16:0/di20:4**;** **tetra18:2;**	
72:7	1449.9802	**16:0/18:1/18:2/20:4;** 16:1/18:1/18:2/20:3	
72:6	1451.9959		
72:5	1454.0116		
72:4	1456.0273	**Tetra18:1**; di18:2/di18:0; di18:1/18:2/18:0	
72:3	1458.043	**Tri18:1/18:0**	
74:11	1469.9487		
74:10	1471.9644	16:0/18:2/di20:4; **16:1/18:1/di20:4;** 16:1/18:2/20:4/20:3	
74:9	1473.9801		
74:8	1475.9958	**16:0/18:0/di20:4;** 16:0/18:1/20:4/20:3 16:0/18:2/20:0/22:6	
74:7	1478.0115		
74:6	1480.0272		

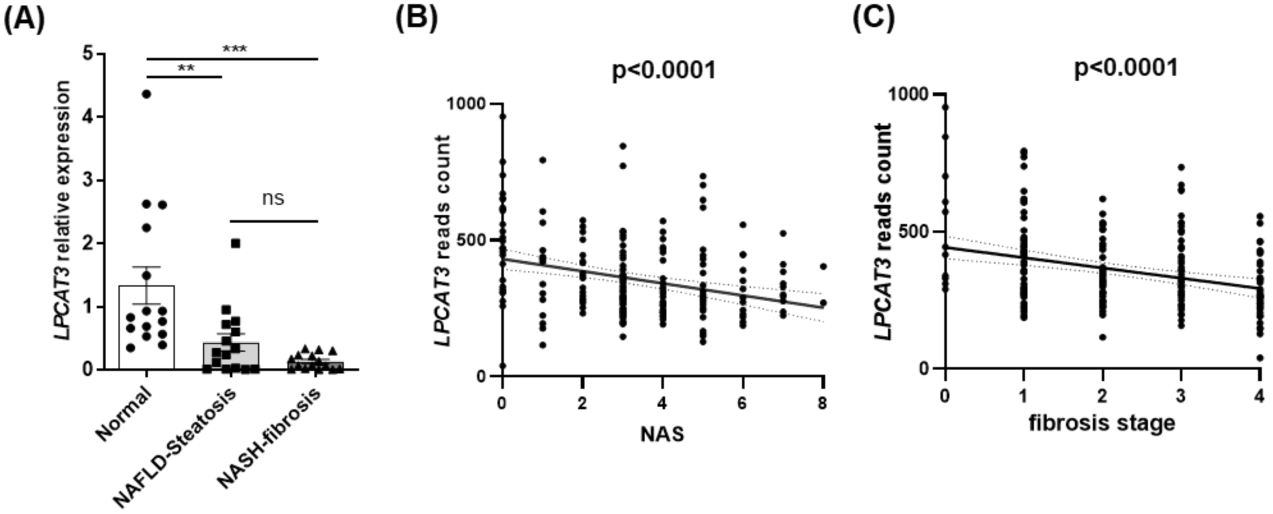

Figure 4.1. LPCAT3 expression is reduced in NASH patients and liver-specific deletion of Lpcat3 leads to NASH and HCC with age.

(A) Hepatic expression of LPCAT3 in human NAFLD/NASH patients. (B-C) Correlation between hepatic LPCAT3 expression and NAFLD Activity Score (NAS) (B) and fibrosis stage (C) in human NASH patients. 95% confidence band of the best fit line was shown by dashed curve.

Data in (A) are presented as means ± SEM. Statistical analysis was performed with one-way ANOVA (A) and linear regression (B-C). $^{**}p < 0.01$, $^{***}p < 0.001$.

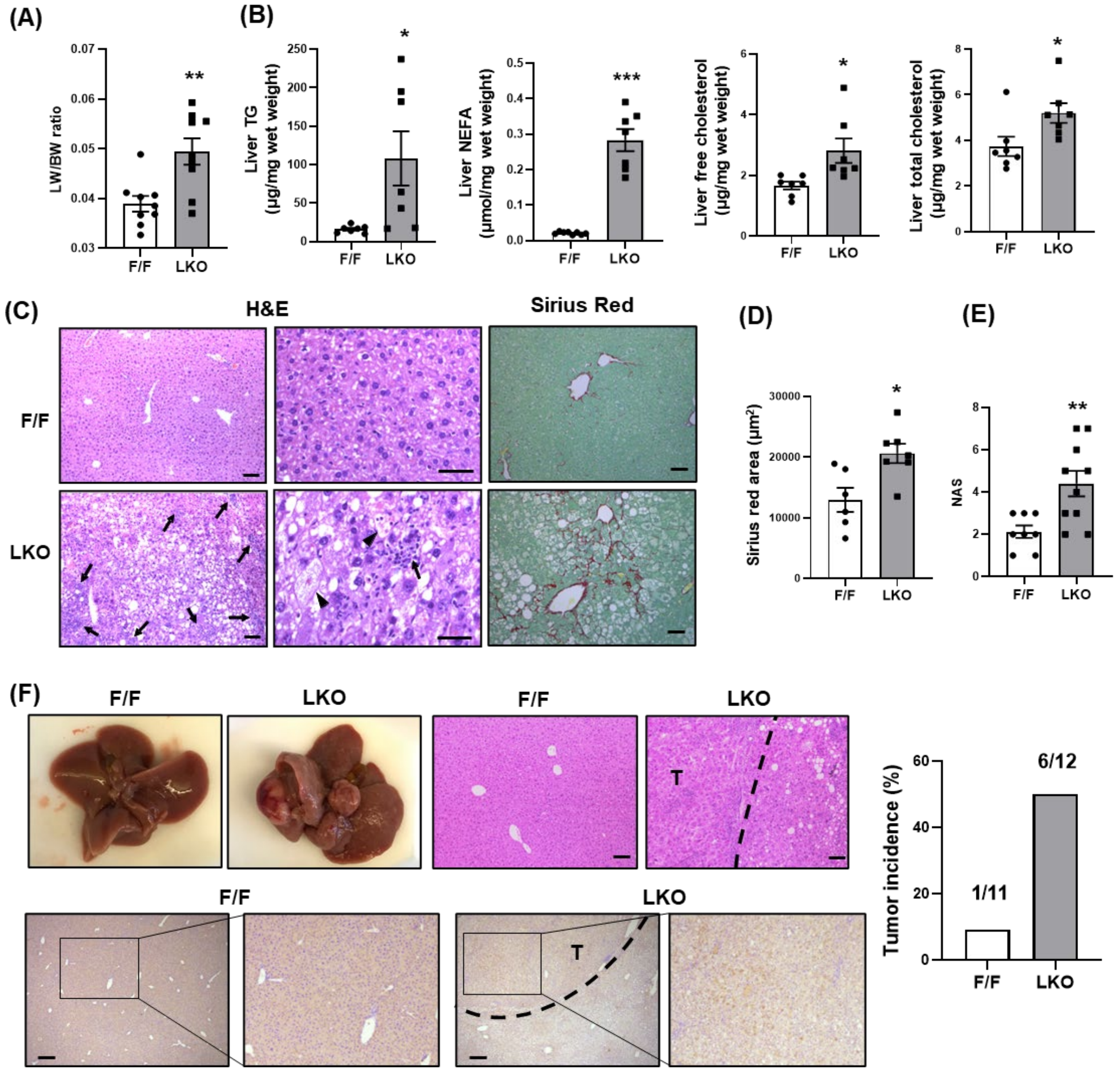

Figure 4.2. Lpcat3 LKO mice develop spontaneous NASH and HCC with age.

(A) Liver weight (LW) to body weight (BW) ratio of 16-24 months old control Lpcat3fl/fl (F/F) and Lpcat3fl/fl Albumin-Cre (LKO) mice on chow diet. (B) Hepatic triglyceride (TG), non-esterified fatty acid (NEFA), free and total cholesterol levels in 16-24 months old F/F and LKO mice on chow diet. (C) Hematoxylin and eosin (H&E) and Sirius Red staining of liver sections from 16-24 months old F/F and LKO mice on chow diet (scale bar, 100 µm). Arrows denote immune cell infiltration and arrow heads show ballooning hepatocytes. (D-E) Quantification of Sirius Red area (D) and NAS (E) for 16-24 months old F/F and LKO mice on chow diet. (F) Liver images, H&E, AFP IHC staining and tumor incidence of 16-24 months old F/F and LKO mice on chow diet (T: tumor. scale bar, 100 µm).

Data are presented as means ± SEM. Statistical analysis was performed with student's t test. $*p < 0.05$, $**p < 0.01$, $***p < 0.001$.

(Figure 4.2 Cont.)

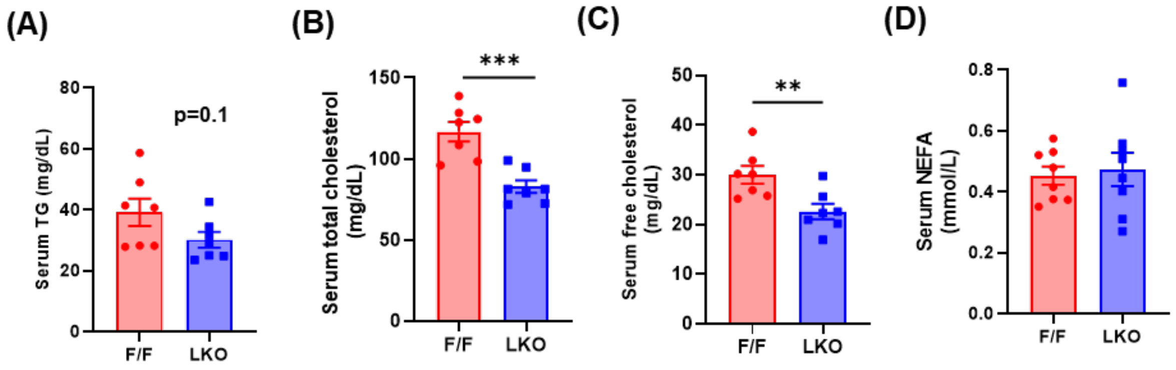

Figure 4.3. LKO mice develop spontaneous NASH and HCC with age.

(A-D) Serum triglyceride (TG) (A), total cholesterol (B), free cholesterol (C) and non-esterified fatty acid (NEFA) (D) levels of 16-24 months old F/F and LKO mice on chow diet.

Data are presented as mean ± SEM. Statistical analysis was performed with student's t test. $^{*}p < 0.05$, $^{**}p < 0.01$, $^{***}p < 0.001$.

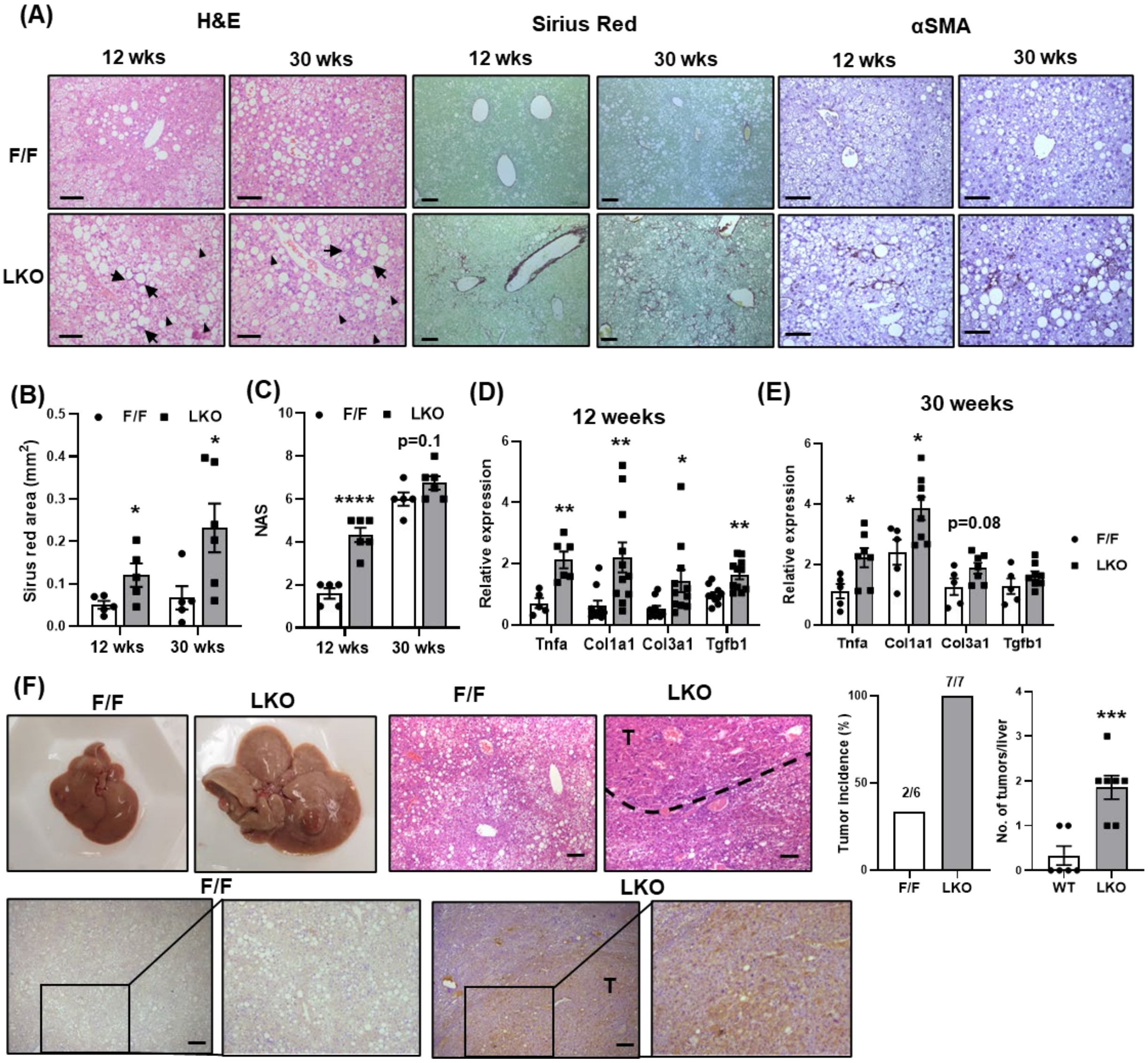

Figure 4.4. Loss of Lpcat3 in the liver promotes diet-induced NASH and HCC.

(A) H&E, Sirius Red and immunohistochemistry of α-smooth muscle actin (α-SMA) of livers from F/F and LKO mice fed NASH diet for 12 and 30 weeks. Arrows denote immune cell infiltration and arrow heads show ballooning hepatocytes (scale bar, 100 μm). (B-C) Quantification of liver Sirius Red area (B) and NAS (C) of F/F and LKO mice fed NASH diet for 12 and 30 weeks. (D-E) Hepatic mRNA levels of Tnfα and genes involved in fibrosis in F/F and LKO mice fed NASH diet for 12 (D) and 30 weeks (E). (F) Liver images, H&E, AFP staining, tumor incidence and number of tumors per liver of F/F and LKO mice fed NASH diet for 54 weeks (T, tumor. scale bar, 100 μm).

Data are presented as means ± SEM. Statistical analysis was performed with student's t test or multiple t test. $*p < 0.05$, $**p < 0.01$, $***p < 0.001$, $****p < 0.0001$.

(Figure 4.4 Cont.)

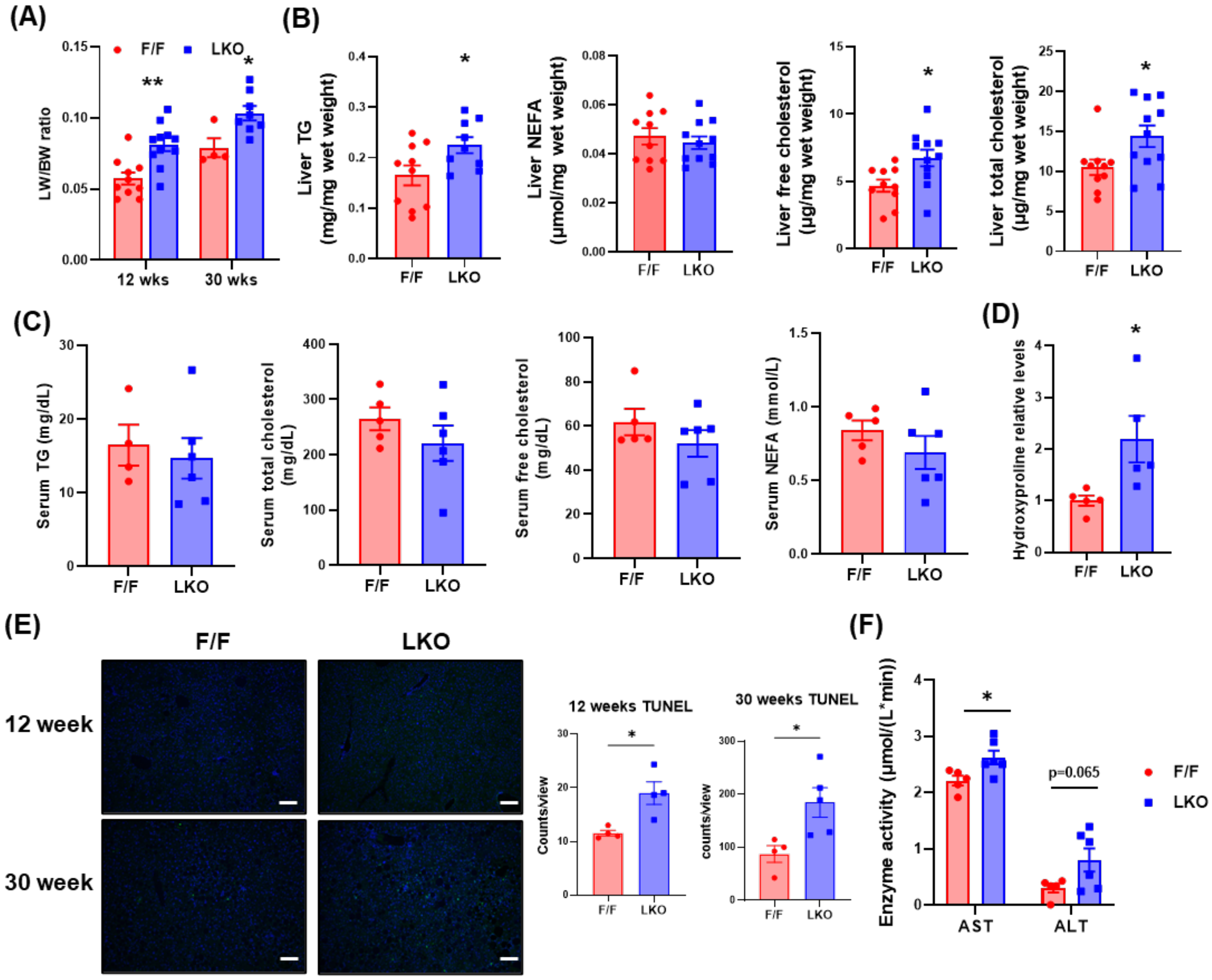

Figure 4.5. Loss of Lpcat3 in the liver promotes diet-induced NASH and HCC.

(A) Liver weight (LW) to body weight (BW) ratio of F/F and LKO mice fed NASH diet for 12 and 30 weeks. (B) Hepatic TG, NEFA, free and total cholesterol levels in F/F and LKO mice fed NASH diet for 12 weeks. (C) Serum TG, total cholesterol, free cholesterol and NEFA levels of F/F and LKO mice fed NASH diet for 12 weeks. (D) Relative hydroxyproline level in livers of F/F and LKO mice fed NASH diet for 12 weeks. (E) TUNEL staining and quantification in livers of F/F and LKO mice fed NASH diet for 12 and 30 weeks (scale bar, 100 μm). (F) Serum aspartate aminotransferase (AST) and alanine aminotransferase (ALT) activity in F/F and LKO mice fed NASH diet for 12 weeks.

Data are presented as mean ± SEM. Statistical analysis was performed with student's t test. *$p < 0.05$.

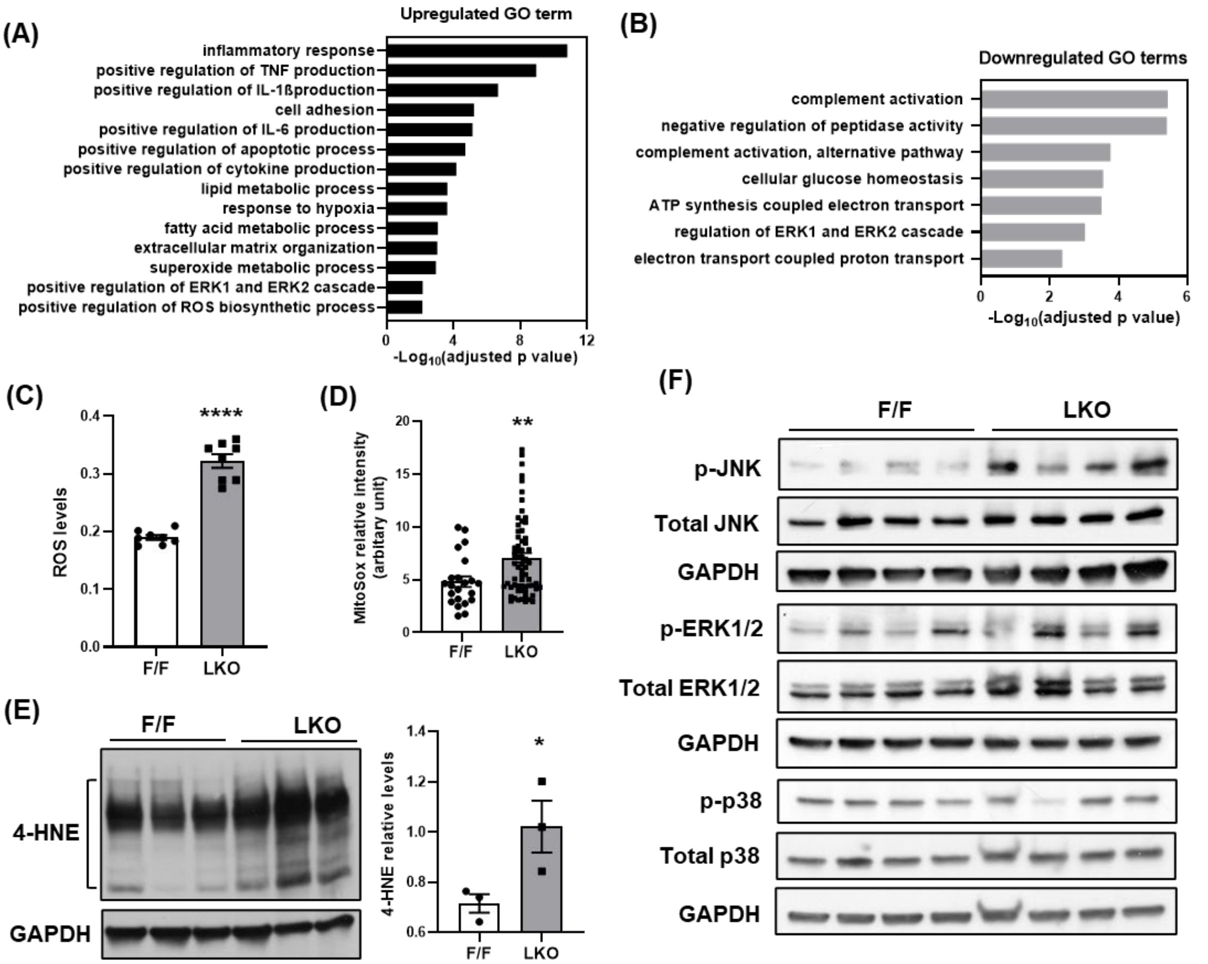

Figure 4.6 Lpcat3 deficiency in the liver induces ROS production and causes oxidative stress. (A-B) Enriched terms from Gene Ontology (GO) analysis of significantly upregulated (A) and downregulated genes (B) in 12-week NASH diet-fed LKO livers compared to control F/F. (C) Total ROS levels in primary hepatocytes isolated from F/F and LKO mice fed with NASH diet for 9 weeks. (D) Quantification of mitosox staining in primary hepatocytes isolated from F/F and LKO mice fed with NASH diet for 9 weeks. (E) Immunoblot and quantification of 4-hydroxynonenal (4-HNE) in livers of F/F and LKO mice fed NASH diet for 12 weeks. (F) Immunoblot of MAPK pathways in livers of F/F and LKO mice fed NASH diet for 12 weeks.

Data are presented as means ± SEM. Statistical analysis was performed with student's t test. $*p < 0.05$, $**p < 0.01$, $****p < 0.0001$.

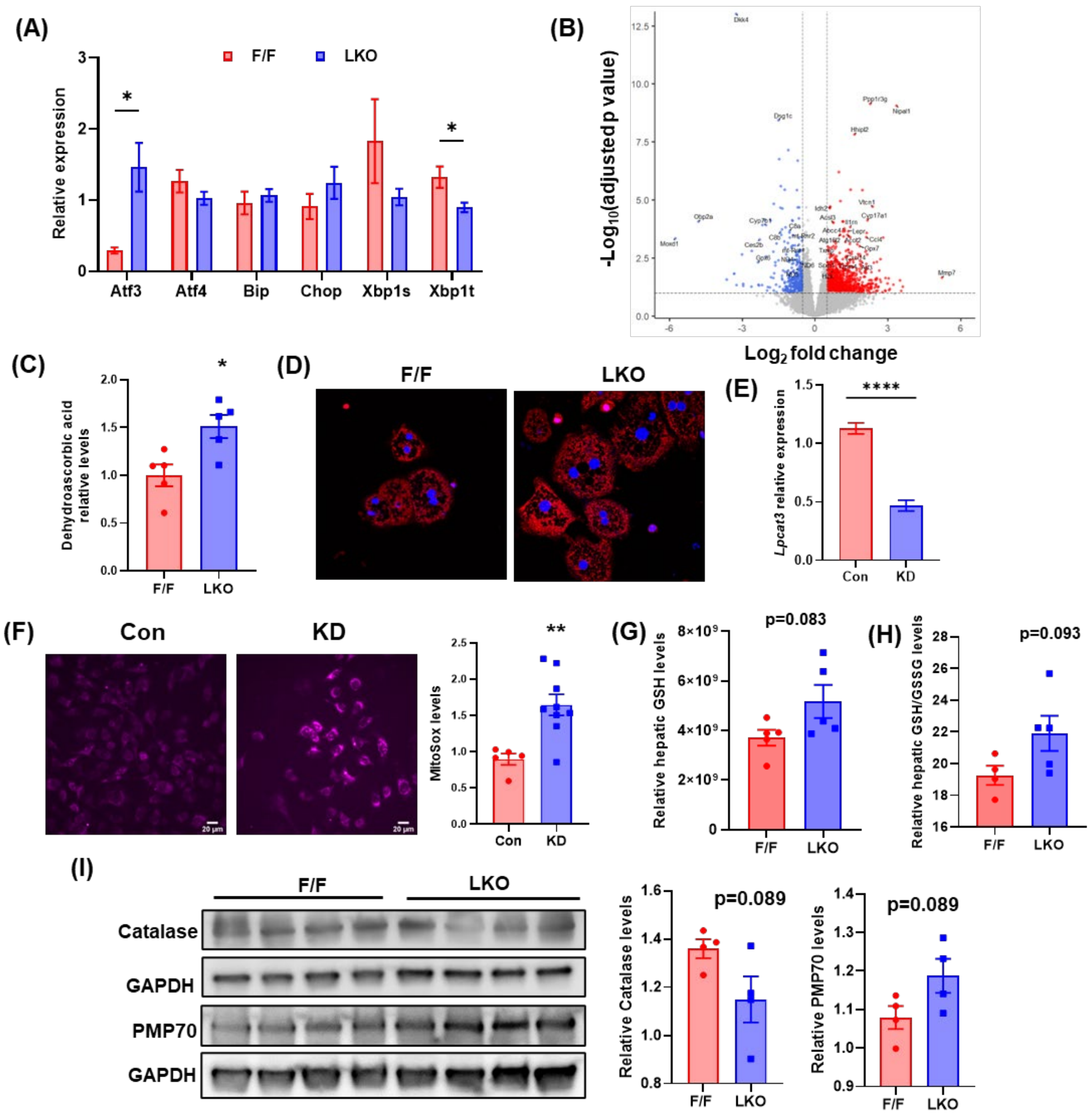

Figure 4.7 Lpcat3 deficiency in the liver induces ROS production and causes oxidative stress. (A) Relative expression of genes involved in ER stress in livers of F/F and LKO mice fed NASH diet for 12 weeks (n=4-6/group). (B) Volcano plot showing the significantly upregulated (red) and downregulated (blue) genes in livers of LKO mice compared to control F/F mice (n=5/group) fed NASH diet for 12 weeks. The absolute fold change > 1.5 and adjusted p value < 0.01 was set as cutoff. (C) Relative dehydroascorbic acid levels in livers of F/F and LKO mice fed NASH diet for 12 weeks. (D) Representative images of mitosox staining of primary hepatocytes isolated from F/F and LKO mice fed NASH diet for 9 weeks (scale bar, 50 μm). (E) Lpcat3 mRNA levels in Hepa

1-6 cells treated with control (Con) or Lpcat3 antisense oligo (KD) for 48 h. (F) Representative images of mitosox staining and quantification of Con and KD Hepa 1-6 cells. (G-H) Relative glutathione (GSH) levels (G) and GSH to oxidized glutathione (GSSG) ratio (H) in livers of F/F and LKO mice fed NASH diet for 12 weeks. (I) Immunoblots and quantification of catalase and PMP70 (peroxisome marker) in livers of F/F and LKO mice fed NASH diet for 12 weeks.

Data are presented as mean ± SEM. Statistical analysis was performed with student's t test. $^{*}p < 0.05$, $^{**}p < 0.01$, $^{****}p < 0.0001$.

(Figure 4.7 Cont.)

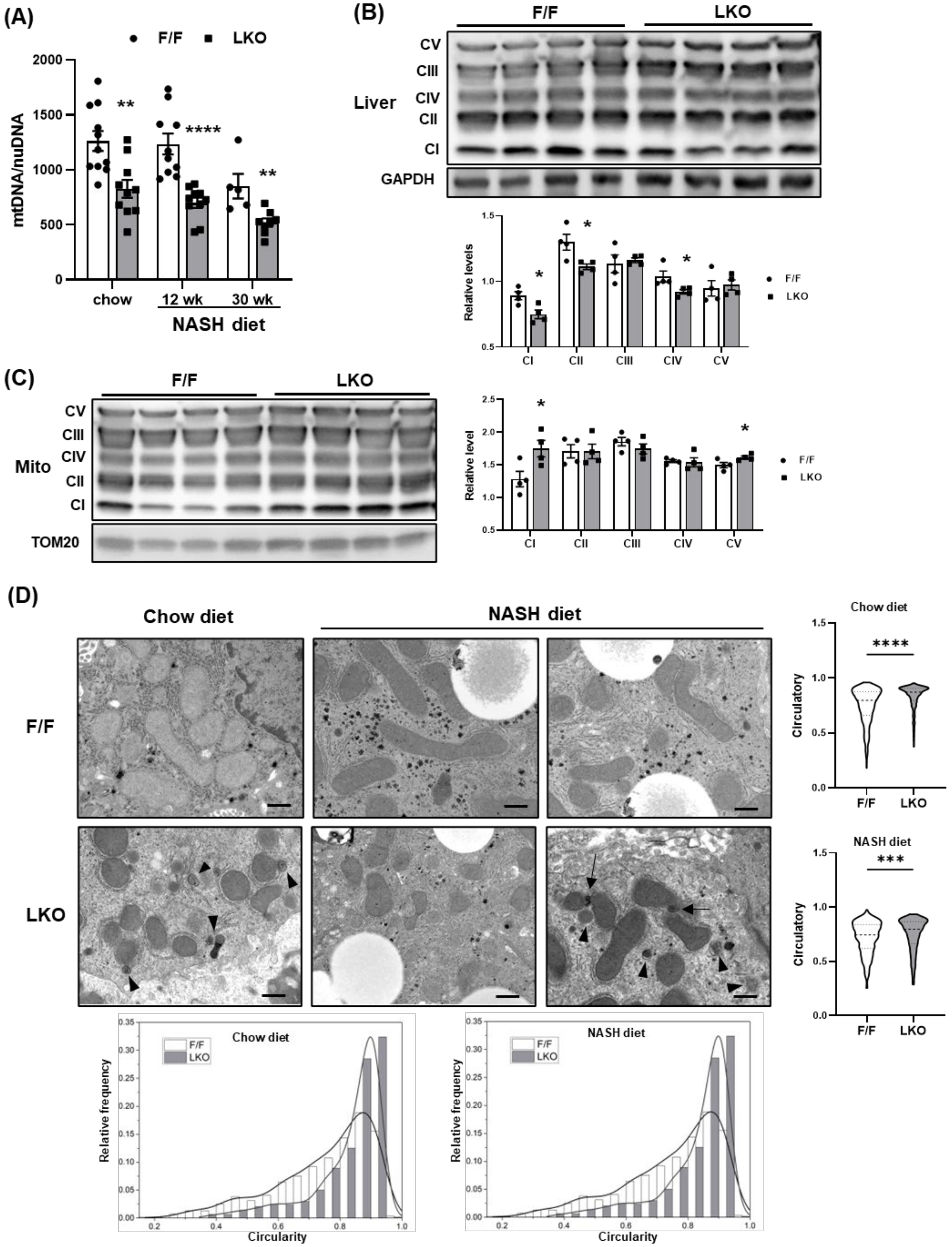

Figure 4.8 Deletion of Lpcat3 in the liver impairs mitochondria homeostasis.

(A) Mitochondrial DNA (mtDNA) content normalized to nuclear DNA (nuDNA) in livers of F/F and LKO mice on chow diet or NASH diet. (B-C) Immunoblots and quantifications of oxidative phosphorylation (OxPhos) complexes in livers (B) or isolated mitochondria (C) from F/F and LKO mice fed NASH diet for 12 weeks. (D) Transmission electron microscopy (TEM) images of liver sections and distribution of hepatic mitochondrial circularity from chow diet or 12-week NASH diet fed mice. Arrows show mitochondria undergoing fission and arrowheads show autophagosome like structures (scale bar, 600 nm).

Data in (A-C) are presented as means ± SEM. Data in (D) show median and quantiles. Statistical analysis was performed with multiple t test (A-C) and Kolmogorov-Smirnov test (D). The distribution curve in (D) was fit by Kernel Smooth. $^{*}p < 0.05$, $^{**}p < 0.01$, $^{***}p < 0.001$, $^{****}p < 0.0001$.

(Figure 4.8 Cont.)

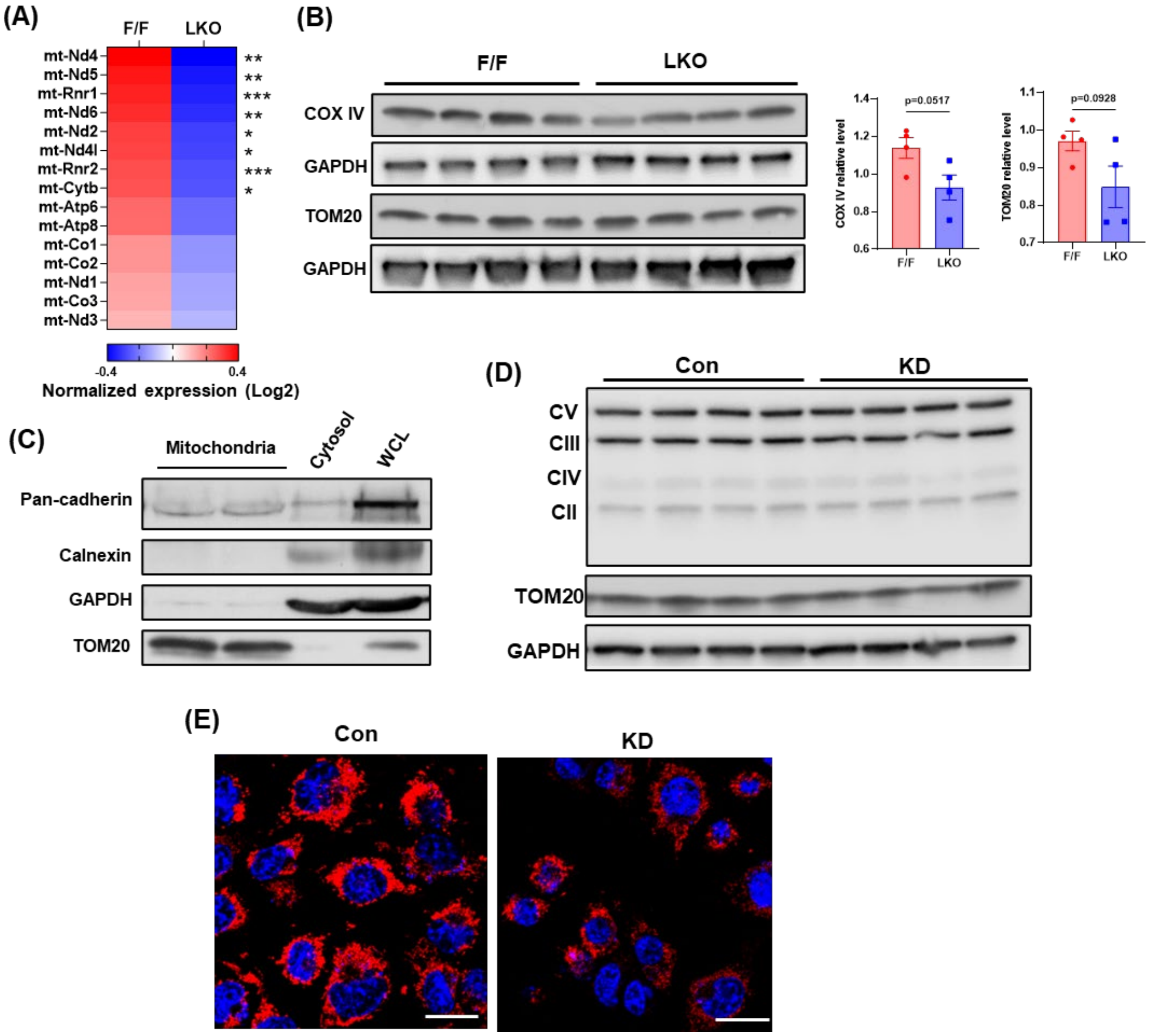

Figure 4.9 Lpcat3 deficiency impairs mitochondrial homeostasis.

(A) Normalized expression of 13 mitochondria encoded genes in livers of F/F and LKO mice fed NASH diet for 12 weeks (n=5/group). (B) Immunoblots and quantification of mitochondrial markers in livers of F/F and LKO mice fed NASH diet for 12 weeks. (C) Immunoblots to confirm the purity of isolated mitochondria from mouse liver. WCL, whole cell lysate. (D) Immunoblots of oxidative phosphorylation (OxPhos) complexes and TOM20 in Con and KD Hepa 1-6 cells. (E) MitoTracker staining of Con and KD Hepa 1-6 cells (scale bar, 50 μm).

Data are presented as mean ± SEM. Statistical analysis was performed with student's t test. $^{*}p < 0.05$, $^{**}p < 0.01$, $^{***}p < 0.001$, $^{****}p < 0.0001$.

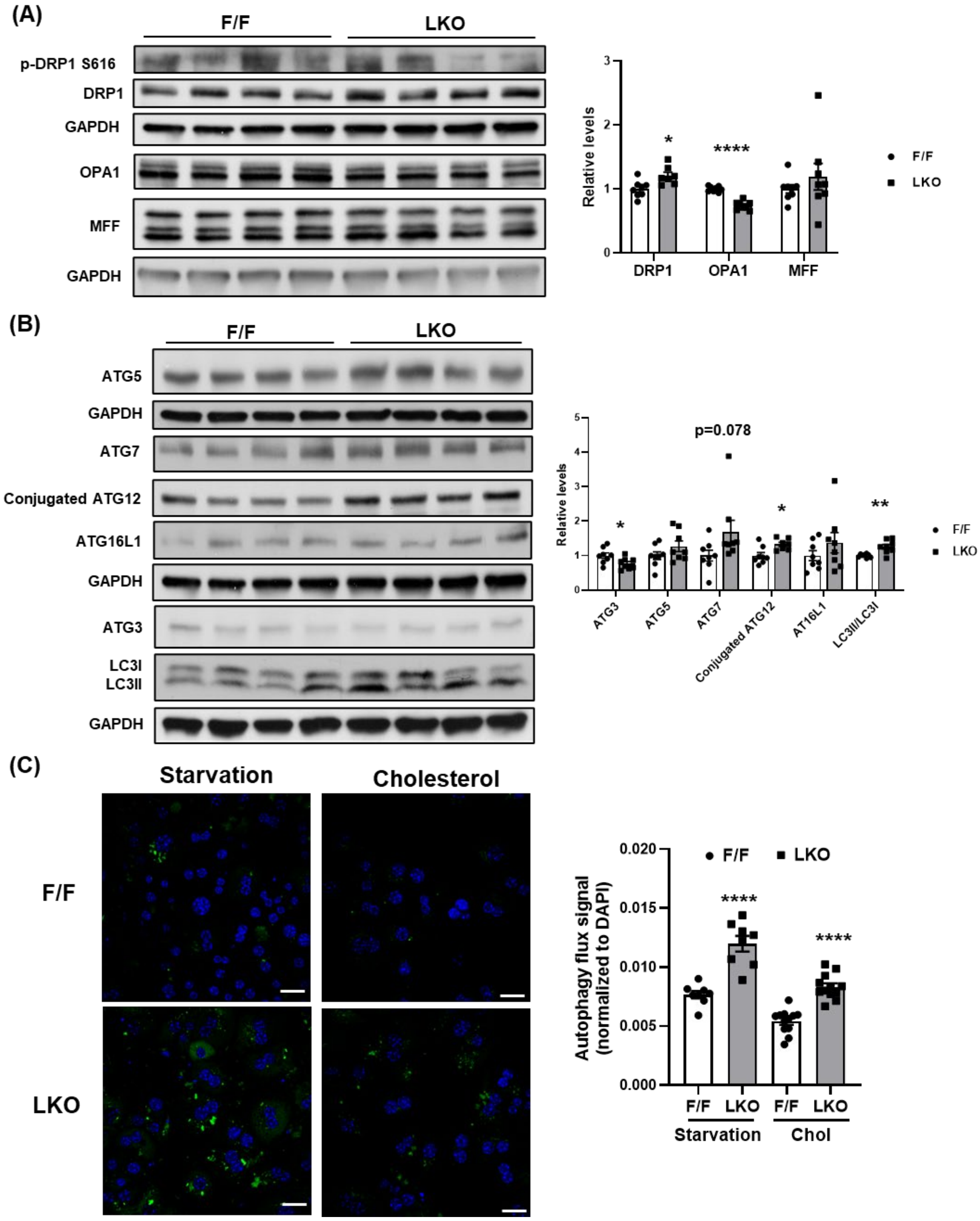

Figure 4.10 Loss of Lpcat3 in the liver alters mitochondrial dynamics and promotes stress induced autophagy.

(A-B) Representative immunoblots and quantifications of proteins involved in mitochondrial fusion and fission (A) and autophagy (B) in livers of F/F and LKO mice fed with NASH diet for 12 weeks. (C) Representative images and fluorescence signal readings of autophagic vacuoles staining in primary hepatocytes cultured in serum free medium or treated with cholesterol overnight.

Data are presented as mean ± SEM. Statistical analysis was performed with student's t test. $*p < 0.05$, $**p < 0.01$, $***p < 0.001$, $****p < 0.0001$.

(Figure 4.10 Cont.)

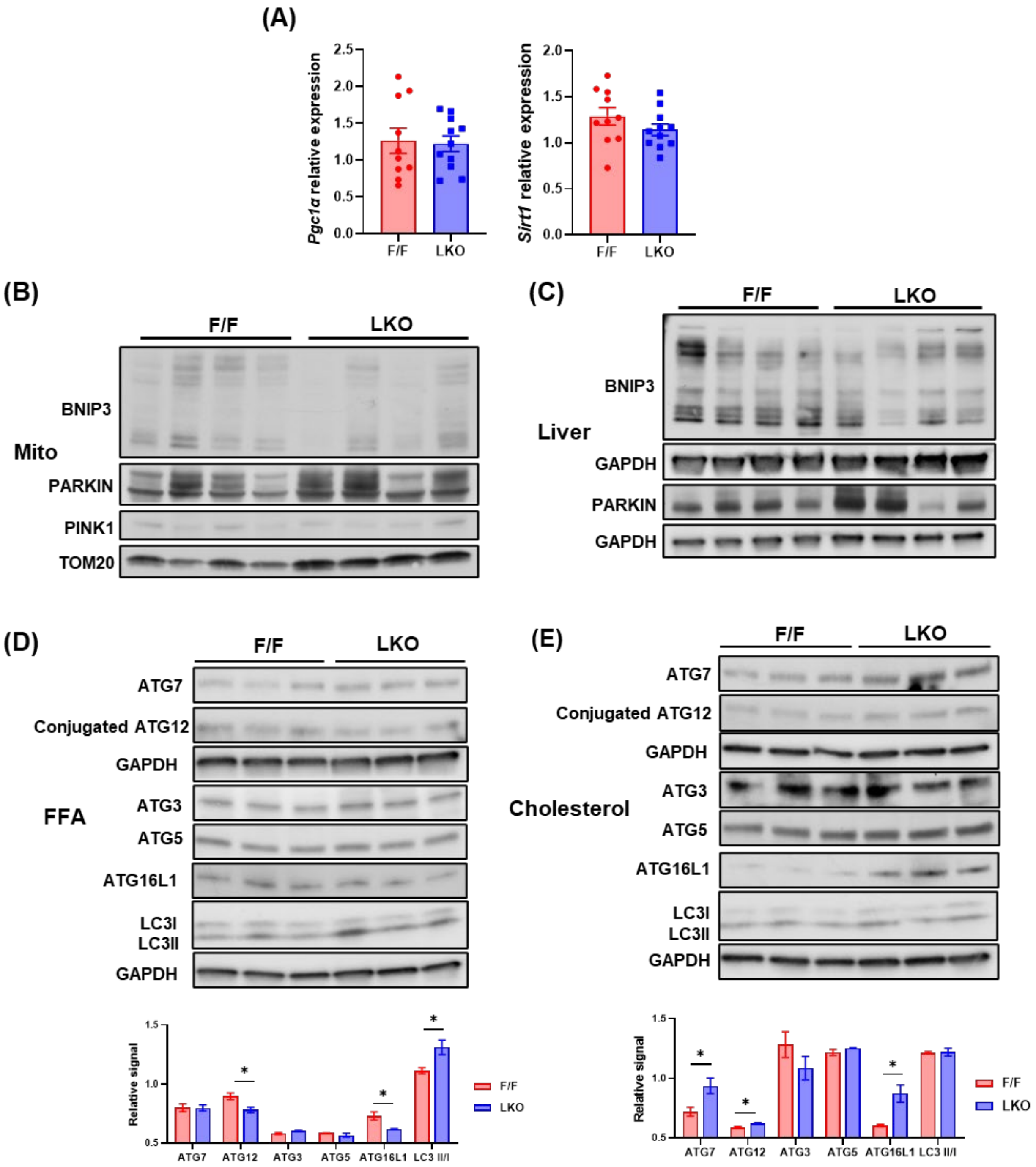

Figure 4.11 Loss of Lpcat3 in the liver alters mitochondrial dynamics and promotes stress-induced autophagy.

(A) Relative expression of Pgc1α and Sirt1 in livers of F/F and LKO mice fed NASH diet for 12 weeks. (B-C) Immunoblots of mitophagy markers in isolated mitochondria (B) and liver tissue (C) of F/F and LKO mice fed NASH diet for 12 weeks. (D-E) Immunoblots and quantification of autophagy markers in primary hepatocytes isolated from chow diet fed F/F and LKO mice. Hepatocytes were treated with BSA-conjugated fatty acid (D) or methyl-β-cyclodextrin conjugated cholesterol (E) for 12 h.

Data are presented as mean ± SEM. Statistical analysis was performed with student's t test. $^*p < 0.05$.

(Figure 4.11 Cont.)

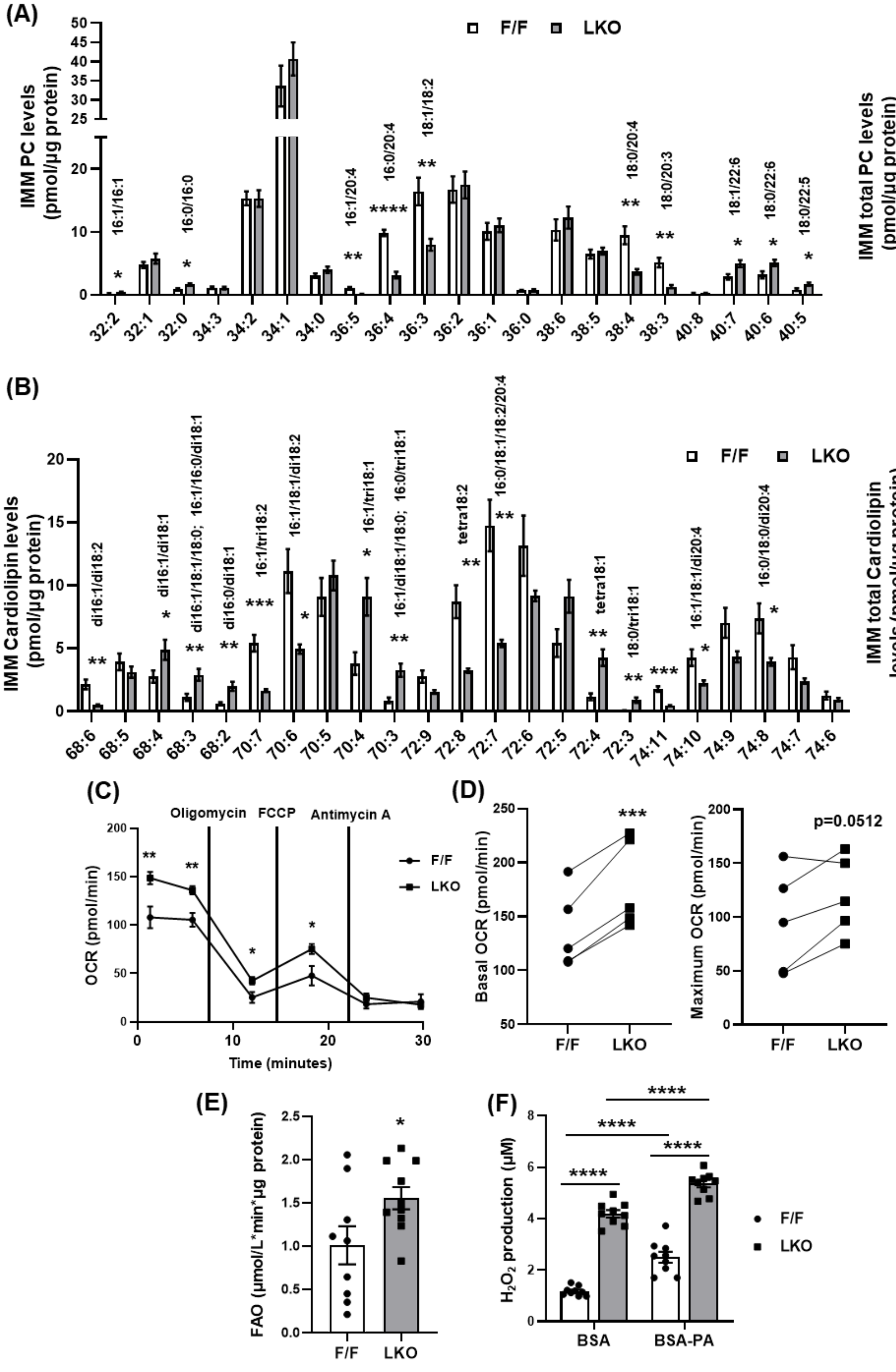

Figure 4.12 Lpcat3 deficiency changes mitochondrial membrane composition and oxidative capacity.

(A-B) Fatty acyl composition and total content of phosphatidylcholine (PC) (A) and cardiolipin (B) in inner mitochondrial membrane (IMM) in livers of F/F and LKO mice fed NASH diet for 12 weeks (n=5~6/group). Indicated (sn-1/sn-2) molecular species were confirmed by product ion scanning for aliphatic composition. (C) Representative data of Seahorse mitochondrial stress test in isolated mitochondria from livers of F/F and LKO mice fed NASH diet for 12 weeks. (D) Basal and maximal oxygen consumption rate (OCR) from Seahorse mitochondrial stress test of isolated mitochondria from livers of F/F and LKO mice on chow diet or NASH diet for 12 weeks. Paired data show repetitive experiments. (E) Fatty acid oxidation (FAO) rate of liver homogenate from F/F and LKO mice fed NASH diet for 12 weeks. (F) H2O2 production in primary hepatocytes isolated from chow diet fed control and LKO mice with or without palmitate (250 μM) treatment.

Data are presented as mean ± SEM. Statistical analysis was performed with multiple t test (A-C), paired t test (D and E), student's t test (F), and two-way ANOVA (G). $^{*}p < 0.05$, $^{**}p < 0.01$, $^{***}p < 0.001$, $^{****}p < 0.0001$.

(Figure 4.12 Cont.)

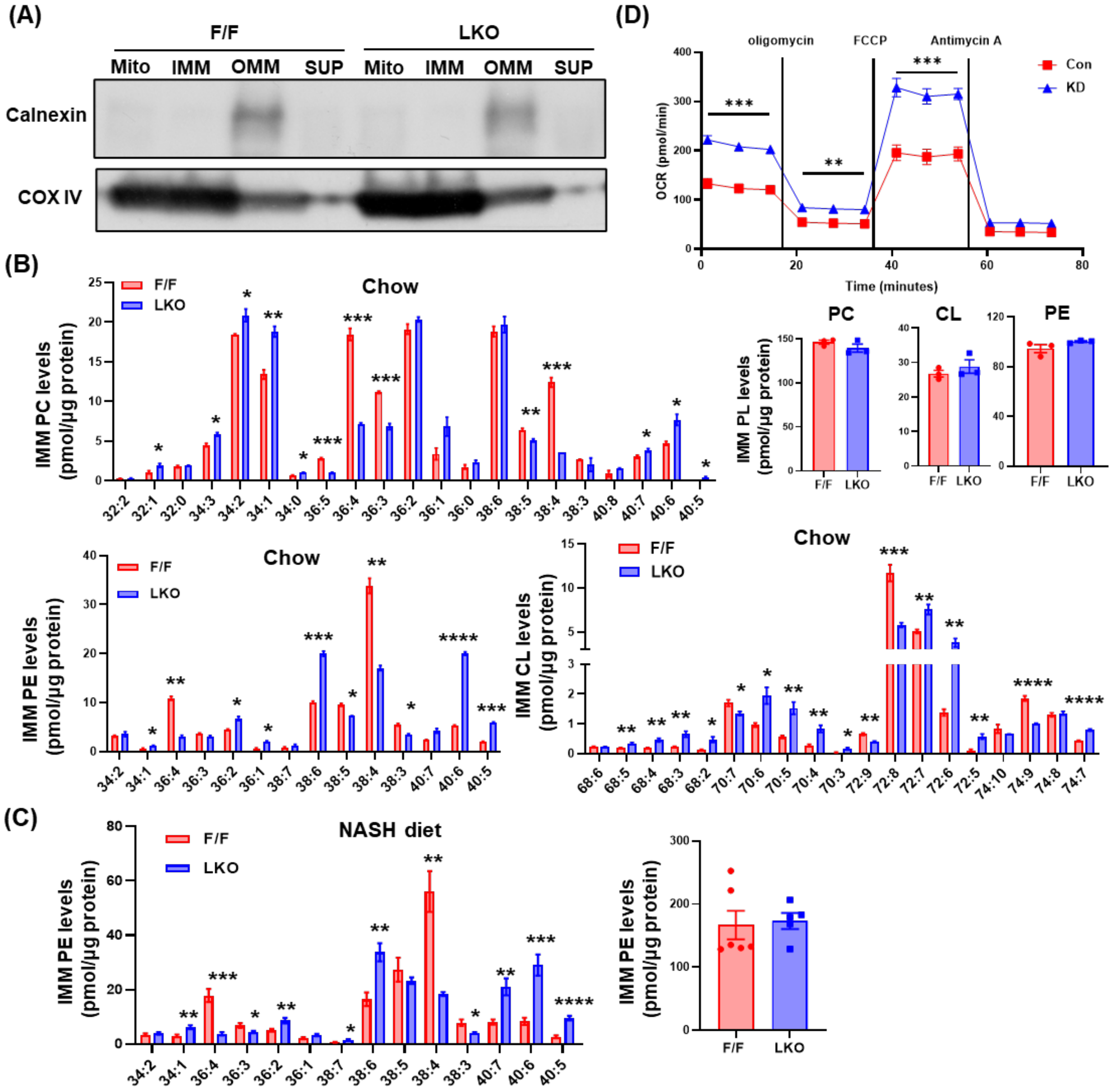

Figure 4.13 Lpcat3 deficiency changes inner mitochondrial membrane PL composition and oxidative capacity.

(A) Immunoblots to confirm the enrichment of inner mitochondrial membrane (IMM) and outer mitochondrial membrane (OMM) from livers of F/F and LKO mice fed NASH diet for 12 weeks. (B-C) Fatty acyl composition and total content of phosphatidylcholine (PC), phosphatidylethanolamine (PE) and cardiolipin (CL) in IMM of F/F and LKO mice fed chow (B) (n=3/group) or NASH diet for 12 weeks (C) (n=5~6/group). (D) Seahorse mitochondrial stress test for Con and KD Hepa 1-6 cells.

Data are presented as mean ± SEM. Statistical analysis was performed with multiple t test. *$p < 0.05$, **$p < 0.01$, ***$p < 0.001$, ****$p < 0.0001$.

(Figure 4.13 Cont.)

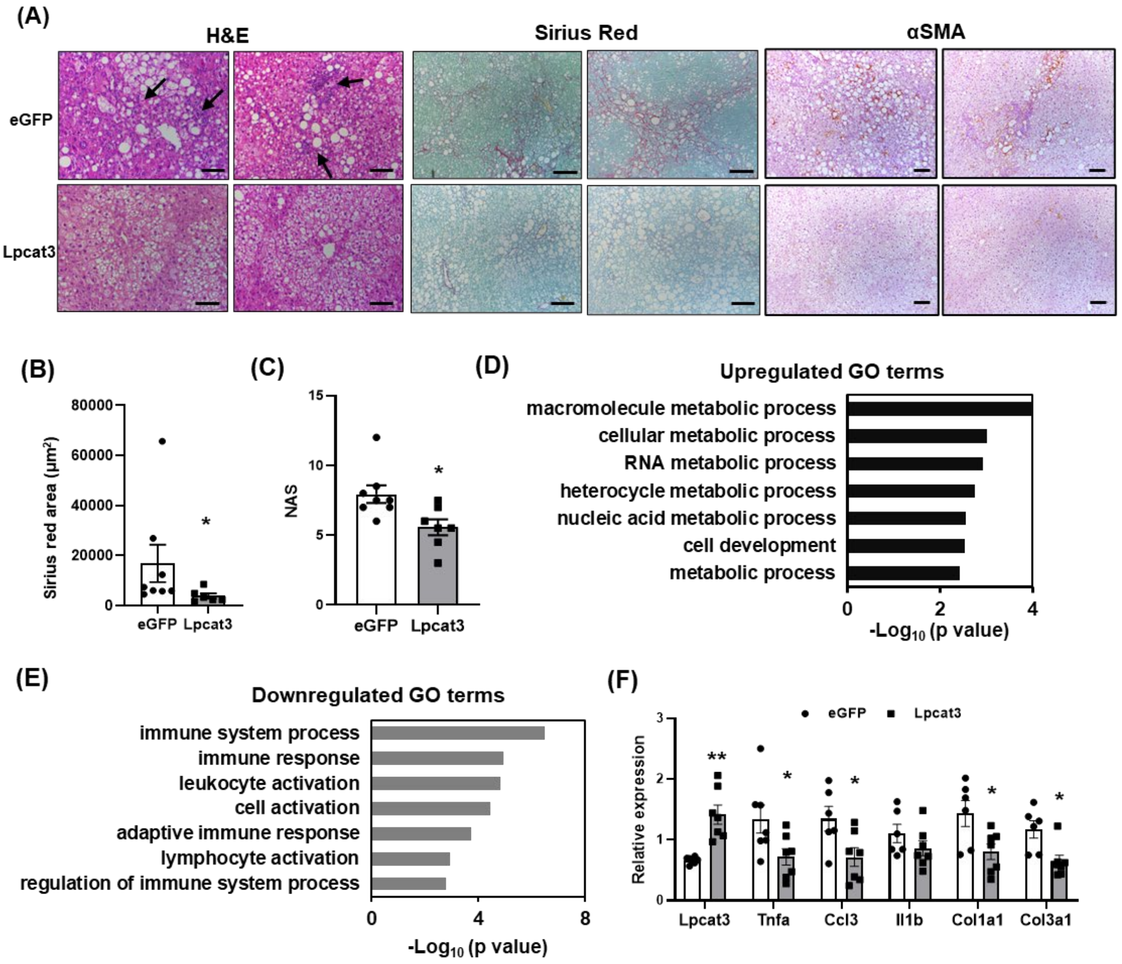

Figure 4.14 Overexpression of Lpcat3 in the liver ameliorates diet-induced NASH progression.

(A) H&E, Sirius Red and immunohistochemistry of α-SMA of livers from eGFP and Lpcat3 injected mice fed NASH diet. Arrows denote immune cell infiltration (scale bar, 100 μm). (B-C) Quantifications of Sirius Red area (B) and NAS (C) of eGFP and Lpcat3 injected mice fed NASH diet. (D-E) Enriched GO terms of significantly upregulated (D) and downregulated genes (E) in livers of Lpcat3 injected mice compared to eGFP injected mice based on RNA sequencing data. (F) Relative expression of Lpcat3, inflammation markers and collagen synthesis genes in livers of eGFP and Lpcat3 injected mice fed NASH diet.

Data are presented as mean ± SEM. Statistical analysis was performed with student's t test or multiple t test. $*p < 0.05$, $**p < 0.01$.

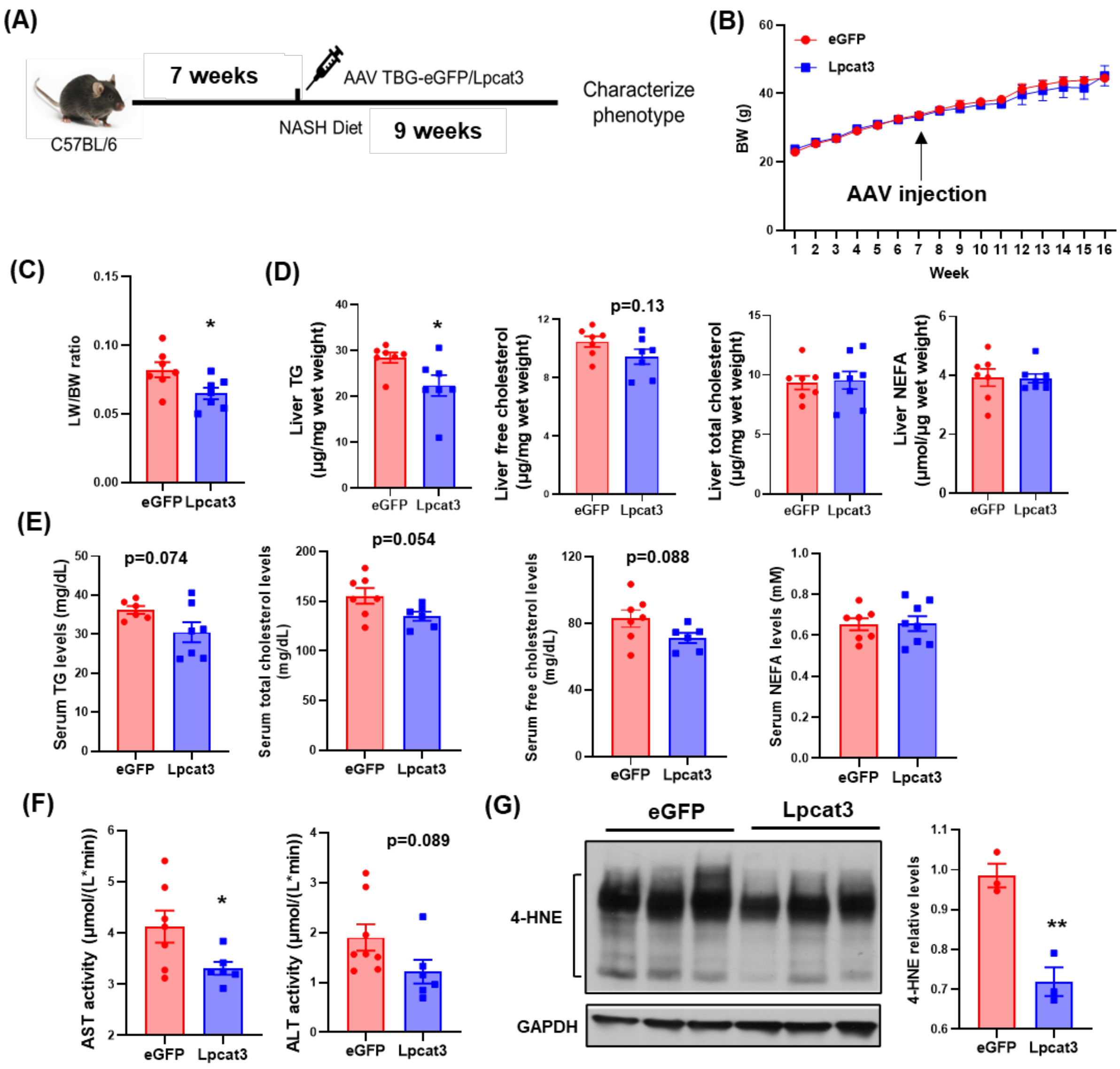

Figure 4.15 Overexpression of Lpcat3 in the liver ameliorates diet-induced NASH progression.

(A) Diagram of experimental strategy to overexpress Lpcat3 in livers of NASH diet fed C57BL/6 mice using adeno-associated virus (AAV). (B) Growth curve of AAV-TBG-eGFP (eGFP) or AAV-TBG-Lpcat3 (Lpcat3) injected C57BL/6 mice (n=7-8/group). (C) Liver weight (LW) to body weight (BW) ratio of NASH diet fed mice injected with AAV-TBG-Lpcat3 (Lpcat3) and AAV-TBG-eGFP (eGFP). (D) Liver TG, free cholesterol, total cholesterol and NEFA levels in livers of Lpcat3 and eGFP injected NASH diet fed C57BL/6 mice. (E) Serum TG, total cholesterol, free cholesterol and NEFA levels in eGFP and Lpcat3 injected NASH diet fed C57BL/6 mice. (F)

Serum AST and ALT activity in eGFP or Lpcat3 injected NASH diet fed C57BL/6 mice. (G) Immunoblots and quantification of 4-hydroxynonenal (4-HNE) in livers of eGFP and Lpcat3 injected mice fed NASH diet.

Data are presented as mean ± SEM. Statistical analysis was performed with student's t test. $^*p < 0.05$, $^{**}p < 0.01$.

(Figure 4.15 Cont.)

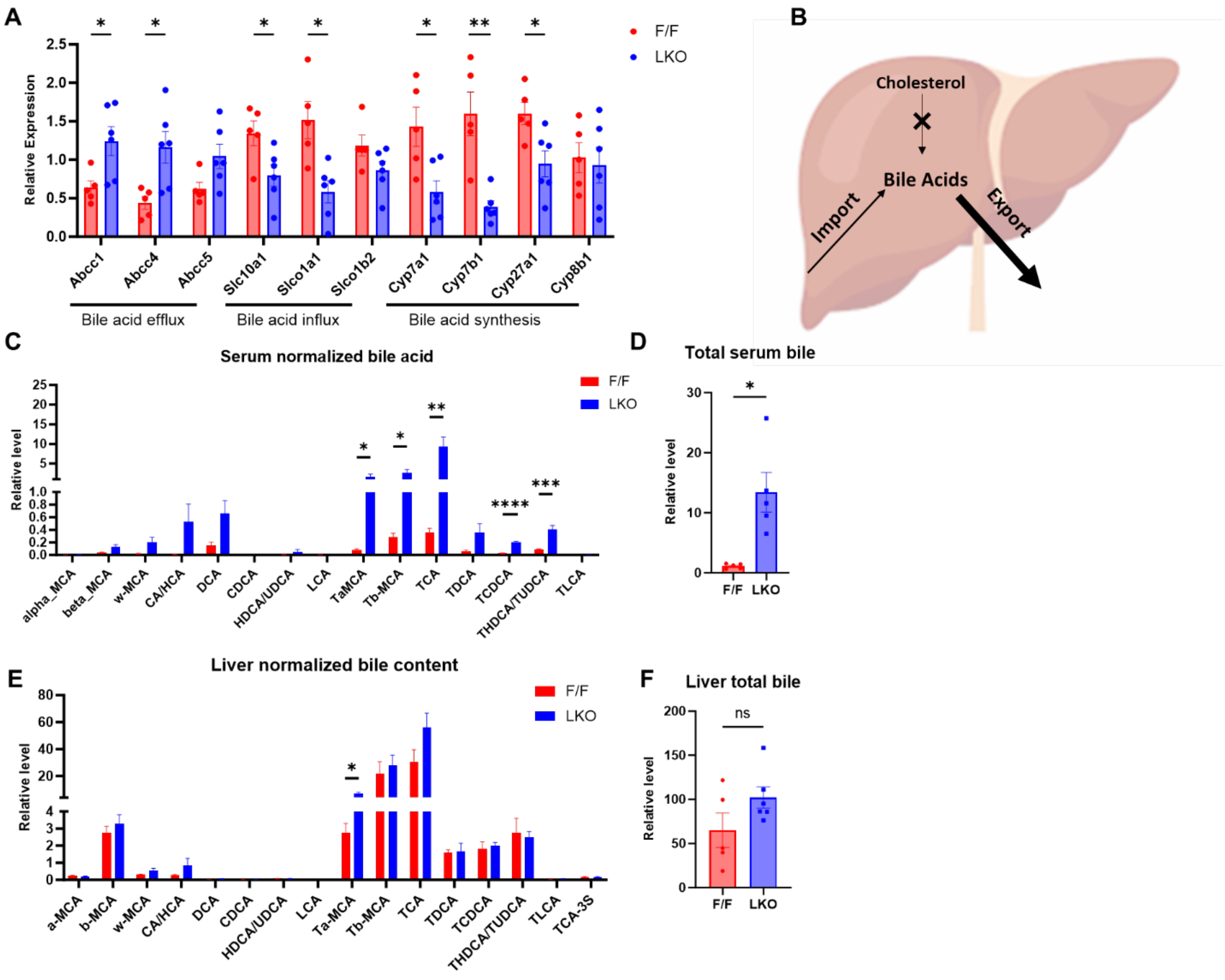

Figure 4.16 Hepatic Lpcat3 deficiency dramatically elevates serum bile acid levels by promoting liver bile clearance.

(A) Relative expression of genes involved in bile acid secretion, uptake and synthesis in livers of F/F and LKO mice fed NASH diet for 12 weeks. (B) Schematic summary of gene expression profile shown in (A). (C-D) Mass spectrum quantification of serum bile acids composition (C) and total levels (D) relative to internal control in F/F and LKO mice fed NASH diet for 12 weeks. (E-F) Mass spectrum quantification of bile acids composition (C) and total levels (D) relative to internal control in livers of F/F and LKO mice fed NASH diet for 12 weeks.

Data are presented as mean ± SEM. Statistical analysis was performed with student's t test. *p < 0.05, **p < 0.01, ***p < 0.001, ****p < 0.0001.

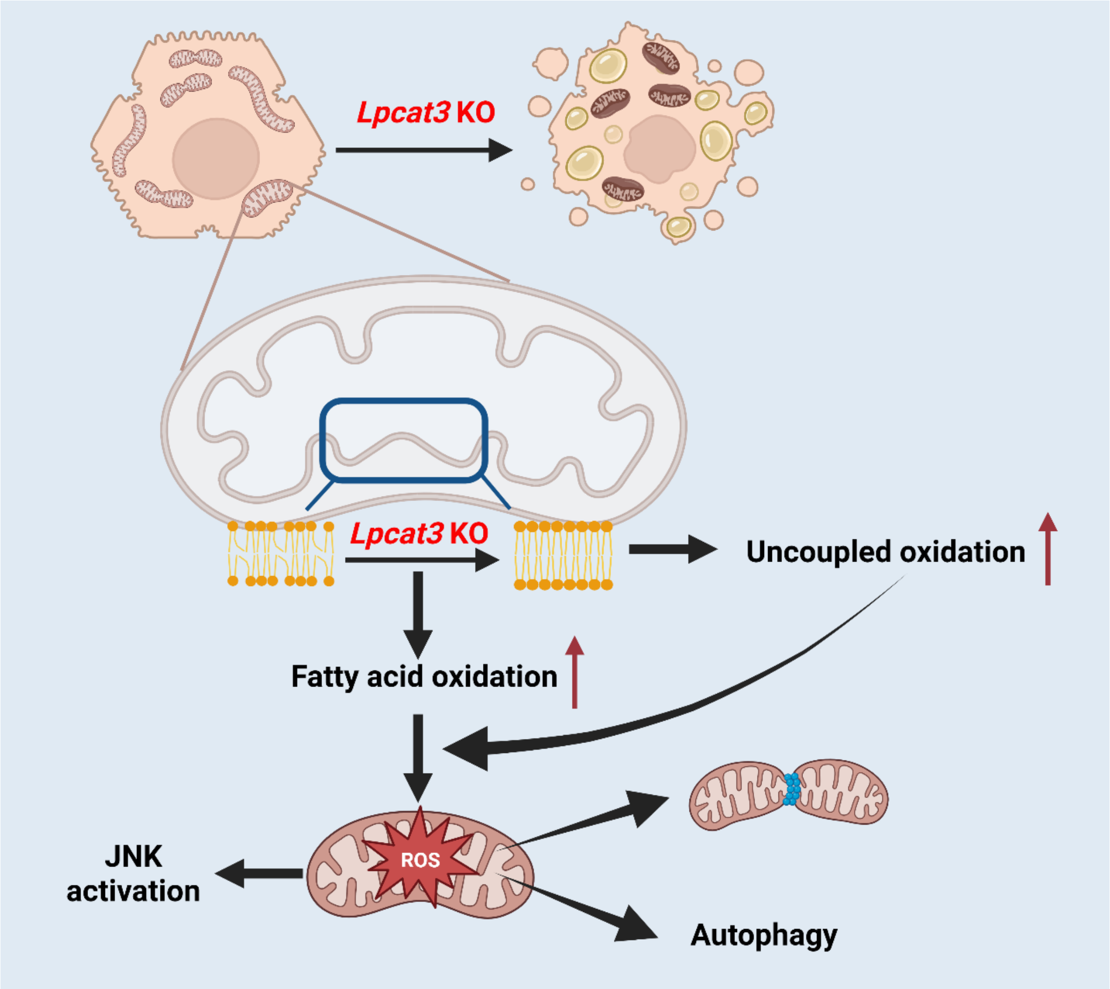

Figure 4.17 Graphical abstract showing membrane phospholipid remodeling promotes NASH by disrupting mitochondria homeostasis.

CHAPTER 5. DISCUSSION

The diversity of membrane lipid composition has long been recognized, yet its physiological and pathological roles were not clear until recently. This shortage of study mainly owes to the lack of tools that can specifically manipulate membrane PL composition. LPCAT3, the PL remodeling enzyme that regulates membrane PL composition in liver, intestine, adipose tissue and muscle, has become a promising target. Previous studies have revealed dramatic impacts of LPCAT3 deficiency on physiology and diseases. In the intestine, PL saturation due to *Lpcat3* depletion leads to blockage of lipid absorption, causing neonatal retardation and drastic weight loss under high fat diet[367]. Furthermore, intestinal cholesterol biosynthesis is significantly promoted after *Lpcat3* deficiency, leading to boosted stem cell proliferation which exacerbates tumorigenesis in $APC^{min/+}$ mice[368]. In the muscle and adipose tissue, loss of *Lpcat3* improved insulin sensitivity by increasing membrane lipid rafts that facilitates insulin receptor signaling[369,370]. In the liver, increased ER membrane saturation promotes ER stress and inflammation, and hinders ER vesicle transportation, causing deficiencies in VLDL secretion and maturation of SREBP-1c[17,233,371]. As a target of LXR, LPCAT3-mediated membrane PL remodeling is thus integrated into lipid metabolism in response to metabolic status.

Here in this study, we further investigated the roles of LPCAT3 activity in the pathogenesis of metabolic disorders. We found that hepatic *Lpcat3* expression can be induced by insulin treatment. Deletion of *Lpcat3* in the liver significantly improved systemic glucose and energy metabolism. In the cellular level, membrane saturation delayed the internalization of InsR, facilitating prolonged insulin signaling. Systemically, loss of hepatic *Lpcat3* ameliorated obesity-linked adipose inflammation, increased energy expenditure and reduced body weight through hepatokine FGF21. However, the alteration of membrane composition in the IMM disrupted the function of mitochondrial ETC, which exacerbated mitochondrial respiration load and produced more ROS from fatty acid oxidation. This prolonged oxidative stress induced spontaneous NASH and promoted diet-induced NASH and HCC. And overexpression of *Lpcat3* in the liver showed significant therapeutic effects on a diet-induced mouse NASH model. These data highlighted the "double-sided sword" roles of LPCAT3 in insulin resistance, obesity and NASH, dissociating these closely intertangled metabolic disorders.

Importantly, this seemingly paradoxical dissociation has its implication in human patients. Although NAFLD is more prevalent in obese individuals, lean NAFLD patients are not rare, with a higher prevalence in Asian ethnics and in favor of males[372]. Lean NAFLD patients exhibits lower rate of diabetes or insulin resistance and lower serum ALT, but with increased lobular inflammation and fibrosis, with worse prognosis outcomes compared to NAFLD patients with obese[372,373]. Interestingly, this dissociation of insulin resistance and NAFLD has also been found in patients with a common genetic factor that is associated with NAFLD and fibrosis, *TM6SF2* E167K[235,374]. Moreover, carriers of E167K mutation had lower serum triglyceride but higher liver fat compared to non-carriers, possibly due to deficient hepatic VLDL secretions[374]. Studies in mouse models of *Tm6sf2* knockout further confirmed the phenotype in human patients and found that the VLDL secretion deficiency potentially owed to degradation of ApoB[173,177]. VLDL is critical for liver lipid removal and systemic lipid redistribution. The deficiency of VLDL secretion leads to accumulating liver lipids, especially free cholesterol, which are major drivers of NASH progression[350]. Therefore, the deficient VLDL secretion contributes to the pathogenesis of lean NAFLD, at least in a proportion of patients.

PL composition is critical to VLDL assembly and secretion. For example, interruptions to PL synthesis by methionine-choline deficient diet is one of the early diet-induced NASH models that acutely induce steatosis and severe fibrosis without obese and insulin resistance[375]. PL scramblases, which maintains the PL composition between bilayers, are also critical to VLDL transportation[44,45]. Interestingly, patients carrying E167K mutations and cells with *TM6SF2* deletion were also found to have altered PL composition, which may explain the deficient VLDL secretions in those patients[376,377]. Disrupted PL remodeling by LPCAT3 deletion also falls into this catalog, with spontaneous steatohepatitis but improved glucose homeostasis. These results further emphasized the importance of PL composition and dynamics in NAFLD progression, which may shed light on the precision therapeutics to lean NAFLD populations.

Hepatic cholesterol can also promote the synthesis and secretion of bile acids, which is another way for cholesterol removal from hepatocytes. Under physiological conditions, hepatocytes excrete bile acids and cholesterol to canaliculus and eventually to the gallbladder through the bile duct. However, bile acids may also “leak” directly to the circulation by basolateral excretion with yet unknown mechanism. After meals, bile is secreted to the intestine to facilitate lipid absorption. The bile acids are then metabolized by the microbiota and recycled back to liver through portal vein, forming an enterohepatic cycle. The serum bile acid concentration is attributed to both hepatic leakage and intestinal recycling. It has been shown that the serum levels of bile acids were significantly increased in NAFLD patients and mouse models, potentially as markers of the severity of disease[235,251,252]. And reducing serum bile acids by blocking ileal bile acid recycling can ameliorate NAFLD progression[256]. However, it is still obscure whether the increased serum bile acids are secondary to NASH-induced liver damage. Surprisingly, dramatically elevated serum levels of bile acids were observed in LKO mice on NASH diet. We did not observe increased ileal bile acid uptake at least in the transcriptional level (data not shown), implying that this increased serum bile acids are mainly from liver. Consistent with this idea, primary bile acids, which are not metabolized by gut microbiota, are among the most significantly altered bile acid species in the serum. The NASH diet contains high cholesterol content (1.25%), which might be the driver of the uncontrolled bile acid synthesis. But further investigations are still required to decipher the reason for this overt "leakage" of bile acids and whether it contributes to the progression of NASH.

The systemic effects of hepatic *Lpcat3* depletion mediated by FGF21 are unexpected phenotypes in this study. The reason for increased hepatic FGF21 secretion is still not clear. We evaluated PPARα, an established upstream regulator of FGF21, but it was not activated. FGF21 can be induced in response to various cellular stresses, including ER stress and mitochondrial stress response (MSR). Previous studies have shown that mitochondrial dysfunction led to increased FGF21 expression through induction of activated transcription factor 4 (ATF4) in both muscle and liver[378,379]. The altered membrane PL composition due to loss of *Lpcat3* induced mitochondrial oxidative stress with overwhelmed oxidation under NASH diet, while still exhibited lower body weight and blood glucose level. It is possible that this effect is mediated by hepatic ATF4 signaling, which requires further verification. At early stages of NAFLD development, *Lpcat3* deficiency overall protects systemic metabolism by retaining excessive lipids in the liver for oxidation, leading to steatosis but sensitized insulin signaling due to membrane change. With chronic stress and injury, this protective endeavor will be gradually exhausted and become the driver for advanced NASH with fibrosis and eventually HCC.

The therapeutic potential of LPCAT3 as a target against NASH is worth investigating. Overexpression of *Lpcat3* in a diet-induced mouse model showed promising outcomes on markers of steatosis, inflammation and fibrosis, although no significant alteration of PL composition was observed after overexpression. Moreover, although loss of *Lpcat3* protected mice from diet-induced insulin resistance, long-term overexpression of *Lpcat3* did not induce insulin resistance nor obesity (data not shown). Therefore, screening for LPCAT3 agonist might be the next step to harvest its therapeutic potential on at least a subgroup of NAFLD patients. The potential of LPCAT3 inhibition targeting insulin resistance was also investigated in Chapter 3. Short-term protective effects are well expected to be seen, but chronic usage may increase the risk of liver damage as we discussed before. LPCAT3 therefore might become a novel therapeutic target on metabolic disorders with multiple potential hits.

REFERENCES

1 Wang, B. & Tontonoz, P. Phospholipid Remodeling in Physiology and Disease. *Annu Rev Physiol* **81**, 165-188 (2019). https://doi.org/10.1146/annurev-physiol-020518-114444

2 Luukkonen, P. K. *et al.* Impaired hepatic lipid synthesis from polyunsaturated fatty acids in TM6SF2 E167K variant carriers with NAFLD. *J Hepatol* **67**, 128-136 (2017). https://doi.org/10.1016/j.jhep.2017.02.014

3 Luukkonen, P. K. *et al.* MARC1 variant rs2642438 increases hepatic phosphatidylcholines and decreases severity of non-alcoholic fatty liver disease in humans. *J Hepatol* **73**, 725-726 (2020). https://doi.org/10.1016/j.jhep.2020.04.021

4 Lands, W. E. Metabolism of glycerolipides; a comparison of lecithin and triglyceride synthesis. *J Biol Chem* **231**, 883-888 (1958).

5 Harayama, T. & Riezman, H. Understanding the diversity of membrane lipid composition. *Nat Rev Mol Cell Biol* **19**, 281-296 (2018). https://doi.org/10.1038/nrm.2017.138

6 Singer, S. J. & Nicolson, G. L. The Fluid Mosaic Model of the Structure of Cell Membranes. *Science* **175**, 720-731 (1972). https://doi.org/10.1126/SCIENCE.175.4023.720

7 Yu, J., Fischman, D. A. & Steck, T. L. Selective solubilization of proteins and phospholipids from red blood cell membranes by nonionic detergents. *Journal of Supramolecular Structure* **1**, 233-248 (1973). https://doi.org/10.1002/JSS.400010308

8 Pike, L. J. Rafts defined: a report on the Keystone symposium on lipid rafts and cell function. *Journal of Lipid Research* **47**, 1597-1598 (2006). https://doi.org/10.1194/JLR.E600002-JLR200

9 Sezgin, E., Levental, I., Mayor, S. & Eggeling, C. The mystery of membrane organization: composition, regulation and roles of lipid rafts. *Nature reviews. Molecular cell biology* **18**, 361-374 (2017). https://doi.org/10.1038/nrm.2017.16

10 Levental, I., Lingwood, D., Grzybek, M., Coskun, Ü. & Simons, K. Palmitoylation regulates raft affinity for the majority of integral raft proteins. *Proceedings of the National Academy of Sciences of the United States of America* **107**, 22050-22054 (2010). https://doi.org/10.1073/PNAS.1016184107/SUPPL_FILE/PNAS.1016184107_SI.PDF

11 Anderson, R. G. W. THE CAVEOLAE MEMBRANE SYSTEM. *https://doi.org/10.1146/annurev.biochem.67.1.199* **67**, 199-225 (2003). https://doi.org/10.1146/ANNUREV.BIOCHEM.67.1.199

12 Parton, R. G. & Simons, K. The multiple faces of caveolae. *Nature Reviews Molecular Cell Biology 2007 8:3* **8**, 185-194 (2007). https://doi.org/10.1038/nrm2122

13 Le Lay, S. *et al.* Cholesterol-Induced Caveolin Targeting to Lipid Droplets in Adipocytes: A Role for Caveolar Endocytosis. *Traffic* **7**, 549-561 (2006). https://doi.org/10.1111/J.1600-0854.2006.00406.X

14 Boothe, T. *et al.* Inter-domain tagging implicates caveolin-1 in insulin receptor trafficking and Erk signaling bias in pancreatic beta-cells. *Mol Metab* **5**, 366-378 (2016). https://doi.org/10.1016/j.molmet.2016.01.009

15 Ferrara, P. J. *et al.* Lysophospholipid acylation modulates plasma membrane lipid organization and insulin sensitivity in skeletal muscle. *J Clin Invest* **131** (2021). https://doi.org/10.1172/JCI135963

16 Pinot, M. *et al.* Lipid cell biology. Polyunsaturated phospholipids facilitate membrane deformation and fission by endocytic proteins. *Science* **345**, 693-697 (2014). https://doi.org/10.1126/science.1255288

17 Rong, X. *et al.* Lpcat3-dependent production of arachidonoyl phospholipids is a key determinant of triglyceride secretion. *Elife* **4** (2015). https://doi.org/10.7554/eLife.06557

18 Simunovic, M., Evergren, E., Callan-Jones, A. & Bassereau, P. Curving Cells Inside and Out: Roles of BAR Domain Proteins in Membrane Shaping and Its Cellular Implications. *https://doi.org/10.1146/annurev-cellbio-100617-060558* **35**, 111-129 (2019). https://doi.org/10.1146/ANNUREV-CELLBIO-100617-060558

19 Mostowy, S. & Cossart, P. Septins: the fourth component of the cytoskeleton. *Nature Reviews Molecular Cell Biology 2012 13:3* **13**, 183-194 (2012). https://doi.org/10.1038/nrm3284

20 Kennedy, E. P. & Weiss, S. B. The function of cytidine coenzymes in the biosynthesis of phospholipides. *The Journal of biological chemistry* **222**, 193-214 (1956). https://doi.org/10.1016/s0021-9258(19)50785-2

21 Bridges, J. P. *et al.* LPCAT1 regulates surfactant phospholipid synthesis and is required for transitioning to air breathing in mice. *The Journal of Clinical Investigation* **120**, 1736-1748 (2010). https://doi.org/10.1172/JCI38061

22 Harayama, T. *et al.* Lysophospholipid acyltransferases mediate phosphatidylcholine diversification to achieve the physical properties required in vivo. *Cell Metabolism* **20**, 295-305 (2014). https://doi.org/10.1016/j.cmet.2014.05.019

23 Abate, W., Alrammah, H., Kiernan, M., Tonks, A. J. & Jackson, S. K. Lysophosphatidylcholine acyltransferase 2 (LPCAT2) co-localises with TLR4 and regulates macrophage inflammatory gene expression in response to LPS. *Scientific Reports 2020 10:1* **10**, 1-13 (2020). https://doi.org/10.1038/s41598-020-67000-x

24 Eslam, M., Valenti, L. & Romeo, S. Genetics and epigenetics of NAFLD and NASH: Clinical impact. *Journal of Hepatology* **68**, 268-279 (2018). https://doi.org/10.1016/j.jhep.2017.09.003

25 Romeo, S., Sanyal, A. & Valenti, L. Leveraging Human Genetics to Identify Potential New Treatments for Fatty Liver Disease. *Cell Metabolism* **31**, 35-45 (2020). https://doi.org/10.1016/J.CMET.2019.12.002

26 Behnia, R. & Munro, S. Organelle identity and the signposts for membrane traffic. *Nature 2005 438:7068* **438**, 597-604 (2005). https://doi.org/10.1038/nature04397

27 Cai, H., Reinisch, K. & Ferro-Novick, S. Coats, Tethers, Rabs, and SNAREs Work Together to Mediate the Intracellular Destination of a Transport Vesicle. *Developmental Cell* **12**, 671-682 (2007). https://doi.org/10.1016/J.DEVCEL.2007.04.005

28 Koike, S. & Jahn, R. SNARE proteins: zip codes in vesicle targeting? *Biochemical Journal* **479**, 273-288 (2022). https://doi.org/10.1042/BCJ20210719

29 Lev, S. Non-vesicular lipid transport by lipid-transfer proteins and beyond. *Nature Reviews Molecular Cell Biology 2010 11:10* **11**, 739-750 (2010). https://doi.org/10.1038/nrm2971

30 Wong, L. H., Gatta, A. T. & Levine, T. P. Lipid transfer proteins: the lipid commute via shuttles, bridges and tubes. *Nature Reviews Molecular Cell Biology 2018 20:2* **20**, 85-101 (2018). https://doi.org/10.1038/s41580-018-0071-5

31 Hsuan, J. & Cockcroft, S. The PITP family of phosphatidylinositol transfer proteins. *Genome Biology 2001 2:9* **2**, 1-8 (2001). https://doi.org/10.1186/GB-2001-2-9-REVIEWS3011

32 Lees, J. A. *et al.* Lipid transport by TMEM24 at ER-plasma membrane contacts regulates pulsatile insulin secretion. *Science* **355** (2017). https://doi.org/10.1126/SCIENCE.AAH6171/SUPPL_FILE/LEES-SM.PDF

33 Schmidt, A. F. *et al.* Cholesteryl ester transfer protein (CETP) as a drug target for cardiovascular disease. *Nature Communications 2021 12:1* **12**, 1-10 (2021). https://doi.org/10.1038/s41467-021-25703-3

34 Hanna, M., Guillén-Samander, A. & Camilli, P. D. RBG Motif Bridge-Like Lipid Transport Proteins: Structure, Functions, and Open Questions. *https://doi.org/10.1146/annurev-cellbio-120420-014634* **39** (2023). https://doi.org/10.1146/ANNUREV-CELLBIO-120420-014634

35 Prinz, W. A., Toulmay, A. & Balla, T. The functional universe of membrane contact sites. *Nature Reviews Molecular Cell Biology 2019 21:1* **21**, 7-24 (2019). https://doi.org/10.1038/s41580-019-0180-9

36 Hernández-Alvarez, M. I. *et al.* Deficient Endoplasmic Reticulum-Mitochondrial Phosphatidylserine Transfer Causes Liver Disease. *Cell* **177**, 881-895.e817 (2019). https://doi.org/10.1016/j.cell.2019.04.010

37 Lange, Y., Swaisgood, M. H., Ramos, B. V. & Steck, T. L. Plasma Membranes Contain Half the Phospholipid and 90% of the Cholesterol and Sphingomyelin in Cultured Human Fibroblasts. *Journal of Biological Chemistry* **264**, 3786-3793 (1989). https://doi.org/10.1016/S0021-9258(19)84918-9

38 Saheki, Y. & De Camilli, P. Endoplasmic Reticulum–Plasma Membrane Contact Sites. *https://doi.org/10.1146/annurev-biochem-061516-044932* **86**, 659-681 (2017). https://doi.org/10.1146/ANNUREV-BIOCHEM-061516-044932

39 Sandhu, J. *et al.* Aster Proteins Facilitate Nonvesicular Plasma Membrane to ER Cholesterol Transport in Mammalian Cells. *Cell* **175**, 514-529.e520 (2018). https://doi.org/10.1016/J.CELL.2018.08.033

40 Xiao, X. *et al.* Hepatic nonvesicular cholesterol transport is critical for systemic lipid homeostasis. *Nature Metabolism 2023*, 1-17 (2023). https://doi.org/10.1038/s42255-022-00722-6

41 Benador, I. Y., Veliova, M., Liesa, M. & Shirihai, O. S. Vol. 29 827-835 (Cell Press, 2019).

42 Benador, I. Y. *et al.* Mitochondria Bound to Lipid Droplets Have Unique Bioenergetics, Composition, and Dynamics that Support Lipid Droplet Expansion. *Cell Metabolism* **27**, 869-885.e866 (2018). https://doi.org/10.1016/J.CMET.2018.03.003

43 Sakuragi, T. & Nagata, S. Regulation of phospholipid distribution in the lipid bilayer by flippases and scramblases. *Nature Reviews Molecular Cell Biology 2023 24:8* **24**, 576-596 (2023). https://doi.org/10.1038/s41580-023-00604-z

44 Huang, D. *et al.* TMEM41B acts as an ER scramblase required for lipoprotein biogenesis and lipid homeostasis. *Cell Metabolism* **33**, 1655-1670.e1658 (2021). https://doi.org/10.1016/J.CMET.2021.05.006

45 Jiang, X. *et al.* Lack of VMP1 impairs hepatic lipoprotein secretion and promotes non-alcoholic steatohepatitis. *Journal of Hepatology* **77**, 619-631 (2022). https://doi.org/10.1016/J.JHEP.2022.04.010

46 Gary M Gary, M. D. Carbohydrate digestion and absorption Role of the small intestine. *N Engl J Med* **292**, 1225-1230 (1975).

47 Zhao, F.-Q. & Keating, A. F. Functional Properties and Genomics of Glucose Transporters. *Current Genomics* **8**, 113-113 (2007). https://doi.org/10.2174/138920207780368187

48 Bogan, J. S. Regulation of Glucose Transporter Translocation in Health and Diabetes. *https://doi.org/10.1146/annurev-biochem-060109-094246* **81**, 507-532 (2012). https://doi.org/10.1146/ANNUREV-BIOCHEM-060109-094246

49 Chavez, J. A., Roach, W. G., Keller, S. R., Lane, W. S. & Lienhard, G. E. Inhibition of GLUT4 Translocation by Tbc1d1, a Rab GTPase-activating Protein Abundant in Skeletal Muscle, Is Partially Relieved by AMP-activated Protein Kinase Activation. *Journal of Biological Chemistry* **283**, 9187-9195 (2008). https://doi.org/10.1074/JBC.M708934200

50 David L. Nelson, M. M. C. A. A. H. *Lehninger's Principle of Biochemistry*. 8th editio edn, (Macmillan, 2021).

51 Farrelly, D. *et al.* Mice mutant for glucokinase regulatory protein exhibit decreased liver glucokinase: A sequestration mechanism in metabolic regulation. *Proceedings of the National Academy of Sciences* **96**, 14511-14516 (1999). https://doi.org/10.1073/PNAS.96.25.14511

52 Okar, D. A. *et al.* PFK-2/FBPase-2: Maker and breaker of the essential biofactor fructose-2,6-bisphosphate. *Trends in Biochemical Sciences* **26**, 30-35 (2001). https://doi.org/10.1016/S0968-0004(00)01699-6

53 Ceulemans, H. & Bollen, M. Functional Diversity of Protein Phosphatase-1, a Cellular Economizer and Reset Button. *Physiological Reviews* **84**, 1-39 (2004). https://doi.org/10.1152/PHYSREV.00013.2003/ASSET/IMAGES/LARGE/9J0140278009.JPEG

54 Hopkins, B. D., Goncalves, M. D. & Cantley, L. C. Insulin–PI3K signalling: an evolutionarily insulated metabolic driver of cancer. *Nature Reviews Endocrinology 2020 16:5* **16**, 276-283 (2020). https://doi.org/10.1038/s41574-020-0329-9

55 Scherer, T., Sakamoto, K. & Buettner, C. Brain insulin signalling in metabolic homeostasis and disease. *Nature Reviews Endocrinology 2021 17:8* **17**, 468-483 (2021). https://doi.org/10.1038/s41574-021-00498-x

56 Haeusler, R. A., McGraw, T. E. & Accili, D. Biochemical and cellular properties of insulin receptor signalling. *Nat Rev Mol Cell Biol* **19**, 31-44 (2018). https://doi.org/10.1038/nrm.2017.89

57 Li, Q. *et al.* The Protein Phosphatase 1 Complex Is a Direct Target of AKT that Links Insulin Signaling to Hepatic Glycogen Deposition. *Cell reports* **28**, 3406-3422.e3407 (2019). https://doi.org/10.1016/J.CELREP.2019.08.066

58 Saltiel, A. R. Insulin signaling in health and disease. *The Journal of Clinical Investigation* **131** (2021). https://doi.org/10.1172/JCI142241

59 Tattersall, R. B. The History of Diabetes Mellitus. *Textbook of Diabetes*, 1-22 (2017). https://doi.org/10.1002/9781118924853.CH1

60 Vol. 102 147-148 (Brussels, Belgium, 2021).

61 Brown, M. S. & Goldstein, J. L. Selective versus total insulin resistance: a pathogenic paradox. *Cell Metab* **7**, 95-96 (2008). https://doi.org/10.1016/j.cmet.2007.12.009

62 Erion, D. M. & Shulman, G. I. Vol. 16 400-402 (2010).

63 Turpin-Nolan, S. M. & Brüning, J. C. The role of ceramides in metabolic disorders: when size and localization matters. *Nature Reviews Endocrinology* **16**, 224-233 (2020). https://doi.org/10.1038/s41574-020-0320-5

64 Lyu, K. *et al.* A Membrane-Bound Diacylglycerol Species Induces PKCϵ-Mediated Hepatic Insulin Resistance. *Cell Metabolism* **32** (2020). https://doi.org/10.1016/j.cmet.2020.08.001

65 Chaurasia, B. *et al.* Targeting a ceramide double bond improves insulin resistance and hepatic steatosis. *Science* **365**, 386-392 (2019). https://doi.org/10.1126/science.aav3722

66 Hammerschmidt, P. *et al.* CerS6-Derived Sphingolipids Interact with Mff and Promote Mitochondrial Fragmentation in Obesity. *Cell* **177**, 1536-1552.e1523 (2019). https://doi.org/10.1016/J.CELL.2019.05.008

67 Park, J. W. *et al.* Ablation of very long acyl chain sphingolipids causes hepatic insulin resistance in mice due to altered detergent-resistant membranes. *Hepatology* **57**, 525-532 (2013). https://doi.org/10.1002/hep.26015

68 Matsuzaka, T. *et al.* Hepatocyte ELOVL Fatty Acid Elongase 6 Determines Ceramide Acyl-Chain Length and Hepatic Insulin Sensitivity in Mice. *Hepatology* **71**, 1609-1625 (2020). https://doi.org/10.1002/HEP.30953

69 Reilly, S. M. & Saltiel, A. R. Adapting to obesity with adipose tissue inflammation. *Nature Reviews Endocrinology 2017 13:11* **13**, 633-643 (2017). https://doi.org/10.1038/nrendo.2017.90

70 Johnson, Andrew M. F. & Olefsky, Jerrold M. The Origins and Drivers of Insulin Resistance. *Cell* **152**, 673-684 (2013). https://doi.org/10.1016/j.cell.2013.01.041

71 El Ouarrat, D. *et al.* TAZ Is a Negative Regulator of PPARγ Activity in Adipocytes and TAZ Deletion Improves Insulin Sensitivity and Glucose Tolerance. *Cell metabolism* (2019). https://doi.org/10.1016/j.cmet.2019.10.003

72 Hall, J. A. *et al.* Obesity-Linked PPARγ S273 Phosphorylation Promotes Insulin Resistance through Growth Differentiation Factor 3. *Cell Metabolism* **32** (2020). https://doi.org/10.1016/j.cmet.2020.08.016

73 Hancock, M. L. *et al.* Insulin Receptor Associates with Promoters Genome-wide and Regulates Gene Expression. *Cell* **177**, 722-736.e722 (2019). https://doi.org/10.1016/j.cell.2019.02.030

74 Choi, E. *et al.* Mitotic regulators and the SHP2-MAPK pathway promote IR endocytosis and feedback regulation of insulin signaling. *Nature Communications* **10**, 1-17 (2019). https://doi.org/10.1038/s41467-019-09318-3

75 Wei, X. *et al.* Fatty acid synthesis configures the plasma membrane for inflammation in diabetes. *Nature Publishing Group* **539** (2016). https://doi.org/10.1038/nature20117

76 Foretz, M., Guigas, B. & Viollet, B. Understanding the glucoregulatory mechanisms of metformin in type 2 diabetes mellitus. *Nature Reviews Endocrinology 2019 15:10* **15**, 569-589 (2019). https://doi.org/10.1038/s41574-019-0242-2

77 Alshawi, A. & Agius, L. Low metformin causes a more oxidized mitochondrial NADH/NAD redox state in hepatocytes and inhibits gluconeogenesis by a redox-independent mechanism. *Journal of Biological Chemistry* **294**, 2839-5691 (2019). https://doi.org/10.1074/JBC.RA118.006670

78 Ma, T. *et al.* Low-dose metformin targets the lysosomal AMPK pathway through PEN2. *Nature 2022*, 1-7 (2022). https://doi.org/10.1038/s41586-022-04431-8

79 Clifford, J. B. & Andrew, J. K. (eds C. Cockram A. Flyvbjerg R.Holt & B. Goldstein) 426-454 (JohnWiley & Sons, Ltd., 2017).

80 Yki-Järvinen, H. Thiazolidinediones. *https://doi.org/10.1056/NEJMra041001* **351**, 1106-1118 (2004). https://doi.org/10.1056/NEJMRA041001

81 Choi, J. H. *et al.* Anti-diabetic drugs inhibit obesity-linked phosphorylation of PPARγ by Cdk5. *Nature 2010 466:7305* **466**, 451-456 (2010). https://doi.org/10.1038/nature09291

82 Ghorpade, D. S. *et al.* Hepatocyte-secreted DPP4 in obesity promotes adipose inflammation and insulin resistance. *Nature* **555**, 673-677 (2018). https://doi.org/10.1038/nature26138

83 Deacon, C. F. Dipeptidyl peptidase 4 inhibitors in the treatment of type 2 diabetes mellitus. *Nature Reviews Endocrinology 2020 16:11* **16**, 642-653 (2020). https://doi.org/10.1038/s41574-020-0399-8

84 Varin, E. M. *et al.* Circulating Levels of Soluble Dipeptidyl Peptidase-4 Are Dissociated from Inflammation and Induced by Enzymatic DPP4 Inhibition. *Cell Metabolism* **29**, 320-334.e325 (2019). https://doi.org/10.1016/j.cmet.2018.10.001

85 Meier, J. J. GLP-1 receptor agonists for individualized treatment of type 2 diabetes mellitus. *Nature Reviews Endocrinology 2012 8:12* **8**, 728-742 (2012). https://doi.org/10.1038/nrendo.2012.140

86 Brown, E., Heerspink, H. J. L., Cuthbertson, D. J. & Wilding, J. P. H. SGLT2 inhibitors and GLP-1 receptor agonists: established and emerging indications. *The Lancet* **398**, 262-276 (2021). https://doi.org/10.1016/S0140-6736(21)00536-5

87 Nie, L. *et al.* The structural basis of fatty acid elongation by the ELOVL elongases. *Nature Structural & Molecular Biology 2021 28:6* **28**, 512-520 (2021). https://doi.org/10.1038/s41594-021-00605-6

88 Evans, R. M. & Mangelsdorf, D. J. Vol. 157 255-266 (Cell Press, 2014).

89 Dubois, V., Eeckhoute, J., Lefebvre, P. & Staels, B. Distinct but complementary contributions of PPAR isotypes to energy homeostasis. *The Journal of Clinical Investigation* **127**, 1202-1214 (2017). https://doi.org/10.1172/JCI88894

90 Preidis, G. A., Kim, K. H. & Moore, D. D. Vol. 127 1193-1201 (American Society for Clinical Investigation, 2017).

91 Gross, B., Pawlak, M., Lefebvre, P. & Staels, B. PPARs in obesity-induced T2DM, dyslipidaemia and NAFLD. *Nature Reviews Endocrinology* **13**, 36-49 (2017). https://doi.org/10.1038/NRENDO.2016.135

92 Owen, J. L. *et al.* Insulin stimulation of SREBP-1c processing in transgenic rat hepatocytes requires p70 S6-kinase. *Proceedings of the National Academy of Sciences of the United States of America* **109**, 16184-16189 (2012). https://doi.org/10.1073/PNAS.1213343109/-/DCSUPPLEMENTAL

93 Shimano, H. & Sato, R. Vol. 13 710-730 (Nature Publishing Group, 2017).

94 Yecies, J. L. *et al.* Akt Stimulates Hepatic SREBP1c and Lipogenesis through Parallel mTORC1-Dependent and Independent Pathways. *Cell Metabolism* **14**, 21-32 (2011). https://doi.org/10.1016/J.CMET.2011.06.002

95 Abdul-Wahed, A., Guilmeau, S. & Postic, C. Vol. 26 324-341 (Cell Press, 2017).

96 Wang, B. & Tontonoz, P. Liver X receptors in lipid signalling and membrane homeostasis. *Nat Rev Endocrinol* **14**, 452-463 (2018). https://doi.org/10.1038/s41574-018-0037-x

97 Ko, C. W., Qu, J., Black, D. D. & Tso, P. Regulation of intestinal lipid metabolism: current concepts and relevance to disease. *Nature Reviews Gastroenterology & Hepatology 2020 17:3* **17**, 169-183 (2020). https://doi.org/10.1038/s41575-019-0250-7

98 Glatz, J. F. C., Luiken, J. J. F. P. & Bonen, A. Membrane fatty acid transporters as regulators of lipid metabolism: Implications for metabolic disease. *Physiological Reviews* **90**, 367-417 (2010). https://doi.org/10.1152/PHYSREV.00003.2009/ASSET/IMAGES/LARGE/Z9J0011025310010.JPEG

99 Hao, J. W. *et al.* CD36 facilitates fatty acid uptake by dynamic palmitoylation-regulated endocytosis. *Nature Communications 2020 11:1* **11**, 1-16 (2020). https://doi.org/10.1038/s41467-020-18565-8

100 Alves-Bezerra, M. & Cohen, D. E. Triglyceride Metabolism in the Liver. *Comprehensive Physiology* **8**, 1-22 (2018). https://doi.org/10.1002/CPHY.C170012

101 Jackson, C. L. Lipid droplet biogenesis. *Current Opinion in Cell Biology* **59**, 88-96 (2019). https://doi.org/10.1016/j.ceb.2019.03.018

102 McLelland, G. L. *et al.* Identification of an alternative triglyceride biosynthesis pathway. *Nature 2023 621:7977* **621**, 171-178 (2023). https://doi.org/10.1038/s41586-023-06497-4

103 Chen, F. J., Yin, Y., Chua, B. T. & Li, P. CIDE family proteins control lipid homeostasis and the development of metabolic diseases. *Traffic (Copenhagen, Denmark)* **21**, 94-105 (2020). https://doi.org/10.1111/TRA.12717

104 Dash, S., Xiao, C., Morgantini, C. & Lewis, G. F. New Insights into the Regulation of Chylomicron Production. *https://doi.org/10.1146/annurev-nutr-071714-034338* **35**, 265-294 (2015). https://doi.org/10.1146/ANNUREV-NUTR-071714-034338

105 Raabe, M. *et al.* Analysis of the role of microsomal triglyceride transfer protein in the liver of tissue-specific knockout mice. *The Journal of clinical investigation* **103**, 1287-1298 (1999). https://doi.org/10.1172/JCI6576

106 Tietge, U. J. F. *et al.* Hepatic overexpression of microsomal triglyceride transfer protein (MTP) results in increased in vivo secretion of VLDL triglycerides and apolipoprotein B. *Journal Lipid Research* **40**, 2134-2139 (1999). https://doi.org/10.1016/S0022-2275(20)32437-8

107 Wang, X. *et al.* Receptor-Mediated ER Export of Lipoproteins Controls Lipid Homeostasis in Mice and Humans ll Article Receptor-Mediated ER Export of Lipoproteins Controls Lipid Homeostasis in Mice and Humans. *Cell Metabolism* **33**, 350-366.e357 (2021). https://doi.org/10.1016/j.cmet.2020.10.020

108 Ouimet, M., Barrett, T. J. & Fisher, E. A. HDL and Reverse Cholesterol Transport. *Circulation Research* **124**, 1505-1518 (2019). https://doi.org/10.1161/CIRCRESAHA.119.312617

109 Cerqueira, N. M. F. S. A. *et al.* Cholesterol Biosynthesis: A Mechanistic Overview. *Biochemistry* **55**, 5483-5506 (2016). https://doi.org/10.1021/ACS.BIOCHEM.6B00342/ASSET/IMAGES/LARGE/BI-2016-00342V_0012.JPEG

110 Ikonen, E. & Zhou, X. Cholesterol transport between cellular membranes: A balancing act between interconnected lipid fluxes. *Developmental Cell* **56**, 1430-1436 (2021). https://doi.org/10.1016/J.DEVCEL.2021.04.025

111 Goldstein, J. L. & Brown, M. S. A century of cholesterol and coronaries: From plaques to genes to statins. *Cell* **161**, 161-172 (2015). https://doi.org/10.1016/j.cell.2015.01.036

112 Zanoni, P. *et al.* Rare variant in scavenger receptor BI raises HDL cholesterol and increases risk of coronary heart disease. *Science* **351**, 1166-1171 (2016). https://doi.org/10.1126/SCIENCE.AAD3517/SUPPL_FILE/AAD3517_ZANONI_SM.PDF

113 Russell, D. W. The enzymes, regulation, and genetics of bile acid synthesis. *Annual Review of Biochemistry* **72**, 137-174 (2003). https://doi.org/10.1146/annurev.biochem.72.121801.161712

114 Chiang, J. Y. L. & Ferrell, J. M. Bile Acids as Metabolic Regulators and Nutrient Sensors. *https://doi.org/10.1146/annurev-nutr-082018-124344* **39**, 175-200 (2019). https://doi.org/10.1146/ANNUREV-NUTR-082018-124344

115 Thomas, C. *et al.* TGR5-Mediated Bile Acid Sensing Controls Glucose Homeostasis. *Cell Metabolism* **10**, 167-177 (2009). https://doi.org/10.1016/j.cmet.2009.08.001

116 van Nierop, F. S. *et al.* Clinical relevance of the bile acid receptor TGR5 in metabolism. *The Lancet Diabetes & Endocrinology* **5**, 224-233 (2017). https://doi.org/10.1016/S2213-8587(16)30155-3

117 Chiang, J. Y. L. Bile Acid Metabolism and Signaling. *Comprehensive Physiology* **3**, 1191-1191 (2013). https://doi.org/10.1002/CPHY.C120023

118 Clifford, B. L. *et al.* FXR activation protects against NAFLD via bile-acid-dependent reductions in lipid absorption. *Cell metabolism* **33**, 1671-1684.e1674 (2021). https://doi.org/10.1016/J.CMET.2021.06.012

119 Shadel, Gerald S. & Horvath, Tamas L. Mitochondrial ROS Signaling in Organismal Homeostasis. *Cell* **163**, 560-569 (2015). https://doi.org/10.1016/J.CELL.2015.10.001

120 Wang, Y. *et al.* SLC25A39 is necessary for mitochondrial glutathione import in mammalian cells. *Nature 2021 599:7883* **599**, 136-140 (2021). https://doi.org/10.1038/s41586-021-04025-w

121 Herzig, S. *et al.* CREB controls hepatic lipid metabolism through nuclear hormone receptor PPAR-γ. *Nature 2003 426:6963* **426**, 190-193 (2003). https://doi.org/10.1038/nature02110

122 Altarejos, J. Y. & Montminy, M. CREB and the CRTC co-activators: sensors for hormonal and metabolic signals. *Nat Rev Mol Cell Biol* **12**, 141-151 (2011). https://doi.org/10.1038/nrm3072

123 Giacomello, M., Pyakurel, A., Glytsou, C. & Scorrano, L. Vol. 21 204-224 (Nature Research, 2020).

124 Lavoie, H., Gagnon, J. & Therrien, M. Vol. 21 607-632 (Nature Research, 2020).

125 Friedman, J. R. *et al.* ER tubules mark sites of mitochondrial division. *Science* **334**, 358-362 (2011). https://doi.org/10.1126/SCIENCE.1207385/SUPPL_FILE/FRIEDMAN.SOM.REV1.PDF

126 Twig, G. *et al.* Fission and selective fusion govern mitochondrial segregation and elimination by autophagy. *EMBO Journal* **27**, 433-446 (2008). https://doi.org/10.1038/SJ.EMBOJ.7601963

127 Bennett, C. F., Latorre-Muro, P. & Puigserver, P. Mechanisms of mitochondrial respiratory adaptation. *Nature Reviews Molecular Cell Biology 2022*, 1-19 (2022). https://doi.org/10.1038/s41580-022-00506-6

128 Cereghetti, G. M. *et al.* Dephosphorylation by calcineurin regulates translocation of Drp1 to mitochondria. *Proceedings of the National Academy of Sciences of the United States of America* **105**, 15803-15808 (2008). https://doi.org/10.1073/PNAS.0808249105/SUPPL_FILE/0808249105SI.PDF

129 Kraus, F., Roy, K., Pucadyil, T. J. & Ryan, M. T. Function and regulation of the divisome for mitochondrial fission. *Nature 2021 590:7844* **590**, 57-66 (2021). https://doi.org/10.1038/s41586-021-03214-x

130 Younossi, Z. M. *et al.* Global epidemiology of nonalcoholic fatty liver disease—Meta-analytic assessment of prevalence, incidence, and outcomes. *Hepatology* **64**, 73-84 (2016). https://doi.org/10.1002/HEP.28431/SUPPINFO

131 Henry, L. *et al.* Review article: the epidemiologic burden of non-alcoholic fatty liver disease across the world. *Alimentary Pharmacology & Therapeutics* **56**, 942-956 (2022). https://doi.org/10.1111/APT.17158

132 Huang, D. Q., El-Serag, H. B. & Loomba, R. Vol. 18 223-238 (Nature Research, 2021).

133 Diehl, A. M. & Day, C. Cause, Pathogenesis, and Treatment of Nonalcoholic Steatohepatitis. *N Engl J Med* **377**, 2063-2072 (2017). https://doi.org/10.1056/NEJMra1503519

134 Eslam, M. & George, J. Genetic contributions to NAFLD: leveraging shared genetics to uncover systems biology. *Nature Reviews Gastroenterology & Hepatology 2019 17:1* **17**, 40-52 (2019). https://doi.org/10.1038/s41575-019-0212-0

135 Romeo, S. *et al.* Genetic variation in PNPLA3 confers susceptibility to nonalcoholic fatty liver disease. *Nature Genetics 2008 40:12* **40**, 1461-1465 (2008). https://doi.org/10.1038/ng.257

136 Anstee, Q. M. & Day, C. P. The genetics of NAFLD. *Nature Reviews Gastroenterology & Hepatology 2013 10:11* **10**, 645-655 (2013). https://doi.org/10.1038/nrgastro.2013.182

137 Pirazzi, C. *et al.* PNPLA3 has retinyl-palmitate lipase activity in human hepatic stellate cells. *Human Molecular Genetics* **23**, 4077-4085 (2014). https://doi.org/10.1093/HMG/DDU121

138 He, S. *et al.* A sequence variation (I148M) in PNPLA3 associated with nonalcoholic fatty liver disease disrupts triglyceride hydrolysis. *The Journal of biological chemistry* **285**, 6706-6715 (2010). https://doi.org/10.1074/JBC.M109.064501

139 Ruhanen, H. *et al.* PNPLA3 mediates hepatocyte triacylglycerol remodeling. *Journal of Lipid Research* **55**, 739-746 (2014). https://doi.org/10.1194/jlr.M046607

140 Parisinos, C. A. *et al.* Genome-wide and Mendelian randomisation studies of liver MRI yield insights into the pathogenesis of steatohepatitis. *Journal of hepatology* **73**, 241-251 (2020). https://doi.org/10.1016/J.JHEP.2020.03.032

141 Emdin, C. A. *et al.* Association of Genetic Variation With Cirrhosis: A Multi-Trait Genome-Wide Association and Gene-Environment Interaction Study. *Gastroenterology* **160**, 1620-1633.e1613 (2021). https://doi.org/10.1053/J.GASTRO.2020.12.011

142 Mahajan, A. *et al.* Refining the accuracy of validated target identification through coding variant fine-mapping in type 2 diabetes. *Nature genetics* **50**, 559-571 (2018). https://doi.org/10.1038/S41588-018-0084-1

143 Kanai, M. *et al.* Genetic analysis of quantitative traits in the Japanese population links cell types to complex human diseases. *Nature genetics* **50**, 390-400 (2018). https://doi.org/10.1038/S41588-018-0047-6

144 Innes, H. *et al.* Genome-Wide Association Study for Alcohol-Related Cirrhosis Identifies Risk Loci in MARC1 and HNRNPUL1. *Gastroenterology* **159**, 1276-1289.e1277 (2020). https://doi.org/10.1053/J.GASTRO.2020.06.014

145 Trépo, E. *et al.* Common genetic variation in alcohol-related hepatocellular carcinoma: a case-control genome-wide association study. *The Lancet. Oncology* **23**, 161-171 (2022). https://doi.org/10.1016/S1470-2045(21)00603-3

146 Kumari, M. *et al.* Adiponutrin Functions as a Nutritionally Regulated Lysophosphatidic Acid Acyltransferase. *Cell Metabolism* **15**, 691-702 (2012). https://doi.org/10.1016/J.CMET.2012.04.008

147 Huang, Y., Cohen, J. C. & Hobbs, H. H. Expression and Characterization of a PNPLA3 Protein Isoform (I148M) Associated with Nonalcoholic Fatty Liver Disease. *Journal of Biological Chemistry* **286**, 37085-37093 (2011). https://doi.org/10.1074/JBC.M111.290114

148 Trépo, E., Romeo, S., Zucman-Rossi, J. & Nahon, P. PNPLA3 gene in liver diseases. *Journal of Hepatology* **65**, 399-412 (2016). https://doi.org/10.1016/J.JHEP.2016.03.011

149 Chen, W., Chang, B., Li, L. & Chan, L. Patatin-like phospholipase domain-containing 3/adiponutrin deficiency in mice is not associated with fatty liver disease. *Hepatology* **52**, 1134-1142 (2010). https://doi.org/10.1002/HEP.23812

150 Basantani, M. K. *et al.* Pnpla3/Adiponutrin deficiency in mice does not contribute to fatty liver disease or metabolic syndrome. *Journal of Lipid Research* **52**, 318-329 (2011). https://doi.org/10.1194/JLR.M011205

151 Li, J. Z. *et al.* Chronic overexpression of PNPLA3I148M in mouse liver causes hepatic steatosis. *The Journal of clinical investigation* **122**, 4130-4144 (2012). https://doi.org/10.1172/JCI65179

152 Luukkonen, P. K. *et al.* Human PNPLA3-I148M variant increases hepatic retention of polyunsaturated fatty acids. *JCI Insight* **4** (2019). https://doi.org/10.1172/jci.insight.127902

153 Smagris, E. *et al.* Pnpla3I148M knockin mice accumulate PNPLA3 on lipid droplets and develop hepatic steatosis. *Hepatology* **61**, 108-118 (2015). https://doi.org/10.1002/HEP.27242/SUPPINFO

154 BasuRay, S., Wang, Y., Smagris, E., Cohen, J. C. & Hobbs, H. H. Accumulation of PNPLA3 on lipid droplets is the basis of associated hepatic steatosis. *Proceedings of the National Academy of Sciences of the United States of America* **116**, 9521-9526 (2019). https://doi.org/10.1073/PNAS.1901974116/SUPPL_FILE/PNAS.1901974116.SAPP.PDF

155 Kumashiro, N. *et al.* Role of patatin-like phospholipase domain-containing 3 on lipid-induced hepatic steatosis and insulin resistance in rats. *Hepatology* **57**, 1763-1772 (2013). https://doi.org/10.1002/HEP.26170

156 Tsuchida, T. & Friedman, S. L. Mechanisms of hepatic stellate cell activation. *Nature Reviews Gastroenterology & Hepatology 2017 14:7* **14**, 397-411 (2017). https://doi.org/10.1038/nrgastro.2017.38

157 Bruschi, F. V. *et al.* The PNPLA3 I148M variant modulates the fibrogenic phenotype of human hepatic stellate cells. *Hepatology* **65**, 1875-1890 (2017). https://doi.org/10.1002/HEP.29041/SUPPINFO

158 Rady, B. *et al.* PNPLA3 downregulation exacerbates the fibrotic response in human hepatic stellate cells. *PLOS ONE* **16**, e0260721-e0260721 (2021). https://doi.org/10.1371/JOURNAL.PONE.0260721

159 Bruschi, F. V. *et al.* PNPLA3 I148M Variant Impairs Liver X Receptor Signaling and Cholesterol Homeostasis in Human Hepatic Stellate Cells. *Hepatology Communications* **3**, 1191-1204 (2019). https://doi.org/10.1002/HEP4.1395

160 Park, J. *et al.* IL-6/STAT3 axis dictates the PNPLA3-mediated susceptibility to non-alcoholic fatty liver disease. *Journal of Hepatology* **78**, 45-56 (2023). https://doi.org/10.1016/j.jhep.2022.08.022

161 Kozlitina, J. *et al.* Exome-wide association study identifies a TM6SF2 variant that confers susceptibility to nonalcoholic fatty liver disease. *Nat Genet* **46**, 352-356 (2014). https://doi.org/10.1038/ng.2901

162 Mahdessian, H. *et al.* TM6SF2 is a regulator of liver fat metabolism influencing triglyceride secretion and hepatic lipid droplet content. *Proceedings of the National Academy of Sciences of the United States of America* **111**, 8913-8918 (2014). https://doi.org/10.1073/pnas.1323785111

163 Liu, Y. L. *et al.* TM6SF2 rs58542926 influences hepatic fibrosis progression in patients with non-alcoholic fatty liver disease. *Nature Communications* **5** (2014). https://doi.org/10.1038/ncomms5309

164 Daly, A. K., Day, C. P., Liu, Y. L. & Anstee, Q. M. TM6SF2 as a genetic risk factor for fibrosis. *Hepatology* **62**, 1321-1321 (2015). https://doi.org/10.1002/hep.27656

165 Zhou, Y. *et al.* Circulating triacylglycerol signatures and insulin sensitivity in NAFLD associated with the E167K variant in TM6SF2. *J Hepatol* **62**, 657-663 (2015). https://doi.org/10.1016/j.jhep.2014.10.010

166 Musso, G., Cassader, M., Paschetta, E. & Gambino, R. TM6SF2 may drive postprandial lipoprotein cholesterol toxicity away from the vessel walls to the liver in NAFLD. *Journal of Hepatology* **64**, 979-981 (2016). https://doi.org/10.1016/J.JHEP.2015.11.036

167 Fan, Y. *et al.* Hepatic Transmembrane 6 Superfamily Member 2 Regulates Cholesterol Metabolism in Mice. *Gastroenterology* **150**, 1208-1218 (2016). https://doi.org/10.1053/J.GASTRO.2016.01.005

168 Ehrhardt, N. *et al.* Hepatic Tm6sf2 overexpression affects cellular ApoB-trafficking, plasma lipid levels, hepatic steatosis and atherosclerosis. *Human Molecular Genetics* **26**, 2719-2731 (2017). https://doi.org/10.1093/HMG/DDX159

169 Smagris, E., Gilyard, S., BasuRay, S., Cohen, J. C. & Hobbs, H. H. Inactivation of Tm6sf2, a Gene Defective in Fatty Liver Disease, Impairs Lipidation but Not Secretion of Very Low Density Lipoproteins. *Journal of Biological Chemistry* **291**, 10659-10676 (2016). https://doi.org/10.1074/JBC.M116.719955

170 O'Hare, E. A. *et al.* TM6SF2 rs58542926 impacts lipid processing in liver and small intestine. *Hepatology* **65**, 1526-1542 (2017). https://doi.org/10.1002/HEP.29021/SUPPINFO

171 Borén, J. *et al.* Effects of TM6SF2 E167K on hepatic lipid and very low-density lipoprotein metabolism in humans. *JCI Insight* **5** (2020). https://doi.org/10.1172/JCI.INSIGHT.144079

172 Luo, F. *et al.* Hepatic TM6SF2 Is Required for Lipidation of VLDL in a Pre-Golgi Compartment in Mice and Rats. *Cmgh* **13**, 879-899 (2022). https://doi.org/10.1016/j.jcmgh.2021.12.008

173 Newberry, E. P. *et al.* Liver-Specific Deletion of Mouse Tm6sf2 Promotes Steatosis, Fibrosis, and Hepatocellular Cancer. *Hepatology* **74**, 1203-1219 (2021). https://doi.org/10.1002/hep.31771

174 Ruhanen, H. *et al.* Depletion of TM6SF2 disturbs membrane lipid composition and dynamics in HuH7 hepatoma cells. *Biochimica et Biophysica Acta (BBA) - Molecular and Cell Biology of Lipids* **1862**, 676-685 (2017). https://doi.org/10.1016/J.BBALIP.2017.04.004

175 Hashidate-Yoshida, T. *et al.* Fatty acyl-chain remodeling by LPCAT3 enriches arachidonate in phospholipid membranes and regulates triglyceride transport. *eLife* **2015**, 1-75 (2015). https://doi.org/10.7554/eLife.06328

176 Wang, B. *et al.* Intestinal Phospholipid Remodeling Is Required for Dietary-Lipid Uptake and Survival on a High-Fat Diet. *Cell Metab* **23**, 492-504 (2016). https://doi.org/10.1016/j.cmet.2016.01.001

177 Li, B. T. *et al.* Disruption of the ERLIN–TM6SF2–APOB complex destabilizes APOB and contributes to non-alcoholic fatty liver disease. *PLOS Genetics* **16**, e1008955-e1008955 (2020). https://doi.org/10.1371/JOURNAL.PGEN.1008955

178 Fagerberg, L. *et al.* Analysis of the Human Tissue-specific Expression by Genome-wide Integration of Transcriptomics and Antibody-based Proteomics. *Molecular & Cellular Proteomics : MCP* **13**, 397-397 (2014). https://doi.org/10.1074/MCP.M113.035600

179 Sampson, N. D. & Hewitt, J. E. SF4 and SFRS14, two related putative splicing factors on human chromosome 19p13.11. *Gene* **305**, 91-100 (2003). https://doi.org/10.1016/S0378-1119(02)01230-1

180 Willer, C. J. *et al.* Newly identified loci that influence lipid concentrations and risk of coronary artery disease. *Nature Genetics 2008 40:2* **40**, 161-169 (2008). https://doi.org/10.1038/ng.76

181 Speliotes, E. K. *et al.* Genome-Wide Association Analysis Identifies Variants Associated with Nonalcoholic Fatty Liver Disease That Have Distinct Effects on Metabolic Traits. *PLoS Genetics* **7**, 1001324-1001324 (2011). https://doi.org/10.1371/JOURNAL.PGEN.1001324

182 DiStefano, J. K. *et al.* Genome-wide analysis of hepatic lipid content in extreme obesity. *Acta Diabetologica* **52**, 373-382 (2014). https://doi.org/10.1007/S00592-014-0654-3/FIGURES/2

183 Zhang, J. *et al.* Disease-Causing Mutations in SF3B1 Alter Splicing by Disrupting Interaction with SUGP1. *Molecular Cell* **76**, 82-95.e87 (2019). https://doi.org/10.1016/J.MOLCEL.2019.07.017

184 Zhang, J. *et al.* DHX15 is involved in SUGP1-mediated RNA missplicing by mutant SF3B1 in cancer. *Proceedings of the National Academy of Sciences of the United States of America* **119**, e2216712119-e2216712119 (2022). https://doi.org/10.1073/PNAS.2216712119/SUPPL_FILE/PNAS.2216712119.SD02.XLSX

185 Kim, M. J. *et al.* SUGP1 is a novel regulator of cholesterol metabolism. *Human Molecular Genetics* **25**, 3106-3116 (2016). https://doi.org/10.1093/HMG/DDW151

186 Gijón, M. A., Riekhof, W. R., Zarini, S., Murphy, R. C. & Voelker, D. R. Lysophospholipid Acyltransferases and Arachidonate Recycling in Human Neutrophils. *Journal of Biological Chemistry* **283**, 30235-30245 (2008). https://doi.org/10.1074/JBC.M806194200

187 Lee, H. C. *et al.* LPIAT1 regulates arachidonic acid content in phosphatidylinositol and is required for cortical lamination in mice. *Molecular Biology of the Cell* **23**, 4689-4700 (2012). https://doi.org/10.1091/mbc.E12-09-0673

188 Buch, S. *et al.* A genome-wide association study confirms PNPLA3 and identifies TM6SF2 and MBOAT7 as risk loci for alcohol-related cirrhosis. *Nature Genetics* **47**, 1443-1448 (2015). https://doi.org/10.1038/ng.3417

189 Mancina, R. M. *et al.* The MBOAT7-TMC4 Variant rs641738 Increases Risk of Nonalcoholic Fatty Liver Disease in Individuals of European Descent. *Gastroenterology* **150**, 1219-1230.e1216 (2016). https://doi.org/10.1053/J.GASTRO.2016.01.032

190 Luukkonen, P. K. *et al.* The MBOAT7 variant rs641738 alters hepatic phosphatidylinositols and increases severity of non-alcoholic fatty liver disease in humans. *Journal of Hepatology* **65**, 1263-1265 (2016). https://doi.org/10.1016/J.JHEP.2016.07.045

191 Teo, K. *et al.* rs641738C>T near MBOAT7 is associated with liver fat, ALT and fibrosis in NAFLD: A meta-analysis. *Journal of hepatology* **74**, 20-30 (2021). https://doi.org/10.1016/J.JHEP.2020.08.027

192 Helsley, R. N. *et al.* Obesity-linked suppression of membrane-bound O-acyltransferase 7 (MBOAT7) drives non-alcoholic fatty liver disease. *eLife* **8**, 1-69 (2019). https://doi.org/10.7554/ELIFE.49882

193 Thangapandi, V. R. *et al.* Loss of hepatic Mboat7 leads to liver fibrosis. *Gut* **70**, 940-950 (2021). https://doi.org/10.1136/GUTJNL-2020-320853

194 Xia, M., Chandrasekaran, P., Rong, S., Fu, X. & Mitsche, M. A. Hepatic deletion of Mboat7 (LPIAT1) causes activation of SREBP-1c and fatty liver. *Journal of Lipid Research* **62**, 100031-100031 (2021). https://doi.org/10.1194/JLR.RA120000856

195 Tanaka, Y. *et al.* LPIAT1/MBOAT7 depletion increases triglyceride synthesis fueled by high phosphatidylinositol turnover. *Gut* **70**, 180-193 (2021). https://doi.org/10.1136/GUTJNL-2020-320646

196 Loss of hepatic Mboat7 leads to liver fibrosis. *Gut* https://doi.org/10.1136/gutjnl-2020-320853

197 Liu, S. *et al.* Molecular cloning and expression analysis of a new gene for short-chain dehydrogenase/reductase 9. *Acta Biochimica Polonica* **54**, 213-218 (2007). https://doi.org/10.18388/abp.2007_3289

198 Abul-Husn, N. S. *et al.* A Protein-Truncating HSD17B13 Variant and Protection from Chronic Liver Disease. *New England Journal of Medicine* **378**, 1096-1106 (2018). https://doi.org/10.1056/NEJMOA1712191/SUPPL_FILE/NEJMOA1712191_DISCLOSURES.PDF

199 Yang, J. *et al.* A 17-Beta-Hydroxysteroid Dehydrogenase 13 Variant Protects From Hepatocellular Carcinoma Development in Alcoholic Liver Disease. *Hepatology (Baltimore, Md.)* **70**, 231-240 (2019). https://doi.org/10.1002/HEP.30623

200 Stickel, F. *et al.* Genetic Variation in HSD17B13 Reduces the Risk of Developing Cirrhosis and Hepatocellular Carcinoma in Alcohol Misusers. *Hepatology (Baltimore, Md.)* **72**, 88-102 (2020). https://doi.org/10.1002/HEP.30996

201 Ma, Y. *et al.* 17-Beta Hydroxysteroid Dehydrogenase 13 Is a Hepatic Retinol Dehydrogenase Associated With Histological Features of Nonalcoholic Fatty Liver Disease. *Hepatology* **69**, 1504-1519 (2019). https://doi.org/10.1002/HEP.30350

202 Anstee, Q. M. *et al.* Genome-wide association study of non-alcoholic fatty liver and steatohepatitis in a histologically characterised cohort☆. *Journal of Hepatology* **73**, 505-515 (2020). https://doi.org/10.1016/J.JHEP.2020.04.003

203 Ma, Y. *et al.* Characterization of essential domains in HSD17B13 for cellular localization and enzymatic activity. *Journal of Lipid Research* **61**, 1400-1409 (2020). https://doi.org/10.1194/JLR.RA120000907

204 Luukkonen, P. K. *et al.* Inhibition of HSD17B13 protects against liver fibrosis by inhibition of pyrimidine catabolism in nonalcoholic steatohepatitis. *Proceedings of the National Academy of Sciences* **120**, e2217543120-e2217543120 (2023). https://doi.org/10.1073/PNAS.2217543120/SUPPL_FILE/PNAS.2217543120.SD01.XLSX

205 Luukkonen, P. K. *et al.* Hydroxysteroid 17-β dehydrogenase 13 variant increases phospholipids and protects against fibrosis in nonalcoholic fatty liver disease. *JCI Insight* **5** (2020). https://doi.org/10.1172/JCI.INSIGHT.132158

206 Mann, J. P. *et al.* Insights into genetic variants associated with NASH-fibrosis from metabolite profiling. *Human Molecular Genetics* **29**, 3451-3463 (2020). https://doi.org/10.1093/hmg/ddaa162

207 Su, W. *et al.* Liver X receptor α induces 17β-hydroxysteroid dehydrogenase-13 expression through SREBP-1c. *American Journal of Physiology - Endocrinology and Metabolism* **312**, E357-E367 (2017). https://doi.org/10.1152/AJPENDO.00310.2016/ASSET/IMAGES/LARGE/ZH10041777180012.JPEG

208 Su, W. *et al.* Phosphorylation of 17β-hydroxysteroid dehydrogenase 13 at serine 33 attenuates nonalcoholic fatty liver disease in mice. *Nature Communications 2022 13:1* **13**, 1-18 (2022). https://doi.org/10.1038/s41467-022-34299-1

209 Adam, M. *et al.* Hydroxysteroid (17β) dehydrogenase 13 deficiency triggers hepatic steatosis and inflammation in mice. *FASEB Journal* **32**, 3434-3447 (2018). https://doi.org/10.1096/FJ.201700914R

210 Ma, Y. *et al.* 17-Beta Hydroxysteroid Dehydrogenase 13 Deficiency Does Not Protect Mice From Obesogenic Diet Injury. *Hepatology* **73**, 1701-1716 (2021). https://doi.org/10.1002/HEP.31517

211 Gruenewald, S. *et al.* The fourth molybdenum containing enzyme mARC: Cloning and involvement in the activation of N-hydroxylated prodrugs. *Journal of Medicinal Chemistry* **51**, 8173-8177 (2008). https://doi.org/10.1021/JM8010417/SUPPL_FILE/JM8010417_SI_001.PDF

212 Klein, J. M. *et al.* The Mitochondrial Amidoxime-reducing Component (mARC1) Is a Novel Signal-anchored Protein of the Outer Mitochondrial Membrane. *Journal of Biological Chemistry* **287**, 42795-42803 (2012). https://doi.org/10.1074/JBC.M112.419424

213 Ott, G., Havemeyer, A. & Clement, B. The mammalian molybdenum enzymes of mARC. *Journal of Biological Inorganic Chemistry* **20**, 265-275 (2015). https://doi.org/10.1007/S00775-014-1216-4/FIGURES/4

214 Schneider, J., Girreser, U., Havemeyer, A., Bittner, F. & Clement, B. Detoxification of Trimethylamine N-Oxide by the Mitochondrial Amidoxime Reducing Component mARC. *Chemical Research in Toxicology* **31**, 447-453 (2018). https://doi.org/10.1021/ACS.CHEMRESTOX.7B00329/ASSET/IMAGES/LARGE/TX-2017-00329E_0004.JPEG

215 Teslovich, T. M. *et al.* Biological, clinical and population relevance of 95 loci for blood lipids. *Nature 2010 466:7307* **466**, 707-713 (2010). https://doi.org/10.1038/nature09270

216 Emdin, C. A. *et al.* A missense variant in Mitochondrial Amidoxime Reducing Component 1 gene and protection against liver disease. *PLoS Genet* **16**, e1008629-e1008629 (2020). https://doi.org/10.1371/journal.pgen.1008629

217 Ott, G. *et al.* Functional Characterization of Protein Variants Encoded by Nonsynonymous Single Nucleotide Polymorphisms in MARC1 and MARC2 in Healthy Caucasians. *Drug Metabolism and Disposition* **42**, 718-725 (2014). https://doi.org/10.1124/DMD.113.055202

218 Hudert, C. A. *et al.* Variants in mitochondrial amidoxime reducing component 1 and hydroxysteroid 17-beta dehydrogenase 13 reduce severity of nonalcoholic fatty liver disease in children and suppress fibrotic pathways through distinct mechanisms. *Hepatology Communications* **6**, 1934-1948 (2022). https://doi.org/10.1002/HEP4.1955

219 Struwe, M. A., Clement, B. & Scheidig, A. Letter to the editor: The clinically relevant MTARC1 p.Ala165Thr variant impacts neither the fold nor active site architecture of the

human mARC1 protein. *Hepatology communications* **6**, 3277-3278 (2022). https://doi.org/10.1002/HEP4.1984

220 Lewis, L. C. *et al.* Hepatocyte mARC1 promotes fatty liver disease. *JHEP Reports* **0**, 100693-100693 (2023). https://doi.org/10.1016/j.jhepr.2023.100693

221 Van Schaftingen, E., Detheux, M. & Da Cunha, M. V. Short-term control of glucokinase activity: role of a regulatory protein. *The FASEB Journal* **8**, 414-419 (1994). https://doi.org/10.1096/FASEBJ.8.6.8168691

222 Goodman, R. P. *et al.* Hepatic NADH reductive stress underlies common variation in metabolic traits. *Nature 2020 583:7814* **583**, 122-126 (2020). https://doi.org/10.1038/s41586-020-2337-2

223 Santoro, N. *et al.* A Variant in the Glucokinase Regulatory Protein (GCKR) Gene is Associated with Fatty Liver in Obese Children and Adolescents. *Hepatology (Baltimore, Md.)* **55**, 781-781 (2012). https://doi.org/10.1002/HEP.24806

224 Chen, J. *et al.* The trans-ancestral genomic architecture of glycemic traits. *Nature Genetics 2021 53:6* **53**, 840-860 (2021). https://doi.org/10.1038/s41588-021-00852-9

225 De La Iglesia, N., Mukhtar, M., Seoane, J., Guinovart, J. J. & Agius, L. The Role of the Regulatory Protein of Glucokinase in the Glucose Sensory Mechanism of the Hepatocyte. *Journal of Biological Chemistry* **275**, 10597-10603 (2000). https://doi.org/10.1074/JBC.275.14.10597

226 Watanabe, H. *et al.* Sirt2 facilitates hepatic glucose uptake by deacetylating glucokinase regulatory protein. *Nature Communications 2017 9:1* **9**, 1-14 (2018). https://doi.org/10.1038/s41467-017-02537-6

227 Beer, N. L. *et al.* The P446L variant in GCKR associated with fasting plasma glucose and triglyceride levels exerts its effect through increased glucokinase activity in liver. *Human Molecular Genetics* **18**, 4081-4088 (2009). https://doi.org/10.1093/HMG/DDP357

228 Kimura, M. *et al.* En masse organoid phenotyping informs metabolic-associated genetic susceptibility to NASH. *Cell* **185**, 4216-4232.e4216 (2022). https://doi.org/10.1016/j.cell.2022.09.031

229 Vaxillaire, M. *et al.* The common P446L polymorphism in GCKR inversely modulates fasting glucose and triglyceride levels and reduces type 2 diabetes risk in the DESIR prospective general French population. *Diabetes* **57**, 2253-2257 (2008). https://doi.org/10.2337/DB07-1807

230 Zain, S. M., Mohamed, Z. & Mohamed, R. A common variant in the glucokinase regulatory gene rs780094 and risk of nonalcoholic fatty liver disease: A meta-analysis. *Journal of Gastroenterology and Hepatology (Australia)* **30**, 21-27 (2015). https://doi.org/10.1111/JGH.12714/SUPINFO

231 Feng, S. *et al.* Effects of Stigmasterol and beta-Sitosterol on Nonalcoholic Fatty Liver Disease in a Mouse Model: A Lipidomic Analysis. *J Agric Food Chem* **66**, 3417-3425 (2018). https://doi.org/10.1021/acs.jafc.7b06146

232 Ooi, G. J. *et al.* Hepatic lipidomic remodeling in severe obesity manifests with steatosis and does not evolve with non-alcoholic steatohepatitis. *Journal of Hepatology* **75**, 524-535 (2021). https://doi.org/10.1016/j.jhep.2021.04.013

233 Rong, X. *et al.* LXRs regulate ER stress and inflammation through dynamic modulation of membrane phospholipid composition. *Cell Metab* **18**, 685-697 (2013). https://doi.org/10.1016/j.cmet.2013.10.002

234 Tian, Y. *et al.* Membrane phospholipid remodeling modulates nonalcoholic steatohepatitis progression by regulating mitochondrial homeostasis. *Hepatology* (2023). https://doi.org/10.1097/HEP.0000000000000375
235 Chen, F. *et al.* Lean NAFLD: A Distinct Entity Shaped by Differential Metabolic Adaptation. *Hepatology* **71**, 1213-1227 (2020). https://doi.org/10.1002/HEP.30908
236 Buzzetti, E., Pinzani, M. & Tsochatzis, E. A. The multiple-hit pathogenesis of non-alcoholic fatty liver disease (NAFLD). *Metabolism: clinical and experimental* **65**, 1038-1048 (2016). https://doi.org/10.1016/J.METABOL.2015.12.012
237 Lebeaupin, C. *et al.* Endoplasmic reticulum stress signalling and the pathogenesis of non-alcoholic fatty liver disease. *Journal of Hepatology* **69**, 927-947 (2018). https://doi.org/10.1016/J.JHEP.2018.06.008
238 Kim, J. Y. *et al.* ER Stress Drives Lipogenesis and Steatohepatitis via Caspase-2 Activation of S1P. *Cell* **175**, 133-145.e115 (2018). https://doi.org/10.1016/j.cell.2018.08.020
239 Nakagawa, H. *et al.* ER stress cooperates with hypernutrition to trigger TNF-dependent spontaneous HCC development. *Cancer Cell* **26**, 331-343 (2014). https://doi.org/10.1016/j.ccr.2014.07.001
240 Dasgupta, D. *et al.* IRE1A Stimulates Hepatocyte-Derived Extracellular Vesicles That Promote Inflammation in Mice With Steatohepatitis. *Gastroenterology* **159**, 1487-1503.e1417 (2020). https://doi.org/10.1053/j.gastro.2020.06.031
241 Fu, S. *et al.* Aberrant lipid metabolism disrupts calcium homeostasis causing liver endoplasmic reticulum stress in obesity. *Nature 2011 473:7348* **473**, 528-531 (2011). https://doi.org/10.1038/nature09968
242 Marí, M. *et al.* Mitochondrial free cholesterol loading sensitizes to TNF- and Fas-mediated steatohepatitis. *Cell Metabolism* **4**, 185-198 (2006). https://doi.org/10.1016/J.CMET.2006.07.006
243 Domínguez-Pérez, M. *et al.* Cholesterol burden in the liver induces mitochondrial dynamic changes and resistance to apoptosis. *Journal of Cellular Physiology* **234**, 7213-7223 (2019). https://doi.org/10.1002/JCP.27474
244 Chaurasia, B. & Summers, S. A. Ceramides – Lipotoxic Inducers of Metabolic Disorders. *Trends in Endocrinology & Metabolism* **26**, 538-550 (2015). https://doi.org/10.1016/J.TEM.2015.07.006
245 Sun, X. *et al.* Neutralization of Oxidized Phospholipids Ameliorates Non-alcoholic Steatohepatitis. *Cell Metabolism* **31**, 1-18 (2020). https://doi.org/10.1016/j.cmet.2019.10.014
246 Sutti, S. & Albano, E. Vol. 17 81-92 (Nature Research, 2020).
247 Samper, E., Nicholls, D. G. & Melov, S. Mitochondrial oxidative stress causes chromosomal instability of mouse embryonic fibroblasts. *Aging Cell* **2**, 277-285 (2003). https://doi.org/10.1046/J.1474-9728.2003.00062.X
248 Woo, D. K. *et al.* Mitochondrial Genome Instability and ROS Enhance Intestinal Tumorigenesis in APCMin/+ Mice. *The American Journal of Pathology* **180**, 24-31 (2012). https://doi.org/10.1016/J.AJPATH.2011.10.003
249 Pinyol, R. *et al.* Molecular characterisation of hepatocellular carcinoma in patients with non-alcoholic steatohepatitis. *Journal of Hepatology* **75**, 865-878 (2021). https://doi.org/10.1016/J.JHEP.2021.04.049/ATTACHMENT/8D73053C-3FF5-4E1E-8D90-4B94DD9D9751/MMC4.XLSX

250 Aranha, M. M. *et al.* Bile acid levels are increased in the liver of patients with steatohepatitis. *European Journal of Gastroenterology and Hepatology* **20**, 519-525 (2008). https://doi.org/10.1097/MEG.0b013e3282f4710a

251 Puri, P. *et al.* The presence and severity of nonalcoholic steatohepatitis is associated with specific changes in circulating bile acids. *Hepatology* **67**, 534-548 (2018). https://doi.org/10.1002/hep.29359

252 Tanaka, N., Matsubara, T., Krausz, K. W., Patterson, A. D. & Gonzalez, F. J. Disruption of phospholipid and bile acid homeostasis in mice with nonalcoholic steatohepatitis. *Hepatology* **56**, 118-129 (2012). https://doi.org/10.1002/HEP.25630

253 Sun, L. *et al.* Bile acids promote diethylnitrosamine-induced hepatocellular carcinoma via increased inflammatory signaling. *American Journal of Physiology-Gastrointestinal and Liver Physiology* **311**, G91-G104 (2016). https://doi.org/10.1152/ajpgi.00027.2015

254 Asgharpour, A. *et al.* A diet-induced animal model of non-alcoholic fatty liver disease and hepatocellular cancer. *Journal of Hepatology* **65**, 579-588 (2016). https://doi.org/10.1016/J.JHEP.2016.05.005

255 Conde de la Rosa, L. *et al.* STARD1 promotes NASH-driven HCC by sustaining the generation of bile acids through the alternative mitochondrial pathway. *Journal of Hepatology* **74**, 1429-1441 (2021). https://doi.org/10.1016/J.JHEP.2021.01.028

256 Rao, A. *et al.* Inhibition of ileal bile acid uptake protects against nonalcoholic fatty liver disease in high-fat diet–fed mice. *Science Translational Medicine* **8**, 357ra122-357ra122 (2016). https://doi.org/10.1126/scitranslmed.aaf4823

257 Friedman, S. L., Neuschwander-Tetri, B. A., Rinella, M. & Sanyal, A. J. Mechanisms of NAFLD development and therapeutic strategies. *Nature Medicine* **24**, 908-922 (2018). https://doi.org/10.1038/s41591-018-0104-9

258 Anstee, Q. M., Reeves, H. L., Kotsiliti, E., Govaere, O. & Heikenwalder, M. From NASH to HCC: current concepts and future challenges. *Nature Reviews Gastroenterology and Hepatology*, 1-1 (2019). https://doi.org/10.1038/s41575-019-0145-7

259 Alkhouri, N., Lawitz, E., Noureddin, M., DeFronzo, R. & Shulman, G. I. GS-0976 (Firsocostat): an investigational liver-directed acetyl-CoA carboxylase (ACC) inhibitor for the treatment of non-alcoholic steatohepatitis (NASH). *Expert Opinion on Investigational Drugs* **29**, 135-141 (2020). https://doi.org/10.1080/13543784.2020.1668374

260 Ratziu, V. *et al.* Aramchol in patients with nonalcoholic steatohepatitis: a randomized, double-blind, placebo-controlled phase 2b trial. *Nature Medicine 2021 27:10* **27**, 1825-1835 (2021). https://doi.org/10.1038/s41591-021-01495-3

261 Vuppalanchi, R., Noureddin, M., Alkhouri, N. & Sanyal, A. J. Therapeutic pipeline in nonalcoholic steatohepatitis. *Nature Reviews Gastroenterology & Hepatology 2021 18:6* **18**, 373-392 (2021). https://doi.org/10.1038/s41575-020-00408-y

262 Francque, S. M. *et al.* A Randomized, Controlled Trial of the Pan-PPAR Agonist Lanifibranor in NASH. *New England Journal of Medicine* **385**, 1547-1558 (2021). https://doi.org/10.1056/nejmoa2036205

263 Younossi, Z. M. *et al.* Obeticholic acid for the treatment of non-alcoholic steatohepatitis: interim analysis from a multicentre, randomised, placebo-controlled phase 3 trial. *The Lancet* **394**, 2184-2196 (2019). https://doi.org/10.1016/S0140-6736(19)33041-7

264 Sanyal, A. J. *et al.* Tropifexor for nonalcoholic steatohepatitis: an adaptive, randomized, placebo-controlled phase 2a/b trial. *Nature Medicine 2023 29:2* **29**, 392-400 (2023). https://doi.org/10.1038/s41591-022-02200-8

265 Kliewer, S. A. & Mangelsdorf, D. J. A Dozen Years of Discovery: Insights into the Physiology and Pharmacology of FGF21. *Cell Metab* **29**, 246-253 (2019). https://doi.org/10.1016/j.cmet.2019.01.004

266 Harrison, S. A. *et al.* Efruxifermin in non-alcoholic steatohepatitis: a randomized, double-blind, placebo-controlled, phase 2a trial. *Nature Medicine 2021 27:7* **27**, 1262-1271 (2021). https://doi.org/10.1038/s41591-021-01425-3

267 Harrison, S. A. *et al.* Licogliflozin for nonalcoholic steatohepatitis: a randomized, double-blind, placebo-controlled, phase 2a study. *Nature Medicine 2022 28:7* **28**, 1432-1438 (2022). https://doi.org/10.1038/s41591-022-01861-9

268 Qu, P. *et al.* DT-109 ameliorates nonalcoholic steatohepatitis in nonhuman primates. *Cell Metabolism* **35**, 742-757.e710 (2023). https://doi.org/10.1016/j.cmet.2023.03.013

269 Colbeau, A., Nachbaur, J. & Vignais, P. M. Enzymac characterization and lipid composition of rat liver subcellular membranes. *Biochimica et Biophysica Acta (BBA) - Biomembranes* **249**, 462-492 (1971). https://doi.org/10.1016/0005-2736(71)90123-4

270 Santoleri, D. & Titchenell, P. M. Resolving the Paradox of Hepatic Insulin Resistance. *Cell Mol Gastroenterol Hepatol* **7**, 447-456 (2019). https://doi.org/10.1016/j.jcmgh.2018.10.016

271 Titchenell, P. M., Lazar, M. A. & Birnbaum, M. J. Unraveling the Regulation of Hepatic Metabolism by Insulin. *Trends Endocrinol Metab* **28**, 497-505 (2017). https://doi.org/10.1016/j.tem.2017.03.003

272 Lin, H. V. & Accili, D. Hormonal regulation of hepatic glucose production in health and disease. *Cell Metab* **14**, 9-19 (2011). https://doi.org/10.1016/j.cmet.2011.06.003

273 Leavens, K. F. & Birnbaum, M. J. Insulin signaling to hepatic lipid metabolism in health and disease. *Crit Rev Biochem Mol Biol* **46**, 200-215 (2011). https://doi.org/10.3109/10409238.2011.562481

274 Spector, A. A. & Yorek, M. A. Membrane lipid composition and cellular function. *J Lipid Res* **26**, 1015-1035 (1985).

275 van Meer, G., Voelker, D. R. & Feigenson, G. W. Membrane lipids: where they are and how they behave. *Nat Rev Mol Cell Biol* **9**, 112-124 (2008). https://doi.org/10.1038/nrm2330

276 Rong, X. *et al.* ER phospholipid composition modulates lipogenesis during feeding and in obesity. *J Clin Invest* **127**, 3640-3651 (2017). https://doi.org/10.1172/JCI93616

277 Wang, B. *et al.* Phospholipid Remodeling and Cholesterol Availability Regulate Intestinal Stemness and Tumorigenesis. *Cell Stem Cell* **22**, 206-220 e204 (2018). https://doi.org/10.1016/j.stem.2017.12.017

278 Tschop, M. H. *et al.* A guide to analysis of mouse energy metabolism. *Nat Methods* **9**, 57-63 (2011). https://doi.org/10.1038/nmeth.1806

279 Muller, T. D., Klingenspor, M. & Tschop, M. H. Revisiting energy expenditure: how to correct mouse metabolic rate for body mass. *Nat Metab* **3**, 1134-1136 (2021). https://doi.org/10.1038/s42255-021-00451-2

280 Bligh, E. G. & Dyer, W. J. A rapid method of total lipid extraction and purification. *Can J Biochem Physiol* **37**, 911-917 (1959). https://doi.org/10.1139/o59-099

281 Demarco, V. G. *et al.* Obesity-related alterations in cardiac lipid profile and nondipping blood pressure pattern during transition to diastolic dysfunction in male db/db mice. *Endocrinology* **154**, 159-171 (2013). https://doi.org/10.1210/en.2012-1835

282 Han, X. & Gross, R. W. Shotgun lipidomics: electrospray ionization mass spectrometric analysis and quantitation of cellular lipidomes directly from crude extracts of biological samples. *Mass Spectrom Rev* **24**, 367-412 (2005). https://doi.org/10.1002/mas.20023

283 de Araujo, M. E., Lamberti, G. & Huber, L. A. Isolation of Early and Late Endosomes by Density Gradient Centrifugation. *Cold Spring Harb Protoc* **2015**, 1013-1016 (2015). https://doi.org/10.1101/pdb.prot083444

284 Lyu, K. *et al.* A Membrane-Bound Diacylglycerol Species Induces PKC-Mediated Hepatic Insulin Resistance. *Cell Metab* **32**, 654-664 e655 (2020). https://doi.org/10.1016/j.cmet.2020.08.001

285 Kim, B. *et al.* Immunogene therapy with fusogenic nanoparticles modulates macrophage response to Staphylococcus aureus. *Nat Commun* **9**, 1969 (2018). https://doi.org/10.1038/s41467-018-04390-7

286 Kim, J. K. Hyperinsulinemic-euglycemic clamp to assess insulin sensitivity in vivo. *Methods Mol Biol* **560**, 221-238 (2009). https://doi.org/10.1007/978-1-59745-448-3_15

287 An, Y. & Scherer, P. E. Mouse Adipose Tissue Protein Extraction. *Bio-protocol* **10**, e3631-e3631 (2020). https://doi.org/10.21769/BioProtoc.3631

288 Lingwood, D. & Simons, K. Detergent resistance as a tool in membrane research. *Nat Protoc* **2**, 2159-2165 (2007). https://doi.org/10.1038/nprot.2007.294

289 Hsieh, W. Y., Williams, K. J., Su, B. & Bensinger, S. J. Profiling of mouse macrophage lipidome using direct infusion shotgun mass spectrometry. *STAR Protoc* **2**, 100235 (2021). https://doi.org/10.1016/j.xpro.2020.100235

290 Kahn, S. E., Hull, R. L. & Utzschneider, K. M. Mechanisms linking obesity to insulin resistance and type 2 diabetes. *Nature* **444**, 840-846 (2006). https://doi.org/10.1038/nature05482

291 Perry, R. J., Samuel, V. T., Petersen, K. F. & Shulman, G. I. The role of hepatic lipids in hepatic insulin resistance and type 2 diabetes. *Nature* **510**, 84-91 (2014). https://doi.org/10.1038/nature13478

292 Henkel, J., Neuschafer-Rube, F., Pathe-Neuschafer-Rube, A. & Puschel, G. P. Aggravation by prostaglandin E2 of interleukin-6-dependent insulin resistance in hepatocytes. *Hepatology* **50**, 781-790 (2009). https://doi.org/10.1002/hep.23064

293 Hall, C., Yu, H. & Choi, E. Insulin receptor endocytosis in the pathophysiology of insulin resistance. *Exp Mol Med* **52**, 911-920 (2020). https://doi.org/10.1038/s12276-020-0456-3

294 Holzer, R. G. *et al.* Saturated fatty acids induce c-Src clustering within membrane subdomains, leading to JNK activation. *Cell* **147**, 173-184 (2011). https://doi.org/10.1016/j.cell.2011.08.034

295 Bergeron, J. J., Di Guglielmo, G. M., Dahan, S., Dominguez, M. & Posner, B. I. Spatial and Temporal Regulation of Receptor Tyrosine Kinase Activation and Intracellular Signal Transduction. *Annu Rev Biochem* **85**, 573-597 (2016). https://doi.org/10.1146/annurev-biochem-060815-014659

296 Bohdanowicz, M. & Grinstein, S. Role of phospholipids in endocytosis, phagocytosis, and macropinocytosis. *Physiol Rev* **93**, 69-106 (2013). https://doi.org/10.1152/physrev.00002.2012

297 Lewis, J. E., Ebling, F. J. P., Samms, R. J. & Tsintzas, K. Going Back to the Biology of FGF21: New Insights. *Trends Endocrinol Metab* **30**, 491-504 (2019). https://doi.org/10.1016/j.tem.2019.05.007

298 Xu, J. *et al.* Fibroblast growth factor 21 reverses hepatic steatosis, increases energy expenditure, and improves insulin sensitivity in diet-induced obese mice. *Diabetes* **58**, 250-259 (2009). https://doi.org/10.2337/db08-0392
299 Camporez, J. P. *et al.* Cellular mechanisms by which FGF21 improves insulin sensitivity in male mice. *Endocrinology* **154**, 3099-3109 (2013). https://doi.org/10.1210/en.2013-1191
300 Markan, K. R. *et al.* Circulating FGF21 is liver derived and enhances glucose uptake during refeeding and overfeeding. *Diabetes* **63**, 4057-4063 (2014). https://doi.org/10.2337/db14-0595
301 Fisher, F. M. *et al.* Obesity is a fibroblast growth factor 21 (FGF21)-resistant state. *Diabetes* **59**, 2781-2789 (2010). https://doi.org/10.2337/db10-0193
302 Samuel, V. T. & Shulman, G. I. Mechanisms for insulin resistance: common threads and missing links. *Cell* **148**, 852-871 (2012). https://doi.org/10.1016/j.cell.2012.02.017
303 Sun, Z. & Lazar, M. A. Dissociating fatty liver and diabetes. *Trends Endocrinol Metab* **24**, 4-12 (2013). https://doi.org/10.1016/j.tem.2012.09.005
304 Simons, K. & Toomre, D. Lipid rafts and signal transduction. *Nat Rev Mol Cell Biol* **1**, 31-39 (2000). https://doi.org/10.1038/35036052
305 Bickel, P. E. Lipid rafts and insulin signaling. *Am J Physiol Endocrinol Metab* **282**, E1-E10 (2002). https://doi.org/10.1152/ajpendo.2002.282.1.E1
306 Balbis, A., Baquiran, G., Bergeron, J. J. & Posner, B. I. Compartmentalization and insulin-induced translocations of insulin receptor substrates, phosphatidylinositol 3-kinase, and protein kinase B in rat liver. *Endocrinology* **141**, 4041-4049 (2000). https://doi.org/10.1210/endo.141.11.7774
307 Murphy, J. E., Padilla, B. E., Hasdemir, B., Cottrell, G. S. & Bunnett, N. W. Endosomes: a legitimate platform for the signaling train. *Proc Natl Acad Sci U S A* **106**, 17615-17622 (2009). https://doi.org/10.1073/pnas.0906541106
308 Owen, B. M. *et al.* FGF21 acts centrally to induce sympathetic nerve activity, energy expenditure, and weight loss. *Cell Metab* **20**, 670-677 (2014). https://doi.org/10.1016/j.cmet.2014.07.012
309 Coskun, T. *et al.* Fibroblast growth factor 21 corrects obesity in mice. *Endocrinology* **149**, 6018-6027 (2008). https://doi.org/10.1210/en.2008-0816
310 Douris, N. *et al.* Central Fibroblast Growth Factor 21 Browns White Fat via Sympathetic Action in Male Mice. *Endocrinology* **156**, 2470-2481 (2015). https://doi.org/10.1210/en.2014-2001
311 Magliano, D. J. & Boyko, E. J. in *IDF DIABETES ATLAS IDF Diabetes Atlas* (2021).
312 Magliano, D. J. *et al.* Trends in incidence of total or type 2 diabetes: systematic review. *BMJ* **366**, l5003 (2019). https://doi.org/10.1136/bmj.l5003
313 Zheng, Y., Ley, S. H. & Hu, F. B. Global aetiology and epidemiology of type 2 diabetes mellitus and its complications. *Nat Rev Endocrinol* **14**, 88-98 (2018). https://doi.org/10.1038/nrendo.2017.151
314 Samuel, V. T. & Shulman, G. I. The pathogenesis of insulin resistance: integrating signaling pathways and substrate flux. *J Clin Invest* **126**, 12-22 (2016). https://doi.org/10.1172/JCI77812
315 Zhao, Y. *et al.* Identification and characterization of a major liver lysophosphatidylcholine acyltransferase. *J Biol Chem* **283**, 8258-8265 (2008). https://doi.org/10.1074/jbc.M710422200

316 Tian, Y. *et al.* Hepatic Phospholipid Remodeling Modulates Insulin Sensitivity and Systemic Metabolism. *Adv Sci (Weinh)*, e2300416 (2023). https://doi.org/10.1002/advs.202300416

317 Shi, R., Lu, W., Tian, Y. & Wang, B. Intestinal SEC16B modulates obesity by regulating chylomicron metabolism. *Mol Metab* **70**, 101693 (2023). https://doi.org/10.1016/j.molmet.2023.101693

318 Shulman, G. I. Cellular mechanisms of insulin resistance. *J Clin Invest* **106**, 171-176 (2000). https://doi.org/10.1172/JCI10583

319 Petersen, M. C. & Shulman, G. I. Mechanisms of Insulin Action and Insulin Resistance. *Physiol Rev* **98**, 2133-2223 (2018). https://doi.org/10.1152/physrev.00063.2017

320 James, D. E., Stockli, J. & Birnbaum, M. J. The aetiology and molecular landscape of insulin resistance. *Nat Rev Mol Cell Biol* **22**, 751-771 (2021). https://doi.org/10.1038/s41580-021-00390-6

321 Yaribeygi, H., Farrokhi, F. R., Butler, A. E. & Sahebkar, A. Insulin resistance: Review of the underlying molecular mechanisms. *J Cell Physiol* **234**, 8152-8161 (2019). https://doi.org/10.1002/jcp.27603

322 Huang, D. Q., El-Serag, H. B. & Loomba, R. Global epidemiology of NAFLD-related HCC: trends, predictions, risk factors and prevention. *Nat Rev Gastroenterol Hepatol* **18**, 223-238 (2021). https://doi.org/10.1038/s41575-020-00381-6

323 Friedman, S. L., Neuschwander-Tetri, B. A., Rinella, M. & Sanyal, A. J. Mechanisms of NAFLD development and therapeutic strategies. *Nat Med* **24**, 908-922 (2018). https://doi.org/10.1038/s41591-018-0104-9

324 Eslam, M., Valenti, L. & Romeo, S. Genetics and epigenetics of NAFLD and NASH: Clinical impact. *J Hepatol* **68**, 268-279 (2018). https://doi.org/10.1016/j.jhep.2017.09.003

325 Sookoian, S., Pirola, C. J., Valenti, L. & Davidson, N. O. Genetic Pathways in Nonalcoholic Fatty Liver Disease: Insights From Systems Biology. *Hepatology* **72**, 330-346 (2020). https://doi.org/10.1002/hep.31229

326 Puri, P. *et al.* A lipidomic analysis of nonalcoholic fatty liver disease. *Hepatology* **46**, 1081-1090 (2007). https://doi.org/10.1002/hep.21763

327 Ooi, G. J. *et al.* Hepatic lipidomic remodeling in severe obesity manifests with steatosis and does not evolve with non-alcoholic steatohepatitis. *J Hepatol* **75**, 524-535 (2021). https://doi.org/10.1016/j.jhep.2021.04.013

328 Kim, Y. C. *et al.* Intestinal FGF15/19 physiologically repress hepatic lipogenesis in the late fed-state by activating SHP and DNMT3A. *Nat Commun* **11**, 5969 (2020). https://doi.org/10.1038/s41467-020-19803-9

329 Fujiwara, N. *et al.* Molecular signatures of long-term hepatocellular carcinoma risk in nonalcoholic fatty liver disease. *Sci Transl Med* **14**, eabo4474 (2022). https://doi.org/10.1126/scitranslmed.abo4474

330 Amunugama, K. *et al.* Identification of novel neutrophil very long chain plasmalogen molecular species and their myeloperoxidase mediated oxidation products in human sepsis. *Redox Biol* **48**, 102208 (2021). https://doi.org/10.1016/j.redox.2021.102208

331 Jung, Y., Zhao, M. & Svensson, K. J. Isolation, culture, and functional analysis of hepatocytes from mice with fatty liver disease. *STAR Protoc* **1**, 100222 (2020). https://doi.org/10.1016/j.xpro.2020.100222

332 Kleiner, D. E. *et al.* Design and validation of a histological scoring system for nonalcoholic fatty liver disease. *Hepatology* **41**, 1313-1321 (2005). https://doi.org/10.1002/hep.20701

333 Dobin, A. *et al.* STAR: ultrafast universal RNA-seq aligner. *Bioinformatics* **29**, 15-21 (2013). https://doi.org/10.1093/bioinformatics/bts635

334 Liao, Y., Smyth, G. K. & Shi, W. The R package Rsubread is easier, faster, cheaper and better for alignment and quantification of RNA sequencing reads. *Nucleic Acids Res* **47**, e47 (2019). https://doi.org/10.1093/nar/gkz114

335 Love, M. I., Huber, W. & Anders, S. Moderated estimation of fold change and dispersion for RNA-seq data with DESeq2. *Genome Biol* **15**, 550 (2014). https://doi.org/10.1186/s13059-014-0550-8

336 Malik, A. N., Czajka, A. & Cunningham, P. Accurate quantification of mouse mitochondrial DNA without co-amplification of nuclear mitochondrial insertion sequences. *Mitochondrion* **29**, 59-64 (2016). https://doi.org/10.1016/j.mito.2016.05.003

337 Frezza, C., Cipolat, S. & Scorrano, L. Organelle isolation: functional mitochondria from mouse liver, muscle and cultured fibroblasts. *Nat Protoc* **2**, 287-295 (2007). https://doi.org/10.1038/nprot.2006.478

338 Tsuchida, T. *et al.* A simple diet- and chemical-induced murine NASH model with rapid progression of steatohepatitis, fibrosis and liver cancer. *J Hepatol* **69**, 385-395 (2018). https://doi.org/10.1016/j.jhep.2018.03.011

339 Zhang, X. Q., Xu, C. F., Yu, C. H., Chen, W. X. & Li, Y. M. Role of endoplasmic reticulum stress in the pathogenesis of nonalcoholic fatty liver disease. *World J Gastroenterol* **20**, 1768-1776 (2014). https://doi.org/10.3748/wjg.v20.i7.1768

340 Zorov, D. B., Juhaszova, M. & Sollott, S. J. Mitochondrial reactive oxygen species (ROS) and ROS-induced ROS release. *Physiol Rev* **94**, 909-950 (2014). https://doi.org/10.1152/physrev.00026.2013

341 Lykkesfeldt, J. Ascorbate and dehydroascorbic acid as reliable biomarkers of oxidative stress: analytical reproducibility and long-term stability of plasma samples subjected to acidic deproteinization. *Cancer Epidemiol Biomarkers Prev* **16**, 2513-2516 (2007). https://doi.org/10.1158/1055-9965.EPI-07-0639

342 Garcia-Ruiz, C. & Fernandez-Checa, J. C. Mitochondrial Oxidative Stress and Antioxidants Balance in Fatty Liver Disease. *Hepatol Commun* **2**, 1425-1439 (2018). https://doi.org/10.1002/hep4.1271

343 Win, S. *et al.* New insights into the role and mechanism of c-Jun-N-terminal kinase signaling in the pathobiology of liver diseases. *Hepatology* **67**, 2013-2024 (2018). https://doi.org/10.1002/hep.29689

344 Li, S. *et al.* The Role of Oxidative Stress and Antioxidants in Liver Diseases. *Int J Mol Sci* **16**, 26087-26124 (2015). https://doi.org/10.3390/ijms161125942

345 Peng, K. Y. *et al.* Mitochondrial dysfunction-related lipid changes occur in nonalcoholic fatty liver disease progression. *J Lipid Res* **59**, 1977-1986 (2018). https://doi.org/10.1194/jlr.M085613

346 Detmer, S. A. & Chan, D. C. Functions and dysfunctions of mitochondrial dynamics. *Nat Rev Mol Cell Biol* **8**, 870-879 (2007). https://doi.org/10.1038/nrm2275

347 Filomeni, G., De Zio, D. & Cecconi, F. Oxidative stress and autophagy: the clash between damage and metabolic needs. *Cell Death Differ* **22**, 377-388 (2015). https://doi.org/10.1038/cdd.2014.150

348 Haberzettl, P. & Hill, B. G. Oxidized lipids activate autophagy in a JNK-dependent manner by stimulating the endoplasmic reticulum stress response. *Redox Biol* **1**, 56-64 (2013). https://doi.org/10.1016/j.redox.2012.10.003

349 Neuschwander-Tetri, B. A. Hepatic lipotoxicity and the pathogenesis of nonalcoholic steatohepatitis: the central role of nontriglyceride fatty acid metabolites. *Hepatology* **52**, 774-788 (2010). https://doi.org/10.1002/hep.23719

350 Ioannou, G. N. The Role of Cholesterol in the Pathogenesis of NASH. *Trends Endocrinol Metab* **27**, 84-95 (2016). https://doi.org/10.1016/j.tem.2015.11.008

351 Shi, Y. Emerging roles of cardiolipin remodeling in mitochondrial dysfunction associated with diabetes, obesity, and cardiovascular diseases. *J Biomed Res* **24**, 6-15 (2010). https://doi.org/10.1016/S1674-8301(10)60003-6

352 Seifert, E. L., Estey, C., Xuan, J. Y. & Harper, M. E. Electron transport chain-dependent and -independent mechanisms of mitochondrial H2O2 emission during long-chain fatty acid oxidation. *J Biol Chem* **285**, 5748-5758 (2010). https://doi.org/10.1074/jbc.M109.026203

353 Arab, J. P., Karpen, S. J., Dawson, P. A., Arrese, M. & Trauner, M. Bile acids and nonalcoholic fatty liver disease: Molecular insights and therapeutic perspectives. *Hepatology (Baltimore, Md.)* **65**, 350-350 (2017). https://doi.org/10.1002/HEP.28709

354 Gabbi, C. & Gustafsson, J.-Å. Bile acids in nonalcoholic steatohepatitis: Inserting nuclear receptors into the circle. *Hepatology* **56**, 2008-2009 (2012). https://doi.org/10.1002/HEP.25812

355 Younossi, Z. *et al.* Global burden of NAFLD and NASH: trends, predictions, risk factors and prevention. *Nat Rev Gastroenterol Hepatol* **15**, 11-20 (2018). https://doi.org/10.1038/nrgastro.2017.109

356 McCullough, A. J. The clinical features, diagnosis and natural history of nonalcoholic fatty liver disease. *Clin Liver Dis* **8**, 521-533, viii (2004). https://doi.org/10.1016/j.cld.2004.04.004

357 Sookoian, S. & Pirola, C. J. Meta-analysis of the influence of I148M variant of patatin-like phospholipase domain containing 3 gene (PNPLA3) on the susceptibility and histological severity of nonalcoholic fatty liver disease. *Hepatology* **53**, 1883-1894 (2011). https://doi.org/10.1002/hep.24283

358 Kozlitina, J. *et al.* Exome-wide association study identifies a TM6SF2 variant that confers susceptibility to nonalcoholic fatty liver disease. *Nat Genet* **46**, 352-356 (2014). https://doi.org/10.1038/ng.2901

359 Emdin, C. A. *et al.* A missense variant in Mitochondrial Amidoxime Reducing Component 1 gene and protection against liver disease. *PLoS Genet* **16**, e1008629 (2020). https://doi.org/10.1371/journal.pgen.1008629

360 Mancina, R. M. *et al.* The MBOAT7-TMC4 Variant rs641738 Increases Risk of Nonalcoholic Fatty Liver Disease in Individuals of European Descent. *Gastroenterology* **150**, 1219-1230 e1216 (2016). https://doi.org/10.1053/j.gastro.2016.01.032

361 Helsley, R. N. *et al.* Obesity-linked suppression of membrane-bound O-acyltransferase 7 (MBOAT7) drives non-alcoholic fatty liver disease. *Elife* **8** (2019). https://doi.org/10.7554/eLife.49882

362 Xia, M., Chandrasekaran, P., Rong, S., Fu, X. & Mitsche, M. A. Hepatic deletion of Mboat7 (LPIAT1) causes activation of SREBP-1c and fatty liver. *J Lipid Res* **62**, 100031 (2021). https://doi.org/10.1194/jlr.RA120000856

363 Pessayre, D. & Fromenty, B. NASH: a mitochondrial disease. *J Hepatol* **42**, 928-940 (2005). https://doi.org/10.1016/j.jhep.2005.03.004

364 George, J. *et al.* Lipid peroxidation, stellate cell activation and hepatic fibrogenesis in a rat model of chronic steatohepatitis. *J Hepatol* **39**, 756-764 (2003).

365 Youle, R. J. & van der Bliek, A. M. Mitochondrial fission, fusion, and stress. *Science* **337**, 1062-1065 (2012). https://doi.org/10.1126/science.1219855

366 Yu, T., Robotham, J. L. & Yoon, Y. Increased production of reactive oxygen species in hyperglycemic conditions requires dynamic change of mitochondrial morphology. *Proc Natl Acad Sci U S A* **103**, 2653-2658 (2006). https://doi.org/10.1073/pnas.0511154103

367 Wang, B. *et al.* Intestinal phospholipid remodeling is required for dietary-lipid uptake and survival on a high-fat diet. *Cell Metabolism* **23**, 492-504 (2016). https://doi.org/10.1016/j.cmet.2016.01.001

368 Wang, B. *et al.* Phospholipid Remodeling and Cholesterol Availability Regulate Intestinal Stemness and Tumorigenesis. *Cell Stem Cell* **22**, 206-220.e204 (2018). https://doi.org/10.1016/j.stem.2017.12.017

369 He, M. *et al.* Inhibiting Phosphatidylcholine Remodeling in Adipose Tissue Increases Insulin Sensitivity. *Diabetes* **72**, 1547-1559 (2023). https://doi.org/10.2337/db23-0317

370 Ferrara, P. J. *et al.* Lysophospholipid acylation modulates plasma membrane lipid organization and insulin sensitivity in skeletal muscle. *Journal of Clinical Investigation* **131** (2021). https://doi.org/10.1172/JCI135963

371 Rong, X. *et al.* ER phospholipid composition modulates lipogenesis during feeding and in obesity. *Journal of Clinical Investigation* **127**, 3640-3651 (2017). https://doi.org/10.1172/JCI93616

372 Wattacheril, J. & Sanyal, A. J. Lean NAFLD: an Underrecognized Outlier. *Current Hepatology Reports* **15**, 134-139 (2016). https://doi.org/10.1007/s11901-016-0302-1

373 Xu, R., Pan, J., Zhou, W., Ji, G. & Dang, Y. Recent advances in lean NAFLD. *Biomedicine & Pharmacotherapy* **153**, 113331 (2022). https://doi.org/https://doi.org/10.1016/j.biopha.2022.113331

374 Kozlitina, J. *et al.* Exome-wide association study identifies a TM6SF2 variant that confers susceptibility to nonalcoholic fatty liver disease. *Nature Genetics* **46**, 352-356 (2014). https://doi.org/10.1038/ng.2901

375 Rinella, M. E. & Green, R. M. The methionine-choline deficient dietary model of steatohepatitis does not exhibit insulin resistance. *Journal of Hepatology* **40**, 47-51 (2004). https://doi.org/https://doi.org/10.1016/j.jhep.2003.09.020

376 Luukkonen, P. K. *et al.* Impaired hepatic lipid synthesis from polyunsaturated fatty acids in TM6SF2 E167K variant carriers with NAFLD. *Journal of Hepatology* **67**, 128-136 (2017). https://doi.org/10.1016/j.jhep.2017.02.014

377 Ruhanen, H. *et al.* Depletion of TM6SF2 disturbs membrane lipid composition and dynamics in HuH7 hepatoma cells. *Biochimica et Biophysica Acta (BBA) - Molecular and Cell Biology of Lipids* **1862**, 676-685 (2017). https://doi.org/https://doi.org/10.1016/j.bbalip.2017.04.004

378 Kim, K. H. *et al.* Autophagy deficiency leads to protection from obesity and insulin resistance by inducing Fgf21 as a mitokine. *Nature Medicine* **19**, 83-92 (2013). https://doi.org/10.1038/nm.3014

379 Bresciani, N. *et al.* The Slc25a47 locus is a novel determinant of hepatic mitochondrial function implicated in liver fibrosis. *Journal of Hepatology* **77**, 1071-1082 (2022). https://doi.org/10.1016/J.JHEP.2022.05.040

Appendix A: Supplemental Videos

The eight supplemental videos correspond to Chapter 2. They were saved as .avi files and were referenced as Video S1-S8. Detailed information is listed below.

advs5661-sup-0002-videos1.avi: Video S1, Cy3-insulin imaging of LKO hepatocyte with PBS treatment.

advs5661-sup-0003-videos2.avi: Video S2, Cy3-insulin imaging of F/F hepatocyte with PBS treatment.

advs5661-sup-0004-videos3.avi: Video S3, Alexa-transferrin imaging of LKO hepatocyte with PBS treatment.

advs5661-sup-0005-videos4.avi: Video S4, Alexa-transferrin imaging of F/F hepatocyte with PBS treatment.

advs5661-sup-0006-videos5.avi: Video S5, Cy3-insulin imaging of F/F hepatocyte treated with DPPC.

advs5661-sup-0007-videos6.avi: Video S6, Cy3-insulin imaging of F/F hepatocyte treated with PAPC.

advs5661-sup-0008-videos7.avi: Video S7, Cy3-insulin imaging of LKO hepatocyte treated with DPPC.

advs5661-sup-0009-videos8.avi: Video S8, Cy3-insulin imaging of LKO hepatocyte treated with PAPC.